Universiteit
Leiden
The Netherlands

Young suns and infant planets: probing the origins of solar systems

Bohn, A.J.

Citation
Bohn, A. J. (2021, September 22). *Young suns and infant planets: probing the origins of solar systems*. Retrieved from https://hdl.handle.net/1887/3213465

Version:	Publisher's Version
License:	Licence agreement concerning inclusion of doctoral thesis in the Institutional Repository of the University of Leiden
Downloaded from:	https://hdl.handle.net/1887/3213465

Note: To cite this publication please use the final published version (if applicable).

Young suns and infant planets

Probing the origins of solar systems

PhD Thesis

Alexander Julian Bohn

Young suns and infant planets
Probing the origins of solar systems

Proefschrift

ter verkrijging van
de graad van doctor aan de Universiteit Leiden,
op gezag van rector magnificus prof.dr.ir. H. Bijl,
volgens besluit van het college voor promoties
te verdedigen op woensdag 22 september 2021
klokke 16:15 uur

door

Alexander Julian Bohn

geboren te Würzburg, Duitsland
in 1993

Promotor:	Prof.dr. C.U. Keller	
Co-promotors:	Dr. M.A. Kenworthy	
	Dr.ir. F. Snik	
Promotiecommissie:	Prof.dr. H.J.A. Röttgering	Universiteit Leiden
	Prof.dr. I.A.G. Snellen	Universiteit Leiden
	Prof.dr. B.A. Biller	The University of Edinburgh
	Prof.dr. P.M. Hinz	University of California Santa Cruz
	Dr. Q.M. Konopacky	University of California San Diego
	Dr. A.-M. Lagrange	Université Grenoble Alpes

ISBN: 978-94-6419-262-9

A digital copy of this thesis can be found at `http://openaccess.leidenuniv.nl`

Cover: The front side of the thesis cover shows the multi-planet system that was detected around YSES 1. On the backside a circumstellar disk around Wray 15-788 is visualized. Based on observations collected at the European Organisation for Astronomical Research in the Southern Hemisphere under ESO programs 0101.C-0153(A) and 0104.C-0265(A).

© A. J. Bohn (2021)

Contents

Contents iii

List of Figures vii

List of Tables xi

1 Introduction **1**
1.1 The search for life in the Universe 1
1.2 The exoplanet revolution 5
1.2.1 Indirect detections of exoplanets 8
1.2.2 Direct detections of exoplanets 14
1.3 Formation of gas giant planets 27
1.3.1 Direct imaging surveys 28
1.3.2 Atmospheric characterization of directly imaged planets 30
1.4 The Young Suns Exoplanet Survey 31
1.5 Thesis outline 33

2 A multiplicity study of transiting exoplanet host stars **37**
2.1 Introduction 39
2.2 Observations 40
2.3 Data reduction 41
2.4 Results and analysis 44
2.4.1 Determining consistent ages for the exoplanet host stars 44
2.4.2 Characterisation of CCs 44
2.4.3 Multiplicity rate 62
2.4.4 Detection limits 62
2.5 Discussion 66
2.5.1 Multiplicity rate 66
2.5.2 Hot Jupiter host stars 66
2.5.3 Correlation between stellar multiplicity and exoplanet eccentricities 68
2.6 Conclusions 68
2.A Observational setup 69
2.B Individual detection limits 69

3 Discovery of a directly imaged disk around the Sco-Cen member Wray 15-788 79
3.1 Introduction . . . 81
3.2 Observations . . . 81
3.2.1 Classical imaging . . . 83
3.2.2 Dual-polarization imaging . . . 83
3.3 Data reduction . . . 84
3.3.1 Classical imaging . . . 84
3.3.2 Dual-polarization imaging . . . 85
3.4 Observational results . . . 85
3.4.1 CI data . . . 86
3.4.2 DPI data . . . 86
3.5 Analysis . . . 87
3.5.1 Association of Wray 15-788 with HD 98363 . . . 87
3.5.2 SED modeling . . . 89
3.5.3 Imaging data . . . 90
3.6 Discussion . . . 98
3.6.1 SED analysis . . . 98
3.6.2 Disk morphology . . . 100
3.6.3 Comparison with HD 98363 . . . 101
3.7 Conclusions . . . 101
3.A Reference star library . . . 102
3.B Other reduction strategies . . . 104
3.B.1 CI data . . . 104
3.B.2 DPI data . . . 105

4 Detection of a directly-imaged planetary mass companion around YSES 1 107
4.1 Introduction . . . 108
4.2 Observations . . . 108
4.2.1 X-SHOOTER . . . 110
4.2.2 SPHERE . . . 110
4.2.3 NACO . . . 112
4.3 Data reduction . . . 112
4.3.1 X-SHOOTER data . . . 112
4.3.2 SPHERE data . . . 113
4.3.3 NACO data . . . 113
4.4 Results and analysis . . . 114
4.4.1 Stellar properties . . . 114
4.4.2 Companion properties . . . 116
4.4.3 Detection limits . . . 122
4.5 Discussion . . . 125
4.5.1 Companion properties . . . 125
4.5.2 Comparison to other directly imaged sub-stellar companions . . . 126
4.5.3 Formation scenarios . . . 127
4.6 Conclusion . . . 128
4.A Proper motion analysis of other point sources . . . 129

5 Two directly imaged planets around the young, solar analog YSES 1 131
5.1 Introduction . . . 132

5.2 Observations and data reduction . . . 132
5.3 Results and analysis . . . 133
5.3.1 Astrometric analysis . . . 133
5.3.2 Photometric analysis . . . 135
5.3.3 Dynamical stability . . . 138
5.4 Conclusions . . . 140
5.A Observational setup and conditions . . . 140
5.B Data reduction . . . 140
5.B.1 SPHERE data . . . 140
5.B.2 NACO data . . . 142
5.C Signal-to-noise assessment . . . 142
5.D Posterior distributions of SED fit . . . 142
5.E Dynamical modeling . . . 143

6 Discovery of a directly imaged planet to the young solar analog YSES 2 147
6.1 Introduction . . . 149
6.2 Nomenclature of YSES planets . . . 150
6.3 Observations and data reduction . . . 150
6.4 Stellar properties . . . 151
6.4.1 Previous studies . . . 152
6.4.2 Spectral analysis of YSES 2 . . . 152
6.4.3 Updated stellar parameters . . . 154
6.5 Observational results and analysis . . . 155
6.5.1 Companion astrometry . . . 155
6.5.2 Companion photometry . . . 157
6.5.3 Detection limits . . . 160
6.6 Discussion . . . 163
6.7 Conclusions . . . 165
6.A Observational conditions and setup . . . 166
6.B Reference library . . . 166
6.C Extraction of companion astrometry and photometry . . . 168
6.D Astrometric analysis of background objects . . . 170

7 Outlook 175
7.1 LEGACYS: The Large Extrasolar Giant planet Abundance Census around Young Suns . . . 175
7.2 Our place in the Universe . . . 177

Bibliography 179

Summary 197
The Young Suns Exoplanet Survey . . . 198
Future prospects . . . 200

Samenvatting 201
De Young Suns Exoplanet Survey . . . 203
Toekomstperspectief . . . 204

Zusammenfassung 205

Die Young Suns Exoplanet Survey 207
Ausblick 208

List of publications **209**
Refereed publications 209
Submitted publications 212
Conference proceedings 212

Curriculum vitae **215**

Software **217**

Acknowledgments **219**

List of Figures

1.1 Confirmed extrasolar and Solar System planets 7
1.2 The radial velocity method 8
1.3 The transit method 10
1.4 Microlensing events 12
1.5 Thermal star to planet contrast as a function of system age 18
1.6 Diffraction versus seeing limited PSFs 20
1.7 Schematic setup of an AO system 21
1.8 Optical design of a basic Lyot coronagraph 22
1.9 Comparison of images obtained without and with a coronagraph 23
1.10 Contrast improvement with ADI 24
1.11 The multi-planetary system around HR 8799 26
1.12 Demographics of directly imaged exoplanets to Sun-like stars 29
1.13 Exemplary field of view of an YSES target 31
1.14 Color magnitude diagram of YSES candidate companions 32

2.1 Newly detected candidate companions around transiting exoplanet host stars from SPHERE/IRDIS data 45
2.2 Previously detected candidate companions around transiting exoplanet host stars from SPHERE/IRDIS data 46
2.3 Proper motion analysis of candidate companions 1 and 2 around HAT-P-57 51
2.4 Proper motion analysis of candidate companion 1 around WASP-7 53
2.5 Proper motion analysis of candidate companion 1 around WASP-54 . . . 55
2.6 Proper motion analysis of candidate companion 1 around WASP-76 . . . 57
2.7 Proper motion analysis of candidate companion 1 around WASP-87 . . . 58
2.8 Proper motion analysis of candidate companion 2 around WASP-108 . . . 59
2.9 Proper motion analysis of candidate companion 1 around WASP-123 . . . 61
2.10 Detection limits of our SPHERE survey for detection of stellar companions to known exoplanet host stars 63
2.11 Histograms of hot Jupiter system properties 67
2.12 Detection limits of individual targets 72

3.1 Reduced SPHERE images of Wray 15-788 85
3.2 Annotated version of Figure 3.1 **b** 87

3.3 Hertzsprung-Russell diagram for the binary system of Wray 15-788 and HD 98363 . . . 88
3.4 De-reddened spectral energy distribution of Wray 15-788 . . . 89
3.5 Signal-to-noise ratio measurements of the disk flux of Wray 15-788 . . . 92
3.6 Polar projection of the disk around Wray 15-788 . . . 93
3.7 Comparison to average images from reduced reference library targets I . 96
3.8 Comparison to average images from reduced reference library targets II . 97
3.9 Contrast and mass limits around Wray 15-788 . . . 99
3.10 Other reductions of SPHERE classical imaging data on Wray 15-788 . . . 104
3.11 Other reductions of SPHERE dual-polarimetric imaging data on Wray 15-788 . . . 105

4.1 Reduced imaging data on YSES 1 . . . 112
4.2 Stellar properties of YSES 1 . . . 115
4.3 Proper motion plot of the companion south-west of YSES 1 . . . 118
4.4 Best-fit result to the spectral energy distribution of YSES 1b . . . 120
4.5 Posterior distributions of best-fit parameters . . . 120
4.6 Color-magnitude diagram for YSES 1b . . . 123
4.7 Detection limits for SPHERE and NACO datasets on YSES 1 . . . 124
4.8 Directly imaged sub-stellar companions around solar-mass stars . . . 127
4.9 Proper motion analysis of other candidate companions around YSES 1 . . 130

5.1 Two planetary-mass companions around YSES 1 . . . 134
5.2 Multiepoch proper motion assessments of YSES 1b, c, and confirmed background objects . . . 135
5.3 SED of YSES 1 . . . 137
5.4 Color–magnitude diagram for YSES 1b and c . . . 139
5.5 Signal-to-noise ratio assessment of YSES 1c . . . 143
5.6 Posterior distributions of the photometric SED fit of YSES 1c . . . 144
5.7 System stability analysis I . . . 145
5.8 System stability analysis II . . . 145

6.1 Spectral energy distribution of YSES 2 . . . 154
6.2 Multi-epoch observations of YSES 2 and its planetary-mass companion . 157
6.3 Proper motion plot for YSES 2b . . . 158
6.4 Color-magnitude diagram for YSES 2b . . . 159
6.5 5σ detection limits of our SPHERE/IRDIS on YSES 2 . . . 161
6.6 Reduced SPHERE data on YSES 2 for the full IRDIS field of view . . . 172
6.7 Proper motion plot for background objects in the SPHERE/IRDIS field of view around YSES 2 . . . 173

7.1 Schematic overview of the LEGACYS project . . . 176
7.2 LEGACYS sample compared to other direct imaging surveys . . . 177

1 Potential formation mechanisms of wide-orbit gas giant planets . . . 198
2 A circumstellar disk around Wray 15-788 . . . 199
3 The planetary systems around YSES 1 and YSES 2 . . . 200

4 Mogelijke ontstaansmechanismes van gasreuzen op wijde banen . . . 202
5 Een circumstellaire schijf rond de ster Wray 15-788 . . . 203

6 De planetenstelsels YSES 1 en YSES 2 204

7 Mögliche Szenarien für die Entstehung weiter Gasriesen 206
8 Eine circum-stellare Scheibe um Wray 15-788 herum 207
9 Die Planetensysteme YSES 1 und YSES 2 208

List of Tables

2.1 Stellar and planetary properties of the targets 42
2.2 Astrometry and photometry of candidate companions within the IRDIS field of view 48
2.3 Contrast performance for all datasets evaluated at discrete separations . . 64
2.4 Observational setup and weather conditions for all acquired data 70

3.1 Stellar parameters of Wray 15-788 and HD 98363 82
3.2 SPHERE observations of Wray 15-788 83
3.3 Ellipse fit parameters 91
3.4 Best fit parameters of the ellipse fitting 93
3.5 Observations of reference stars used for PSF subtraction 103

4.1 Stellar properties of YSES 1 109
4.2 High-contrast observations of YSES 1 111
4.3 Astrometry of YSES 1b 117
4.4 Photometry of YSES 1b and its host 119

5.1 Photometry of YSES 1c and its host 136
5.2 High-contrast observations of YSES 1 141

6.1 Stellar properties of YSES 2 153
6.2 Astrometry, photometry, and derived masses of YSES 2b 156
6.3 SPHERE observations of YSES 2. 167
6.4 Reference library for the data reduction in H band. 169
6.5 Reference library for the data reduction in K_s band. 171

Chapter 1

Introduction

Are we alone in the Universe? This question has fascinated humans for thousands of years, and it is still one of the most intriguing yet unsolved problems to date. For many centuries and millenia, this question has been of mostly philosophical nature, driven by the human desire to understand their place and purpose within the cosmos. In this thesis introduction I will briefly review past discourses on humanity's belief in extraterrestrial life (see Section 1.1). From a theoretical concept that was already discussed more than 2'000 years ago, an active search for signposts of intelligent life outside Earth emerged within the last century. Merely three decades ago, humankind started to discover planets around other stars than our Sun, of which some even might exhibit favorable conditions to host *life*. In Section 1.2 I will introduce this recent *exoplanet revolution*. I will discuss planet detection methods, challenges, and future prospects in this rapidly evolving field. Several vital questions remain unanswered, as for instance regarding the formation and evolution of planetary systems. In Section 1.3 I will describe how current research aims to understand these phenomena. Special focus will be given to the contributions that originated from my work during the past four years (see Section 1.4). Driven by this enormous progress and supported by major technological developments, humankind might even succeed in obtaining first signs of life outside Earth within the next century.

1.1 The search for life in the Universe

Already in ancient Greece, philosophers of various schools were arguing whether our Earth was unique, or there exist several other worlds that might harbor equally intelligent life. For instance, Metrodorus of Chios (4$^{\text{th}}$ century BCE) was a keen supporter of the theory on the plurality of worlds (Pseudo-Plutarch, Placita Philosophorum 879b-c; Greek version published by Bernardakis 1893; translation provided by Goodwin 1874):

> Μητρόδωρος δέ φησιν ἄτοπον εἶναι ἐν μεγάλῳ πεδίῳ ἕνα στάχυν γενηθῆναι καὶ ἕνα κόσμον ἐν τῷ ἀπείρῳ.
>
> ὅτι δ᾽ ἄπειρος κατὰ τὸ πλῆθος, δῆλον ἐκ τοῦ ἄπειρα τὰ αἴτια εἶναι:

> To Metrodorus it seems absurd, that in a large field one only stalk should grow, and in an infinite space one only world exist;
>
> and that this universe is infinite is manifest by this, that there are causes infinite.

εἰ γὰρ ὁ μὲν κόσμος πεπερασμένος, ὅτι δ᾽ αἴτια πάντα ἄπειρα, ἐξ ὧν ὅδε ὁ κόσμος γέγονεν, ἀνάγκη ἀπείρους εἶναι.	Now if this world were finite and the causes which produced it infinite, it is necessary that the worlds likewise be infinite;
ὅπου γὰρ τὰ πάντα αἴτια, ἐκεῖ καὶ τὰ ἀποτελέσματα αἴτια δ᾽ ἤτοι αἱ ἄτομοι ἢ τὰ στοιχεῖα.	for where all causes do concur, there the effects also must appear, let the causes be what they will, either atoms or elements.

Opposing to this *principle of plenitude* (Lovejoy 1936), several of the most renowned natural scientists from this time did not believe in the existence of further Earth analogs. Among them was Plato ($5^{th} - 4^{th}$ century BCE), who argued (Plato, Timaeus 31a-b; Greek version published by Burnet 1903; translation provided by Lamb 1925):

πότερον οὖν ὀρθῶς ἕνα οὐρανὸν προσειρήκαμεν, ἢ πολλοὺς καὶ ἀπείρους λέγειν ἦν ὀρθότερον;	Are we right, then, in describing the Heaven as one, or would it be more correct to speak of heavens as many or infinite in number?
ἕνα, εἴπερ κατὰ τὸ παράδειγμα δεδημιουργημένος ἔσται.	One it must be termed, if it is to be framed after its Pattern.
τὸ γὰρ περιέχον πάντα ὁπόσα νοητὰ ζῷα μεθ᾽ ἑτέρου δεύτερον οὐκ ἄν ποτ᾽ εἴη:	For that which embraces all intelligible Living Creatures could never be second, with another beside it;
πάλιν γὰρ ἂν ἕτερον εἶναι τὸ περὶ ἐκείνω δέοι ζῷον, οὗ μέρος ἂν εἴτην ἐκείνω, καὶ οὐκ ἂν ἔτι ἐκείνοιν ἀλλ᾽ ἐκείνῳ τῷ περιέχοντι τόδ᾽ ἂν ἀφωμοιωμένον λέγοιτο ὀρθότερον.	for if so, there must needs exist yet another Living Creature, which should embrace them both, and of which they two would each be a part; in which case this Universe could no longer be rightly described as modeled on these two, but rather on that third Creature which contains them both.
ἵνα οὖν τόδε κατὰ τὴν μόνωσιν ὅμοιον ᾖ τῷ παντελεῖ ζῴῳ, διὰ ταῦτα οὔτε δύο οὔτ᾽ ἀπείρους ἐποίησεν ὁ ποιῶν κόσμους, ἀλλ᾽ εἷς ὅδε μονογενὴς οὐρανὸς γεγονὼς ἔστιν καὶ ἔτ᾽ ἔσται.	Wherefore, in order that this Creature might resemble the all perfect Living Creature in respect of its uniqueness, for this reason its Maker made neither two Universes nor an infinite number, but there is and will continue to be this one generated Heaven, unique of its kind.

Also Aristotle (4^{th} century BCE), one of Plato's most famous apprentices, was heavily disputing the theory of life outside Earth, as this hypothesis was in stark contrast with his physical model of the cosmos. Even though some ancient scholars did not agree with this geocentric viewpoint of Aristotle, the broad majority accepted this cosmology in the years to come. Among the small opposition was the Roman philosopher Lucretius (1^{st} century BCE), who said (Lucretius, De Rerum Natura, Liber II, 1067-1076; translation provided by Rouse & Smith 1924):

Praeterea cum materies est multa parata,/ cum locus est praesto nec res nec causa moratur/ ulla, geri debent ni mirum et confieri res./	Besides, when abundant matter is ready, when space is to hand, and no thing and no cause hinders, things must assuredly be done and completed.
nunc et seminibus si tanta est copia, quantam/ enumerare aetas animantum non queat omnis,/	And if there is at this moment both so great store of seeds as all the time of living existence could not suffice to tell,

quis eadem natura manet, quae semina rerum/ conicere in loca quaeque queat simili ratione/ atque huc sunt coniecta, necesse est confiteare/ esse alios aliis terrarum in partibus orbis/ et varias hominum gentis et saecla ferarum.	and if the same power and the same nature abides, able to throw the seeds of things together in any place in the same way as they have been thrown together into this place, then you are bound to confess that there are other worlds in other regions and different races of men and generations of wild beasts.

Despite these doubts, the Aristotelian model – that postulates the uniqueness of Earth and its unparalleled ability to harbor life in the Universe – was allowed to endure, and dominated humanity's view of the world for several centuries until the late Middle Ages. Accordingly, this model was also promoted by the Church, as it was well in line with the uniqueness of Jesus Christ and the clerical, geocentric view of the cosmos. Nevertheless, there remained some inconsistencies between the Christian and Aristotelian philosophy. Albert Magnus (13th century CE) pointed out that if there was an omnipotent God, why should he create just the one Earth and not all possible realizations of it (Grant 1936). In the end, he neglected this flaw in his reasoning, because a plurality of worlds could just not be congruent with the uniqueness of Jesus Christ. As a pious bishop, there was no way this fundamental principle of the unique incarnation – the Christian concept that God became human (flesh),[1] embodied in his son Jesus Christ – could not be valid.

This dogma began to change with the advent of the Copernican revolution that began to emerge in the early 16th century. Based on his astronomical observations, Nicolaus Copernicus (1473–1543 CE) introduced the heliocentric model of our Solar System, which was disputing to the geocentric model of Ptolemy (2nd century CE) that had been widely accepted before. These developments were carefully observed by the Church, which continued propagating Earth as the center of the Universe. Scholars that were opposing this theory were oppressed and silenced. The most prominent victims of this rigorous policy of clear denial of scientific facts were Giordano Bruno (1548–1600 CE) and Galileo di Vincenzo Bonaiuti de' Galilei (1564–1642 CE). Bruno was an Italian monk who was inspired by the recent discoveries of Copernicus. The refutation of Earth as the center of the Solar System let alone the origin of the surrounding Universe motivated Bruno to revive the historic belief in plurality. For the first time this concept was partly supported by scientific facts, which made Bruno postulate (Bruno, De l'Infinito, Universo e Mondi, Dialogo Terzo; translation provided by Ponnamperuma 1964):

Uno dunque è il cielo, il spacio immenso, il seno, il continente universale, l'eterea regione per la quale il tutto discorre e si muove.	Sky, Universe, all-embracing ether, and immeasurable space alive with movement – all these are of one nature.
Ivi innumerabili stelle, astri, globi, soli e terre sensibilmente si veggono [...]. [...]	In space there are countless constellations, suns, and planets [...]. [...]
Sono dunque soli innumerabili, sono terre infinite, che similmente circuiscono quei soli; come veggiamo questi sette circuire questo sole a noi vicino. [...]	There are also numberless earths circling around their suns, no worse and no less inhabited than this globe of ours. [...]

[1] Incarnation is derived from the Latin word *caro*, which means flesh.

> La raggione è, perché noi veggiamo gli soli, che son gli più grandi, anzi grandissimi corpi, ma non veggiamo le terre, le quali, per esserno corpi molto minori, sono invisibili; [...].
>
> We see only the suns because they give light; the planets remain invisible, for they are small and dark; [...].

As this theory was openly disputing the uniqueness of the incarnation, the Church did not endorse this concept which challenged one of the main pillars of Christianity. Bruno was tried and burnt at the stake in 1600, making him one of the earliest martyrs of science (Paterson 1971). His beliefs, however, were not purely scientific but arose from his theologically motivated criticism of the Christian concept of a unique incarnation (Yates 1964). In fact, Bruno's work was a huge setback for scholars that were promoting the Copernican view of the cosmos for scientific reasons. By condemning Bruno and his theories, the Church also had to dispute the heliocentric model and the underlying scientific facts. People including Galileo Galilei, who insisted on promoting this theory, were denounced as heretics and subjected to the clerical inquisition.

Even though Galilei himself did not believe that other planets might be inhabited by forms of life (Drake 1957), his technological developments supported questioning the uniqueness of Earth and its position in the cosmos. The advent of optical telescopes revealed craters and elevations on the lunar surface, satellites of Jupiter, and a plenitude of stars that has not been visible to the naked eye before. Paired with the recent discovery of the Americas in the 15th century, these new astronomical insights fostered an open mindset towards further undiscovered phenomena far beyond the imagination of previous generations (e.g., Fontenelle 1686). The Dutch astronomer Christiaan Huygens (1629–1695 CE) strongly believed in the existence of a multitude of worlds similar to ours (Huygens, Cosmotheoros Huygens & Huygens 1698):[2]

> What a wonderful and amazing Scheme have we here of the magnificent Vastness of the Universe! So many Suns, so many Earths, and every one of them stock'd with so many Herbs, Trees and Animals, and adorn'd with so many Seas and Mountains! And how must our wonder and admiration be encreased when we consider the prodigious distance and multitude of the Stars?
>
> [...] how vast those Orbs must be, and how inconsiderable this Earth, the Theatre upon which all our mighty Designs, all our Navigations, and all our Wars are transacted, is when compared to them. A very fit consideration, and matter of Reflection, for those Kings and Princes who sacrifice the Lives of so many People, only to flatter their Ambition in being Masters of some pitiful corner of this small Spot.

These words reflect the so-called *principle of mediocrity* which postulates that the likelihood of an item, if randomly drawn from a sample that contains several subsets, is proportional to the sizes of the individual subsets. Transferred to the question regarding the uniqueness of a habitable Earth, this principle implies that life should also exist on Earth-like planets throughout the Universe, as it does exist on Earth (e.g., Rauchfuss 2008).

Based on these technical developments and new discoveries, the belief in the plurality of worlds was widely spread by the end of the 18th century. The idea that there could exist unknown and strange civilizations in the Universe was not dis-

[2] As I could not find the original Latin version of Huygens' Cosmotheoros, only the English translation is provided.

regarded as an impossible scenario any longer. Accordingly, this theme began to appear in literature of the 19th century, for instance in the novels of Jules Gabriel Verne (1828 − 1905; e.g., Autour de la Lune) or Herbert George Wells (1866 − 1946; e.g., The War of the Worlds). Driven by these fictional influence, searches for signs of such an extraterrestrial intelligence emerged. These efforts predominately focused on Solar System objects, owing to the technical limitations of this time. Inspired by the previous observations of Giovanni Schiaparelli (1835–1910),[3] Percival Lowell (1855–1916) was convinced that he had detected canals on Mars reminiscent of intelligent inhabitants of the red planet (Lowell 1895, 1906). Even though Evans & Maunder (1903) argued that the supposed canals are most likely an optical illusion, and higher-resolution images collected in 1909 showed that these features were in fact geological structures, the belief of intelligent Martian inhabitants remained.

Up to the present day, no unambiguous evidence for the existence of extraterrestrial life in our Solar System has been found. In addition to this local search for extraterrestrial intelligence in our immediate neighborhood, larger surveys emerged that were hunting for signs of such civilizations beyond the borders of our Solar System. Cocconi & Morrison (1959) suggested to search for such technosignatures at radio wavelengths that might also be used for communication among other intelligent forms of life. This approach was pursued by pioneers such as Frank Donald Drake, who searched for radio signals from nearby stars such as ϵ Eridani or τ Ceti, yet without any success (Drake 1961, 1979). Nevertheless, the search for extraterrestrial intelligence (SETI) emerged from these pioneering efforts and began to gain recognition among the astronomical community (Sagan 1982). This search still continues, driven by humanity's desire to know whether there are Earth analogs that harbor similar forms of intelligent life. Privately funded projects like the Breakthrough Listen Search for Intelligent Life continue to monitor interesting stellar host stars to find evidence for such civilizations in our galactic neighborhood (e.g., Worden et al. 2017). For a more detailed overview of the past, present, and future of SETI, the reader is referred to Tipler (1981), Papagiannis (1985), or Shuch (2011).

1.2 The exoplanet revolution

Despite all these mostly theoretical considerations, planets outside our Solar System – which are the necessary requirement for extraterrestrial life – remained a theoretical construct without any physical evidence until the end of the 20th century. In 1992 Wolszczan & Frail discovered two planetary-mass objects around the millisecond pulsar PSR B1257+12 with the Arecibo radio observatory in Puerto Rico. This discovery came as a big surprise, as planets were not expected to survive the supernova that must have preceded the current post-main sequence state the system was observed in. It was hypothesized that these planets actually formed after the main sequence period of the host, within a debris disk that was composed of the remains of the pulsar's stellar binary companion (Wolszczan 1994). Recent simulations by Fagginger Auer & Portegies Zwart (2021), however, indicate that planets might even stay bound during and after a supernova if the host system is a stellar binary.

[3]The Italian astronomer Giovanni Schiaparelli observed Mars in 1877 and reported the detection of several *canali* on the planet's surface. Whereas the original Italian word means as much as *channels* (which can be geological structures), it was mistranslated as *canals* (e.g., Sheehan 1988). As canals are by definition human-made, this unfortunate translation supported the belief in life on Mars.

Only three years after the discovery of these pulsar planets, Mayor & Queloz (1995) succeeded in detecting a gas giant planet around the solar-type star 51 Peg. This remarkable discovery of the fist planetary-mass object orbiting a main sequence star was awarded the Nobel prize in physics in 2019. Most peculiar though was the short orbit that this planet exhibits. An orbital period of merely 4.2 days indicated a semi-major axis of $\sim$0.05 au, which is twenty times smaller than the Earth-Sun distance in our Solar System and about 13 % of Mercury's semi-major axis.

With these intriguing discoveries it became clear that indeed planets do exist around celestial bodies outside our Solar System; the system architectures and formation scenarios of these extrasolar environments, however, can be vastly different from what we have observed in our immediate neighborhood.

The initial discoveries of planets outside our Solar System by Wolszczan & Frail (1992) and Mayor & Queloz (1995) launched a new era of extraterrestrial planetology, leading to 4375 confirmed exoplanets that are listed in the NASA exoplanet archive[4] as of April 10, 2021. The semi-major axes and masses of all these exoplanets are shown in Figure 1.1. Together with the Solar System planets, a parameter space of almost 6 orders of magnitude is covered by both weight and orbital separations. As such, TRAPPIST-1 b is one of the lowest-mass exoplanets with a mass equivalent to that of the Earth and a semi-major axis of merely 0.01 au (Gillon et al. 2016, 2017; Grimm et al. 2018), whilst GU Psc b is more than 2000 au away from its stellar host and about 11 times as massive as Jupiter (Naud et al. 2014). The colors used in Figure 1.1 are indicative of the different detection methods that were used to discover these exoplanets. The techniques that are commonly used to detect and characterize extrasolar planets can be divided into two broad categories: direct and indirect methods. Whereas indirect methods infer the presence of a planetary companion by monitoring of stellar observables (such as its reflex motion or flux intensity), direct imaging aims for obtaining spatially resolved images of extrasolar planetary systems.

The clustering of planets that are detected with the same technique indicates that each method favors a specific region of the parameter space for the detection of extrasolar planets. Whereas the transit method succeeds in detecting planets at small semi-major axes that are usually smaller than 1 au, direct imaging excels for separations that are significantly larger than 10 au. The underlying causes that are shaping the individual discovery space for each method are briefly discussed in the following Sections 1.2.1 and 1.2.2. A substantial part of the parameter space exhibits no significant number of exoplanet detections. For instance, we do not know any extrasolar planet that is less massive than Jupiter and more than 20 au away from its host star. This void, however, must not be interpreted as the absence of such planets around stars other than our Sun; it is rather the manifestation of the limitations that each of the discovery methods exhibits. Even though there might be a plethora of exoplanets that are residing within these unprobed regimes in Figure 1.1, our current instrumentation is not sensitive enough to reveal this as of yet undiscovered population.

Our knowledge of extrasolar planetary systems is limited by the available data, which is also obvious from a comparison to the Solar System planets in Figure 1.1. Jupiter is the only planet that has extrasolar analogs of similar mass and semi-major axis. Again, this is not a confirmation that our Solar System planets are unique and that similar objects do not exist around other stars; it is rather a strong indication that

[4] https://exoplanetarchive.ipac.caltech.edu/

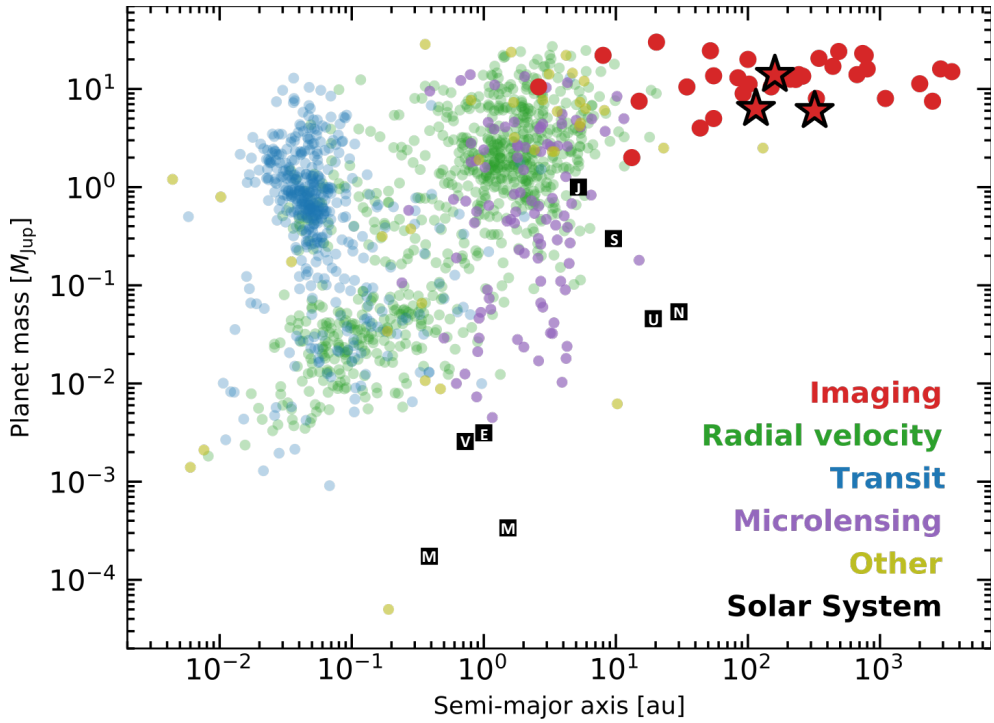

Figure 1.1: Confirmed extrasolar and Solar System planets as of April 10, 2021. The data were collected from the NASA exoplanet archive.[4] We present the planet mass as a function of its semi-major axis. The exoplanets are categorized with respect to their primary detection method as indicated by the colored labels in the bottom right. The red stars highlight the planets that were discovered as part of this thesis. As the orbital parameters for many directly imaged companions are poorly constrained, the semi-major axes are usually approximated by the projected separations; the masses of the directly imaged planets are inferred from theoretical models. For the majority of the planets that are detected by RV measurements, the presented mass is just the minimum mass $M \sin(i)$, as the true mass is degenerate with the orbit inclination.

we are missing a large fraction of extrasolar planets due to limitations of our current technologies. Especially the next generation of large ground and space-based observatories will play a crucial role in exploring this uncharted territory of exoplanet parameter space. The direct detection of Earth-like planets might actually be in reach of first-generation instruments at the Extremely Large Telescope (ELT) of the European Southern Observatory (ESO). Quanz et al. (2015) simulate that the Mid-infrared ELT Imager and Spectrograph (METIS; Brandl et al. 2014) will be sensitive enough to detect ∼10 terrestrial planets with equilibrium temperatures between 200 and 500 K around the nearest stars. METIS is expected to see first light in the late 2020s; accordingly, the first image of an Earth analog outside our Solar System might even be collected within this decade. Future space-based observatories such as the Large Ultraviolet Optical Infrared Surveyor (LUVOIR; The LUVOIR Team 2019) and the Habitable Exoplanet Imaging Mission (HabEx; Mennesson et al. 2016; Gaudi et al. 2020) might accompany these ground-based efforts within the next decades. Even bigger mission such as the Large Interferometer For Exoplanets (LIFE; Quanz et al.

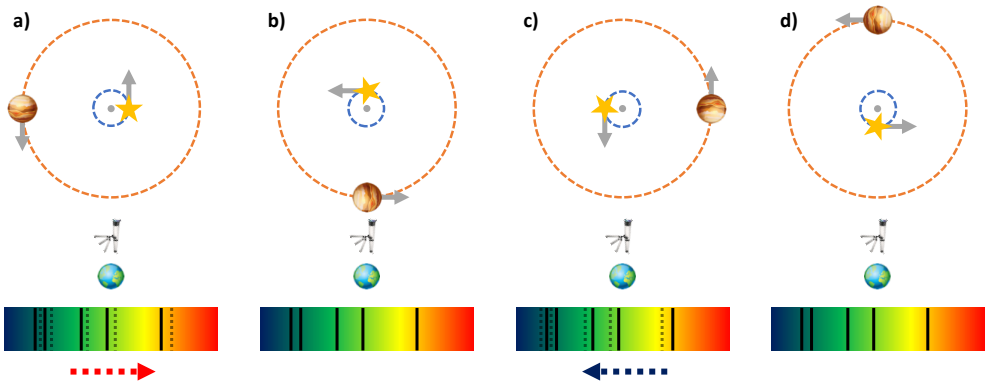

Figure 1.2: The radial velocity method for the detection of exoplanets. In a two-body system both planet and star orbit around the common center of mass (grey dot). Therefore, the presence of a planet induces a periodic change of the stellar velocity vector. The radial component of this velocity change can be measured by monitoring the stellar spectrum. If the star moves away from Earth (panel a) spectral lines are red-shifted and if the star moves towards us the same lines appear blue-shifted (panel c). The solid black lines in the spectral inlays represent the rest-frame spectrum of the star; the dotted lines indicate the redshift (panel a) and blueshift (panel c) of absorption lines due to the orbital motion of the planet. Measuring this periodic change in the stellar radial velocity allows us to infer the orbital period and the minimum mass of the exoplanet.

2019, 2021) are currently designed. LIFE is supposed to characterize the atmospheres of terrestrial exoplanets, and might be able to reveal the first biosignatures outside Earth. Despite the enormous technical challenges that still need to be overcome to conduct such a measurement, humankind might be able to answer the initial question as to whether we are alone in the Universe before the end of the 21st century.

1.2.1 Indirect detections of exoplanets

The majority of known exoplanets have been detected by indirect detection methods (see Figure 1.1): the NASA Exoplanet Archive lists 4324 out of 4375 (∼99 %) to have been discovered indirectly as of April 10, 2021. These indirect techniques infer the presence of an extrasolar planet from the analysis of stellar observables such as its reflex motion (as for instance radial velocity or astrometric measurements) or intensity variations of the primary star that are caused by planetary transit or microlensing events. In this section I will give a brief overview of the main indirect detection techniques, their strengths and limitations. For a more complete review of this topic the reader is referred to Wright & Gaudi (2013).

The radial velocity method (837 discovered planets as of April 10, 2021)

The first exoplanet around a main sequence star was discovered by Mayor & Queloz (1995) who evaluated RV measurements of the G2 star 51 Peg as part of a larger survey for potential extrasolar planets. As visualized in Figure 1.2, a planet that is in orbit around a star introduces a periodic motion of the host, as both star and planet are revolving around their common center of mass. Of course, the reflex motion of the star is several orders of magnitude smaller than the orbital motion of the planet.

Jupiter for instance has an orbital velocity of approximately $13\,\mathrm{km\,s^{-1}}$, but it induces an RV amplitude of only $12.4\,\mathrm{m\,s^{-1}}$ to the motion of the Sun, when viewed from a location within the orbital plane (e.g., Cochran & Hatzes 1996). For Earth in orbit around the Sun the amplitude of velocity change is $0.1\,\mathrm{m\,s^{-1}}$. Nevertheless, it is possible to detect perturbations to stellar velocities in the order of $1\,\mathrm{m\,s^{-1}}$ that can be attributed to orbiting exoplanets (e.g., Pepe et al. 2021). The radial component of this movement can be identified by spectroscopic analysis since absorption lines in the stellar spectrum are blue-shifted when the star moves towards Earth and red-shifted when it moves away from Earth. Observations that cover a full orbit of the exoplanet allow us to identify its orbital period. A minimum mass of the planet can be derived as its true mass is degenerate with the system inclination: a heavy planet on a close-to face-on orbit can cause the same RV signal as a low-mass planet that is orbiting almost edge-on. This degeneracy can be broken by inferring the planet's inclination by other means, for instance if the planet is transiting (e.g., Barbieri et al. 2007), the companion can be imaged (e.g., Maire et al. 2020), precise astrometric data is available (e.g., Benedict et al. 2006), or circumstellar material provides hints towards the most likely system geometry (e.g., Trilling & Brown 1998).

The sensitivity of RV measurements scales as

$$(\mathrm{S/N})_{\mathrm{RV}} \propto M_{\mathrm{p}} P^{-\frac{1}{3}} M_{\star}^{-\frac{2}{3}} \propto M_{\mathrm{p}} a^{-\frac{1}{2}} M_{\star}^{-\frac{1}{2}} \,, \tag{1.1}$$

where $M_{\star}$ is the mass of the primary star and M_{p} denotes the planet mass, P its orbital period and a its semi-major axis (Wright & Gaudi 2013). This method, therefore, favors the detection of massive planets in close orbits around their hosts. This bias is clearly visible in Figure 1.1, as the majority of RV planets exhibit masses above $1\,M_{\mathrm{Jup}}$ and semi-major axes that are smaller than 1 au. Although the signal-to-noise ratio of RV measurements theoretically increases with decreasing host star mass, this does not necessarily mean that M dwarfs are the best targets for large surveys to search for RV planets. Other factors such as the decreasing luminosity and the activity of these low-mass stars have a significant impact on the feasibility to detect planets via this method (e.g., Saar et al. 1998). Yet scientists were able to overcome these challenges in some cases, and detected Earth-sized planets around the two closest M dwarfs to Earth: Ribas et al. (2018) discovered a planet with a minimum mass of $3.2\,M_{\oplus}$ around Barnard's star; and Proxima Centauri, the closest star to Earth at a distance of 1.3 pc, was found to harbor two super-Earths, of which the inner one might be able to support liquid water on its surface (Anglada-Escudé et al. 2016; Damasso et al. 2020).

Transiting exoplanets (3325 discovered planets as of April 10, 2021)

The first planet that was detected by the transit method was HD 209458 b (Henry et al. 2000; Charbonneau et al. 2000), yet the existence of the planet was already confirmed with RV measurements by the time the transit observations were carried out. Indeed, OGLE-TR-56 b is the first extrasolar planet whose discovery can be attributed to the transit technique (Konacki et al. 2003). This method exploits the fact that some exoplanets must move across the line of sight between Earth and their host star during their orbit. As visualized in Figure 1.3 this obscuration results in a periodic dimming of the stellar brightness, similar to a solar eclipse observed here on Earth, yet of much smaller magnitude. The amplitude of the dimming event is

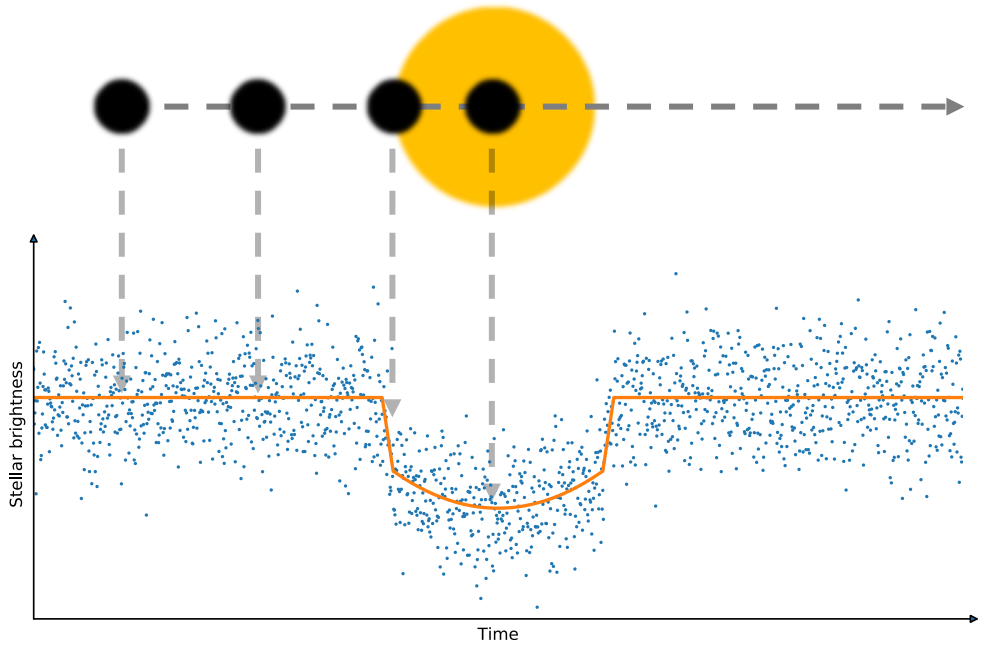

Figure 1.3: The transit method for the detection of exoplanets. Planets can move across the line of sight between observer and primary star. This results in a periodic dimming event that can be measured via continuous monitoring of the stellar luminosity.

directly related to the planetary and stellar radii involved. Based on purely geometrical considerations the stellar fractional intensity reduction, the so-called transit depth, is modeled as

$$\frac{\Delta I}{I} = \frac{R_\mathrm{p}^2}{R_\star^2}\,, \tag{1.2}$$

where R_p and $R_\star$ denote the radii of the planet and the star, respectively. If the stellar radius is well known, the planetary radius can be inferred from a transiting event. For solar-type stars the mangitudes of these eclipsing events are in the order of 1 % for Jovian companions and 0.01 % for terrestrial planets. Due to the smaller stellar radii, M dwarfs are particularly favorable to search for Earth-sized planets with the transit method. The transit depth is increased compared to solar-type primaries and therefore easier to detect. Instruments like TRAPPIST (Gillon et al. 2011; Jehin et al. 2011) or SPECULOOS (Delrez et al. 2018) exploit this advantage in the search for transiting, terrestrial exoplanets. One of the most intriguing results from these surveys was the discovery of seven temperate Earth-sized planets around the M dwarf TRAPPIST-1 (Gillon et al. 2017) that launched a cascade of follow-up observations. An even larger transit depth of ∼57 % is exhibited by the planetary system around the white dwarf WD 1856+534, which is hosting a Jupiter-sized companion that is eclipsing its post-main sequence host in a grazing transit (Vanderburg et al. 2020).

A single stellar dimming event, however, is not a solid indicator for a transiting planet. To confirm a companion, the transit has to occur periodically, which allows us to determine the planet's orbital period. If the stellar mass is known, the orbital

semi-major axis can be derived from the period. But even periodic stellar dimming events might originate from other sources than transiting exoplanets (e.g. Brown 2003; Charbonneau et al. 2004). There is a variety of non-planetary sources that could mimic transit-like events, such as stellar variability and other unfortunate stellar constellations. For instance, grazing eclipses of stellar binaries can look like planetary transit signatures. Another frequent source of false-positive detections are eclipsing stellar binaries that are close to the scientific target on sky, yet not resolved by the recording telescope. When extracting the stellar flux, the contributions of all stars in the aperture are combined, which can mimic the signal of a transiting exoplanet. To test for the two latter scenarios, high-contrast imaging at high spatial resolution as introduced in Section 1.2.2 is a powerful technique. The detection of astronomical objects that are hidden below the angular resolution limit of transit survey telescopes is important to correct the derived planetary parameters for the flux contribution of the identified contaminant (e.g. Evans et al. 2016b; Southworth et al. 2020). This can lead to revised planetary radii that differ by up to 10% from the previously derived values, unaware of the close contaminant (for the exoplanet WASP-20 b; Evans et al. 2016b). Such follow-up observations of transiting exoplanet host stars at higher spatial resolution can also reveal gravitationally bound stellar companions (e.g. Daemgen et al. 2009; Faedi et al. 2013a; Bergfors et al. 2013; Adams et al. 2013; Ngo et al. 2015). Studying the multiplicity of exoplanet host systems is important to understand the formation and evolution of planetary environments. This topic will be discussed extensively in Chapter 2 of this thesis.

The majority of exoplanets has been discovered by space-based transit surveys, which fundamentally contributed to our knowledge of planetary occurrence rates and the diversity of planetary system architectures. The Kepler space mission has contributed more than 2'500 objects to our census of extrasolar planets (Borucki et al. 2010), and the Transiting Exoplanet Survey Satellite (TESS; Ricker et al. 2015) is currently expanding the sample of short-period planets around bright and nearby stars. But also ground-based surveys successfully detected planets via the transit method: especially the Wide Angle Search for Planets (WASP; Pollacco et al. 2006) discovered more than 150 transiting exoplanets.

Despite this plethora of discoveries, there are a few shortcomings associated with exoplanet detections via the transit method. First, there is no intrinsic possibility to derive a planetary mass from the observed dimming event. These parameters have to be obtained via follow-up measurements using other techniques such as the RV method. Second, the probability of a planet to eclipsing its host star, p_{transit}, decreases with the semi-major axis a of the planet as per

$$p_{\mathrm{transit}} \propto \frac{R_\star}{a} \,, \tag{1.3}$$

again purely based on geometric considerations (Borucki & Summers 1984). Wright & Gaudi (2013) derive a sensitivity of

$$(\mathrm{S/N})_{\mathrm{transit}} \propto p_{\mathrm{transit}}^{-\frac{1}{3}} R_\mathrm{p}^2 M_\star^{-\frac{5}{3}} \propto a^{-\frac{1}{2}} R_\mathrm{p}^2 M_\star^{-\frac{3}{2}} \tag{1.4}$$

to detect transiting planets, when assuming that the stellar radius scales linearly with the stellar mass. This assumption is a decent approximation for stars with masses up to $1\,M_\odot$. Accordingly, the population of transiting exoplanets is heavily biased towards short-period giant planets with typical planet masses between $10\,M_\oplus$ and $10\,M_\mathrm{Jup}$ at separations of 10^{-2} au to 1 au (see Figure 1.1).

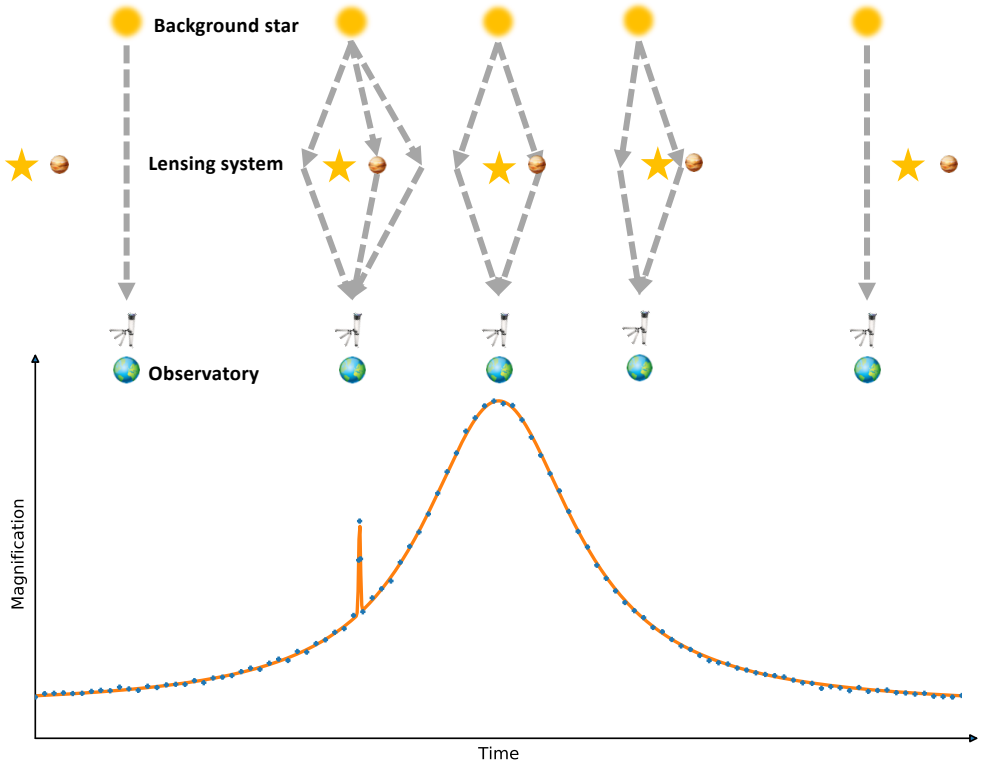

Figure 1.4: Microlensing events for the detection of exoplanets. According to Einstein's general theory of relativity light curves are bent in the presence of matter. Hence, a foreground star that is passing across the line of sight from Earth, can artificially magnify the recorded intensity of a more distant background object, similar to a lens in optical physics. A planet in the lensed system can be identified as perturbation of the magnification lightcurve that is resembling the gravitational lensing of a single star.

Microlensing events (108 discovered planets as of April 10, 2021)

The microlensing method to detect extrasolar planets makes use of Einstein's general theory of relativity (Einstein 1916). This framework postulates that matter curves space-time, and hence massive objects can bend the trajectories of light. Dyson et al. (1920) were able to experimentally confirm this theoretical concept for the first time, by measuring the angular displacement of stars due to the gravitational influence of the Sun during a solar eclipse in 1919. As visualized in Figure 1.4 this concept is also applicable to other stellar constellations that can be observed here on Earth. If a foreground star is moving across the line of sight, the light emitted by a background star is deflected due to general relativity. Accordingly, this foreground star can act as a lens that is magnifying the background source's intensity measured on a detector. If the lensing system harbors a planetary companion, the gravitational influence of this planet can create an additional magnification on top of the intensity variations caused by its stellar host. This second-order magnification is of much smaller magnitude and acts on much shorter time-scales than the primary magnification. Yet with sufficient

temporal sampling of the lightcurve of the background star, this variation can be identified and attributed to a planet.

This method was successfully employed by Bond et al. (2004) for the first time to detect OGLE 2003-BLG-235L b (MOA 2003-BLG-53L b). The observed microlensing event was attributed to a binary system with a mass ratio of $q = 0.0039$ between the primary star and its companion. As this observational technique just provides this mass ratio and not the individual masses of both objects, follow-up measurements were necessary to break this degeneracy. Bennett et al. (2006) identified the lensing star in Hubble Space Telescope data, determined its spectral type, and concluded that OGLE 2003-BLG-235L b is likely a gas giant planet with a mass of $2.6\,M_{\mathrm{Jup}}$ with an orbital semi-major axis of 4.3 au. Indeed, microlensing detections of exoplanets are not possible for arbitrary system geometries. The method heavily favors the detection of planets that are close to the Einstein radius (Einstein 1936) of the lensing foreground star. The optimal separation of a planet to be detected via these means is

$$a_{\mathrm{opt}} \approx 2.85\,\mathrm{au}\sqrt{\frac{2M_\star}{M_\odot}} \tag{1.5}$$

(see Wright & Gaudi 2013). Due to this intrinsic bias, the majority of microlensing planets have been detected in a range of semi-major axes from approximately 1 au to 10 au (see Figure 1.1). Future missions such as the Nancy Grace Roman Space Telescope (Spergel et al. 2015) are supposed to discover more than one thousand bound exoplanets by microlensing events (Penny et al. 2019). Furthermore, this mission might reveal a significant population of unbound planetary companions that are freely floating through our Galaxy (Barclay et al. 2017). Such isolated planets were observed in the past (Sumi et al. 2011); they are are postulated to be ejected from their natal circum-stellar systems (e.g., Rasio & Ford 1996).

Other indirect detection methods (54 discovered planets as of April 10, 2021)

There are several other indirect methods that can detect extrasolar planets. The number of planets detected via these means, however, is small compared to the three major indirect methods discussed above. Future instrumentation might enable a plethora of new detections – a planet population that is just out of reach of current observatories.

Astrometry The reflex motion of a planetary host star that is induced by an orbiting companion does not only have a radial component as probed by RV measurements. The star also moves perpendicular to the line of sight in the plane of the sky. This motion can be measured and associated with a planetary-mass companion. The combination of RV observations with astrometric measurements breaks the mass degeneracy by revealing the orbital inclination (Tuomi et al. 2009). However, extremely high astrometric precision is required to reveal the presence of an exoplanet: whereas a Jupiter analog orbiting a Sun-like star creates an astrometric signal in the order of $\sim$0.1 mas, the astrometric amplitude of an Earth analog is about 0.1 µas (Wright & Gaudi 2013). Hence only a handful of planets were claimed to be discovered by this technique (e.g., Muterspaugh et al. 2010; Sahlmann et al. 2013), and most of the results need to be confirmed by longer observational baselines or complementary

detection methods. The *Gaia* space observatory of the European Space Agency (Gaia Collaboration et al. 2016) is the most promising mission to significantly increase the small number of astrometrically confirmed exoplanets. *Gaia* is monitoring the motions of more than 1 billion stars with unprecedented precision during a nominal mission duration of 5 years. Perryman et al. (2014) simulated that these data should reveal about 21'000 new planets via the astrometric wobbles of their respective host stars.

Transit timing When a system with a single planet is aligned such that this companion is transiting, this transit occurs strictly periodically. If further planets are present, their gravitational influence will affect the orbit of the initial planet. Even if the additional planets do not transit themselves, their presence manifests itself in a deviation from the strict periodicity of the initial transit signal. Using this technique, non-transiting planets can thus be detected in known transiting planet-hosting systems (e.g., Nesvorný et al. 2012).

Pulsar timing Even though the first exoplanets were discovered by this method (Wolszczan & Frail 1992), the absolute number of pulsar planets is small: Only seven planets are associated with this category according to the NASA exoplanet archive. The method relies on modulations of the pulsar period by an orbiting plant. Due to the induced motion the frequency of the pulsar is altered, which allows us to derive the mass and the orbital period of the planetary companion.

Pulsation timing Similar to the modulation of the pulsar frequency, orbiting planets can affect the arrival time of lightcurve modulations due to stellar variability. Silvotti et al. (2007) used this technique to reveal a Jovian gas giant orbiting the extreme horizontal branch star V391 Pegasi. The second planet discovered by the pulsation timing method was found around KIC 7917485 in the Kepler field of view (Murphy et al. 2016).

Disk kinematics One of the most recently developed techniques to indirectly detect exoplanets is the analysis of kinematic structures in protoplanetary disks. The advent of the Atacama Large Millimeter/submillimeter Array (ALMA) facilitated studies at radio wavelengths with unprecedented spectral and spatial resolution (e.g., Ansdell et al. 2016; Andrews et al. 2018). Forming planets will impact the gas dynamics in the protoplanetary disk, and therefore these signatures can be searched in the spectroscopic data. Teague et al. (2018) and Pinte et al. (2018) exploited these novel opportunities and announced the detection of several protoplanets around the young star HD 163296; yet other methods could not confirm these proposed protoplanets so far (e.g., Mesa et al. 2019a).

1.2.2 Direct detections of exoplanets

Only $\sim$1 % of all known exoplanets have been discovered by taking a direct image of the companion (51 out of 4375 as of April 10, 2021). This small number is due to the challenging nature of the problem to image a faint planet right next to its host star that is many orders of magnitude brighter. Hence, the nature of the underlying problem for our imaging system is twofold: not only the huge contrast between star

and planet has to be overcome, but this sensitivity has to be provided at very small angular separations from the star.

Huge contrast and small angular separation: the main challenges of direct imaging

The typical angular separations when trying to image Solar System analogs can be assessed geometrically and scaled with the distance of the targeted system. Whereas a Jupiter analog to a star at 5 pc is separated 1″ from its primary, the same system geometry at 100 pc corresponds to an angular separation of 0.″05. An Earth twin would have an angular separation of 0.″2 and 0.″01 for a system at 5 pc and 100 pc, respectively. For comparison, a 10 m-class telescope (which is the largest category of currently operating optical telescopes) has a diffraction limit of about 0.″015 at optical wavelengths (600 nm) and 0.″05 in the near infrared (2 µm). But this diffraction limit based on the Rayleigh criterion (see equation 1.11) is not equivalent to the true spatial resolving power of a ground-based observatory, as discussed later. From these geometrical considerations, it seems plausible that the direct imaging search for exoplanets should focus on the stars that are closest to the Sun. These provide more favorable angular separations for Solar System equivalents, and planets should be easier to detect.

The second variable, however, that needs to be considered in this problem is the contrast between the star and the planet. To quantify the magnitude of this challenge, one has to investigate the different types of electromagnetic radiation that are emitted by a planetary-mass companion. Planets cool down after their formation, as their masses and hence the internal temperatures are too low to fuse hydrogen or deuterium in the core (e.g., Burrows et al. 1997). The major sources of electromagnetic radiation that can be detected from such a planetary-mass object are

1. reflected light of the host star
2. and thermal radiation
   a) from reprocessed starlight
   b) or due to release of gravitational energy.

To first order, sources 1 and 2a do not depend on the age of the system, as they just rely on the stellar radiation that is either reflected or absorbed by the planet. The spectral energy distribution (SED) of reflected light from an exoplanet is shaped by the emission spectrum of its primary star, altered by atmospheric molecular absorption and scattering processes (e.g., Selsis et al. 2008). The reflected light contrast between star and planet $c_{\mathrm{ref}}(\lambda)$ can be approximated by

$$c_{\mathrm{ref}}(\lambda) = A_{\mathrm{g}}(\lambda) \left(\frac{R_{\mathrm{p}}}{a} \right)^2 f_{\mathrm{ref}}(\lambda, \alpha) \,, \tag{1.6}$$

where $A_{\mathrm{g}}(\lambda)$ and $f_{\mathrm{ref}}(\lambda, \alpha)$ denote the wavelength-dependent geometric albedo and phase function of the planet (e.g., Seager 2010). The latter quantity also depends on the phase angle α of the planet, which determines the amount of flux reflected off the planet towards the direction of Earth. For a fixed planet radius, geometric albedo, and phase angle, the reflected light contrast at a certain wavelength becomes more favorable the higher the stellar irradiation, i.e. the smaller the planet's semi-major axis.

Of course, this effect is exactly the opposite in our imaging system, whose contrast degrades the closer a source is to the primary star (when assuming a regular Airy-shaped point spread function for both sources; see, e.g., Figure 1.6). For an Earth analog with a geometric albedo of 0.4 and a phase function of 0.5, equation (1.6) provides a reflected light contrast in the order of 4×10^{-10} at visible wavelengths. The detection of Jupiter analogs is not much more favorable in reflected light, as the larger semi-major axes reduce the amount of stellar irradiation, providing contrasts in the order of 2×10^{-9}. These requirements are significantly lower than the sensitivities of current instrumentation. Ground-based optical studies can achieve a total intensity contrast of approximately 1×10^{-6}, which is more than three orders of magnitude higher than the required specifications (e.g., Hunziker et al. 2020). Future space-based observatories such as the Nancy Grace Roman Space Telescope might be able to achieve these challenging requirements (e.g., Robinson et al. 2016; Trauger et al. 2016; Zimmerman et al. 2016; Girard et al. 2020).

As the reflected light spectrum of an exoplanet roughly follows the SED of the stellar primary, leading to the extremely challenging contrasts $10^{-9} - 10^{-10}$, the thermal emission of a planet is usually better suited for its direct detection. The SED maximum of solar or earlier type stars is located at visible wavelengths, whereas the peak emission of much cooler planets is in the near to mid infrared wavelength regime. In this region, the stellar luminosity decreases as a function of λ^{-4} according to the Rayleigh–Jeans limit of its approximated blackbody emission. This leads to more favorable star-to-planet contrasts at near to mid infrared wavelengths. When approximating both star and planet as a blackbody $B_\lambda(T)$, the thermal planet contrast is

$$c_{\text{therm}}(\lambda) = \left(\frac{R_\text{p}}{R_\star}\right)^2 \frac{B_\lambda(T_\text{p})}{B_\lambda(T_\star)}\,, \tag{1.7}$$

with T_p and $T_\star$ denoting the planetary and stellar temperatures, respectively (Wright & Gaudi 2013). Assuming that we observe both blackbodies in the Rayleigh–Jeans limit, equation (1.7) simplifies to

$$c_{\text{therm}}(\lambda) = \left(\frac{R_\text{p}}{R_\star}\right)^2 \frac{T_\text{p}}{T_\star}\,, \tag{1.8}$$

which can be written as

$$c_{\text{therm}}(\lambda) = \left(\frac{R_\text{p}}{R_\star}\right)^2 \frac{T_\text{eq}}{T_\star}\,, \tag{1.9}$$

when requiring the planet to be in thermal equilibrium ($T_\text{p} = T_\text{eq}$). T_eq denotes the theoretical equilibrium temperature of a planet, which is derived under the assumption that the energy from the absorbed stellar irradiation is completely re-emitted as thermal blackbody radiation of the planet: in this framework it is assumed that the planet is isothermal (i.e. there are no temperature gradients across its surface) and that it has no intrinsic source of energy. Utilizing our example of an Earth and Jupiter analog with equilibrium temperatures of 250 K (Earth) and 110 K (Jupiter) and an effective solar temperature of 5'800 K, provides contrast ratios of 4×10^{-6} and 2×10^{-4}, respectively. This is an improvement of 4–5 orders of magnitude compared to the previously discussed reflected light contrasts.

However, no such Solar System planet analog with a similar age and equilibrium temperature could be directly observed so far. The reason for this shortcoming is simple: for equation (1.9) to hold, we assumed that λ is in the Rayleigh–Jeans limit of the Planck function, which requires that

$$\lambda \gg \frac{hc}{k_\mathrm{B} T} \,. \tag{1.10}$$

The right-hand side of this inequality is in the order of 50 µm for a terrestrial equilibrium temperature of 250 K. Observations at this wavelength range are impossible from the ground as our own atmosphere is not transparent at these frequencies. Another issue that comes along with observations in the infrared is closely related to the reason that favors the detection of terrestrial planets in this frequency regime. As everything on Earth has a temperature similar to this equilibrium temperature of 250 K, the amount of noise originating from the atmosphere, the telescope, and other surfaces is exponentially increasing for wavelengths that are longer than 1 µm. Observations at 10 µm are feasible, but the background noise is usually larger than the signal from any astrophysical source (e.g., Absil et al. 2004). When going to shorter wavelengths, condition (1.10) is violated and the star-to-planet contrast degrades drastically, due to the exponential dependence of $B_\lambda(T)$ in the opposing Wien regime. Evaluation of the initial equation (1.7) provides a thermal contrast of 5×10^{-10} when observing an Earth analog at 5 µm and even 7×10^{-17} at 2 µm. So, space-based observatories are strictly mandatory for the direct detection of old, evolved exoplanets with equilibrium temperatures below 300 K. But even then, these observatories must be actively cooled to minimize the thermal noise of the observations. Besides, the ability to resolve star and planet scales inversely proportional with wavelength leading to enormous aperture sizes that are required to provide the additionally required spatial resolution. A solution might be a space-based nulling interferometer such as the proposed LIFE mission (Quanz et al. 2021).

The only class of exoplanets that could be directly probed with current instrumentation are those of category 2b that emit additional energy released by the gravitational contraction following their recent formation. In other words, these are young exoplanets that exhibit higher temperatures and that are therefore more luminous than their older counterparts. Young Jovian giants with ages that are smaller than 20 Myr and masses in the range of $1\,M_\mathrm{Jup} - 13\,M_\mathrm{Jup}$ usually have temperatures of 1'000 K – 2'000 K. For solar-type host stars with $T_\star = 5'800\,\mathrm{K}$ and $R_\star = 1\,R_\odot$ and Jupiter-sized planets ($R_\mathrm{p} = 1\,R_\mathrm{Jup}$), this corresponds to contrasts in the order of $2 \times 10^{-5} - 7 \times 10^{-4}$ and $4 \times 10^{-4} - 2 \times 10^{-3}$ at 2 µm and 5 µm, respectively (see equation 1.7). This regime is well probable with current telescopes and instruments as discussed below.

In Figure 1.5 we visualize the thermal contrast of gas giant companions as a function of age for several wavelengths. We used AMES-Cond evolutionary models (Allard et al. 2001; Chabrier et al. 2000) to obtain the effective temperatures for planets of various masses at ages in the range 1 Myr – 10 Gyr. We simulated a solar-like primary whose effective temperature as a function of age was determined in a similar fashion using MIST models (Dotter 2016; Choi et al. 2016). For host star and planet we applied radii of $1\,R_\odot$ and $1\,R_\mathrm{Jup}$, respectively, which we assumed to be constant in time. It is clearly visible that the star to planet contrast, c_therm, for a fixed object mass decreases as a function of time, mainly driven by the cooling of

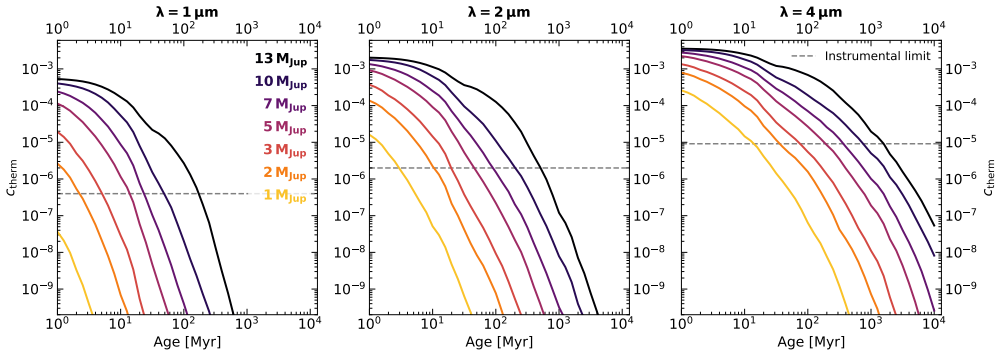

Figure 1.5: Thermal star-to-planet contrast as a function of system age. The contrasts are derived using equation (1.7). Planetary and stellar temperatures are derived from AMES-Cond and MIST evolutionary models, respectively. A range of planet masses are assessed as indicated in the top right of the left panel. We further assume a constant planetary and stellar radius of 1 R_{Jup} and 1 $R_{\odot}$, respectively. The contrast is evaluated for infrared wavelengths of 1 µm (left panel), 2 µm (middle panel), and 4 µm (right panel). The dashed lines represent instrumental contrast limits for SPHERE (1 µm and 2 µm; simulated with the SPHERE exposure time calculator[6]) and NACO (4 µm; Launhardt et al. 2020).

the planetary object. Independent of age, the contrast is more favorable for higher-mass objects, which also agrees with the higher temperatures that are associated with heavier objects.[5] When evaluating c_{therm} for different wavelengths, it becomes clear that the planet contrast becomes more favorable at longer wavelengths. As noted before, the thermal background noise on our detectors increases at longer wavelengths as well, deteriorating the achievable contrast. To obtain reasonable estimates for actual instrumental sensitivities at the wavelengths of this comparison (1 µm, 2 µm, and 4 µm), we relied on the performance of advanced high-contrast imaging instruments for each corresponding wavelength regime: for 1 µm and 2 µm this was the Spectro-Polarimetric High-contrast Exoplanet REsearch instrument (SPHERE; Beuzit et al. 2019) and for 4 µm the NAOS adaptive optics system combined with the CONICA camera (NACO; Lenzen et al. 2003; Rousset et al. 2003). The NACO contrast at 4 µm was adopted from data on ϵ Eridani ($m_{4\mu\mathrm{m}} \approx 1.6$ mag) published by Launhardt et al. (2020). For SPHERE we utilized the dedicated exposure time calculator[6] and simulated the contrast for 1 h on-target integration on a bright, solar-type star ($m = 0$ mag). For both instruments, we assessed the contrast performance at 1″, which is visualized by the dashed lines in Figure 1.5. As expected, the instrumental contrast performance decreases when going to longer wavelengths. A wavelength of 4 µm seems to be most favorable for the detection of young planets: for system ages that are smaller than 10 Myr planets with masses down to 1 M_{Jup} can be detected, and for older systems planets with masses close to the deuterium burning limit of $\sim$13 M_{Jup} seem to be within reach of NACO. But this must not be interpreted as a general conclusion. First, the angular resolution is proportional to wavelength, which means that at shorter wavelengths smaller angular scales can be probed. Second, these simulations rely on synthetic evolutionary models for sub-stellar objects

[5] Note that the energy budget to calculate the planetary luminosity does not include any reprocessed stellar light in this scenario.

[6] Online available at `https://www.eso.org/observing/etc/`

which have their own uncertainties. And third, observations at shorter wavelengths are usually more efficient as longer integration times can be applied and less time is spent off-target to monitor and model the thermal sky background. It is true though that wavelengths from H to L band are best suited for the detection of gas giant exoplanets as all undisputed planet discoveries by direct imaging were exclusively made in this wavelength regime (e.g., Marois et al. 2008, 2010; Lagrange et al. 2010; Rameau et al. 2013; Macintosh et al. 2015; Chauvin et al. 2017b; Keppler et al. 2018). Besides, younger planets are brighter and therefore easier to detect. Due to this relation, the majority of directly imaged planets exhibit ages that are younger than 100 Myr. Particularly favorable are young stellar associations with ages of even less than 20 Myr. As these are mostly farther away than 100 pc from Earth, the physical scales that can be probed with current instrumentation are usually larger than the semi-major axis of Jupiter in the Solar System: for instance, an inner working angle of $0\farcs1$ as minimum angular separation, at which state-of-the-art instruments can detect planetary-mass companions, would correspond to detectable planet semi-major axes that are larger than 10 au for systems that are farther away than 100 pc.

From these considerations it is clear that the development of observing strategies for the direct detection of planetary companions is a high-dimensional problem that cannot easily be optimized. There is certainly no perfect strategy to detect such companions, and several trade-offs have to be considered such as

- observing at longer wavelengths (as planets are brighter in this regime) versus the increasing background noise and the lower angular resolution of the imaging system (going hand in hand with a reduced sensitivity, especially at small angular separations);
- or targeting comparably older systems close to Earth (to probe physicals scales of a few Astronomical Units) versus more distant, young associations (for which the planet contrast is more favorable due to the younger ages).

The past decade has shown us that current instrumentation is capable of imaging young, self-luminous gas giant planets, yet significant technical advances were required to obtain these achievements.

Techniques required for the direct detection of exoplanets

The main deliverable required of a system for the imaging of extra solar planets is the high-contrast that has to be provided at small angular separations. The fundamental resolution limit of an imaging device with an unobstructed, circular aperture is determined by the Rayleigh criterion, which defines the minimum angular separation ϑ_{min} that can be resolved with an aperture size D when observing at wavelength λ as

$$\vartheta_{\mathrm{min}} \approx 1.22 \frac{\lambda}{D} \,. \tag{1.11}$$

This leads to the conclusion that for a fixed wavelength a large aperture size is required to probe tiny angular scales in the order of a few tens of milliarcsecond (10 mas $\widehat{=}$ 1 au at 100 pc). While this assumption is in theory correct, there are other effects that need to be considered when performing observations from the ground.

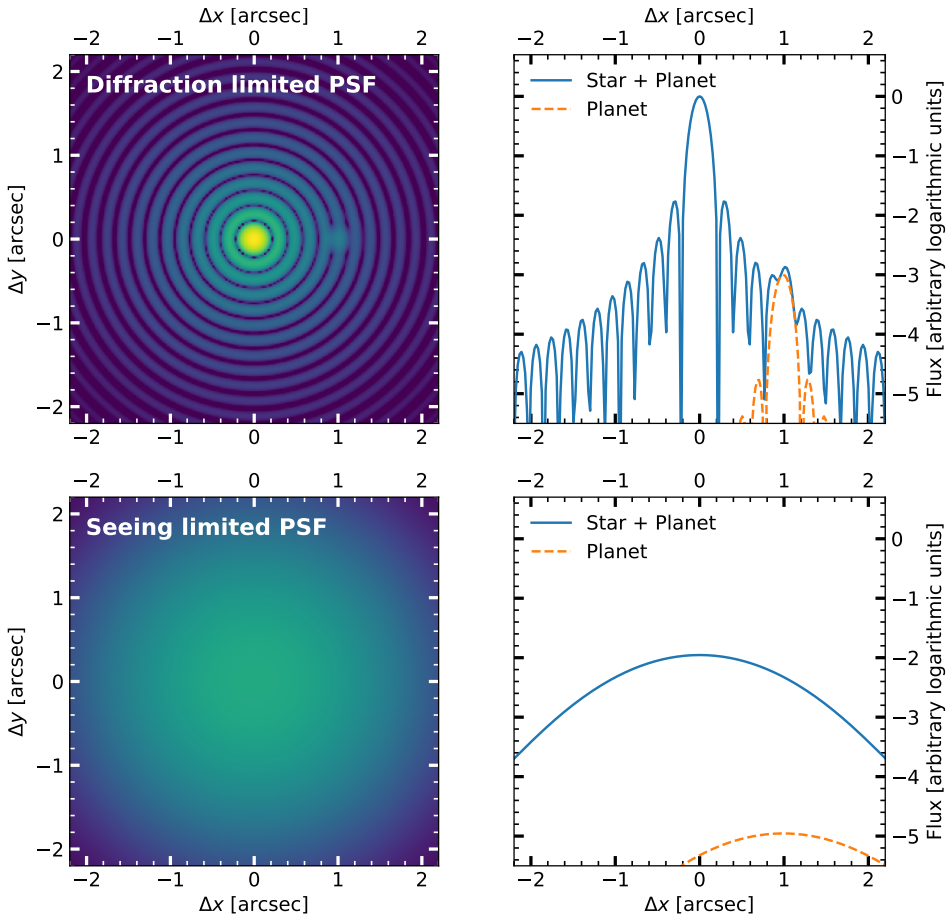

Figure 1.6: The effect of astronomical seeing on the angular resolution of an imaging system. *Top panel*: Diffraction limited PSF of a stellar point source and a planetary companion at an angular separation of $1''$ with a contrast of 10^{-3}. The left panel shows an image of both sources, and the right panel represents the intensity profile along the x direction for $y = 0''$. *Bottom panel*: Same as top panel but with a simulated seeing of $0''.8$.

Adaptive optics systems Unfortunately, the true resolution of an imaging system is usually not equal to the Rayleigh criterion in equation (1.11), which must rather be interpreted as a lower limit of physically possible resolutions. This deviation is caused by wavefront aberrations induced to the collected light before being focused onto the detector. Especially for ground-based observatories the inhomogeneous and turbulent temperature profile of Earth's atmosphere is severely perturbing the plane wavefronts that are approaching from a distant point source such as a star or an exoplanet. This effect commonly known as astronomical seeing convolves the theoretical Airy-like point spread function (PSF) with a kernel that can be approximated by a Gaussian function to first order. The full width at half maximum (FWHM) of this Gaussian function depends on the strength of the atmospheric turbulence, which can be parameterized by the Fried parameter r_0 (Fried 1966). Instead of a diffraction limited PSF that is scaling as λ/D, the collected image is seeing limited with

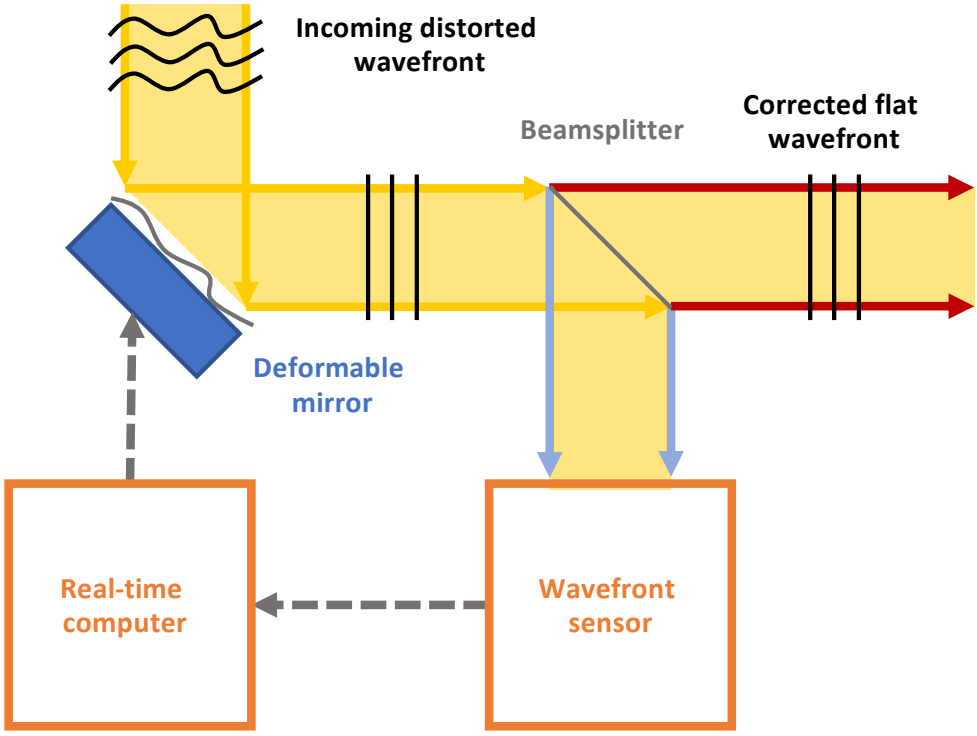

Figure 1.7: Schematic setup of an AO system. The distorted incoming wavefront is corrected by a deformable mirror. This mirror is controlled by a real-time computer that is analyzing the wavefront distortions that are measured with a wavefront sensor. This sensor is usually fed with the blue part of the incoming spectrum that is separated by a beam splitter. The aberrations of the red part of the light are corrected and focused on a detector.

$\theta \propto \mathrm{FWHM} \propto \lambda/r_o$. Accordingly, the achieved resolution does not depend on the telescope aperture size any longer, but is purely determined by the strength of the seeing. FWHMs smaller than $0\farcs8$ are usually considered as good seeing conditions; at prime sites of ground-based astronomical research these values can even go as low as $0\farcs4$ in some exceptional nights. The impact of this effect on the imaging of exoplanets is visualized in Figure 1.6. Whilst an off-axis companion at $(\Delta x, \Delta y) = (1'', 0'')$ with a contrast of 10^{-3} is visible in the diffraction-limited image (top panel of Figure 1.6), it is clearly hidden below the seeing halo of the primary star in the bottom panel of Figure 1.6.

To image faint exoplanets at close angular separations, it is therefore paramount to have an imaging system that is working close to the diffraction limit of the corresponding telescope. The effect of the seeing can be reverted by so-called adaptive optics (AO) systems (Babcock 1953; Hardy 1998). A schematic overview of such a system is presented in Figure 1.7. The blue part of the distorted, incoming light is analyzed by a wavefront sensor that sends information about the residual aberrations to a real-time computer. This computer calculates and alters the shape of a deformable mirror to correct for the remaining aberrations. This correction process has to be applied in real time to correct for quickly varying aberrations. Whereas the

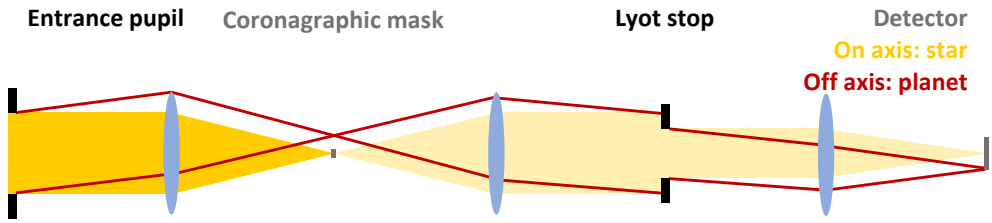

Figure 1.8: Optical design of a basic Lyot coronagraph. The light propagating through the entrance pupil is focused, and a coronagraphic mask is occulting the central part of the image (i.e. where a bright source is located). When the beam is reimaged afterwards, the majority of the remaining light from the on-axis source is distributed at the edges of the pupil image. This beam passes a Lyot stop that is blocking this residual light from the central star and transmitting photons from off-axis sources (red lines). When imaged on the detector, the bulk of stellar light is removed and faint, off-axis point sources become visible.

blue part of the corrected light is directed towards the wavefront sensor, the red part propagates as an almost flat wavefront towards the science detector.

Usually, the Strehl ratio is used as a metric to measure the performance of an AO system. Strehl is defined as the ratio between the peak intensity of a recorded PSF to the peak intensity of the theoretical diffraction-limited PSF. Extreme AO systems such as the SPHERE AO for eXoplanet Observation (SAXO; Fusco et al. 2006) can achieve on-sky Strehl ratios of more than 90 % in the H band.

Coronagraphy The use of (extreme) AO is usually not sufficient to reveal faint exoplanets with contrast in the order of 10^{-5} at angular separations of less than $1''$. As presented in the top panel of Figure 1.6, Airy rings of the stellar PSF are still brighter than the Airy core of such a potential companion. To reduce the amount of stellar flux at separations that are larger than the diffraction limit of the system, so-called coronagraphs are used. The concept of coronagraphy was developed by the French astronomer Bernard Lyot, who aimed to study the solar corona (hence the name of the device; Lyot 1939). Inspired by the concept of a solar eclipse, Lyot tried to block the bulk of solar intensity without requiring the moon to move across the line of sight. The basic concept of such a Lyot coronagraph is presented in Figure 1.8; and this setup can also be used to decrease the intensity of unresolved stars. The light that enters the entrance pupil of the telescope is focused, and the central part is blocked by an opaque mask. Afterwards, the pupil is reimaged and residual starlight is removed by a Lyot stop in the pupil plane. Eventually, the stellar intensity in the final image is reduced drastically, whereas this design does not significantly affect the throughput of off-axis sources. In this way a faint planet that is usually hidden by the PSF of the primary star can become visible. In Figure 1.9 we present two exemplary images that emphasize the importance of a coronagraph in high-contrast imaging observations. A faint off-axis point source that is barely visible in the non-coronagaphic frame (left panel of Figure 1.9) is detected at high signal-to-noise ratio when using a coronagraph (right panel of Figure 1.9). By adding this additional piece of optic to the instrument, the contrast in the science images improves significantly.

Despite many developments to improve the performance of such focal-plane coronagraphs (e.g., Guyon 2003; Soummer 2005), the underlying principles of this basic

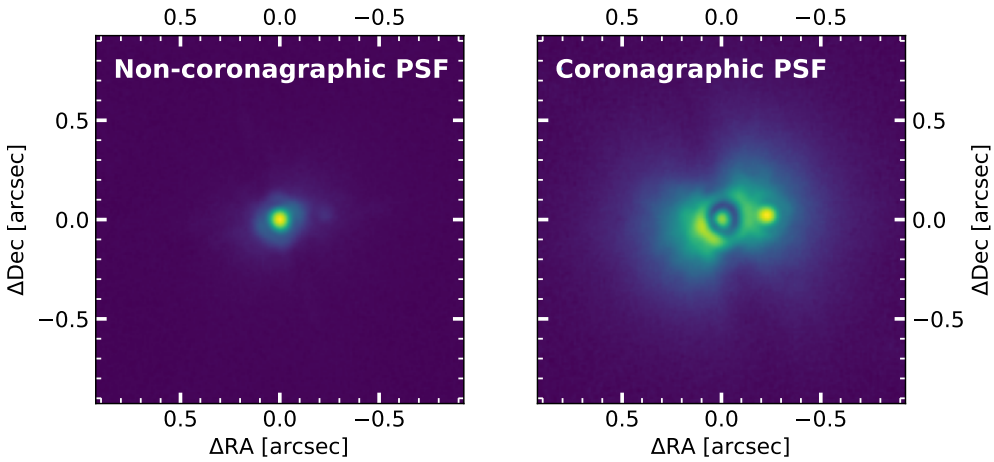

Figure 1.9: Comparison of images obtained without and with coronagraph. *Left panel*: SPHERE non-coronagraphic K_s band image of a point source with a faint companion. The exposure time is 2 s, and a neutral density filter attenuates the collected flux by a factor of 6.9. *Right panel*: SPHERE coronagraphic K_s band image of the same system. The exposure time is 8 s and no neutral density filter is placed in the optical path.

concept that was developed almost a century ago are still in use in modern high-contrast imaging instruments. Another class of coronagraphs are mounted in the instrument's pupil plane instead (e.g., Soummer et al. 2003; Codona et al. 2006; Kenworthy et al. 2007; Snik et al. 2012). These alter the stellar PSF and create dark holes around the primary star by destructive interference of light. For a recent review about past, current, and future coronagraphic concepts and technologies the reader is referred to the review articles of Mawet et al. (2012) and Ruane et al. (2018).

Observation strategies and post-processing In addition to AO systems and coronagraphs, the final contrast can further be optimized based on suitable observing and post-processing strategies. Usually, this contrast improvement is achieved by modeling and subtraction of the stellar PSF.

Angular differential imaging It is most common to carry out high-contrast imaging observations in pupil-stabilized mode, which enables so-called angular differential imaging (ADI; Marois et al. 2006a) techniques in post-processing. In this observing mode the telescope's field-derotator is disabled. This leads to a rotation of the imaged field of view throughout the observing sequence. The general idea of this setup is that the stellar PSF halo, residual aberrations, and speckles in the focal plane around the target star are (quasi) static, whereas a potential off-axis companion would rotate according to its parallactic angle. Due to this artificially created diversity, the stellar PSF can be modeled by taking the median along the time dimension. If the parallactic rotation in the datset is sufficient, this PSF model only contains a negligible amount of signal from the off-axis point source. Hence, this model can be subtracted from each individual image; afterwards, the residuals are derotated and stacked to increase the signal-to-noise ratio of a potential companion.

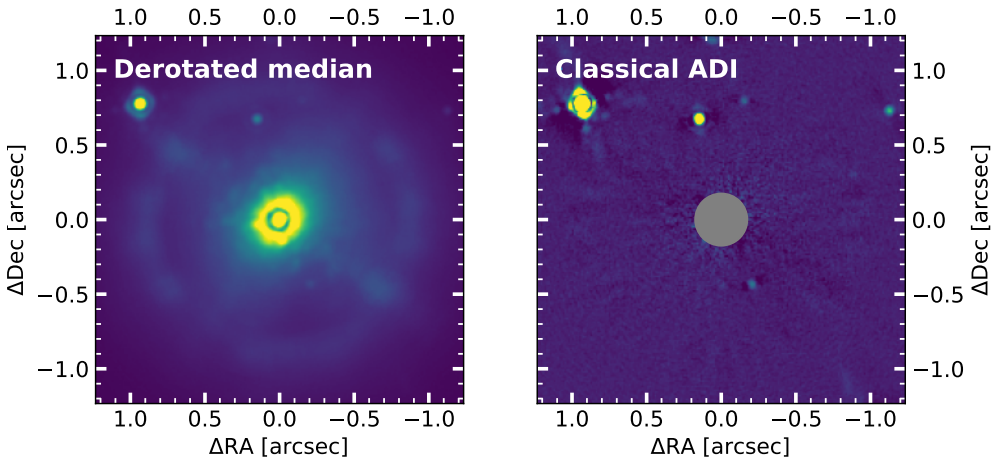

Figure 1.10: Contrast improvement with ADI. *Left panel*: Derotated and median combined image from an observing sequence collected in pupil-stabilized mode. *Right panel*: Classical ADI residuals for the same dataset. Several point sources that were hidden by stellar noise are now visible in the image. The inner region around the coronagraph is obscured by an artificial mask.

The contrast gain that can be obtained by this post-processing method is demonstrated in Figure 1.10.

Instead of just taking the median along the temporal dimension, there exist more advanced methods to obtain a PSF model from the data. The first class of these sophisticated PSF modeling algorithms relied on a Locally Optimized Combination of Images (LOCI; Lafrenière et al. 2007a); several advanced versions of the original LOCI code are available today (e.g., Marois et al. 2014; Wahhaj et al. 2015). Another class of PSF reconstruction algorithms relies on principal component analysis (PCA; Kendall 1957; Deeming 1964) that is creating an orthogonal set of basis vectors from the images via singular value decomposition. First PSF subtraction schemes that relied on this low rank approximation were `PynPoint` (Amara & Quanz 2012) and KLIP (Soummer et al. 2012); Meshkat et al. (2014) presented an optimized version of the original algorithm that includes frame rejection and different cutoff radii. Several additional PSF subtraction algorithms have been proposed in the past years, such as low-rank plus sparse decompositions (Gomez Gonzalez et al. 2016) or non-negative matrix factorization (Ren et al. 2018).

Spectral differential imaging The latest generation of extreme AO high-contrast imaging instruments such as the SPHERE, the Gemini Planet Imager (GPI; Macintosh et al. 2014), or the Subaru Coronagraphic Extreme Adaptive Optics System (SCExAO; Jovanovic et al. 2015) are all equipped with integral field spectrographs (IFS) that provide low resolution spectra ($R \sim 50$) for a field of view in the order of $2'' \times 2''$ (e.g., Claudi et al. 2008; Larkin et al. 2014; Peters et al. 2012; Groff et al. 2015). As the size of the stellar PSF, along with residual speckles, scales as a function of wavelength, the position of a planetary companion, however, is constant in the field of view, IFS observations deliver another option to discriminate between off-axis signals and contaminating stellar flux. Similar to ADI, this spectral diversity can be used to model and remove the stellar PSF without subtracting the signal of a potential planet. The

idea of using simultaneous images of different wavelengths to subtract stellar light was first introduced by Racine et al. (1999); Sparks & Ford (2002) recognized the potential of this strategy and proposed coronagraphic imaging with an IFS for an improved sensitivity to faint extrasolar planets. By now, spectral differential imaging (SDI) has become a standard technique for post-processing of high-contrast imaging IFS data, and SDI is included in several reduction algorithms (e.g., Marois et al. 2006b; Janson et al. 2008; Pueyo et al. 2012; Rameau et al. 2015; Galicher et al. 2018). SDI can also be combined with ADI, leading to improved contrasts compared to either of these methods applied by themselves (Vigan et al. 2010; Christiaens et al. 2019; Kiefer et al. subm).

Reference star differential imaging One of the oldest methods to subtract the PSF of a primary star is by observing a reference star, whose PSF is used as a template for the science target. Smith & Terrile (1984) used this technique to detect a dusty disk around the young star β Pictoris.[7] For the same primary star, Lagrange et al. (2009) later found a giant Jovian planet that was located inside the dusty debris disk. Lagrange et al. discovered the companion β Pictoris b in archival NACO data from 2004, which were reassessed by subtraction of a reference PSF acquired on HR 2435, a nearby star of similar spectral type. This basic concept of reference star differential imaging (RDI) proved to be very useful to study especially circumstellar environments (Mawet et al. 2009; Rameau et al. 2012). ADI does not work particularly well for these science cases, as the angular variety of disks observed at low inclinations is small; this leads to remaining disk signal in the subtracted PSF model and hence the over-subtraction of scattered light signal (e.g., Milli et al. 2012). RDI reductions were significantly improved by the introduction of PCA-based processing schemes. Especially the Archival Legacy Investigations of Circumstellar Environments (ALICE; Hagan et al. 2018) project revealed several circum-stellar disks from archival HST data that were previously undiscovered (e.g., Soummer et al. 2014; Choquet et al. 2014, 2016, 2017).

But RDI has also been successfully employed for the detection and characterization of extrasolar planets (e.g. Soummer et al. 2011; Wahhaj et al. 2021). Especially our Young Suns Exoplanet Survey (YSES, see Section 1.4) heavily relies on an RDI-based data reduction strategy; and with the combination of RDI and PCA we discovered disks and planets (see Bohn et al. 2019, 2021).

Other approaches Instead of traditional PSF subtraction algorithms, there are also other methods to identify planets in high-contrast imaging data. These rely either on a forward model, such as ANDROMEDA (Cantalloube et al. 2015) and TRAP (Samland et al. 2021); statistical discrimination between speckles and planet signals as proposed by Gladysz & Christou (2008), or as implemented in several variants of the PACO algorithm (Flasseur et al. 2018, 2020), the STIM map (Pairet et al. 2019), and the RSM detection map (Dahlqvist et al. 2020, 2021); machine learning algorithms (e.g., Gomez Gonzalez et al. 2018; Gebhard et al. 2020); or other iterative approaches such as MAYONNAISE (Pairet et al. 2021). For a recent performance evaluation of various post-processing algorithms the reader is referred to Cantalloube et al. (2020).

[7] Note that the final image presented in Smith & Terrile (1984) is a ratio image and not a differential image. According to the authors' description, such a difference image, which showed the circum-stellar disk, was created as well.

Results and prospects of direct detections of exoplanets

By overcoming all these challenges, direct imaging of exoplanets is indeed possible. The first planetary-mass companion that was discovered by direct imaging is 2MASS J12073346-3932539 b that is orbiting its M type primary at an angular separation of more than 55 au (Chauvin et al. 2004). One of the most emblematic environments that could be directly imaged so far is the multi-planetary system around HR 8799 (see Figure 1.11). Marois et al. (2008, 2010) revealed four gas giant planets in orbits of 15 au to 70 au around this A type[8] star. Continuous monitoring of this intriguing system showed significant amounts of orbital motion,[9] revealing that the system exhibits an almost face-on geometry (e.g., Maire et al. 2015; Wang et al. 2016).

Direct imaging is currently only sensitive to young, super-Jovian planets that are widely separated (usually $\geq 0\farcs2$) from their primary stars. This bias is clearly visible in Figure 1.1, where the directly imaged planets exclusively occupy the upper right of the mass versus semi-major axis parameter space. As this technique cannot reliably probe Solar System scales in terms of planet masses and physical separations, it seems to be inferior to other methods that can at least partly detect these Solar System analogs. Indeed, this current bias can also be interpreted as a particular strength unique to the direct imaging method as no other exoplanet detection technique is capable to probe numerous planets with semi-major axes that are larger than 5 au. Direct imaging thus provides unique insights into the wide-orbit architectures of planetary systems up to thousands of Astronomical Units (e.g. Naud et al. 2014). These extreme scales are not even accessible in our own Solar System, which is hypothesized to host an additional, undiscovered Planet 9 at several hundreds of Astronomical Units (Batygin & Brown 2016).

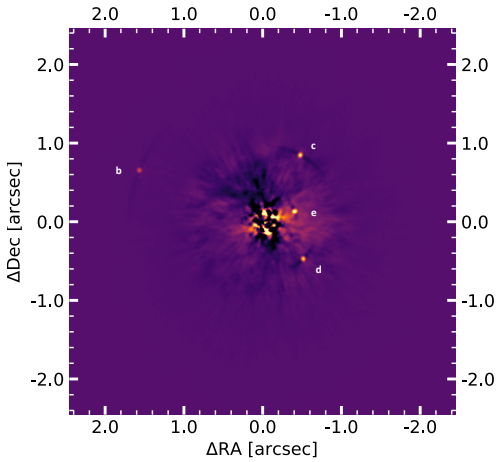

Figure 1.11: The multi-planetary system around HR 8799. The star is located at the center of the image and post-processing with ADI plus PCA is performed to remove the stellar halo. Four planets (labeled b, c, d, and e) are clearly visible in the image. North points up and east towards the left. The data was collected with VLT/SPHERE on the night of 2017 October 11 (ESO ID: 099.C-0588(A); PI: Biller) and published in Biller et al. (2021).

Direct imaging is the only technique which spatially resolves the planet and its host star. This facilitates unique opportunities of planet characterization that are hardly accessible by indirect detection methods. Even though spectra of transiting planets can be obtained by evaluation of the transit depth for several wavelengths (Brown 2001), the spectra of directly imaged companions usually exhibit

[8]The spectral type of HR 8799 is controversial as different tracers provide various estimates ranging from A5 to F0 (Gray & Kaye 1999).

[9]A nice visualization of the planets orbiting around the star is available online: `https://en.wikipedia.org/wiki/HR_8799#/media/File:HR_8799_Orbiting_Exoplanets.gif`

much higher signal-to-noise ratios and can be obtained with much higher efficiency: observations can be collected in a continuous observing sequence, whereas the combination of several transit measurements is required to perform transit spectroscopy. Despite several ground-breaking results from transit spectroscopy – such as measurements of the cloud coverage on Kepler-7b (Demory et al. 2013), the detection of Na I in the atmosphere of HD 189733b (Wyttenbach et al. 2015), and atomic iron and titanium in the atmosphere of Kelt-9b (Hoeijmakers et al. 2018a) – direct imaging is by far the most promising method to characterize the atmospheres and to evaluate the habitability of terrestrial planets in the future (e.g., Biller & Bonnefoy 2018), particularly due to the special system geometry that is required for the planet to transit and the time-intensive nature of transit-based characterizations.

One of the first directly imaged exoplanets that was characterized by consecutive spectroscopic measurements with Keck/OSIRIS (Larkin et al. 2006) was HR 8799b (Barman et al. 2011). Barman et al. found a hydrogen-dominated atmosphere, and the authors were able to constrain the planet's temperature, luminosity, and surface gravity. Further major results from these spatially resolved exoplanets are among others: water and carbon monoxide absorption features detected in the atmopshere of HR 8799c (Konopacky et al. 2013); rotation period measurements of the fast-spinning super-Jupiter β Pictoris b (Snellen et al. 2014); and the detection of two accreting protoplanets that are carving out the gap around the young T-Tauri star PDS 70 (Keppler et al. 2018; Wagner et al. 2018; Haffert et al. 2019). Interferometric observations with VLTI/GRAVITY (Gravity Collaboration et al. 2017) exhibit an enormous potential to perform medium resolution spectroscopy ($R \sim 500$) of Jovian exoplanet atmospheres even beyond the diffraction limit of current 10 m-class optical telescopes (Gravity Collaboration et al. 2019, 2020; Nowak et al. 2020; Wang et al. 2021).

Even though terrestrial planets are too faint to be directly characterized by the current generation of telescopes, future observatories and instruments might provide the required angular resolution, contrast performance, and sensitivity. These might be either space-based telescopes with large apertures such as LUVOIR (The LUVOIR Team 2019) or HabEx (Mennesson et al. 2016; Gaudi et al. 2020) or ground-based extremely large telescopes that will become available over the coming decades. The European ELT, currently under construction, will have an unprecedented primary mirror diameter of 39 m (Gilmozzi & Spyromilio 2007). METIS, one of the first-light instruments at the ELT, is expected to image and characterize terrestrial exoplanets around the nearest stellar neighbors (Quanz et al. 2015). Ambitious future projects such as LIFE might be required in the end to reveal first unambiguous signs of biosignatures outside Earth (Quanz et al. 2019, 2021).

1.3 Formation of gas giant planets

The technical advances of the past decades facilitated the direct detection of several gas giant planets outside our Solar System. Whereas some of these reside within orbits that are comparable to those of Jupiter, Saturn, Uranus, or Neptune (e.g., β Pictoris b at $\sim$8 au, Lagrange et al. 2009, 2010; Quanz et al. 2010; 51 Eridani b at $\sim$13 au, Macintosh et al. 2015; PDS 70 b at $\sim$22 au, Keppler et al. 2018; PDS 70 c at $\sim$30 au, Haffert et al. 2019), the majority of these Jovian giants exhibit significantly larger semi-major axes ($>$50 au) than all Solar System planets (e.g., Chauvin et al.

2005; Schmidt et al. 2008; Rameau et al. 2013; Bailey et al. 2014; Chauvin et al. 2017a; Bohn et al. 2020a,b). The formation pathway and early evolution of these wide-orbit systems is poorly understood. It remains unclear whether these gas giants have formed in situ by (A) fragmentation processes of the collapsing proto- stellar cloud – thus representing the lower-mass threshold of the stellar binary population (Kroupa 2001; Chabrier 2003) – or if they were born at closer separations to the star (B) via core accretion mechanisms (e.g., Pollack et al. 1996; Alibert et al. 2005; Dodson-Robinson et al. 2009; Lambrechts & Johansen 2012), followed by a potential outward migration that is driven by scattering events (e.g., Veras et al. 2009; Mustill et al. 2021). In situ formation via core accretion is thought to be very unlikely as the timescales to build up a solid core that is massive enough to accrete a gaseous atmosphere are too long at separations larger than 50 au compared to typical disk lifetimes (Haisch et al. 2001; Rafikov 2011). A third scenario that supports planet formation for a wide range of orbital separations is (C) the disk instability paradigm that postulates the formation of planetary cores from gravitational collapse of dense regions in the protoplanetary disk (Boss 1997, 2011; Rafikov 2005; Durisen et al. 2007; Kratter et al. 2010; Kratter & Lodato 2016).

There are two common approaches to evaluate the efficiencies of these planet formation scenarios:

1. In a statistical framework, simulated planet occurrence rates based on the various formation mechanisms (e.g., Mordasini et al. 2009a,b; Forgan & Rice 2013; Forgan et al. 2018) are compared to observational survey results, to place constraints on the efficiency of the corresponding formation pathway.

2. Spectral characterization of identified wide-orbit gas giants can further link the atmospheric molecular and isotopologue abundance ratios of these companions to their natal environments.

I will further discuss these scenarios in Sections 1.3.1 and 1.3.2, respectively.

1.3.1 Direct imaging surveys

Several direct imaging surveys have been conducted in the past years (e.g., Lafrenière et al. 2007b; Kasper et al. 2007; Biller et al. 2013; Nielsen et al. 2013; Galicher et al. 2016; Bowler 2016), and the analyses of the most relevant studies are still ongoing. The preliminary statistical evaluation of the first 150 stars observed as part of the the SpHere INfrared survey for Exoplanets (SHINE; Vigan et al. 2020) indicates that substellar companions (with masses in the range $1\,M_{\rm Jup} - 75\,M_{\rm Jup}$) around M-type stars likely formed via either protostellar fragmentation processes (A) or gravitational instabilities (C), whereas the occurrence rates of objects of the same mass around B and A-type stars are consistent with planet populations from core accretion simulations (B). The statistical data for the intermediate category of F, G, and K-type stars does not favor a single formation pathway, but can be explained best by a combination of all scenarios. These findings are corroborated by the Gemini PLanet Imager Exoplanet Survey (GPIES; Macintosh et al. 2018). Nielsen et al. (2019) find that giant planetary companions with masses between $1\,M_{\rm Jup}$ and $13\,M_{\rm Jup}$ are predominately created by bottom-up formation mechanisms (B), whilst the population of brown dwarf companions with masses in the range $13\,M_{\rm Jup} - 80\,M_{\rm Jup}$ is rather compatible with top-down formation mechanisms (A,C). These distinct formation pathways for

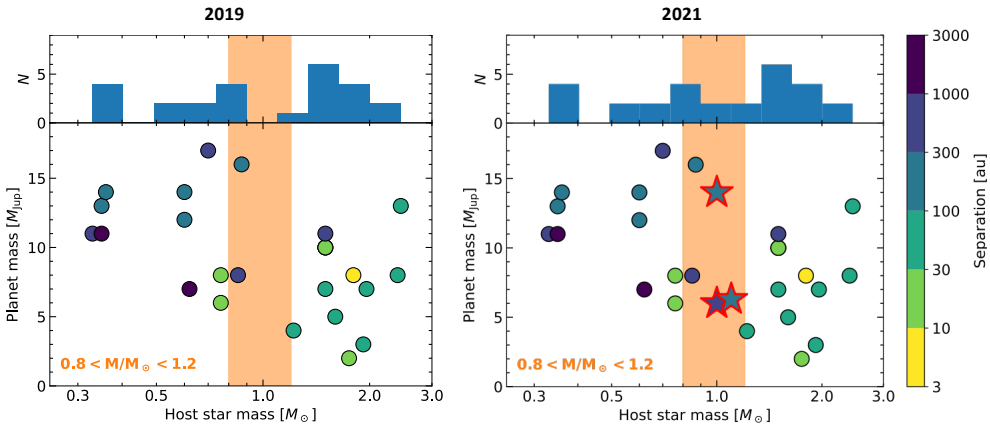

Figure 1.12: Demographics of directly imaged exoplanets in 2019 (*left panel*) and 2021 (*right panel*). The orange box highlights solar-like host stars with $0.8 < M/M_\odot < 1.2$. The stellar markers with the red outlines indicate new planetary-mass companions that were discovered as part of our Young Suns Exoplanet Survey (see Section 1.4).

the sample of giant planets and brown dwarfs are in perfect agreement with recent results from Bowler et al. (2020). Based on analyses of orbital parameters of directly imaged companions, Bowler et al. find that the eccentricity distributions show clear evidence for two distinct populations, indicative of different formation channels.[10] Both Vigan et al. (2020) and Nielsen et al. (2019) find that heavier mass stars are more likely to harbor gas giant companions with semi-major axes in the range 5 au − 100 au, which is confirmed by results from RV surveys for planets with shorter periods (Johnson et al. 2010; Ghezzi et al. 2018). To study if this relation even holds for stars with masses that are larger than 2 $M_\odot$, Janson et al. (2021) are currently carrying out the B-star Exoplanet Abundance Study (BEAST) that is targeting the most massive stellar members of the Scorpius-Centaurus association (Sco-Cen; de Zeeuw et al. 1999).

All these results indicate that planet formation depends heavily on the mass of the primary star. Especially for the intriguing sub-class of Sun-like stars, no dominant formation pathway of gas giant companions could be established so far. This can also be attributed to the small number of exoplanets that have been found around solar-type host stars. As presented in the left panel of Figure 1.12, there seems to be a void of planets around solar analogs (until 2019). However, this might also be an observational bias as young (<20 Myr), solar-type stars were largely neglected in past direct imaging searches for extrasolar planets. This is mostly due to the fact that the majority of such young targets are located at distances of more than 100 pc, and therefore exhibit R band magnitudes that are fainter than 10 mag. As the quality of the AO correction is usually degrading with a decreasing flux from the natural guide star, previous surveys focused on the significantly brighter population

[10] Note that Bowler et al. (2020) apply slight different thresholds than Nielsen et al. (2019) for objects to be considered either giant planet or brown dwarfs. In Bowler et al. (2020) giant planets are selected with masses in the range 2 M_{Jup} − 15 M_{Jup} and brown dwarfs are identified as objects with masses between 15 M_{Jup} and 75 M_{Jup}.

of B, A, and F type stars of these associations.[11] Despite the worse AO correction on young G and K type stars at distances of more than 100 pc, these targets can be observed with the latest generation of high-contrast imaging instruments, and the astrometric precision is sufficient for the required proper motions checks (see Chapters 4, 5, and 6). It is thus vital to use the capabilities of these state-of-the-art instruments to systematically study a population of young, Sun-like stars with statistical significance. Such observations might reveal important clues regarding the origin of wide-orbit Jovian companions in young, Sun-like environments.

1.3.2 Atmospheric characterization of directly imaged planets

To identify the birthplaces of individual gas giants, Öberg et al. (2011) proposed to use elemental abundances in the planetary atmosphere as a tracer. The C/O ratio might be indicative of the natal environment of a planet in a circum-stellar disk. Due to a radial temperature gradient in the disk, certain molecules freeze out at characteristic separations from the primary star. These transition regions are called icelines (or snow lines when talking especially about H_2O; Stevenson & Lunine 1988; Lodders 2004; Kuchner & Seager 2005). These processes affect the abundance ratios of molecules that are either in the solid or gas phase. For a typical young, solar-type star the H_2O snowline is located at approximately 3 au (e.g., Hayashi 1981; Podolak & Zucker 2004; Martin & Livio 2012). Farther out water molecules are predominantly present in their solid phase, whereas carbon bearing species such as CO_2 or CO are still in their gas phase. Accordingly, the C/O ratio in the gas increases when radially moving outward across the H_2O snowline, whereas the C/O ratio in the grains decreases (as the amount of oxygen in the gas phase is rising, whilst the carbon fraction remains unaltered). Similarly, the carbon to oxygen ratio is altered at the CO_2 and CO icelines, which are located at approximately 10 au and 40 au in the protosolar nebular, respectively (Öberg et al. 2011; Andrews & Williams 2007). The atmosphere of a gas giant planet should therefore exhibit imprints of this variable atmospheric abundance ratio; indicative of its natal environment with respect to the primary star. But disk evolution or enrichment by planetesimals can alter these primordial abundances and hence should be considered in the interpretation (Ali-Dib et al. 2014; Mordasini et al. 2016; Eistrup et al. 2016, 2018). Planet migration and structural inhomogeneities in the natal disk complicate establishing links between present day abundances and the planetary birth environment (e.g., Madhusudhan et al. 2014; Cridland et al. 2016). These issues are extensively discussed in recent review articles of Pudritz et al. (2018), Lammer & Blanc (2018), Madhusudhan (2019), and Öberg & Bergin (2021). Nevertheless, the study of a large sample of giant planetary atmospheres is necessary to identify potential correlations that might be indicative of planet formation history. New GRAVITY data on β Pictoris b revealed a subsolar carbon to oxygen abundance ratio for this super-Jovian gas giant (Gravity Collaboration et al. 2020). This was interpreted as an indication for its formation via the core-accretion channel (B), followed by a strong enrichment by icy planetesimals that exhibit a C/O ratio that is below the solar standard.

These unique insights into the formation history of planetary systems might even be further corroborated when measuring isotope abundance ratios such as D/H or

[11] The SPHERE user manual predicts median (H band Strehl ratio of $50-75\,\%$) to poor (H band Strehl ratio $< 50\,\%$) AO performances for stars that are fainter than $R = 9$ mag: `https://www.eso.org/sci/facilities/paranal/instruments/sphere/overview.html`

$^{12}C/^{13}C$, which impose additional constraints on the location of the natal environment (Mollière & Snellen 2019; Morley et al. 2019). Such a measurement in an exoplanet atmosphere, could not be conducted thus far. New instrumentation such as VLT/CRIRES^{+} (Dorn et al. 2014), VLT/ERIS (Davies et al. 2018), and the James Webb Space Telescope (JWST; Gardner et al. 2006), which will all become available shortly, might provide the required sensitivity to measure isotopologues contents of an exoplanet atmosphere for the first time. In addition to the large statistical surveys described in Section 1.3.1, characterization studies of known wide-orbit gas giants and measurements of their atmospheric compositions are thus promising next steps to understand the origins and formation pathways of gas giant Jovian companions.

1.4 The Young Suns Exoplanet Survey

To enhance the low number of planetary companions to Sun-like primaries and to test their formation scenarios at statistical significance, we started the Young Suns Exoplanet Survey (YSES) that targets a homogeneous sample of 70 young, solar-mass members of the Lower Centaurus-Crux (LCC) subgroup of Sco-Cen. This subgroup has an average age of 15 ± 3 Myr (Pecaut & Mamajek 2016); latest parallax and proper motion measurements provided by the third early data release of the *Gaia* space mission of the European Space Agency clearly confirm the LCC membership of our targets (*Gaia* ERD3; Gaia Collaboration et al. 2021). The YSES sample has an average distance of 118 ± 20 pc, and it consists exclusively of stars with masses in the range $0.8\,M_{\odot} - 1.2\,M_{\odot}$. Therefore, it is a unique collection of the nearest statistically significant sample of young, Sun-like stars to our Sun. There is no closer (≤ 120 pc) and younger (≤ 100 Myr) association with so many stars of about $1\,M_{\odot}$, making the YSES sample particularly significant for statistically constraining the wide-separation planetary population around young solar analogs.

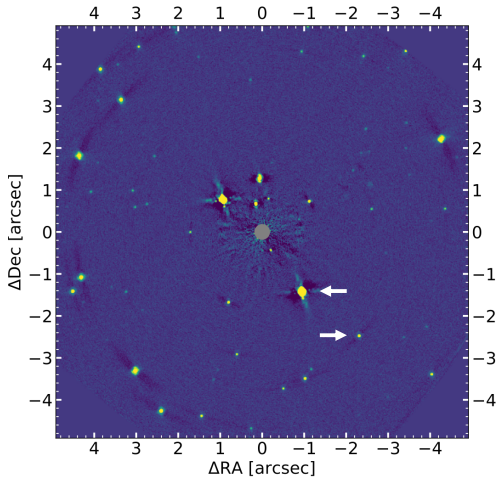

Figure 1.13: Exemplary field of view of an YSES target. As most of the stars from the sample are close to the galactic plane, there is a very high-fraction of background contaminants. From a single image as presented here, it is not possible to distinguish planetary companions (white arrows) from unassociated background stars (all other off-axis point sources in the image). The primary star is located at the image center behind an artificial mask.

YSES is still ongoing: at the moment, we have observed each of the 70 stars once with SPHERE. Our data reduction strategy is based on short snapshot observation in the order of $\sim$2 min per target and filter, in combination with RDI. As all stars within our sample are coeval, at the same distance, and of similar spectral type, they exhibit similar magnitudes at both optical and near-infrared wavelengths. This homogeneity facilitates highly consistent observing conditions in terms of recorded near-infrared flux and

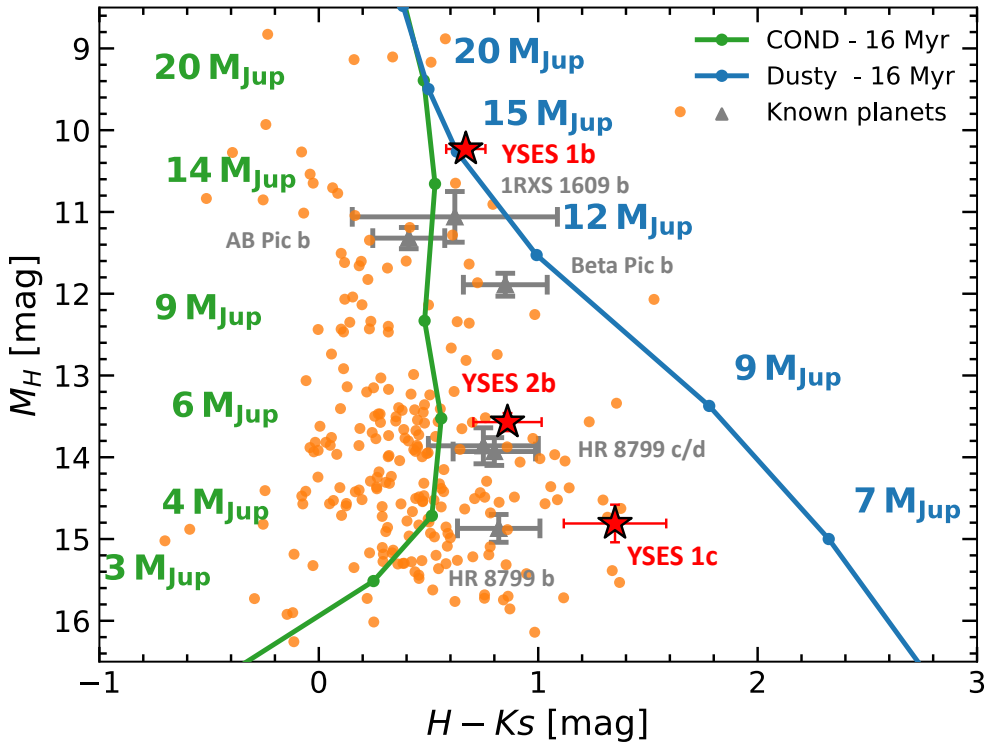

Figure 1.14: Color magnitude diagram of YSES candidate companions. The orange circles indicate off-axis objects detected within the scope of our survey. The red stars highlight actual companions that we discovered. The grey markers represent previously known directly imaged companions and the green and blue lines are from synthetic evolutionary models that were evaluated at the approximate age of LCC.

instrumental AO performance. Hence we can use all frames collected for YSES as a reference library, which we can analyze with PCA. For each target, the stellar PSF is then modeled by a certain number of principal components, and subtracted. In Chapter 6 we asses the performance of this reduction method and show that it is superior to other potential reduction schemes.

Our first epoch observations revealed a plethora of companion candidates. As LCC is close to the galactic plane, a high fraction of associated background stars is therefore expected to be revealed by our observations. This is impressively demonstrated by the image presented in Figure 1.13. More than 50 off-axis point sources are detected around the primary star. From a single snapshot like this, we cannot tell whether one of these objects is indeed a planetary companion or rather a background contaminant. For that reason, we took data in an additional filter to analyze the detected companion candidates in a color-magnitude diagram. As presented in Figure 1.14, almost all the candidate companions that we detected around the sample of 70 young suns are compatible with predictions from evolutionary models or known sub-stellar companions. Since sub-stellar objects around the L-T transition can appear colorless or even blue in the near infrared (Burgasser et al. 2002; Cushing et al. 2005), this pre-selection of interesting candidate companions by color-

magnitude analysis did not work well. Instead we established that second epoch observations and checks for common proper motion with the primary are indispensable measures to confirm gravitationally bound companions around our YSES targets (e.g., Nielsen et al. 2017).

As we did not want to bias our selection of candidate companions by angular separation cutoffs (with preference for small angular separations), we decided to follow-up all targets with candidate companions in the instrument field of view. This turned out to be the right choice as we found gravitationally bound companions at unexpectedly large separations of more than 100 au. For eight targets we could acquire second epoch-observations; these data revealed three planetary-mass companions to two of our stars. Most intriguing was the discovery of the first multi-planet system that was imaged around a Sun-like star (see Chapter 5). We found that YSES 1 (TYC 8998-760-1) hosts two giant planets of $14 \pm 3\,M_{\rm Jup}$ and $6 \pm 2\,M_{\rm Jup}$ at physical separations of more than 160 au and 320 au, respectively. Due to their moderate separations, this system is a prime laboratory to perform consecutive characterization measurements to probe their atmospheric composition and potential formation scenarios. The latest addendum to the small group of directly imaged planets to Sun-like stars is YSES 2b (see Chapter 6): a $6.3^{+1.6}_{-0.9}\,M_{\rm Jup}$ planet at a projected separation of 115 au. This gas giant is challenging current theories of giant planet formation: it is too far separated from the star to have formed in situ via core accretion mechanisms (B), yet it is not massive enough to be compatible with latest models of gravitational instabilities in circum-stellar disks (C). Follow-up measurements of this intriguing system might be able to probe further companions to YSES 2, that could have scattered YSES 2b to its current separation.

Follow-up observations for 44 remaining targets with candidate companions are still pending. We might have been extremely lucky in the selection of our 8 systems that were chosen for follow-up, but it is also likely that there are indeed more planet discoveries from YSES ahead. Even though the survey is not completed yet, YSES already contributed significantly to populate the previously sparsely sampled group of wide-orbit giant planet to solar-type host stars. As shown in the right panel of Figure 1.12, our three detections from YSES already helped to fill the apparent void of such companions; this is tentatively indicating that it was indeed an observational bias, as young Sun-like systems have not been systematically studied at statistical significance prior to our survey. Future prospects of this extremely successful and efficient program are discussed in Chapter 7.

1.5 Thesis outline

Except for Chapter 2 this thesis mainly focuses on the results from YSES. A brief description of the most important results and conclusions reported in each chapter is provided below.

Chapter 2: A multiplicity study of transiting exoplanet host stars

In this chapter we aim to study the stellar multiplicity of known systems to transiting exoplanets. We use VLT/SPHERE to study 45 transiting exoplanet host stars at unprecedented spatial resolution and contrast. We discovered new stellar companion candidates to 13 stars from the sample, which need to be validated by further proper motion measurements. Instead we assigned a likelihood for each companion to be

bound by evaluating stellar population synthesis models. In addition we could detect and confirm previously known companions to 13 other stars from our sample. Based on these data we derived a likelihood of $55.4^{+5.9}_{-9.4}$ % for transiting exoplanet host stars to be part of a multiple system. This measurement is in good agreement with previous surveys and with multiplicity estimates of stars that do not harbor any known planets.

Chapter 3: Discovery of a directly imaged disk in scattered light around the Sco-Cen member Wray 15-788

This chapter presents the first detection of YSES. Around the ∼11 Myr-old K3 star Wray 15-788 we detect clear scattered-light signals from a protoplanetary disk. SED modeling indicates that this disk is at a transition stage, and we detect clear structures of an outer and inner arc, separated by a gap of reduced scattered light flux. Even though the outer arc of the disk is detected almost face on with an inclination of 21 deg ±6 deg, we do not detect disk signal for all phase angles. We hypothesize that this lack of scattered light flux originates from a misaligned inner disk, interior to the inner working angle of our observations, that is casting a shadow on the outer structures that we see in the SPHERE images. This misalignment might be caused by a massive companion in the system. We further identify Wray 15-788 as secondary to the A type primary HD 98363 with a projected separation of about 7000 au. This massive primary hosts a debris disk that was first revealed in scattered light by GPI after the publication of our paper (Hom et al. 2020). The different evolutionary stages of these two coeval disks tentatively support the giant companion hypothesis. Such a companion could cause pressure bumps in the disk that are trapping dust grains at certain separations, leading to the observed gapped geometry (e.g., Pinilla et al. 2015). Future observations with both SPHERE and ALMA will shed light on this fascinating circum-stellar environment.

Chapter 4: Detection of a wide orbit planetary mass companion to a solar-type Sco-Cen member

In this chapter, we present the first planetary-mass companion that was detected by YSES. YSES 1b (TYC 8998-760-1 b) has a mass of $14 \pm 3\,M_{\rm Jup}$ and sits thus directly at the boundary between gas giant planets and low mass brown dwarfs. We measure a projected separation of ∼160 au which is indicative of an orbital period of more than 1'000 yr. The combination of high mass and wide separation favor formation via top down scenarios (A,C); yet further evidence to corroborate this theory is required.

Chapter 5: Two directly imaged, wide-orbit giant planets around the young, solar analog YSES 1

In data obtained to characterize YSES 1b, we identified a very red point source, which turned out to be another planet around this solar-type primary. This discovery is described in Chapter 5 of this thesis. YSES 1c has a lower mass ($6 \pm 2\,M_{\rm Jup}$) than the previously identified YSES 1b. The new planet is even farther separated from its primary star with a projected separation of ∼320 au. This discovery marked the first image of a multi-planet system around a Sun-like star. Further analysis of this intriguing environment might provide vital insights into the formation processes and the dynamical evolution that were shaping this system.

Chapter 6: Discovery of a directly imaged planet to the young solar analog YSES 2

This chapter presents the latest YSES discovery: A new planet to the 1.1 $M_{\odot}$ host star YSES 2 (TYC 8984-2245-1). YSES 2b has a mass of $6.3^{+1.6}_{-0.9}\,M_{\rm Jup}$ and a minimum physical separation of 115 au with respect to its primary star. This companion is especially fascinating due to its dubious origin: in situ core accretion (B) can be ruled out due to the large separation; yet gravitational instabilities (C) tend to produce heavier mass companions. As YSES 2b might have been scattered to its current location, a deep search for additional companions in the system is required.

Chapter 7: Outlook

In this chapter, we present the next steps that are required for the conclusion of the YSES program. We further propose a potential successor program that is observing a large sample of young, Sun-like stars with ages in the range $1 - 20$ Myr, to obtain a temporally resolved insight into the occurrence rates of gas giant companions to solar analogs. This program is likely to reveal several planetary-mass companions that allow for statistical testing of planet formation mechanisms, and detailed atmospheric characterization studies. Lastly, we come back to the initial question as to whether we are alone in the Universe, and present some speculations regarding potential insight that we might gain within the next decades.

Chapter 2

A multiplicity study of transiting exoplanet host stars. I.
High-contrast imaging with VLT/SPHERE

Many main-sequence stars are part of multiple systems. The effect of stellar multiplicity on planet formation and migration, however, is poorly understood. We study the multiplicity of stars hosting known transiting extrasolar planets to test competing theories on the formation mechanisms of hot Jupiters. We observed 45 exoplanet host stars using the infrared dual imaging spectrograph (IRDIS) of the Spectro-Polarimetric High-Contrast Exoplanet Research (SPHERE) instrument at the Very Large Telescope (VLT) to search for potential companions. For each identified candidate companion we determined the probability that it is gravitationally bound to its host by performing common proper motion checks and modeling of synthetic stellar populations around the host. In addition, we derived contrast limits as a function of angular separation to set upper limits on further companions in these systems. We converted the derived contrast into mass thresholds using AMES-Cond, AMES-Dusty, and BT-Settl models. We detected new candidate companions around K2-38, WASP-72, WASP-80, WASP-87, WASP-88, WASP-108, WASP-118, WASP-120, WASP-122, WASP123, WASP-130, WASP-131, and WASP-137. The closest candidates were detected at separations of $0\farcs124 \pm 0\farcs007$ and $0\farcs189 \pm 0\farcs003$ around WASP-108 and WASP-131; the measured K -band contrasts indicate that these are stellar companions of $0.35 \pm 0.02\,M_{\odot}$ and $0.62^{+0.05}_{-0.04}\,M_{\odot}$, respectively. Including the re-detection and confirmation of previously known companions in 13 other systems, we derived a multiplicity fraction of $55.4^{+5.9}_{-9.4}$ %. For the representative subsample of 40 hot Jupiter host stars among our targets, the derived multiplicity rate is $54.8^{+6.3}_{-9.9}$ %. Our data do not confirm any trend that systems with eccentric planetary companions are preferably part of multiple systems. On average, we reached a magnitude contrast of 8.5 ± 0.9 mag at an angular separation of $0\farcs5$. This allows us to exclude additional stellar companions with masses higher than $0.08\,M_{\odot}$ for almost all observed systems; around the closest and youngest systems, this sensitivity is achieved at physical separations as small as 10 au. Our study shows that SPHERE is an ideal instrument for detecting and characterizing close companions to exoplanetary host stars. Although the second data release of the Gaia mission also provides useful constraints for some of the systems, the achieved sensitivity provided by the

current data release of this mission is not good enough to measure parallaxes and proper motions for all detected candidates. For 14 identified companion candidates further astrometric epochs are required to confirm their common proper motion at 5σ significance.

Adapted from
A. J. Bohn, J. Southworth, C. Ginski, M. A. Kenworthy, P. F. L. Maxted, and D. F. Evans
Astronomy & Astrophysics, **635**, A73 (2020)

2.1 Introduction

The detection and characterization of extrasolar planets has evolved rapidly during the past decades. Many large-scale radial velocity surveys (RV; e.g. Baranne et al. 1996; Mayor et al. 2003; Cosentino et al. 2012) and transit surveys (e.g., Bakos et al. 2004; Pollacco et al. 2006; Auvergne et al. 2009; Borucki et al. 2010) have provided a statistically highly significant sample consisting of several thousands of exoplanets with various physical properties that mostly differ from what we had known from the solar system so far. Already the first exoplanet detected around a main sequence star, 51 Peg b (Mayor & Queloz 1995), showed drastically deviating attributes compared to all Solar System planets. With the detection of several similarly behaved Jovian planets on very close-in orbits with periods of a few days (Butler et al. 1997; Fischer et al. 1999), a new class of so-called hot Jupiters was established. These gas giants typically have masses higher than $0.3\,M_{Jup}$ and separations to their host stars that are smaller than 0.1 au.

Although hundreds of hot Jupiter systems are known today, there is no consensus on a consistent formation pathway of these environments. Shortly after the discovery of 51 Peg b, Lin et al. (1996) argued that in situ formation of hot Jupiters through core accretion is disfavored because the typical temperatures in protoplanetary discs at their characteristic separations are too high to facilitate the condensation of solids, hence preventing rocky cores from forming in these regions (Pollack et al. 1996). Simulations of Bodenheimer et al. (2000) and more recent results of Boley et al. (2016) and Batygin et al. (2016), however, challenge this hypothesis: previous assumptions on the amount of condensable solids in the circumstellar disc were based on abundances in the solar nebula, which might be too simplistic to cope with the huge variety observed in exoplanetary systems.

Alternatively to the in situ formation scenario, hot Jupiters might form at wider separations of several astronomical units and migrate inwards towards their detected position (Lin et al. 1996). Theories that describe this migration process, however, are still a highly controversial topic. Potential scenarios of this inward migration are required not only to reproduce the small orbital separations, but also to provide useful explanations for other properties of known hot Jupiters, for instance highly eccentric orbits (Udry & Santos 2007) or orbital misalignments with respect to the stellar rotation axis (Winn et al. 2010). Recent research shows that the observed spin-orbit misalignments may have a primordial origin caused by either magnetic fields of the star interacting with the protoplanetary disc (Lai et al. 2011) or gravitational interaction with massive stellar binaries (Batygin 2012). The high eccentricities, however, are not reproduced by an inward migration, as first proposed by Lin et al. (1996), due to damping of excited modes caused by gravitational interaction with material of the circumstellar disc (Kley & Nelson 2012). Other theories hypothesize a high-eccentricity migration of the companion after its formation (Socrates et al. 2012): after the planet has formed in a circular orbit of several astronomical units, it becomes excited to high eccentricities, and tidal dissipation at subsequent periastron passages reduces the orbital semi-major axis as well as the eccentricity gained. The excitation of high eccentricities may be caused by planet-planet scattering (Rasio & Ford 1996; Chatterjee et al. 2008; Wu & Lithwick 2011), through Kozai-Lidov (KL) oscillations due to a stellar binary (Eggleton & Kiseleva-Eggleton 2001; Wu & Murray 2003; Fabrycky & Tremaine 2007), or by a combination of these mechanisms (Nagasawa et al. 2008).

To test these theories, additional data of exoplanet host systems is required. Especially stellar binaries may play an important role in the evolution of exoplanetary systems because they are essential ingredients for explaining primordial spin-orbit misalignments or high-eccentricity migration due to KL mechanisms. Current estimates on the multiplicity fractions among transiting exoplanet host stars are not very conclusive and range from 7.6±2.3% (Ngo et al. 2017) to 13.5% (Law et al. 2014) for RV planet hosts, but are usually higher for transiting planetary systems as the sample selection criteria for RV surveys impose an intrinsic bias against multiple stellar systems. Ngo et al. (2015) recently estimated a much higher multiplicity rate of 49±9% for systems with transiting hot Jupiters compared to their RV analogues. To reduce the uncertainties on these ratios, it is necessary to expand the samples to achieve statistically more significant results.

For transiting planet hosts stars, observations at high spatial resolution are also an important tool to reject other scenarios that might cause the periodic dip in the light curve, in particular background eclipsing binaries. Furthermore, the derived properties of the exoplanet and its host star are normally measured under the assumption that all the light from the system comes from the host star, that is, there is no contamination from unresolved sources at very small projected separations. If this assumption is violated and the data are not corrected for the contaminating light, its presence may cause both the mass and radius of the planet to be systematically underestimated. In the worst-case scenario, a not-much-fainter nearby star could even be the planet host star, and measurements of the planet mass and radius under the assumption that the brightest star is the host would lead to planetary properties that are severely biased away from their true values (e.g., Evans et al. 2016b). In a companion paper (Southworth et al. 2020) we reanalyze the most strongly affected of the planetary systems included in the current work, in order to correct measurements of their physical properties for the light arising from the nearby companion stars we have found.

A powerful method for the detection of stellar companions at small angular separations is adaptive optics (AO)-assisted coronagraphic high-contrast imaging. We therefore launched a direct-imaging survey targeting host stars of transiting exoplanets. Starting with the TEPCat catalog (Southworth 2011), we selected all targets that are observable from the Very Large Telescope (VLT) and that have an R -band magnitude brighter than 11 mag to enable the AO system to lock on the source as a natural guide star. A detailed list of the 45 studied objects and their properties is presented in Table 2.1.

In Section 2.2 of this article we describe the observations we have carried out, and in Section 2.3 we explain the applied data reduction techniques. We present the detected candidate companions (CCs), analyze the likelihood of each to be a gravitationally bound component within a multiple stellar system, and present detection limits for all targets of our sample in Section 2.4. Finally, we discuss our results within the scope of the previous literature in Section 2.5, and we conclude in Section 2.6.

2.2 Observations

Our observations (PI: D. F. Evans) were carried out with the Spectro-Polarimetric High-contrast Exoplanet REsearch (SPHERE; Beuzit et al. 2019) instrument that is

mounted on the Nasmyth platform of Unit 3 telescope (UT3) at the ESO VLT. SPHERE is assisted by the SAXO extreme AO system (Fusco et al. 2006) to obtain diffraction-limited data. The targets were observed using the integral field spectrograph (IFS, Claudi et al. 2008) of the instrument and the infrared dual imaging spectrograph (IRDIS, Dohlen et al. 2008) simultaneously. Within the scope of this article we focus on the analysis of the IRDIS data, which provide similar inner working angle (IWA) capabilities down to 100 mas (Wilby et al. in prep.), but a much larger field of view up to 5.″5 in radial separation than the IFS. IRDIS was operated in classical imaging (CI, Vigan et al. 2010) mode applying a broadband K_s-band filter (Filter ID: `BB_Ks`). The filter has a bandwidth of $\Delta\lambda^{K_s} = 313.5\,\mathrm{nm}$ centred around $\lambda_c^{K_s} = 2181.3\,\mathrm{nm}$. To suppress the stellar flux, an apodised pupil Lyot coronagraph (Soummer 2005; Carbillet et al. 2011; Guerri et al. 2011) was used (coronagraph ID: `N_ALC_YJH_S`). To locate the star position behind the coronagraphic mask, center frames were taken alongside the science observations. For these frames, a sinusoidal pattern was applied to the deformable mirror to create four reference spots around the star. To perform precise photometry of potential companions, we obtained additional unsaturated non-coronagraphic flux images of each target with a neutral density filter in place. Furthermore, the observations in ESO period 98 were conducted in pupil-stabilized imaging mode, whereas the data in period 99 were collected in field-stabilized mode. A detailed description of the observational setup and the atmospheric conditions for all observations are presented in Appendix 2.A.

2.3 Data reduction

The data reduction was performed using a custom processing pipeline based on the latest release of PynPoint (version 0.8.1; Stolker et al. 2019) that includes standard dark and flatfield calibrations. Bad pixels were replaced by the average inside a 5×5 box around the corresponding pixel. Furthermore, we corrected for the instrumental anamorphic distortion according to the description in the SPHERE manual. To achieve photon-noise-limited sensitivities, an accurate model of the thermal background is essential for K_s -band imaging. Unfortunately, no sky images without any source in the field of view were taken alongside the science observations of the program. We thus searched the ESO archive to find useful calibration files that were obtained with the same instrumental setup (i.e. exposure time, coronagraph, and filter choice). Within these constraints, we found exactly one suitable sky image taken as part of another program (PI: M. Kenworthy, ESO ID: 0101.C-0153). For an optimal background subtraction, we performed the sky subtraction for both sides of the detector individually. We cropped all images around the rough position of the star in the science frames and aligned the sky images to prominent features induced by the substrate of the inserted coronagraph. The alignment was performed using a cross-correlation in Fourier space according to Guizar-Sicairos et al. (2008) and Fienup (1997). While masking a region of 0.″86 around the star, the aligned sky image was fitted to each individual science frame by a simple linear least-squares approach. This yielded one optimized scaling coefficient per science frame that the sky image had to be multiplied with, before the subtraction. The sky subtraction afterwards was applied to the full frame to ensure a precise background subtraction even for the location of the star. After sky subtraction, the science images were shifted to correct for their corresponding dither positions and centered by using the

Table 2.1: Stellar and planetary properties of the targets.

Star	$M_\star$ ($M_\odot$)	$R_\star$ ($R_\odot$)	$T_{\rm eff}$ (K)	Distance[a] (pc)	Age (Gyr)	Period (d)	Eccentricity	$M_{\rm p}$ ($M_{\rm Jup}$)	$R_{\rm p}$ ($R_{\rm Jup}$)	$T_{\rm eq}$ (K)	References
HAT-P-41	1.418	1.683	6390	$337.7^{+3.7}_{-3.8}$	2.32 ± 0.42	2.694	0	0.800	1.685	1941	1
HAT-P-57	1.47	1.500	7500	$279.9^{+3.2}_{-3.2}$	1.04 ± 0.47	2.465	0		1.413	2200	2
K2-2	0.775	0.716	5089	$62.4^{+0.2}_{-0.2}$	5.65 ± 3.63	9.121	0.205	0.037	0.226	690	3
K2-24b	1.07	1.16	5625	$170.6^{+1.3}_{-1.4}$	6.49 ± 1.81	20.890	0.06	0.057	0.482	767	4, 5
K2-24c	1.07	1.16	5625	$170.6^{+1.3}_{-1.4}$	6.49 ± 1.81	42.339	0	0.048	0.669	606	4, 5
K2-38b	1.07	1.10	5757	$192.7^{+2.6}_{-2.7}$	2.51 ± 1.40	4.016	0	0.038	0.138	1184	6
K2-38c	1.07	1.10	5757	$192.7^{+2.6}_{-2.7}$	2.51 ± 1.40	10.561	0	0.031	0.216	858	6
K2-39	1.192	2.93	4912	$307.5^{+4.6}_{-4.7}$	4.71 ± 0.92	4.605	0.152	0.125	0.509	1670	7, 8
K2-99	1.60	3.1	5990	$519.2^{+12.4}_{-13.0}$	2.12 ± 0.09	18.249	0.19	0.97	1.29		9
KELT-10	1.112	1.209	5948	$188.4^{+2.1}_{-2.2}$	2.82 ± 1.45	4.166	0	0.679	1.399	1377	10
WASP-2	0.851	0.823	5170	$153.2^{+1.6}_{-1.6}$	7.40 ± 2.83	2.152	0	0.880	1.063	1286	11, 12
WASP-7	1.317	1.478	6520	$162.3^{+1.3}_{-1.3}$	2.05 ± 0.47	4.955	0	0.98	1.374	1530	13, 12
WASP-8	1.030	0.945	5600	$90.0^{+0.4}_{-0.4}$	3.27 ± 2.05	8.159	0.3100	2.25	1.038		14
WASP-16	0.980	1.087	5630	$194.1^{+1.9}_{-1.9}$	8.93 ± 2.17	3.119	0	0.832	1.218	1389	15, 16
WASP-20	1.089	1.142	6000	235^{+20}_{-20}	4.34 ± 1.76	4.900	0	0.378	1.28	1282	43
WASP-21	0.890	1.136	5924	$258.4^{+2.8}_{-2.9}$	8.47 ± 1.63	4.323	0	0.276	1.162	1333	17, 18
WASP-29	0.825	0.808	4875	$87.6^{+0.3}_{-0.3}$	10.10 ± 4.05	3.923	0.03	0.244	0.776	970	19, 20
WASP-30	1.249	1.389	6190	$353.5^{+8.8}_{-9.3}$	3.42 ± 0.70	4.157	0	62.5	0.951	1474	21, 22
WASP-54	1.213	1.828	6296	$251.3^{+4.3}_{-4.5}$	3.02 ± 0.57	3.694	0.067	0.636	1.653	1759	23
WASP-68	1.24	1.69	5910	$226.4^{+1.6}_{-1.6}$	3.02 ± 0.57	5.084	0	0.95	1.24	1490	24
WASP-69	0.826	0.813	4700	$50.0^{+0.1}_{-0.1}$	13.52 ± 2.80	3.868	0	0.260	1.057	963	25
WASP-70	1.106	1.215	5700	$222.4^{+2.8}_{-2.9}$	9.35 ± 2.01	3.713	0	0.590	1.164	1387	25
WASP-71	1.559	2.26	6180	$362.7^{+6.7}_{-7.0}$	2.22 ± 0.45	2.904	0	2.242	1.46	2049	26
WASP-72	1.386	1.98	6250	$434.8^{+8.2}_{-8.5}$	3.55 ± 0.82	2.217	0	1.461	1.27	2210	27
WASP-73	1.34	2.07	6030	$316.7^{+2.9}_{-3.0}$	3.59 ± 0.94	4.087	0	1.88	1.16	1790	24
WASP-74	1.191	1.536	5984	$149.2^{+1.1}_{-1.1}$	3.67 ± 0.48	2.138	0	0.826	1.404	1926	28, 29
WASP-76	1.46	1.70	6250	$194.5^{+5.8}_{-6.2}$	2.72 ± 0.46	1.810	0	0.87	1.73	2154	44
WASP-80	0.596	0.593	4145	$49.8^{+0.1}_{-0.1}$	10.51 ± 4.45	3.068	0	0.562	0.986	825	30, 31
WASP-87	1.204	1.627	6450	$298.4^{+3.5}_{-3.6}$	4.04 ± 1.00	1.683	0	2.18	1.385	2322	32
WASP-88	1.45	2.08	6430	$523.8^{+8.5}_{-8.8}$	2.60 ± 0.65	4.954	0	0.56	1.70	1772	24
WASP-94	1.45	1.62	6170	$211.2^{+2.5}_{-2.5}$	3.07 ± 0.61	3.950	0	0.452	1.72	1604	33

Table 2.1 (continued).

Star	$M_\star$ ($M_\odot$)	$R_\star$ ($R_\odot$)	$T_{\rm eff}$ (K)	Distance[a] (pc)	Age (Gyr)	Period (d)	Eccentricity	$M_{\rm p}$ ($M_{\rm Jup}$)	$R_{\rm p}$ ($R_{\rm Jup}$)	$T_{\rm eq}$ (K)	References
WASP-95	1.11	1.13	5830	$137.5^{+0.8}_{-0.8}$	5.62 ± 2.59	2.185	0	1.13	1.21	1570	34
WASP-97	1.12	1.06	5670	$151.1^{+0.5}_{-0.5}$	4.65 ± 2.33	2.073	0	1.32	1.13	1555	34
WASP-99	1.48	1.76	6150	$158.7^{+0.8}_{-0.8}$	3.26 ± 0.80	5.753	0	2.78	1.10	1480	34
WASP-108	1.167	1.215	6000	$258.8^{+3.2}_{-3.3}$	4.64 ± 1.94	2.676	0	0.892	1.284	1590	32
WASP-109	1.203	1.346	6520	$356.1^{+4.8}_{-5.0}$	2.68 ± 0.92	3.319	0	0.91	1.443	1685	32
WASP-111	1.50	1.85	6400	$293.1^{+6.2}_{-6.4}$	2.59 ± 0.59	2.311	0	1.83	1.443	2140	32
WASP-117	1.126	1.170	6040	$158.0^{+0.6}_{-0.6}$	4.98 ± 1.89	10.022	0.302	0.275	1.021	1024	35
WASP-118	1.319	1.754	6410	$376.7^{+10.6}_{-11.2}$	2.34 ± 0.44	4.046	0	0.52	1.394	1753	36, 37
WASP-120	1.393	1.87	6450	$381.2^{+3.2}_{-3.2}$	2.66 ± 0.51	3.611	0.057	4.85	1.473	1880	38
WASP-121	1.353	1.458	6460	$269.9^{+1.6}_{-1.6}$	1.90 ± 0.60	1.275	0	1.183	1.865	2358	39
WASP-122	1.239	1.52	5720	$250.1^{+1.5}_{-1.5}$	6.24 ± 1.93	1.710	0	1.284	1.743	1970	38
WASP-123	1.166	1.285	5740	$198.0^{+3.0}_{-3.1}$	7.17 ± 2.11	2.978	0	0.899	1.318	1520	38
WASP-130	1.04	0.96	5600	$172.3^{+1.4}_{-1.4}$	2.82 ± 1.87	11.551	0	1.23	0.89	833	40
WASP-131	1.06	1.53	5950	$200.1^{+2.6}_{-2.7}$	7.25 ± 1.55	5.322	0	0.27	1.22	1460	40
WASP-136	1.41	2.21	6250	$275.6^{+4.5}_{-4.6}$	3.71 ± 0.67	5.215	0	1.51	1.38	1742	41
WASP-137	1.216	1.52	6100	$286.5^{+3.6}_{-3.7}$	4.29 ± 1.24	3.908	0	0.681	1.27	1601	42

Notes. [a] Distances are based on Gaia DR2 parallaxes (Gaia Collaboration et al. 2018) and calculations by Bailer-Jones et al. (2018). The distance estimate for WASP-20 presented in Bailer-Jones et al. (2018) is $1383.1^{+526.1}_{-813.6}$, which does not agree with previous literature on this system. This disagreement might be caused by confusion due the binary nature of this target. For this reason, we adopt the distance derived by Evans et al. (2016b) for WASP-20.

References. (1) Hartman et al. (2012); (2) Hartman et al. (2015); (3) Vanderburg et al. (2015); (4) Petigura et al. (2016); (5) Petigura et al. (2018); (6) Sinukoff et al. (2016); (7) Van Eylen et al. (2016); (8) Petigura et al. (2017); (9) Smith et al. (2017); (10) Kuhn et al. (2016); (11) Collier Cameron et al. (2007); (12) Southworth (2012); (13) Hellier et al. (2009); (14) Queloz et al. (2010); (15) Lister et al. (2009); (16) Southworth et al. (2013); (17) Bouchy et al. (2010); (18) Ciceri et al. (2013); (19) Hellier et al. (2010); (20) Gibson et al. (2013); (21) Anderson et al. (2011); (22) Triaud et al. (2013a); (23) Faedi et al. (2013b); (24) Delrez et al. (2014); (25) Anderson et al. (2014b); (26) Smith et al. (2013); (27) Gillon et al. (2013); (28) Hellier et al. (2015); (29) Mancini et al. (2019); (30) Triaud et al. (2013b); (31) Mancini et al. (2014); (32) Anderson et al. (2014a); (33) Neveu-VanMalle et al. (2014); (34) Hellier et al. (2014); (35) Lendl et al. (2014); (36) Hay et al. (2016); (37) Močnik et al. (2017); (38) Turner et al. (2016); (39) Delrez et al. (2016); (40) Hellier et al. (2017); (41) Lam et al. (2017); (42) Anderson et al. (2018); (43) Evans et al. (2016b); (44) Brown et al. (2017).

center frames as described in the SPHERE manual. At this stage we averaged both detector sides for each exposure to dampen noise introduced by bad pixels. Finally, we de-rotated the data that were obtained in pupil-stabilized mode according to the difference in parallactic angle. An additional constant pupil offset of -135°.99 was taken into account as well. The rotation was skipped for data that were taken in field-stabilized imaging mode. For both pupil- and field-stabilized data, we finally performed a correction for the true north position given by a rotation of -1°.75 according to Maire et al. (2016). No further point spread function (PSF) removal was performed, and our final image was obtained as the median of the processed stack.

2.4 Results and analysis

2.4.1 Determining consistent ages for the exoplanet host stars

We used version 1.2 of the program `bagemass`[1] (Maxted et al. 2015) to estimate the age of each star based on the observed values of $T_{\rm eff}$, [Fe/H] and the mean stellar density $\rho_\star$. These values were obtained from the references listed in Table 2.1. The methods and assumptions used for the calculation of the stellar model grid using the GARSTEC stellar evolution code are described in Serenelli et al. (2013) and Maxted et al. (2015). We set lower limits of 80 K on the standard error for $T_{\rm eff}$ and 0.07 dex for the standard error on [Fe/H] and assumed flat prior distributions for the stellar mass and age. The ages derived are shown in Table 2.1. The values and errors quoted are the median and standard deviation of the sampled posterior age distributions provided by `bagemass`.

2.4.2 Characterisation of CCs

In the IRDIS data we detected 27 off-axis point sources around 23 stars of our sample. Compilations of these detections are presented in Figure 2.1 and Figure 2.2, which show new detections by our survey and previously known sources, respectively. Sixteen of the 27 CCs have not been detected by similar surveys of the multiplicity of these exoplanet host stars. This impressively demonstrates the ability of high-contrast imaging with SPHERE. Only 256 s of on-target integration are sufficient to reach better sensitivities than previous surveys that have been carried out either with different AO-assisted instruments or with other observing strategies such as lucky imaging.

Because we did not perform any PSF subtraction, we characterized the companions directly in the median-combined images, applying the standard astrometric solution of IRDIS with a plate scale of 12.265 mas in K_s band. For the astrometric characterization, we fitted a two-dimensional Gaussian function to the PSF of the companion. The magnitude contrast was estimated with aperture photometry that we applied on both flux and science image around the previously determined centroid. We used an aperture size that is equivalent to the full width at half-maximum (FWHM) of the SPHERE PSF in K_s band of 55 mas and scaled the counts from the flux image to account for the difference in exposure time and applied neutral density filter. A detailed list of all detected CCs including their separations, position angles (PAs), and magnitude contrasts is presented in Table 2.2. Furthermore, we calculated

[1] `https://sourceforge.net/projects/bagemass/`

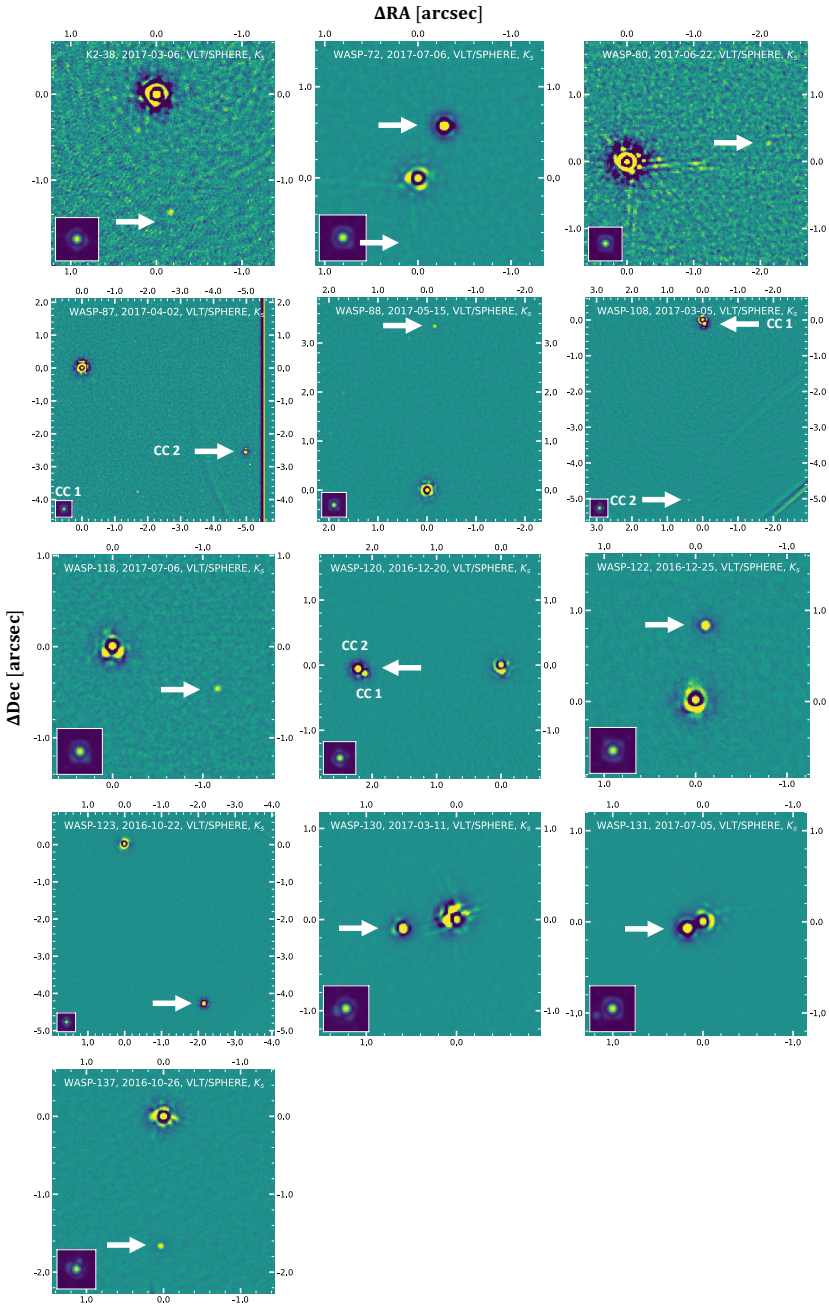

Figure 2.1: Newly detected CCs around transiting exoplanet host stars from the SPHERE/IRDIS data. An unsharp mask was applied to highlight point sources. The origin of the axes is located at the position of the host star. The images are displayed using a logarithmic scale with arbitrary offsets and stretches to highlight the CCs. In all images north points up and east towards the left. The lower left corner of each image shows the reduced non-coronagraphic flux image with the same spatial scale and field orientation.

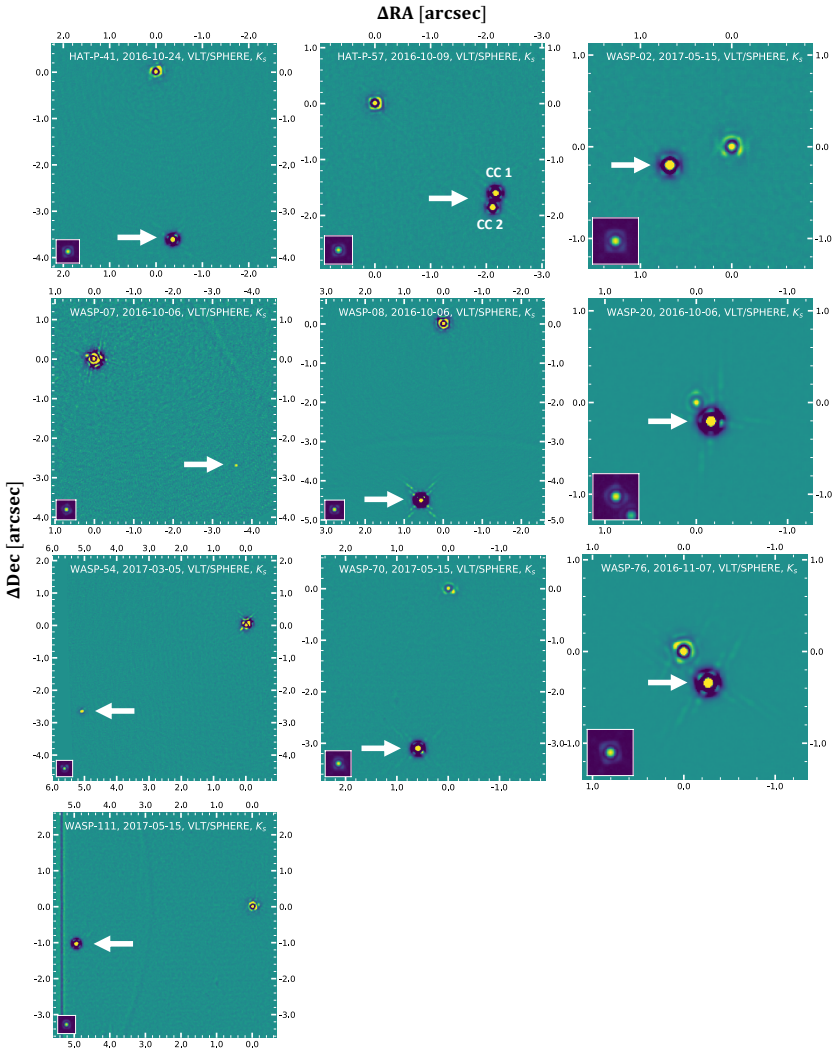

Figure 2.2: Previously detected CCs around transiting exoplanet host stars from the SPHERE/IRDIS data. An unsharp mask was applied to highlight point sources. The origin of the axes is located at the position of the host star. The images are displayed using a logarithmic scale with arbitrary offsets and stretches to highlight the CCs. In all images north points up and east towards the left. The lower left corner of each image shows the reduced non-coronagraphic flux image with the same spatial scale and field orientation.

mass and temperature estimates based on the derived photometry using evolutionary models of (sub-)stellar objects (e.g., Allard et al. 2001; Baraffe et al. 2003). Because various physical processes play major roles for objects of different temperatures, we used AMES-Cond, AMES-Dusty, and BT-Settl models for the characterization of CCs with $T_{\rm eff} < 1400\,K$, $1400\,K < T_{\rm eff} < 2700\,K$, and $T_{\rm eff} > 2700\,K$, respectively.

There are three potential scenarios, depending on the available data, with which the likelihood can be assessed that a CC is gravitationally bound to its host:

1. Gaia DR2 provides parallax and proper motion of the CC.
2. Previous studies have detected the CC and provide astrometric measurements of it. This includes the case that Gaia DR2 only provides the position of the CC at reference epoch J2015.5, but no parallax or proper motion estimates.
3. None of the information above is accessible.

In the first case, the hypothesis whether the CC is bound or not could be easily tested by the provided parallaxes and proper motions of primary and CC. For the second scenario, we tested the proper motion of the object instead and determined whether its astrometry over several epochs agrees with a co-moving companion. When no other data on the CC were available, we estimated the likelihood of its companionship by a synthetic model of the stellar population around the stellar coordinates. This analysis was performed in a similar way to that described by Dietrich & Ginski (2018). First we used TRILEGAL (Girardi et al. 2005) to simulate a stellar population for one square degree centered around the exoplanet host star. We chose the 2MASS *K*-band filter, which is in good agreement with the actual SPHERE filter used for the observations. The limiting magnitude provided for the simulation was based on the maximum contrast we reached around the particular target (see Section 2.4.4). Other than this, we used the default parameters of TRILEGAL v1.6. Following the description of Lillo-Box et al. (2014), we measured the likelihood of a CC to be a background object as

$$p^{\rm B} = \pi r^2 \rho_{\rm sim}\,, \tag{2.1}$$

where $\rho_{\rm sim}$ denotes the number of simulated stars per square degree around the exoplanet host and r is the radial separation of the corresponding CC. Because this analysis is purely based on statistical arguments, we did not classify the CCs within this category as background or bound, but rather flagged them as ambiguous objects, whose common proper motion needs to be confirmed by future studies. Because we base the further analysis of these ambiguous candidates only on the derived background probabilities (see Section 2.4.3), this classification does not affect the derived multiplicity fractions in any way. A detailed analysis for each detected CC is presented in the following subsections.

Most of the CCs that we detected with IRDIS are unresolved in the 2MASS catalogue (Cutri et al. 2012a), which we used for calibrating the *K* -band magnitude of the host star. Only for WASP-8, WASP-111, and WASP-123 does the 2MASS catalog provide spatially resolved flux measurements for the primary and CC. For the remaining cases, we had to assume that the flux of potential CCs is contributing to the listed 2MASS *K* -band magnitude of the primary, but of course this contribution is negligible for large contrasts between both components. The corrected *K* -band

Table 2.2: Astrometry and photometry of CCs within the IRDIS field of view. Furthermore, we present the primary K -band magnitudes corrected for the contribution of the CCs (see equation 2.2).

Star	CC ID	Epoch (yyyy-mm-dd)	Separation ($''$)	PA ($^\circ$)	$K_\star$ (mag)	ΔK (mag)	Status[a]	p^{B} (%)	M^b ($M_\odot$)	$T_{\mathrm{eff}}{}^b$ (K)
HAT-P-41	1	2016-10-24	3.621 ± 0.004	183.9 ± 0.1	9.83	2.50 ± 0.21	C	-	$0.69^{+0.06}_{-0.05}$	4336^{+250}_{-199}
HAT-P-57	1	2016-10-09	2.688 ± 0.004	231.8 ± 0.1	9.55	2.91 ± 0.05	C	-	$0.59^{+0.01}_{-0.01}$	3942^{+50}_{-37}
HAT-P-57	2	2016-10-09	2.807 ± 0.004	226.9 ± 0.1	9.55	3.47 ± 0.05	C	-	$0.50^{+0.01}_{-0.01}$	3684^{+40}_{-23}
HAT-P-57	1	2017-05-15	2.689 ± 0.004	231.8 ± 0.1	9.55	2.90 ± 0.12	C	-	$0.59^{+0.03}_{-0.03}$	3944^{+114}_{-75}
HAT-P-57	2	2017-05-15	2.809 ± 0.004	227.0 ± 0.1	9.55	3.45 ± 0.12	C	-	$0.50^{+0.03}_{-0.03}$	3691^{+77}_{-48}
K2-38	1	2017-03-06	1.378 ± 0.014	185.2 ± 0.6	9.47	8.72 ± 0.31	A	1.59	$0.07^{+0.01}_{-0.01}$	1699^{+150}_{-106}
WASP-2	1	2017-05-15	0.710 ± 0.003	104.9 ± 0.2	9.73	2.55 ± 0.07	C	-	$0.40^{+0.02}_{-0.02}$	3523^{+28}_{-19}
WASP-7	1	2016-10-06	4.474 ± 0.007	231.5 ± 0.1	8.40	8.70 ± 0.27	B	-	-	-
WASP-8	1	2016-10-06	4.520 ± 0.005	170.9 ± 0.1	8.09	2.29 ± 0.08	C	-	$0.53^{+0.02}_{-0.02}$	3758^{+47}_{-43}
WASP-20	1	2016-10-06	0.259 ± 0.003	216.0 ± 0.6	9.79	0.86 ± 0.06	A	0.004	$0.88^{+0.08}_{-0.07}$	5235^{+270}_{-275}
WASP-54	1	2017-03-05	5.728 ± 0.006	115.9 ± 0.1	9.04	5.94 ± 0.06	C	-	$0.19^{+0.01}_{-0.01}$	3216^{+26}_{-25}
WASP-70	1	2017-05-15	3.160 ± 0.004	167.4 ± 0.1	9.85	1.38 ± 0.18	C	-	$0.70^{+0.06}_{-0.05}$	4504^{+263}_{-213}
WASP-72	1	2017-07-06	0.639 ± 0.003	331.9 ± 0.3	9.67	3.34 ± 0.06	A	0.02	$0.66^{+0.02}_{-0.02}$	4234^{+80}_{-81}
WASP-76	1	2016-11-07	0.436 ± 0.003	215.9 ± 0.4	8.37	2.30 ± 0.05	C	-	$0.79^{+0.03}_{-0.03}$	4824^{+128}_{-132}
WASP-80	1	2017-06-22	2.132 ± 0.010	275.5 ± 0.3	8.35	9.25 ± 0.28	A	3.29	$0.07^{+0.01}_{-0.01}$	1306^{+84}_{-53}
WASP-87	1	2017-04-02	4.109 ± 0.016	202.3 ± 0.2	9.56	8.48 ± 1.19	A	19.83	$0.08^{+0.02}_{-0.01}$	2289^{+540}_{-621}
WASP-87	2	2017-04-02	5.569 ± 0.007	241.0 ± 0.1	9.56	5.57 ± 0.70	B	-	-	-
WASP-88	1	2017-05-15	3.350 ± 0.015	355.5 ± 0.5	10.32	7.60 ± 0.53	A	1.65	$0.11^{+0.03}_{-0.02}$	2844^{+155}_{-209}
WASP-108	1	2017-03-05	0.124 ± 0.007	203.0 ± 3.3	9.83	3.90 ± 0.06	A	32.82	$0.35^{+0.02}_{-0.02}$	3471^{+18}_{-18}
WASP-108	2	2017-03-05	5.039 ± 0.019	174.2 ± 0.2	9.83	7.48 ± 0.43	B	-	-	-
WASP-111	1	2017-05-15	5.039 ± 0.005	100.1 ± 0.1	9.08	3.01 ± 0.17	C	-	$0.67^{+0.05}_{-0.04}$	4285^{+195}_{-172}
WASP-118	1	2017-07-06	1.251 ± 0.004	246.5 ± 0.2	9.79	6.73 ± 0.13	A	0.09	$0.15^{+0.01}_{-0.01}$	3034^{+52}_{-52}
WASP-120	1	2016-12-20	2.124 ± 0.004	91.7 ± 0.1	9.95	4.44 ± 0.23	A	0.47	$0.39^{+0.04}_{-0.04}$	3504^{+60}_{-44}
WASP-120	2	2016-12-20	2.221 ± 0.005	89.8 ± 0.1	9.95	3.27 ± 0.32	A	0.51	$0.57^{+0.06}_{-0.06}$	3897^{+227}_{-167}

Table 2.2 (continued).

Star	CC ID	Epoch (yyyy-mm-dd)	Separation ($''$)	PA ($^\circ$)	$K_\star$ (mag)	ΔK (mag)	Status[a]	$p^{\rm B}$ (%)	M^b ($M_\odot$)	$T_{\rm eff}{}^b$ (K)
WASP-122	1	2016-12-25	0.837 ± 0.003	350.7 ± 0.2	9.43	5.09 ± 0.30	A	0.50	$0.23^{+0.04}_{-0.04}$	3311^{+60}_{-63}
WASP-123	1	2016-10-22	4.786 ± 0.005	205.0 ± 0.1	9.36	3.47 ± 0.11	C	-	$0.40^{+0.02}_{-0.02}$	3524^{+37}_{-26}
WASP-130	1	2017-03-11	0.600 ± 0.003	98.0 ± 0.3	9.50	3.73 ± 0.12	A	0.22	$0.30^{+0.03}_{-0.02}$	3410^{+29}_{-32}
WASP-131	1	2017-07-05	0.189 ± 0.003	111.5 ± 0.9	8.65	2.82 ± 0.20	A	0.01	$0.62^{+0.05}_{-0.04}$	4109^{+200}_{-163}
WASP-137	1	2016-10-26	1.660 ± 0.003	177.0 ± 0.1	9.46	6.20 ± 0.28	A	0.14	$0.17^{+0.02}_{-0.02}$	3106^{+85}_{-85}

Notes. [(a)] Status is either companion (C), background (B), or ambiguous (A). The latter classification indicates that neither the background nor the companion hypothesis are confirmed by proper motion analysis at the 5σ level. For the ambiguous cases we also present the background probability $p^{\rm B}$ based on our TRILEGAL analysis (equation 2.1) in the next column. [(b)] For confirmed background objects, we do not provide masses and effective temperatures because these parameters depend on the distance to the object, which is not known in these cases. For all dubious cases the distances and temperatures are calculated for the case that the object is at the same distance as the primary.

magnitude for primary j from our sample that is hosting n_j CCs with corresponding magnitude contrasts of $\Delta K_{j,\ell}$ for $\ell = 1, \ldots, n_j$, is

$$K_j = K_{\mathrm{2MASS},j} + 2.5 \log_{10} \left(1 + \sum_{\ell=1}^{n_j} \left(10^{-\frac{\Delta K_{j,\ell}}{2.5}} \right) \right) . \tag{2.2}$$

We applied this correction directly to the 2MASS system magnitudes that are presented in Table 2.4. The updated K -band magnitudes of primaries with companions that are unresolved in 2MASS photometric data are listed in Table 2.2 instead.

HAT-P-41

In the discovery paper of a transiting hot Jupiter around HAT-P-41, Hartman et al. (2012) detected a potential stellar companion south of the star. The candidate was also detected by the lucky-imaging surveys of Wöllert et al. (2015) and Wöllert & Brandner (2015). Based on stellar population synthesis models, these studies concluded that the object is probably bound. Ngo et al. (2016) also detected the CC in Keck/NIRC2 K_s data and their color analysis supported the theory that HAT-P-41 is a candidate multiple stellar system. Evans et al. (2016a) carried out an additional high-resolution imaging campaign, and they determined a common proper motion with 2σ significance. An additional companion to the system that was also detected by Evans et al. (2016a) was ruled out at a later stage and identified as an instrumental artifact (Evans et al. 2018). Therefore, previous studies have presented much evidence that HAT-P-41 is indeed a binary system. A conclusive common proper motion analysis and an accurate distance determination has not been published so far, however.

These previous results were confirmed by our SPHERE survey. We detected exactly one off-axis point source within the IRDIS field of view at the position of the previously detected CC with a separation of $3\farcs621 \pm 0\farcs004$ and a position angle of $183\fdg9 \pm 0\fdg1$. Furthermore, this companion was also detected by the second data release of the Gaia mission (Gaia DR2; Gaia Collaboration et al. 2018). Bailer-Jones et al. (2018) provided distance estimates based on the Gaia parallaxes of 348 ± 4 pc and 338 ± 4 pc for HAT-P-41 and the CC, respectively. Considering the reported proper motions of $(\mu_\alpha^A, \mu_\delta^A) = (-3.28 \pm 0.06, -6.39 \pm 0.04)$ mas per year for the primary and $(\mu_\alpha^B, \mu_\delta^B) = (-3.71 \pm 0.05, -6.78 \pm 0.04)$ mas per year for the secondary, we could conclude that both sources are co-distant and co-moving. Thus, the former CC is proven to be a stellar binary to HAT-P-41 and should be named HAT-P-41 B accordingly. From our comparison to BT-Settl models we derived a mass of $0.71^{+0.06}_{-0.05}\,\mathrm{M}_\odot$ for the secondary component of the system.

HAT-P-57

We re-detected the binary pair southwest of HAT-P-57 that has been found in the discovery paper of the transiting exoplanet HAT-P-57 b (Hartman et al. 2015). Hartman et al. (2015) have concluded that HAT-P-57 b must orbit the primary star because the detected binary is too faint in the optical to be responsible for the measured transit depth. Additional RV data of the system confirmed this hypothesis. From photometric H and L band analysis in a color-magnitude diagram, Hartman et al. (2015) concluded that both binary components are co-evolutionary with the primary.

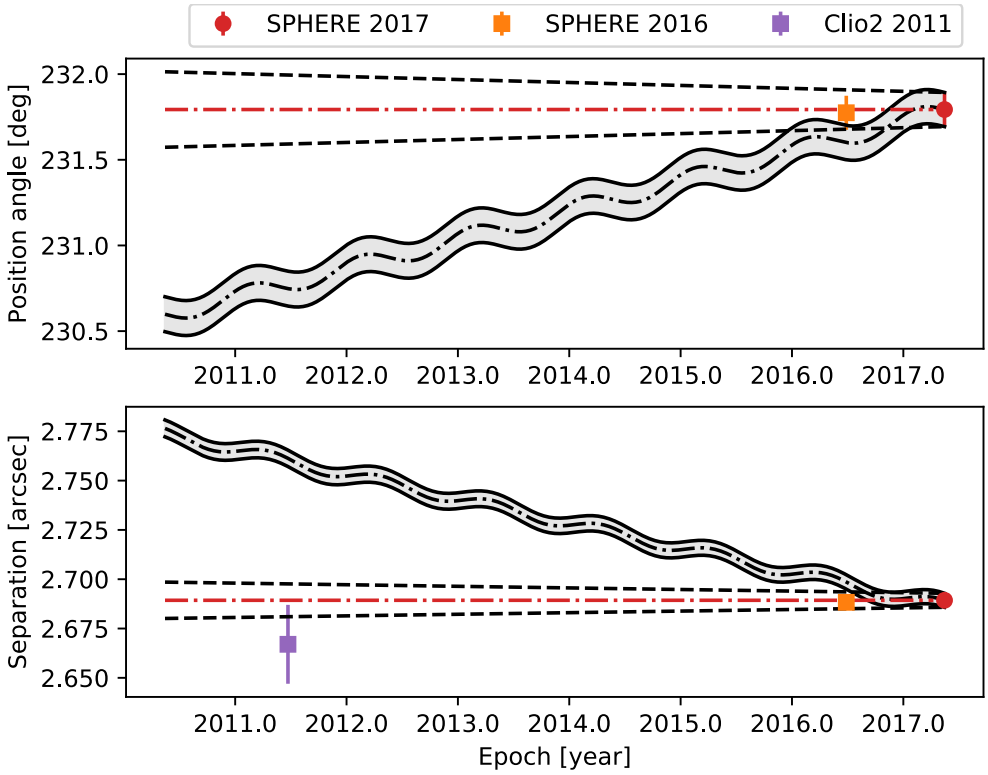

Figure 2.3: Proper motion analysis of CC 1 and 2 detected around HAT-P-57. PA and separation are evaluated individually. The dashed cone presents the expected position of a gravitationally bound companion considering potential orbital motion of the object. The grey trajectory represents the expected location of a stationary background object, instead. For the MMT/Clio2 data we adopted the separation measurement presented Hartman et al. (2015); no PA of the source at this epoch is provided.

Consequently, they argued that all three stars form a hierarchical triple system and should be named HAT-P-57 ABC. The masses of the smaller companions were estimated as $0.61 \pm 0.10\,M_\odot$ and $0.53 \pm 0.08\,M_\odot$. However, no other test for actual companionship, such as a common proper motion analysis, was performed.

With the two SPHERE epochs, we aimed to perform such an analysis. Hartman et al. (2015) only provided a separation of $2\farcs667 \pm 0\farcs001$ from the primary to the binary pair and a separation of $0\farcs225 \pm 0\farcs002$ between the two components of the binary itself. No individual separations from the primary to each component of the binary and no PAs were presented in their article. For this reason, we considered the binary pair as a single component and performed the proper motion test by splitting up the evaluation of separation and PA. The results of this analysis are visualized in Figure 2.3.

Already the two SPHERE epochs imply that the binary agrees better with the hypothesis of being bound to HAT-P-57 than with being an unrelated background object. The additional separation measurement adapted from Hartman et al. (2015) that is based on MMT/Clio2 data from 2011 June 22 confirmed this hypothesis.

Because their presented uncertainty in separation, only 1 mas, seemed to be very optimistic (the primary is heavily saturated), we adjusted this value to 20 mas to also account for the difference in separation of both CCs. This analysis proved that the binary pair is clearly incompatible with a stationary background object at more than 5σ significance. Therefore, CC 1 and CC 2 should be named HAT-P-57 B and HAT-P-57 C, respectively.

From the K_s-band photometry, we derived masses of $0.60^{+0.02}_{-0.01}\,M_\odot$ and $0.51^{+0.01}_{-0.01}\,M_\odot$ for components B and C, respectively. Furthermore, we measured separations of $0\farcs260 \pm 0\farcs004$ and $0\farcs261 \pm 0\farcs004$ as well as PAs of $168\fdg3 \pm 0\fdg1$ and $168\fdg4 \pm 0\fdg1$ between components B and C for the SPHERE epochs. This is compatible with the increasing trend in separation when the separation of $0\farcs225 \pm 0\farcs002$ between the two components in 2011 is also considered (Hartman et al. 2015). For a conclusive orbital motion fit of these two objects, a detailed analysis and another epoch at high astrometric precision are required, which is beyond the scope of the current work.

K2-38

Evans et al. (2018) reported a potential companion around K2-38 at a separation of $10\farcs7752 \pm 0\farcs0950$, which is unfortunately outside the IRDIS field of view. The potential companion, however, was picked up by Gaia DR2, and together with two additional sources listed that were previously considered unlikely to be bound by Evans et al. (2018), these three objects were clearly proven to be background based on their parallaxes.

In our SPHERE data we detected a previously unknown CC south of the star at a separation of $1\farcs378 \pm 0\farcs014$. Because no other astrometric data of this CC are available, we estimated its likelihood to be a background object using TRILEGAL. This provided a probability of 1.59% that the candidate is a background object.

WASP-2

In addition to the detection of the hot Jupiter WASP-2 b, Collier Cameron et al. (2007) also reported a potential stellar companion to WASP-2 b at a separation of $0\farcs7$ and a magnitude contrast of $\Delta H = 2.7$ mag. This companion was detected by several follow-up surveys (Daemgen et al. 2009; Bergfors et al. 2013; Adams et al. 2013; Ngo et al. 2015; Wöllert et al. 2015) and photometric analysis suggests a spectral type of late-K to early-M dwarf. The most recent astrometric measurements by Evans et al. (2016a) proved a common proper motion of the companion with its host at more than 5σ significance. Furthermore, they detected a linearly decreasing separation between the stellar companion and the primary, implying a nearly edge-on orbital solution, which we could confirm with our data.

WASP-7

Evans et al. (2016a) reported a CC around WASP-7 at a separation of $4\farcs414 \pm 0\farcs011$ and a PA of $228\fdg73 \pm 0\fdg12$. However, no extensive analysis was performed to determine whether this candidate is actually bound to the exoplanet host star. The separation and PA presented in Evans et al. (2016a) are an average of three individual epochs obtained on 2014 April 25, May 9, and May 16. As presented in Figure 2.4, the astrometry based on the data from 2014 April 25 does not agree with the two later

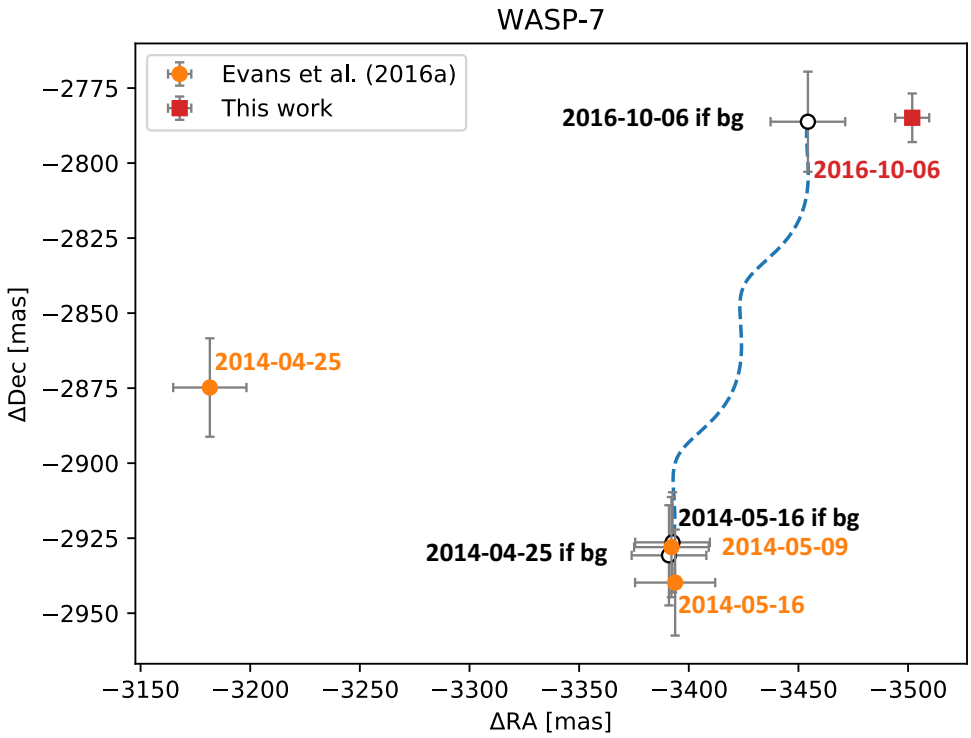

Figure 2.4: Proper motion analysis of CC 1 around WASP-7. The dashed blue line represents the trajectory of a static background (bg) object.

epochs. Instead of averaging over all three datapoints, we used the data from 2014 May 9 as baseline for a further proper motion analysis[2].

We also detected the candidate in our IRDIS data with a separation of $4''.474 \pm 0''.007$ at a PA of $231°.51 \pm 0°.11$. Including this new epoch in a proper motion analysis, as presented in Figure 2.4, clearly showed that the object better agrees with the background trajectory than with being a bound companion.

WASP-8

We re-detected WASP-8 B south of the primary at a separation $4''.520 \pm 0''.005$ and with a PA of $170°.9 \pm 0°.1$. This stellar companion was first detected by Queloz et al. (2010), who classified it as an M-type dwarf. Further studies by Ngo et al. (2015) and Evans et al. (2016a) confirmed the companionship status by common proper motion at more than 5σ significance. This was consolidated by additional Gaia DR2 astrometric measurements, which provide parallaxes of 11.09 ± 0.04 mas and 11.02 ± 0.04 mas as well as proper motions of $(\mu_\alpha^A, \mu_\delta^A) = (109.75 \pm 0.06, 7.61 \pm 0.06)$ mas per

[2]We present the common proper motion tests in a plot that displays the candidate's differential offsets in right ascension and declination to the host, henceforth. Using one datapoint as baseline, we simulate the trajectory of a static background object based on the parallax and proper motion of the exoplanet host star. Several measurements of the CC astrometry help to discern whether it is orbiting the primary or a background contaminant.

year $(\mu_\alpha^B, \mu_\delta^B) = (110.26 \pm 0.06, 5.57 \pm 0.06)$ mas per year for primary A and secondary B, respectively.

WASP-20

Using the same SPHERE data as presented in this article, Evans et al. (2016b) reported the detection of a bright close-in binary to WASP-20. Our new evaluation of these data showed, however, that the companion's position angle given in Evans et al. (2016b) is not correct. We found this to be because Evans et al. (2016b) treated the data as being collected in field-stabilized imaging mode, whereas it was actually obtained in pupil-stabilized mode. Our new analysis of the data yielded measurements of the separation and magnitude contrast that agree within the uncertainties with the values derived by Evans et al. (2016b); the correct position angle of WASP-20 B is $216\overset{\circ}{.}0 \pm 0\overset{\circ}{.}6$.

Furthermore, we inferred a slightly higher effective temperature estimate for WASP-20 B that is, however, consistent within the uncertainties with the value of 5060 ± 250 K as presented in Evans et al. (2016b). This discrepancy can be explained by the ATLAS9 (Castelli & Kurucz 1994) models used by Evans et al. (2016b) in comparison to the more recent BT-Settl models that we used instead. Unfortunately, no precise parallax measurement of the host was provided by Gaia DR2, probably because of the binary nature of the system. This resulted in the rather large uncertainties in effective temperature as presented in Table 2.2, which may be constrained by better distance estimates based on future Gaia data releases.

Because the object was only observed in a single epoch, Evans et al. (2016b) were unable to assess the common proper motion. Furthermore, the CC is not detected in Gaia DR2, therefore we evaluated the companionship with TRILEGAL instead. This analysis provided a probability of 0.004% for the CC to be a background contaminant.

WASP-54

A companion candidate around WASP-54 was first detected by Evans et al. (2016a). Further proper motion analysis presented in Evans et al. (2018) led to the preliminary conclusion that the object is a bound companion. The authors stated, however, that additional measurements are required to confirm this hypothesis.

We combined the data presented in Evans et al. (2016a) and Evans et al. (2018) with the latest SPHERE epoch and additional astrometric data from Gaia DR2. The latter only provided coordinates of the CC and no proper motion that could be used to confirm its companionship. In Figure 2.5 we analyze these data in a proper motion diagram. The data presented in Evans et al. (2016a) consist of five individual epochs obtained in 2014 May. The individual measurements had an intrinsic scatter larger than the provided uncertainties. For this reason, we averaged the single measurements using the standard deviation of the datapoints as an uncertainty of the combined measurement. One of these datapoints, obtained on 2014 April 18, deviated by more than 3σ from the average of the remaining measurements. We therefore removed this datapoint from our combined astrometry solution for this first epoch.

Evans et al. (2018) presented two additional epochs, 2015 April 29 and 2016 May 3. As shown in Figure 2.5, the first of these epochs agrees well with the expected position of a static background object. The second epoch, however, assigns the companion a position in the opposite direction as expected from a background object.

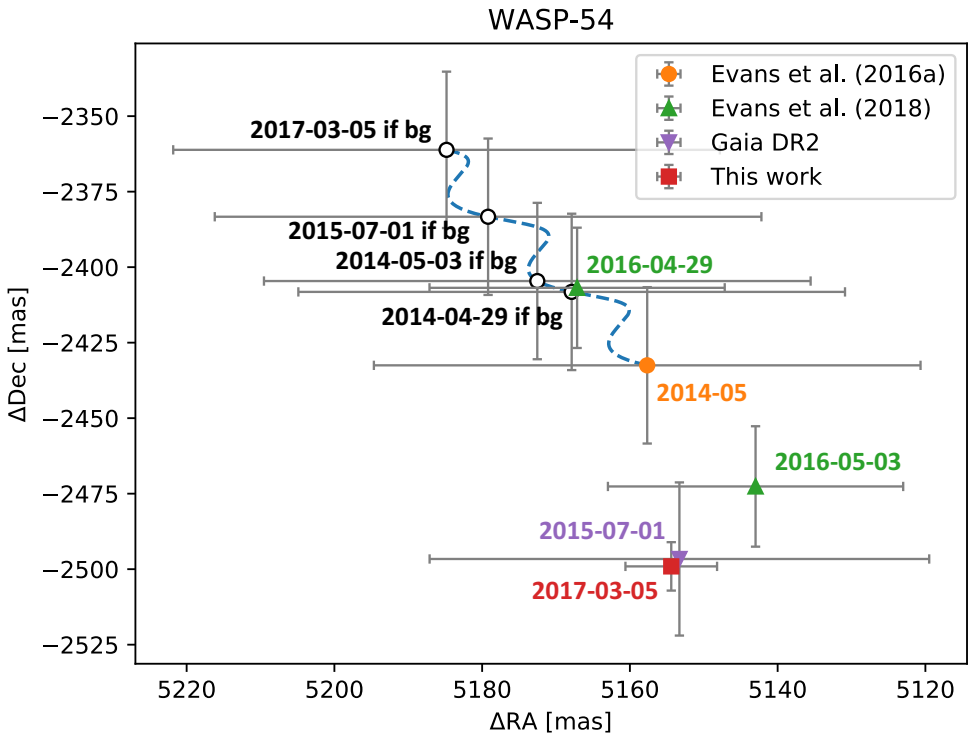

Figure 2.5: Proper motion analysis of CC 1 around WASP-54. The first measurement from Evans et al. (2016a) (orange circle) is the average of four individual epochs, collected from 2014 May 6 until May 8. The dashed blue line represents the trajectory of a static background (bg) object.

Because both epochs do not agree within their uncertainties, it is likely that the results of Evans et al. (2018) were subject to a source of systematic error that was not accounted for in the quoted uncertainties.

No clear conclusion could be drawn from these data alone, but adding Gaia and our latest SPHERE measurements facilitated an unambiguous classification of the potential companion. Both additional datapoints were not compatible with the trajectory of a static background object but are consistent with a co-moving companion. Therefore we conclude that WASP-54 B is a stellar binary to WASP 54 A. From our K_s-band photometry we derived a mass of $0.19^{+0.01}_{-0.01}\,M_\odot$.

WASP-68

Candidate companion 1 presented in Evans et al. (2018), at a separation of approximately 13.″1 and with a position angle of 119.°7, was confirmed as a co-moving stellar companion by Gaia DR2 parallaxes of 4.39 ± 0.03 mas and 4.19 ± 0.15 mas for primary and secondary, respectively. Additional proper motion measurements of $(\mu_\alpha^A, \mu_\delta^A) = (-11.17 \pm 0.06, -6.21 \pm 0.04)$ mas per year $(\mu_\alpha^B, \mu_\delta^B) = (-11.45 \pm 0.24, -6.24 \pm 0.17)$ mas per year strengthened the claim that the CC is WASP-68 B, a stellar companion to WASP-68 A. However, we did not detect any CCs around WASP-68 within the IRDIS field of view.

WASP-70

A K3 stellar companion was found to exoplanet host WASP-70 by Anderson et al. (2014b), and we also detected the object in our SPHERE data. Previous studies (e.g., Wöllert & Brandner 2015; Evans et al. 2016a, 2018) stated a common proper motion of the companion at 5σ significance. This was also confirmed by Gaia DR2, which provided parallaxes of 4.47 ± 0.06 mas and 4.35 ± 0.03 mas as well as proper motions of $(\mu_\alpha^A, \mu_\delta^A) = (33.24 \pm 0.08, -30.04 \pm 0.05)$ mas per year $(\mu_\alpha^B, \mu_\delta^B) = (44.77 \pm 0.05, -30.11 \pm 0.03)$ mas per year. From our K_s-band photometry we derived a mass of $0.70^{+0.06}_{-0.05}\,M_\odot$ for WASP-70 B.

WASP-72

We detected a CC to WASP-72 at a separation of $0\farcs639 \pm 0\farcs003$ and a position angle of $331\fdg9 \pm 0\fdg3$ that was previously unknown. By stellar population synthesis models we derived a probability of 0.02% that the CC is an unassociated background or foreground object. For the case of confirmed common proper motion, we calculated a mass estimate of $0.66^{+0.02}_{-0.02}\,M_\odot$.

WASP-76

We re-detected the stellar CC to WASP-76 that was first detected by Wöllert & Brandner (2015). Follow-up studies led by Ginski et al. (2016a) and Ngo et al. (2016) suggested that the companion shows common proper motions with its host. We confirmed this trend with our additional SPHERE epoch as presented in Figure 2.6; a background object could be ruled out at 5σ significance. For the stellar companion WASP-76 B we estimated a mass of $0.78^{+0.03}_{-0.03}\,M_\odot$ based on our K_s-band photometry.

WASP-80

We report the detection of a new CC around WASP-80 at a separation of $2\farcs132 \pm 0\farcs010$ and a position angle of $275\fdg5 \pm 0\fdg3$. Although the system was explored by previous studies of Wöllert & Brandner (2015), Evans et al. (2016a), and Evans et al. (2018) no CCs were revealed by these programs. This is in good agreement with the large magnitude contrast of 9.25 ± 0.28 mag at which we detected the companion just above the noise level. This is below the detection threshold of previous surveys, which explains why it remained previously undetected. From our TRILEGAL analysis we derived a probability of 3.29% that the CC is not associated with WASP-80. Assuming the object is gravitationally bound to the exoplanet host, we estimated a mass of $0.07^{+0.01}_{-0.01}\,M_\odot$ based on the K_s magnitude.

WASP-87

In the discovery paper reporting a hot Jupiter around WASP-87, Anderson et al. (2014a) also detected a potential stellar companion south-east of the star at a separation of $8\farcs2$. Evans et al. (2018) suggested that the proper motion analysis presented in Anderson et al. (2014a) based on UCAC4 data (Zacharias et al. 2013) is not supported by other catalogs. Based on its color, Evans et al. (2018) concluded that the two components are nevertheless bound. This assumption was confirmed by Gaia DR2 parallaxes of 3.32 ± 0.04 mas and 3.19 ± 0.04 mas for WASP-87 A and WASP-87 B, respec-

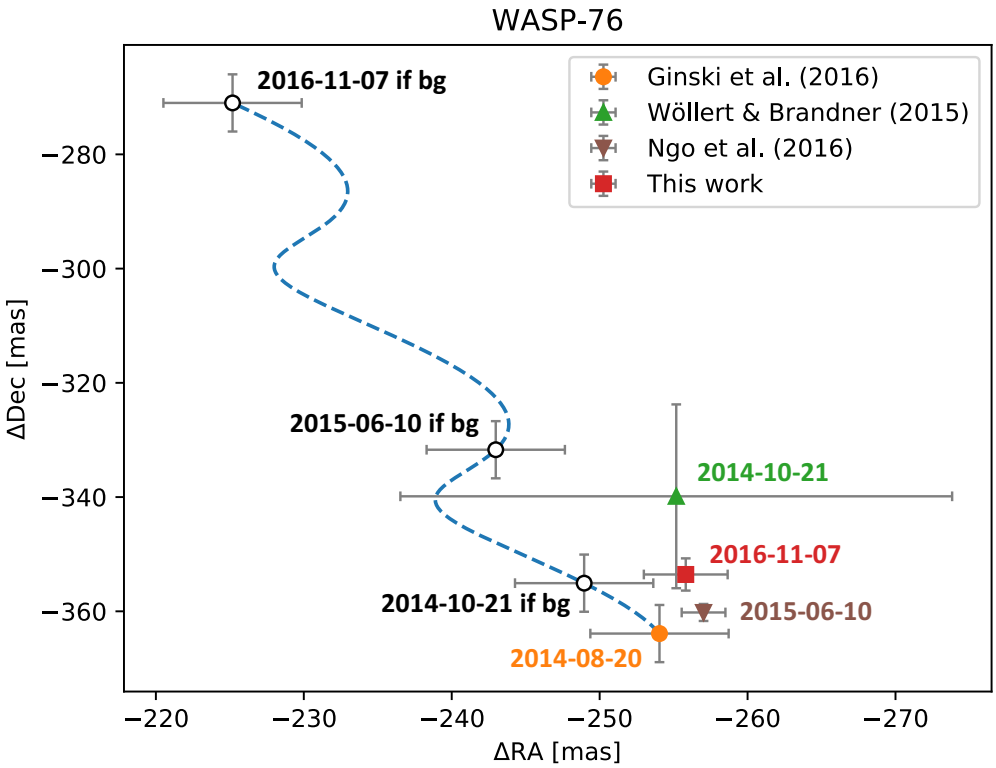

Figure 2.6: Proper motion analysis of CC 1 around WASP-76. The dashed blue line represents the trajectory of a static background (bg) object.

tively. Furthermore, the proper motions of $(\mu_\alpha^A, \mu_\delta^A) = (-1.36 \pm 0.06, 3.92 \pm 0.04)$ mas per year and $(\mu_\alpha^B, \mu_\delta^B) = (-1.73 \pm 0.04, 4.20 \pm 0.04)$ mas per year were absolutely compatible with a gravitationally bound binary system.

Within the IRDIS field of view, we detected two additional point sources southeast of the star. Both were also detected by Gaia DR2, but the catalog provided a parallax estimate only for CC 2, whereas only the celestial position was measured for CC 1. Based on the parallax measurement of 0.02 ± 0.14 mas for CC 2, we clearly confirm this object as a background source. Because for CC 1 only the position was provided by Gaia DR2, we performed a common proper motion analysis as presented in Figure 2.7. This analysis placed CC 1 close to the expected position of a stationary background object. Because of the large magnitude contrast of CC 1, however, the SPHERE detection was only marginal. Therefore the uncertainties of the derived astrometric precision were too large to either confirm CC 1 as a co-moving companion or to show that it is a background object. Our TRILEGAL analysis provided a probability of 19.83% that CC 1 is not associated with WASP-87.

WASP-88

We report the detection of a new CC north of WASP-88. It is rather faint, with a magnitude contrast of 7.60 ± 0.53 mag. From our stellar population synthesis model

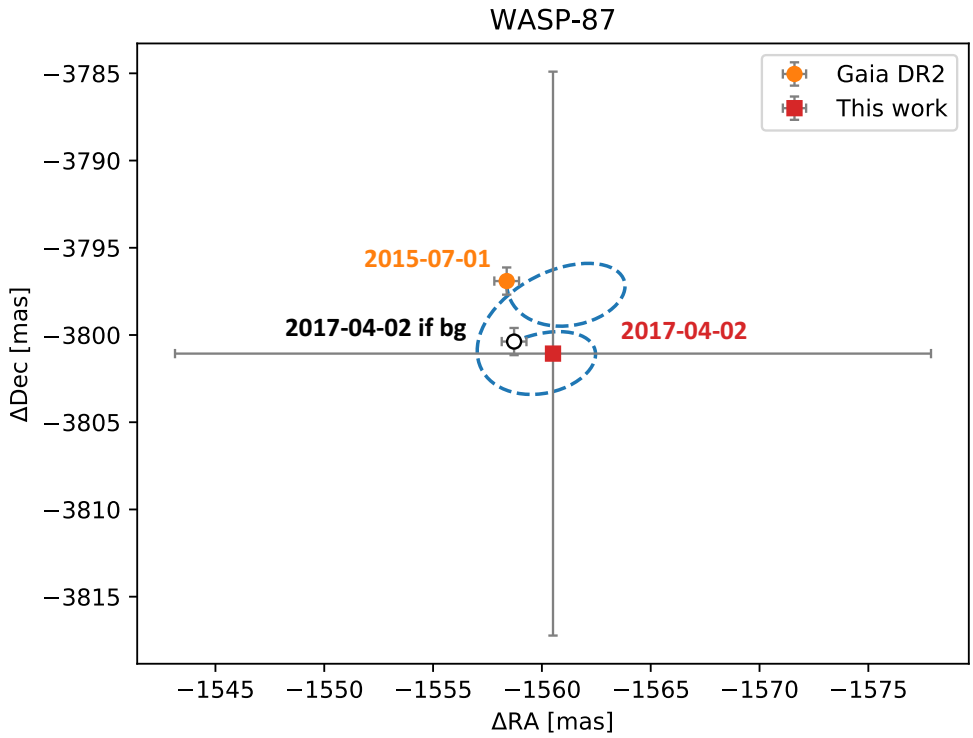

Figure 2.7: Proper motion analysis of CC 1 around WASP-87. The dashed blue line represents the trajectory of a static background (bg) object.

analysis, we derived a probability of 1.65% that this CC is a background object and not bound to WASP-88.

WASP-108

The system was explored within the scope of one previous multiplicity study of exoplanet host stars (Evans et al. 2018). Evans and collaborators reported several CCs, but the colors of only two of them are consistent with being bound to the planet host star. Because WASP-108 lies within a crowded field, Evans et al. (2018) did not rule out the possibility that both sources are background stars. Instead they explicitly stated the necessity of additional tests. Evans et al. (2018) estimated that the first object at 19.″4563 to the north-east is likely to be background, based on differing proper motion from the host reported in UCAC4, NOMAD, and PPMXL catalogs. This was confirmed by the latest Gaia astrometry, which provided a parallax of 0.18 ± 0.03 mas, which contradicts the measured value for WASP-108 itself of 3.84 ± 0.05 mas. For the second CC discussed by Evans et al. (2018), no proper motion data were available at the time of their analysis. The latest Gaia astrometry proved that the object is in good agreement with a co-moving companion. Gaia Collaboration et al. (2018) reported a parallax of 2.93 ± 0.47 mas for the companion. to which we refer as WASP-108 B henceforth. The proper motions of $(\mu_\alpha^A, \mu_\delta^A) = (25.80 \pm 0.13, -22.57 \pm 0.08)$ mas per year and $(\mu_\alpha^B, \mu_\delta^B) = (24.76 \pm 0.97, -21.13 \pm 0.69)$ mas per year also confirmed the hypothesis that this is a gravitationally bound binary.

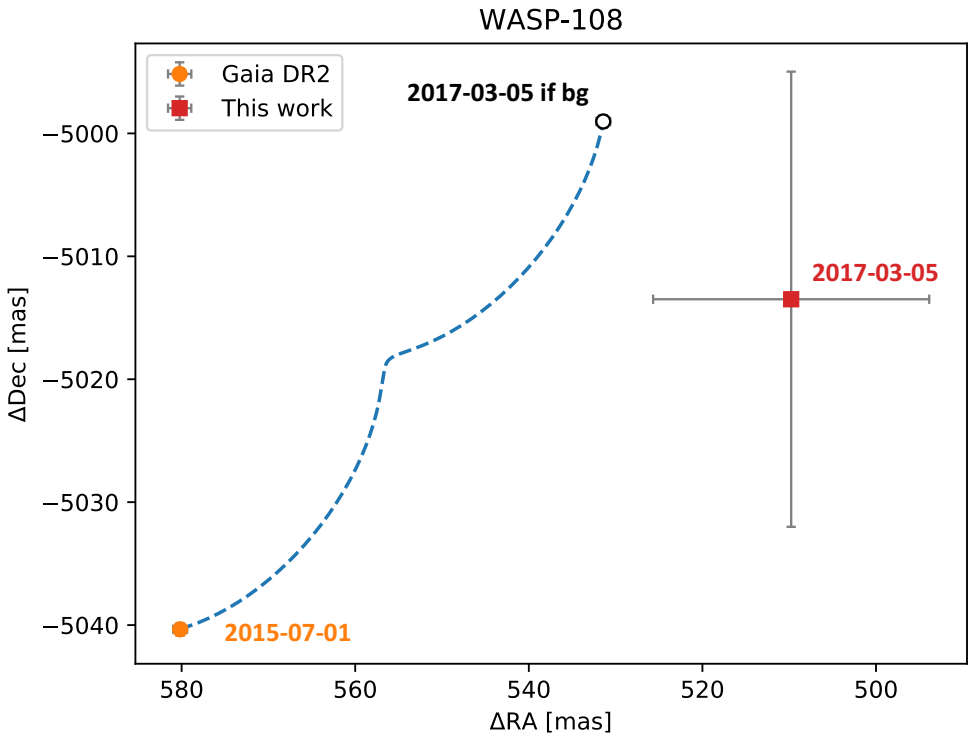

Figure 2.8: Proper motion analysis of CC 2 around WASP-108. The dashed blue line represents the trajectory of a static background (bg) object.

In addition, we found two CCs within the IRDIS field of view. CC 1 is very close to WASP-108 at a magnitude contrast of $\Delta K_s = 3.90 \pm 0.06$ mag. Because of its proximity it is likely to be gravitationally bound to the primary. This agrees very well with our TRILEGAL analysis, which provided a probability of 0.02% that CC 1 is rather an unrelated background or foreground contaminant. The second CC in the IRDIS data was detected south of the star at a separation of $5''.039 \pm 0''.005$. We performed a proper motion check based on Gaia DR2 and our SPHERE data as presented in Figure 2.8. This analysis indicated that CC 2 is compatible with a background object that has a non-zero proper motion; this hypothesis was supported by a background probability of 32.82% based on our TRILEGAL analysis. Because of the large uncertainties in the SPHERE astrometry, however, further tests are necessary to confirm this theory.

WASP-111

In the IRDIS data we re-detected the companion that was first identified by Evans et al. (2018) east of WASP-111 at a separation of $5''.039 \pm 0''.005$. Gaia DR2 data confirmed that the companion is bound because WASP-111 A and WASP-111 B were measured to be co-moving with $(\mu_\alpha^A, \mu_\delta^A) = (12.88 \pm 0.10, -4.31 \pm 0.11)$ mas per year and $(\mu_\alpha^B, \mu_\delta^B) = (13.35 \pm 0.10, -5.15 \pm 0.10)$ mas per year, and they are co-distant with parallaxes of 3.33 ± 0.07 mas and 3.39 ± 0.07 mas.

WASP-118

We detected a new CC around WASP-118 at a separation of $1\farcs251 \pm 0\farcs004$ and with a position angle of $246\fdg5 \pm 0\fdg2$. TRILEGAL analysis provided a probability of 0.09% that this CC is not associated with WASP-118. For the case that the CC is actually gravitationally bound to the host, we derived a mass of $0.15^{+0.01}_{-0.01}\,M_\odot$.

WASP-120

The IRDIS data revealed a potential binary companion east of WASP-120 at a separation of approximately $2\farcs2$. Our simulated stellar population around the position of the primary predicted background probabilities of 0.47% and 0.51% for CC 1 and 2, respectively. This supports the hypothesis that WASP-120 is a hierarchical triple system WASP-120 ABC. Further astrometric measurements are required to confirm this theory.

WASP-122

We detected a new CC north of WASP-122 at a separation of approximately $0\farcs8$. The TRILEGAL analysis yielded a probability of 0.50% that this CC is not associated with the exoplanet host star. We derived a mass estimate of $0.23^{+0.04}_{-0.04}\,M_\odot$ for the case that the CC is actually co-moving with WASP-122.

WASP-123

Evans et al. (2018) detected a CC south of WASP-123 at a separation of $4\farcs8$ that is marginally consistent with a bound object based on its color. No conclusive result was presented whether this companion is co-moving. By combining the data from Evans et al. (2018), Gaia DR2 astrometry, and our IRDIS data, we analyzed the proper motion of the CC as presented in Figure 2.9. This clearly demonstrates that the CC is not compatible with a stationary background object with a significance greater than 5σ. Therefore we conclude that the CC is actually WASP-123 B, a stellar companion to WASP-123 A with a mass of approximately $0.40^{+0.02}_{-0.02}\,M_\odot$.

WASP-130

We detected a bright CC east of WASP-130 at a separation of $0\farcs6$. Although the target was also included in previous exoplanet host star multiplicity surveys, no companion was detected by any of these (Evans et al. 2018). The TRILEGAL analysis yielded a probability of 0.22% that this CC is a background or foreground contaminant. Assuming the object is gravitationally bound to WASP-130, we derived a mass estimate of $0.30^{+0.03}_{-0.02}\,M_\odot$.

WASP-131

We detected a very close-in CC to WASP-131 at a separation of $0\farcs189 \pm 0.003$ and with a position angle of $111\fdg5 \pm 0\fdg9$ that had not been detected by any previous surveys. Due to the proximity and no other objects in the field of view, it is very likely to orbit the primary. This assumption is in good agreement with a background probability of only 0.01%, which is based on our synthetic stellar population models around

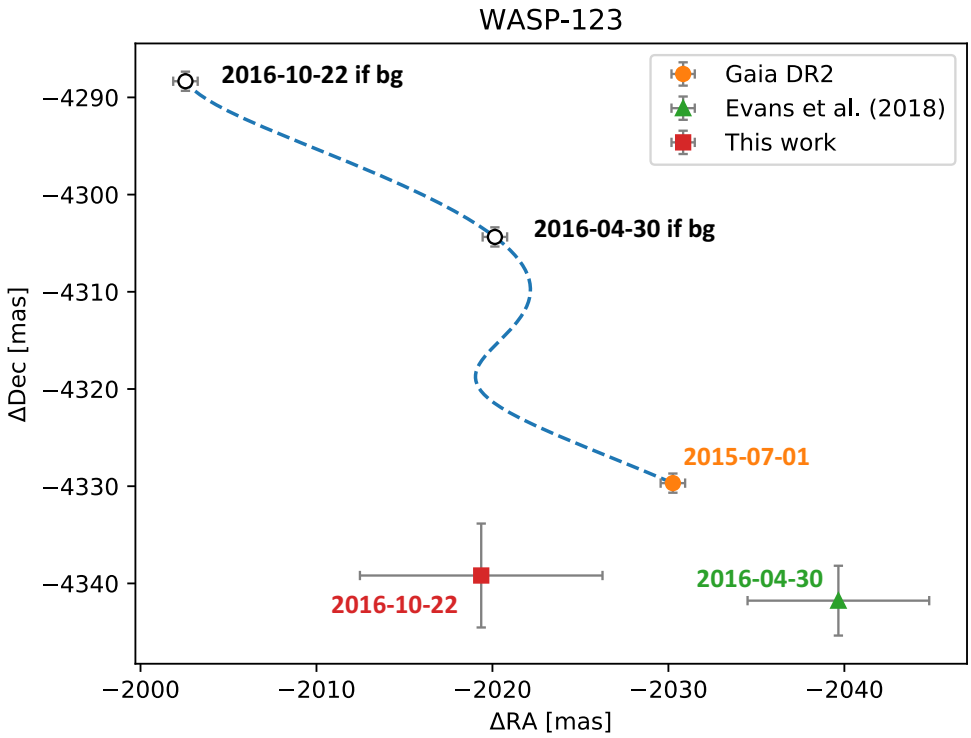

Figure 2.9: Proper motion analysis of CC 1 around WASP-123. The dashed blue line represents the trajectory of a static background (bg) object.

the host. If confirmed, WASP-131 B, would be a stellar companion with a mass of $0.62^{+0.05}_{-0.04}\,M_{\odot}$.

WASP-137

We report the first detection of a CC south of WASP-137. Our TRILEGAL analysis suggested a probability of only 0.14% that this object is not associated with the exoplanet host. From the K_s-band photometry, we estimated a mass of $0.17^{+0.02}_{-0.02}\,M_{\odot}$ for the CC, assuming it is gravitationally associated.

Non-detection of confirmed companions

Because the IRDIS field of view is limited to approximately 5″.5 in radial separation, some companions to stars from our sample were not detected within the scope of this survey. These confirmed multiple systems are K2-02 (Vanderburg et al. 2015; Evans et al. 2018) and WASP-94 (Neveu-VanMalle et al. 2014; Evans et al. 2018). Furthermore, we could confirm previous CCs outside the IRDIS field of view around WASP-68 (Evans et al. 2018, and section 2.4.2 of this work), WASP-87 (Evans et al. 2018, and section 2.4.2 of this work), and WASP-108 (Evans et al. 2018, and section 2.4.2 of this work) as actual co-moving companions based on Gaia DR2 astrometry.

2.4.3 Multiplicity rate

For our sample of 45 observed exoplanet host stars, we reported 9 targets (HAT-P-41, HAT-P-57, WASP-2, WASP-8, WASP-54, WASP-70, WASP-76, WASP-111, and WASP-123) that harbor at least one companion within the IRDIS field of view that shows clear common proper motion with the primary from several epochs of observations. Furthermore, 5 additional stars from the sample were confirmed multiple systems with binary components lying outside the IRDIS field of view: the confirmation of these binaries was either performed by previous studies (K2-2 and WASP-94) or by evaluation of Gaia DR2 astrometric measurements for former CCs within this work (WASP-68, WASP-87, and WASP-108). In addition, we found 12 systems that show ambiguous CCs, where future checks to prove common proper motion at 5σ significance are necessary[3] (K2-38, WASP-20, WASP-72, WASP-80, WASP-87, WASP-88, WASP-118, WASP-120, WASP-122, WASP-130, WASP-131, and WASP-137).

We simulated the stellar multiplicity rate of the exoplanet host stars in our sample as

$$\eta_i = \frac{1}{N} \sum_{j=1}^{N} \left(\bigvee_{k=1}^{n_j} B_{ijk}(n = 1, p_{jk}^{\mathrm{C}}) \right) , \tag{2.3}$$

where i describes the index of the simulation (to be repeated 10^6 times), N denotes the sample size of 45 exoplanet host stars, n_j is the number of CCs around target j, and B_{ijk} describes a draw from a binomial distribution with $n = 1$ and p_{jk}^{C}, where the latter refers to the probability that CC k around target j is actually bound to its host. CCs that were confirmed to be gravitationally bound (labeled 'C' in Table 2.2 plus five additional confirmed companions outside the IRDIS field of view) were assigned $p^{\mathrm{C}} = 1$. Targets without any CCs or CCs that were proven to be background were assigned $p^{\mathrm{C}} = 0$, accordingly. The remaining ambiguous cases were assigned $p^{\mathrm{C}} = 1 - p^{\mathrm{B}}$, with p^{B} denoting the previously determined probability of being a background contaminant based on our TRILEGAL analysis (equation 2.1).

The outcome of B_{ijk} is either 0 or 1, therefore we calculated the logical disjunction over all CCs of an individual target to simulate whether this host is part of a multiple system. Making 10^6 independent draws for each CC and accounting for the sample size of $N = 45$ resulted in a multiplicity rate of $55.4^{+5.9}_{-9.4}$ %. The uncertainties were obtained as the 68% confidence level around the average of the simulated η_i. However, this analysis only addresses the statistical errors that might occur due to our inconclusive characterization of some CCs and the limited size of the sample. Of course there might be other intrinsic biases caused by sample selection, or size of the used field of view, that were not considered in this multiplicity estimate.

2.4.4 Detection limits

To assess the sensitivity we achieved around each target as a function of angular separation, we estimated the contrast in our reduced IRDIS images. For this purpose, we used the non-coronagraphic flux frames and fitted a two-dimensional Gaussian function to the unsaturated PSF. We took the best-fit amplitude of this function as an

[3]WASP-87 and WASP-108, although harboring CCs within the IRDIS field of view, have previously been proven to be multiple systems with companions at greater separations (see Sections 2.4.2 and 2.4.2).

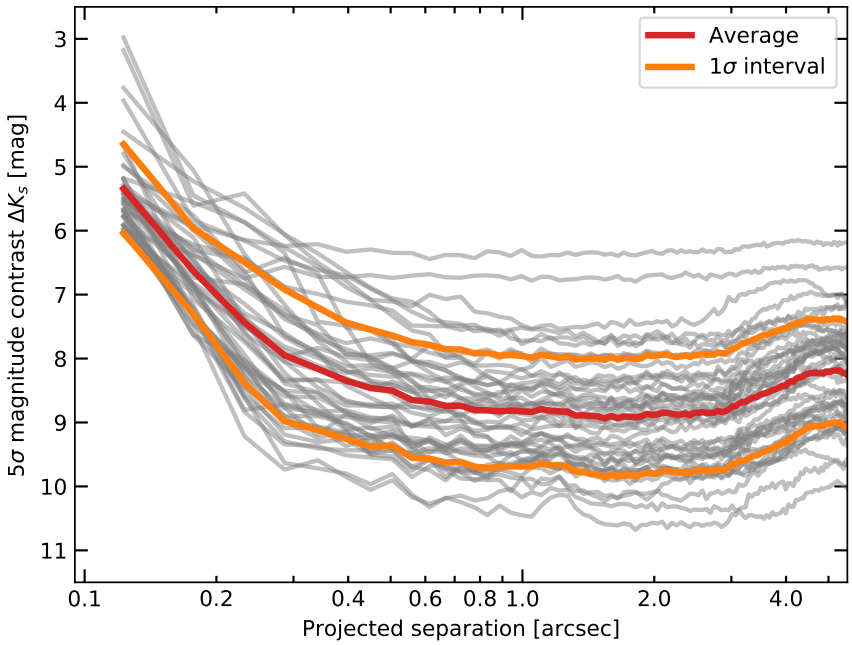

Figure 2.10: Detection limits of our SPHERE survey for detection of stellar companions to known exoplanet host stars. The grey lines represent all individual targets and epochs as presented in Table 2.4, and the red curve and orange curves indicate the average contrast performance and the corresponding 1σ interval.

estimate of the stellar flux and scaled it to account for exposure time difference to the science images and attenuation by potential neutral density filters. The noise was estimated directly from the post-processed coronagraphic images in radial annuli with a width of 55 mas. The annuli were centered around the position of the star behind the coronagraphic mask, and we chose 100 discrete steps of equidistant radii, growing from the inner working angle of approximately 100 mas (Wilby et al. in prep.) up to the edge of the detector. Afterwards, we determined the standard deviation inside each annulus to obtain an estimate for the noise as a function of separation.

For HAT-P-57, where two epochs of the target were obtained, we continued analyzing just the slightly deeper contrast that was obtained on the night of 2016 October 9. The 5σ detection limits for all datasets are presented in Figure 2.10. The spread in contrast performance between different datasets can be explained by the strongly varying atmospheric conditions for different observations of the program as presented in Table 2.4. On average we reached a magnitude contrast of 7.0 ± 0.8 mag at a separation of 200 mas, and we were background limited with an average magnitude contrast of 8.9 ± 0.9 mag at separations larger than $1''$. Because of the missing sky frames and the imperfect background subtraction, a slight decrease of the contrast performance was observed for all datasets. This was the case for separations

Table 2.3: Contrast performance for all datasets evaluated at discrete separations. The magnitude contrast is converted into a mass limit using AMES-Cond, AMES-Dusty, and BT-Settl models as described in Section 2.4.2.

Star	Contrast at 0.″2		Contrast at 0.″5		Contrast at 1.″0		Contrast at 2.″5		Contrast at 5.″0	
	(mag)	(M_{Jup})	(mag)	(M_{Jup})	(mag)	(M_{Jup})	(mag)	(M_{Jup})	(mag)	(M_{Jup})
HAT-P-41	6.59 ± 0.12	154^{+8}_{-8}	8.16 ± 0.08	89^{+1}_{-1}	8.62 ± 0.07	83^{+1}_{-1}	8.61 ± 0.06	83^{+1}_{-1}	7.74 ± 0.05	97^{+1}_{-1}
HAT-P-57	7.91 ± 0.11	90^{+7}_{-2}	9.00 ± 0.07	73^{+17}_{-3}	9.02 ± 0.06	73^{+16}_{-3}	8.79 ± 0.04	76^{+13}_{-3}	8.07 ± 0.04	87^{+6}_{-1}
K2-02	5.62 ± 0.11	99^{+2}_{-2}	8.21 ± 0.07	72^{+5}_{-1}	9.36 ± 0.05	69^{+11}_{-1}	9.84 ± 0.03	70^{+15}_{-3}	9.18 ± 0.02	69^{+9}_{-1}
K2-24	5.97 ± 0.11	133^{+8}_{-8}	7.07 ± 0.08	91^{+1}_{-1}	7.77 ± 0.06	82^{+1}_{-1}	7.69 ± 0.05	83^{+1}_{-1}	7.01 ± 0.04	92^{+1}_{-1}
K2-38	7.66 ± 0.11	83^{+4}_{-1}	8.90 ± 0.08	71^{+12}_{-2}	8.96 ± 0.06	71^{+12}_{-2}	8.95 ± 0.05	71^{+12}_{-2}	8.18 ± 0.04	78^{+6}_{-1}
K2-39	7.75 ± 0.11	144^{+8}_{-8}	9.19 ± 0.07	88^{+1}_{-1}	9.45 ± 0.05	85^{+1}_{-1}	9.51 ± 0.03	84^{+1}_{-1}	9.03 ± 0.02	91^{+1}_{-1}
K2-99	5.40 ± 0.11	393^{+26}_{-27}	7.05 ± 0.07	185^{+7}_{-7}	7.72 ± 0.05	142^{+6}_{-6}	7.63 ± 0.04	147^{+5}_{-5}	7.20 ± 0.03	175^{+5}_{-5}
KELT-10	7.67 ± 0.11	84^{+2}_{-1}	8.77 ± 0.07	73^{+7}_{-1}	8.78 ± 0.05	73^{+7}_{-1}	8.79 ± 0.04	73^{+7}_{-1}	8.25 ± 0.03	78^{+4}_{-1}
WASP-2	6.51 ± 0.11	89^{+1}_{-2}	7.92 ± 0.08	75^{+1}_{-1}	8.17 ± 0.06	74^{+1}_{-1}	8.24 ± 0.05	74^{+1}_{-1}	7.71 ± 0.04	77^{+1}_{-1}
WASP-7	7.37 ± 0.11	98^{+1}_{-3}	9.44 ± 0.07	71^{+3}_{-1}	9.82 ± 0.05	68^{+4}_{-2}	9.86 ± 0.03	68^{+4}_{-2}	9.19 ± 0.03	74^{+2}_{-1}
WASP-8	8.21 ± 0.11	75^{+8}_{-1}	9.92 ± 0.07	66^{+18}_{-3}	10.16 ± 0.05	65^{+18}_{-3}	10.36 ± 0.03	63^{+18}_{-4}	9.67 ± 0.02	67^{+16}_{-2}
WASP-16	7.35 ± 0.12	85^{+1}_{-1}	8.71 ± 0.08	74^{+1}_{-1}	8.82 ± 0.06	74^{+1}_{-1}	8.71 ± 0.05	74^{+1}_{-1}	7.99 ± 0.05	79^{+1}_{-1}
WASP-20	6.24 ± 0.12	147^{+19}_{-18}	7.70 ± 0.08	89^{+3}_{-4}	8.43 ± 0.07	81^{+2}_{-2}	8.56 ± 0.06	80^{+3}_{-1}	7.87 ± 0.06	87^{+3}_{-3}
WASP-21	6.37 ± 0.13	115^{+9}_{-9}	7.24 ± 0.10	90^{+1}_{-2}	7.52 ± 0.09	86^{+1}_{-1}	7.79 ± 0.08	83^{+1}_{-1}	7.47 ± 0.08	87^{+1}_{-1}
WASP-29	7.98 ± 0.11	74^{+1}_{-1}	9.53 ± 0.07	69^{+1}_{-1}	9.66 ± 0.05	69^{+2}_{-1}	9.77 ± 0.03	74^{+2}_{-1}	9.00 ± 0.03	71^{+1}_{-1}
WASP-30	6.01 ± 0.13	167^{+11}_{-11}	6.34 ± 0.10	146^{+9}_{-9}	6.31 ± 0.09	148^{+8}_{-8}	6.34 ± 0.08	146^{+8}_{-8}	6.20 ± 0.07	155^{+8}_{-8}
WASP-54	6.65 ± 0.11	153^{+9}_{-9}	9.19 ± 0.07	78^{+1}_{-1}	9.31 ± 0.06	77^{+1}_{-1}	9.31 ± 0.04	77^{+1}_{-1}	8.54 ± 0.04	84^{+1}_{-1}
WASP-68	6.81 ± 0.11	134^{+7}_{-7}	8.40 ± 0.07	84^{+1}_{-1}	8.73 ± 0.05	81^{+1}_{-1}	8.63 ± 0.03	82^{+1}_{-1}	7.97 ± 0.03	90^{+1}_{-1}
WASP-69	7.85 ± 0.11	74^{+1}_{-1}	9.82 ± 0.07	74^{+1}_{-4}	10.45 ± 0.05	72^{+1}_{-1}	10.59 ± 0.03	71^{+1}_{-1}	10.01 ± 0.02	73^{+1}_{-1}
WASP-70	7.04 ± 0.11	95^{+2}_{-1}	7.93 ± 0.08	82^{+1}_{-1}	7.93 ± 0.06	82^{+1}_{-1}	7.87 ± 0.05	83^{+1}_{-1}	7.57 ± 0.04	86^{+1}_{-1}
WASP-71	7.75 ± 0.11	116^{+9}_{-9}	9.14 ± 0.07	83^{+1}_{-1}	9.32 ± 0.05	81^{+1}_{-1}	8.92 ± 0.03	86^{+1}_{-1}	8.22 ± 0.03	97^{+1}_{-1}
WASP-72	7.16 ± 0.11	160^{+9}_{-9}	8.21 ± 0.07	100^{+2}_{-2}	8.46 ± 0.06	95^{+2}_{-1}	8.41 ± 0.04	97^{+1}_{-1}	7.83 ± 0.04	117^{+5}_{-5}
WASP-73	7.78 ± 0.11	114^{+8}_{-8}	9.44 ± 0.07	81^{+1}_{-1}	9.60 ± 0.05	79^{+1}_{-1}	9.49 ± 0.04	80^{+1}_{-1}	8.61 ± 0.03	91^{+1}_{-1}
WASP-74	7.43 ± 0.11	96^{+1}_{-3}	9.21 ± 0.07	75^{+1}_{-1}	9.59 ± 0.05	73^{+1}_{-1}	9.72 ± 0.03	72^{+1}_{-1}	9.13 ± 0.02	76^{+1}_{-1}
WASP-76	7.74 ± 0.11	102^{+4}_{-8}	8.92 ± 0.07	83^{+1}_{-1}	9.88 ± 0.05	74^{+1}_{-1}	9.84 ± 0.03	74^{+1}_{-1}	9.12 ± 0.03	81^{+1}_{-1}
WASP-80	7.13 ± 0.11	74^{+1}_{-1}	8.76 ± 0.07	69^{+1}_{-1}	9.40 ± 0.05	72^{+4}_{-1}	9.55 ± 0.03	72^{+4}_{-1}	9.00 ± 0.02	74^{+2}_{-1}

Table 2.3 (continued).

Star	Contrast at 0″.2		Contrast at 0″.5		Contrast at 1″.0		Contrast at 2″.5		Contrast at 5″.0	
	(mag)	(M_{Jup})	(mag)	(M_{Jup})	(mag)	(M_{Jup})	(mag)	(M_{Jup})	(mag)	(M_{Jup})
WASP-87	6.31 ± 0.12	166^{+9}_{-9}	7.76 ± 0.09	94^{+2}_{-2}	7.94 ± 0.07	91^{+1}_{-1}	7.93 ± 0.06	91^{+1}_{-1}	7.21 ± 0.06	109^{+4}_{-5}
WASP-88	6.53 ± 0.12	180^{+9}_{-9}	6.74 ± 0.09	168^{+7}_{-7}	6.72 ± 0.07	169^{+6}_{-6}	6.70 ± 0.06	170^{+6}_{-6}	6.59 ± 0.06	177^{+5}_{-5}
WASP-94	7.97 ± 0.11	89^{+1}_{-2}	9.57 ± 0.07	73^{+1}_{-1}	9.63 ± 0.05	73^{+1}_{-1}	9.67 ± 0.03	73^{+1}_{-1}	8.81 ± 0.03	80^{+1}_{-1}
WASP-95	7.45 ± 0.11	88^{+1}_{-1}	9.33 ± 0.07	73^{+2}_{-1}	9.58 ± 0.05	72^{+2}_{-1}	9.74 ± 0.04	71^{+2}_{-1}	8.91 ± 0.03	74^{+1}_{-1}
WASP-97	7.78 ± 0.11	81^{+1}_{-1}	9.40 ± 0.07	71^{+4}_{-1}	9.37 ± 0.05	71^{+4}_{-1}	9.40 ± 0.04	71^{+4}_{-1}	8.76 ± 0.03	74^{+2}_{-1}
WASP-99	7.65 ± 0.11	97^{+1}_{-2}	9.39 ± 0.07	76^{+1}_{-1}	9.89 ± 0.05	72^{+1}_{-1}	10.13 ± 0.03	71^{+2}_{-1}	9.55 ± 0.02	74^{+1}_{-1}
WASP-108	7.19 ± 0.12	95^{+2}_{-1}	8.41 ± 0.09	79^{+1}_{-1}	8.48 ± 0.08	79^{+1}_{-1}	8.51 ± 0.07	78^{+1}_{-1}	7.73 ± 0.06	86^{+1}_{-1}
WASP-109	5.53 ± 0.11	196^{+9}_{-9}	7.11 ± 0.08	101^{+2}_{-2}	7.48 ± 0.06	93^{+1}_{-2}	7.46 ± 0.05	94^{+1}_{-1}	7.02 ± 0.05	103^{+1}_{-2}
WASP-111	7.80 ± 0.11	102^{+3}_{-6}	8.95 ± 0.07	83^{+1}_{-1}	9.19 ± 0.05	81^{+1}_{-1}	9.08 ± 0.04	82^{+1}_{-1}	8.50 ± 0.03	89^{+1}_{-1}
WASP-117	7.35 ± 0.11	91^{+2}_{-2}	9.23 ± 0.07	73^{+1}_{-1}	9.46 ± 0.05	72^{+1}_{-1}	9.52 ± 0.04	72^{+1}_{-1}	8.75 ± 0.03	76^{+1}_{-1}
WASP-118	6.85 ± 0.11	149^{+11}_{-11}	8.14 ± 0.08	92^{+2}_{-2}	8.17 ± 0.06	92^{+2}_{-2}	8.08 ± 0.05	93^{+2}_{-2}	7.55 ± 0.04	104^{+2}_{-6}
WASP-120	6.92 ± 0.12	140^{+8}_{-8}	8.37 ± 0.08	87^{+1}_{-1}	8.39 ± 0.07	87^{+1}_{-1}	8.32 ± 0.06	88^{+1}_{-1}	7.66 ± 0.05	100^{+1}_{-1}
WASP-121	6.78 ± 0.11	134^{+8}_{-8}	8.13 ± 0.08	87^{+2}_{-1}	8.87 ± 0.06	79^{+3}_{-1}	8.92 ± 0.05	78^{+3}_{-1}	7.88 ± 0.05	91^{+1}_{-1}
WASP-122	6.30 ± 0.12	150^{+7}_{-7}	7.75 ± 0.08	90^{+1}_{-1}	8.74 ± 0.06	79^{+1}_{-1}	8.84 ± 0.05	78^{+1}_{-1}	7.83 ± 0.05	88^{+1}_{-1}
WASP-123	5.69 ± 0.11	160^{+8}_{-8}	7.32 ± 0.07	89^{+1}_{-1}	8.51 ± 0.06	77^{+1}_{-1}	8.58 ± 0.04	77^{+1}_{-1}	7.86 ± 0.04	83^{+1}_{-1}
WASP-130	5.60 ± 0.12	141^{+8}_{-8}	8.54 ± 0.08	73^{+14}_{-1}	8.75 ± 0.07	71^{+16}_{-1}	8.64 ± 0.06	72^{+15}_{-1}	7.78 ± 0.05	80^{+6}_{-1}
WASP-131	6.12 ± 0.11	184^{+8}_{-8}	8.75 ± 0.07	82^{+1}_{-1}	9.12 ± 0.05	79^{+1}_{-1}	9.32 ± 0.03	77^{+1}_{-1}	8.74 ± 0.02	82^{+1}_{-1}
WASP-136	7.00 ± 0.11	158^{+9}_{-9}	9.07 ± 0.07	83^{+1}_{-1}	9.34 ± 0.06	81^{+1}_{-1}	9.41 ± 0.04	80^{+1}_{-1}	8.72 ± 0.04	88^{+1}_{-1}
WASP-137	6.85 ± 0.11	131^{+8}_{-8}	8.28 ± 0.07	86^{+1}_{-1}	8.31 ± 0.06	86^{+1}_{-1}	8.26 ± 0.04	86^{+1}_{-1}	7.67 ± 0.04	96^{+1}_{-1}

larger than 3″ and the strength of the effect in of the order of half a magnitude. The detailed contrast performance for each individual target evaluated at discrete separations of 0.″2, 0.″5, 1.″0, 2.″0, and 5.″0 is presented in Table 2.3. We converted the magnitude contrast into mass limits by the same metric as illustrated in Section 2.4.2 using AMES-Cond, AMES-Dusty, and BT-Settl models (Allard et al. 2001; Baraffe et al. 2003). The corresponding contrast curves for each individual target are presented in Appendix 2.B.

For almost all targets within the sample we were sensitive to stellar companions with masses higher than $0.1\,M_\odot$ at separations larger than 0.″5, and for most of them we even reached the threshold to the regime of brown dwarfs around $0.08\,M_\odot$. In the five cases where we did not achieve this sensitivity, this was caused by the large distances to the corresponding targets of more than 350 pc and/or poor AO conditions. It is clear that the sensitivity achieved in only 256 s of integration with SPHERE in mediocre conditions outperformed similar studies based on lucky imaging or conducted with other AO-assisted instruments.

2.5 Discussion

2.5.1 Multiplicity rate

We derived a multiplicity rate of $55.4^{+5.9}_{-9.4}$ % from our sample of exoplanet host stars. This value seems to be higher than estimates of many previous near-infrared surveys targeting transiting exoplanet host stars to search for stellar companions, which derive multiplicity fractions of 21 ± 12 % (Daemgen et al. 2009), 38 ± 15 % (Faedi et al. 2013a), 29 ± 12 % (Bergfors et al. 2013), and 33 ± 15 % (Adams et al. 2013) among their samples. Although the sample sizes of these studies were considerably smaller than the number of targets studied within the scope of this survey, this discrepancy in multiplicity rates most likely originates from the incompleteness of these previous surveys. As most of these programs were carried out using lucky-imaging strategies or with the first generation of AO-assisted imagers, the sensitivity achieved at small separation to the host stars was lower than that achievable with SPHERE. A more accurate assessment of this incompleteness was presented by Ngo et al. (2015), who derived a raw multiplicity fraction of 34 ± 7 % for their sample of 50 transiting exoplanet hosts. After simulating the population of binaries that were missed because of the instrument sensitivity and limited field of view, they presented a corrected fraction of 49 ± 9 % instead. This value agrees very well with the rate derived from our sample because we already considered previously detected companions outside of the SPHERE field of view for the statistical analysis.

2.5.2 Hot Jupiter host stars

A large sub-sample of the targets studied within this survey are host stars to transiting hot Jupiters. To study all stars from our sample that harbor giant planets with masses higher than $0.1\,M_{\rm jup}$ and semi-major axes smaller than 0.1 au, we only needed to dismiss K2-2, K2-24, K2-38, K2-99, and WASP-130 from the original set. Reiterating the analysis as described in Section 2.4.3 provided a multiplicity rate of $54.8^{+6.3}_{-9.9}$ % for this sub-sample of hot Jupiter hosts. Consequently, we aimed to assess whether this sub-sample of 40 targets is representative for the general population of host Jupiter host stars.

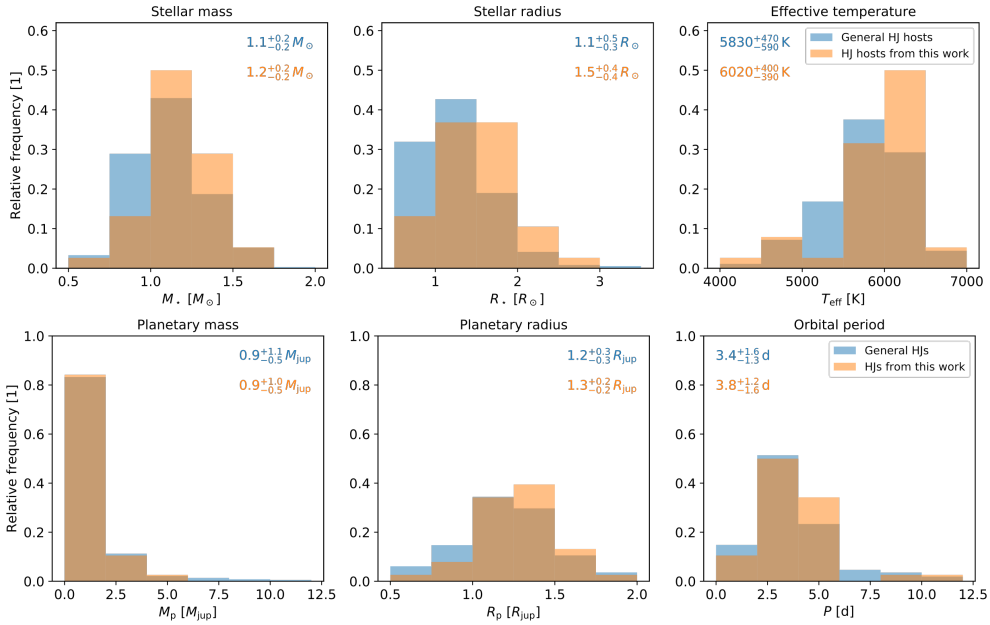

Figure 2.11: Histograms of hot Jupiter (HJ) system properties. We compare the targets analyzed within the scope of this study (orange bars) to a general sample of hot Jupiter environments (blue bars). In the *top panel* the relative frequency distributions of stellar masses $M_\star$, radii $R_\star$, and effective temperatures $T_{\rm eff}$ among both samples are presented. The *lower panel* shows properties of the transiting companions such as planetary masses $M_{\rm p}$, planetary radii $R_{\rm p}$, and orbital periods P . In the upper part of each plot, we present the 68 % confidence intervals around the medians of the corresponding distributions.

As described in Section 2.1, our target selection was purely restricted by the position on sky because we required the objects to be observable with the VLT, and the targets' R band magnitude to enable AO-assisted imaging. All hot Jupiter host stars that met these criteria were observed within this survey, even if they had been considered in previous studies. To further evaluate the quality of our sub-sample, we compiled a control group of 366 objects from the Exoplanet Orbit Database (Han et al. 2014), considering all hosts to transiting planets with masses higher than 0.1 $M_{\rm jup}$ and semi-major axes smaller than 0.1 au. We compared our sub-sample of hot Jupiters to the control group using six observables, of which three describe properties of the hosts and three characterize the transiting giant planets. These parameters are the stellar masses $M_\star$, stellar radii $R_\star$, effective temperatures $T_{\rm eff}$, planetary masses $M_{\rm p}$, planetary radii $R_{\rm p}$, and orbital periods P. In Figure 2.11 we present the relative frequency distributions of these observables among control group and targets used for this study. There seems to be a trend towards slightly higher mass stars in our sample with respect to the general population of hot Jupiter hosts. This agrees well with the applied magnitude cutoff, which induces a marginal bias towards brighter and thus more massive host stars. The same trend is marginally detected for the planetary properties as well. Nevertheless, the distributions of all observables presented in Figure 2.11 agree well between our sample and the control group, and the 68 % confidence intervals we determined for both samples intersect significantly for each

of the parameter distributions. We therefore argue that the targets analyzed within the scope of this study can be considered a good representation of typical hot Jupiter systems.

2.5.3 Correlation between stellar multiplicity and exoplanet eccentricities

Nine systems in our sample harbor a transiting exoplanet that shows a non-zero eccentricity. To test theories on the formation of these particular systems, we evaluated the multiplicity rates among these environments and in comparison to the systems that do not have any known eccentric transiting planets. For this purpose, we repeated the analysis from Section 2.4.3 for the two sub-samples of eccentric and non-eccentric planet host stars. From this analysis we obtained multiplicity rates of 44^{+15}_{-19} % and 58^{+6}_{-11} % for the systems that host eccentric planetary companions and those that do not, respectively. The large uncertainties on especially the first value arise from the very limited sample size of nine systems with the required properties. Nevertheless, there is no statistically significant difference between the multiplicity rates amongst eccentric and non-eccentric sub-samples. This agrees well with previous results from Ngo et al. (2015) and Ngo et al. (2017).

2.6 Conclusions

We have observed a sample of 45 transiting exoplanet host stars with the IRDIS instrument of VLT/SPHERE to search for stellar companions. Our results are listed below.

- We detected 11 CCs that had been identified by previous studies around 10 targets of our sample. For these CCs, we were able to confirm 9 as co-moving binaries with common proper motion, proving HAT-P-41, HAT-P-57, WASP-2, WASP-8, WASP-54, WASP-70, WASP-76, and WASP-111 to be multiple systems. One candidate around WASP-7 has been confirmed to be a background object. The status of a very bright and close companion to WASP-20 is still ambiguous because only one epoch of astrometric data was available. Synthetic stellar population models, however, suggest that WASP-20 B is a gravitationally bound binary, which is in agreement with the conclusions from Evans et al. (2016b).
- We detected 16 candidates that have not been reported by previous studies. These candidates are distributed among 13 different systems. By combining SPHERE and Gaia astrometry, we were able to show that WASP-123 is a binary system, whereas we could prove CCs around WASP-87 (CC 2) and WASP-108 (CC 2) to be background objects. For new CCs detected around K2-38, WASP-72, WASP-80, WASP-88, WASP-108 (CC 1), WASP-118, WASP-120, WASP-122, WASP-120, WASP-131, and WASP-137 too few astrometric measurements were available to prove common proper motion at 5σ significance. Based on stellar population synthesis models, we derived the probability that the candidates are instead background contaminants. The most promising candidates with background probabilities lower than 0.1% were detected around WASP-131, WASP-72, and WASP-118.
- Additional proper motion checks need to be performed to test the companionship of these newly identified candidates and WASP-20 B.

- We derived detection limits for all of our targets and showed that we reach an average magnitude contrast of 7.0 ± 0.8 mag at a separation of $0\farcs2$, while we were background limited for separations about $1\farcs0$ with an average magnitude contrast of 8.9 ± 0.9 mag. For each individual target we converted the derived contrast into a threshold of detectable mass by applying AMES-Cond, AMES-Dusty, and BT-Settl models depending on the effective temperature of the object. For 40 targets, we were able to exclude companions with masses higher than $0.1\,M_\odot$ for separations that are larger than $0\farcs5$, and in 20 cases we reached the lower mass limit for potential stellar companions of approximately $0.08\,M_\odot$.
- Based on our results, we derived a stellar multiplicity rate of $55.4^{+5.9}_{-9.4}$ % among our sample, which agrees well with results from previous surveys. For the representative sub-sample of 40 host stars to transiting hot Jupiters, the derived multiplicity fraction is $54.8^{+6.3}_{-9.9}$ %.
- We did not detect any correlation between the multiplicity of stellar systems and the eccentricity of planets that are detected around these stars.

We have shown that SPHERE is a great instrument for carrying out studies like this. The precision of the Gaia mission, especially the claimed performance of future data releases, is also a valuable tool to find stellar companions to exoplanet host stars.

In a companion work (Southworth et al. 2020) we will revisit the systems for which we have identified relatively bright nearby companions in the current work. We will use new and existing photometric and spectroscopic observations to redetermine the properties of the systems, corrected for the light contributed by the nearby companion stars.

2.A Observational setup

The detailed observational setup and the weather conditions of the individual observations are presented in Table 2.4.

2.B Individual detection limits

The detection limits for each individual target are presented in Figure 2.12. We used AMES-Cond, AMES-Dusty, and BT-Settl models (Allard et al. 2001; Baraffe et al. 2003) as illustrated in Section 2.4.2 to convert magnitude contrast into detectable Jupiter masses. The data used for creating these plots will be published online in the Strasbourg astronomical Data Center (CDS).

Table 2.4: Observational setup and weather conditions for all acquired data.

Star	V^a (mag)	K^b (mag)	Observation date (yyyy-mm-dd)	Mode^c	NDITH×NDIT×DIT^d (1×1×s)	$\langle\omega\rangle^e$ ($''$)	$\langle X\rangle^f$	$\langle\tau_0\rangle^g$ (ms)
HAT-P-41	11.36	9.73	2016-10-24	P	26×4×4	1.53	1.24	5.70
HAT-P-57	10.47	9.43	2016-10-09	P	16×4×4	0.61	1.52	7.61
HAT-P-57	10.47	9.43	2017-05-15	F	16×4×4	0.92	1.22	2.94
K2-02	10.19	8.03	2017-05-15	F	16×4×4	0.99	1.50	2.77
K2-24	11.28	9.18	2017-06-23	F	16×4×4	2.13	1.58	1.60
K2-38	11.39	9.47	2017-03-06	P	16×4×4	0.56	1.01	7.38
K2-39	10.83	8.52	2017-05-15	F	16×4×4	1.13	1.21	2.47
K2-99	11.15	9.72	2017-08-28	F	16×4×4	0.66	1.83	3.17
KELT-10	10.70	9.34	2017-05-15	F	16×4×4	0.96	1.09	3.14
WASP-2	11.98	9.63	2017-05-15	F	16×4×4	1.04	1.27	2.38
WASP-7	9.48	8.40	2016-10-06	P	16×4×4	0.69	1.17	4.90
WASP-8	9.77	8.09	2016-10-06	P	16×4×4	0.69	1.03	4.82
WASP-16	11.31	9.59	2017-03-06	P	16×4×4	0.52	1.07	9.41
WASP-20	10.79	9.39	2016-10-06	P	16×4×4	0.94	1.02	3.20
WASP-21	11.59	9.98	2016-10-24	P	16×4×4	0.94	1.42	2.84
WASP-29	11.21	8.78	2016-10-09	P	16×4×4	0.46	1.04	11.84
WASP-30	11.46	10.20	2017-05-15	F	16×4×4	1.05	1.37	3.12
WASP-54	10.42	9.04	2017-03-05	P	16×4×4	0.57	1.23	5.81
WASP-68	10.68	8.95	2017-06-29	F	16×4×4	1.41	1.01	1.78
WASP-69	9.87	7.46	2016-10-06	P	12×4×4	0.69	1.08	4.90
WASP-70	10.79	9.58	2017-05-15	F	16×4×4	1.28	1.07	2.49
WASP-71	10.56	9.32	2016-11-08	P	16×4×4	0.76	1.63	9.40
WASP-72	10.87	9.62	2017-07-06	F	16×4×4	0.95	1.22	3.41
WASP-73	10.48	9.03	2016-10-09	P	26×4×4	0.56	1.20	7.79
WASP-74	9.76	8.22	2017-06-22	F	16×4×4	1.07	1.10	2.23
WASP-76	9.53	8.24	2016-11-07	P	16×4×4	0.81	1.76	9.40
WASP-80	11.87	8.35	2017-06-22	F	16×4×4	1.25	1.08	2.56

Table 2.4 (continued).

Star	V^a (mag)	K^b (mag)	Observation date (yyyy-mm-dd)	Mode^c	NDITH×NDIT×DIT^d (1×1×s)	$\langle\omega\rangle^e$ ($''$)	$\langle X\rangle^f$	$\langle\tau_0\rangle^g$ (ms)
WASP-87	10.74	9.60	2017-04-02	F	16×4×4	1.74	1.19	1.54
WASP-88	11.39	10.32	2017-05-15	F	16×4×4	0.93	1.14	2.90
WASP-94	10.06	8.87	2016-10-09	P	16×4×4	0.54	1.01	9.59
WASP-95	10.09	8.56	2016-10-21	P	16×4×4	0.84	1.25	2.78
WASP-97	10.58	9.03	2016-10-09	P	16×4×4	0.47	1.17	11.72
WASP-99	9.48	8.09	2017-07-06	F	16×4×4	0.78	1.23	3.32
WASP-108	11.22	9.80	2017-03-05	P	16×4×4	0.81	1.10	6.20
WASP-109	11.44	10.20	2017-07-23	F	12×4×4	1.41	1.62	2.65
WASP-111	10.26	9.00	2017-05-15	F	16×4×4	1.26	1.11	2.24
WASP-117	10.15	8.78	2016-10-21	P	16×4×4	0.78	1.14	3.37
WASP-118	11.02	9.79	2017-07-06	F	16×4×4	1.12	1.23	3.41
WASP-120	10.96	9.88	2016-12-20	P	9×4×4	0.86	1.07	7.61
WASP-121	10.52	9.37	2016-12-25	P	16×4×4	1.39	1.04	2.51
WASP-122	11.00	9.42	2016-12-25	P	16×4×4	1.41	1.07	2.26
WASP-123	11.03	9.36	2016-10-22	P	16×4×4	0.89	1.17	2.20
WASP-130	11.11	9.46	2017-03-11	P	16×4×4	0.42	1.20	11.18
WASP-131	10.08	8.57	2017-07-05	F	16×4×4	1.01	1.66	2.77
WASP-136	9.98	8.81	2016-10-25	P	16×4×4	1.45	1.26	5.70
WASP-137	10.89	9.46	2016-10-26	P	6×4×4	0.58	1.49	8.47

Notes. [(a)] V-band apparent magnitudes are from a range of sources and are those reported in TEPCat (Southworth 2011). [(b)] K-band system magnitudes from 2MASS (Cutri et al. 2012a). [(c)] Observation mode is either pupil (P) or field (F) stabilized [(d)] NDITH denotes the number of dithering positions, NDIT describes the number of integrations per dithering position, and DIT is the detector integration time for each individual exposure. [(e)] $\langle\omega\rangle$ denotes the average seeing conditions during the observation. [(f)] $\langle X\rangle$ denotes the average airmass during the observation. [(g)] $\langle\tau_0\rangle$ denotes the average coherence time during the observation.

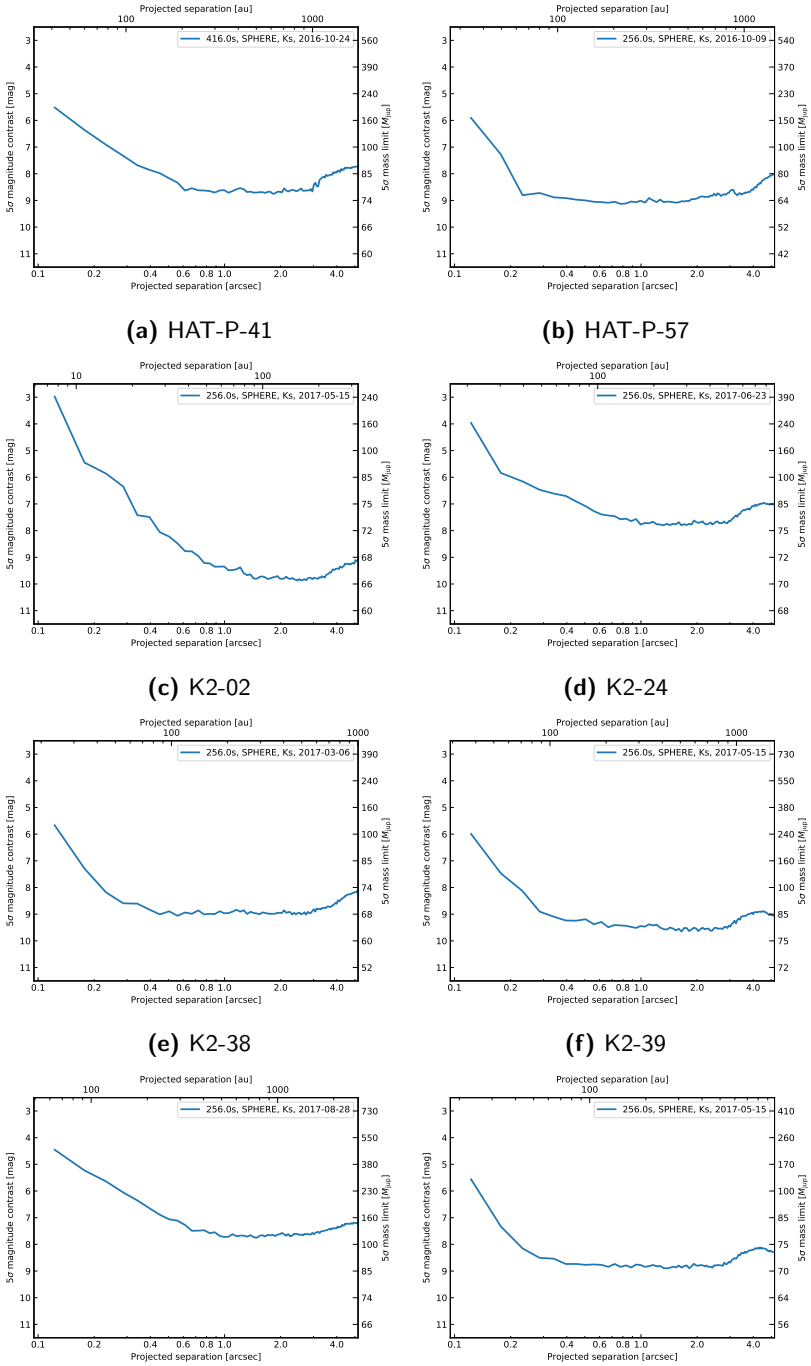

(a) HAT-P-41 **(b)** HAT-P-57

(c) K2-02 **(d)** K2-24

(e) K2-38 **(f)** K2-39

(g) K2-99 **(h)** KELT-10

Figure 2.12: Detection limits of individual targets. We convert projected angular separations into projected physical separations using the distances presented in Table 2.1. The mass limits arise from comparison to AMES-Cond, AMES-Dusty, and BT-Settl models as described in Section 2.4.2.

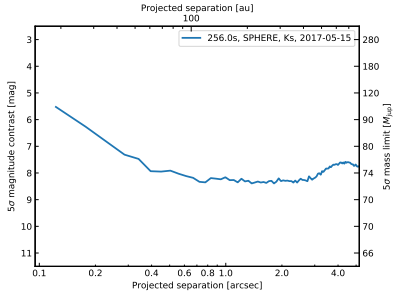

(i) WASP-2

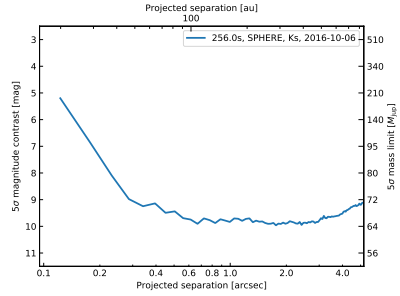

(j) WASP-7

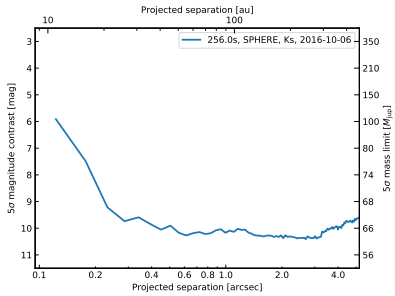

(k) WASP-8

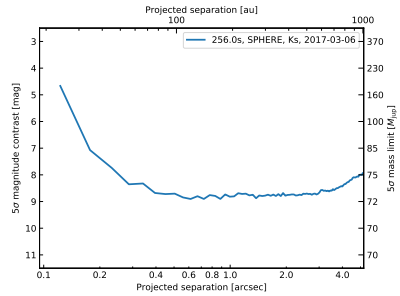

(l) WASP-16

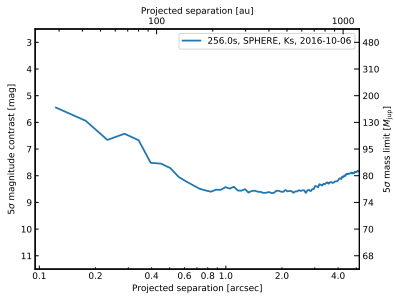

(m) WASP-20

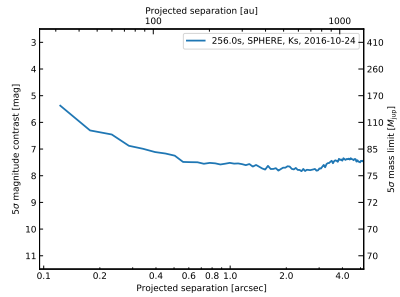

(n) WASP-21

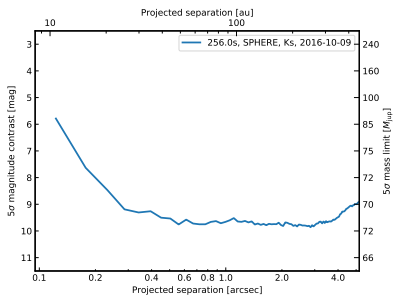

(o) WASP-29

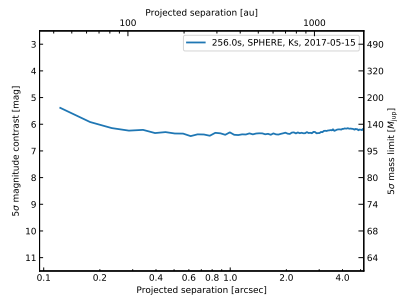

(p) WASP-30

Figure 2.12 (continued).

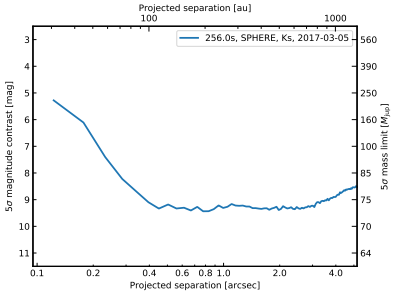

(q) WASP-54

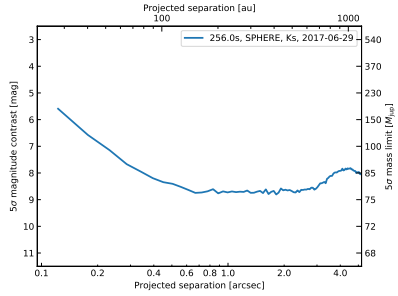

(r) WASP-68

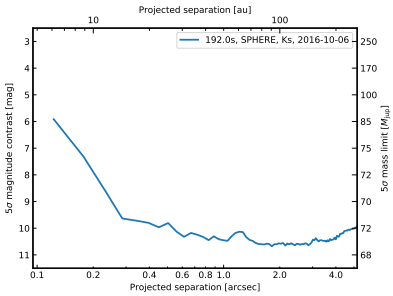

(s) WASP-69

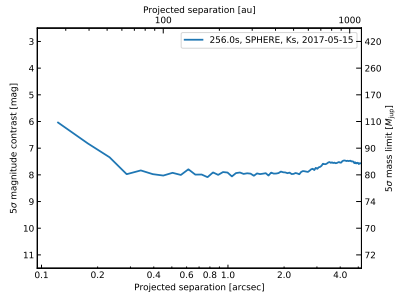

(t) WASP-70

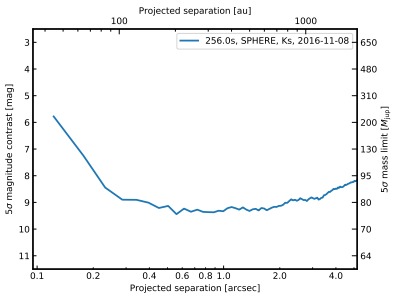

(u) WASP-71

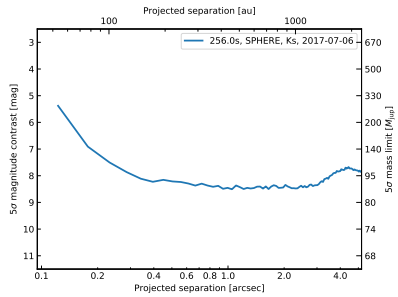

(v) WASP-72

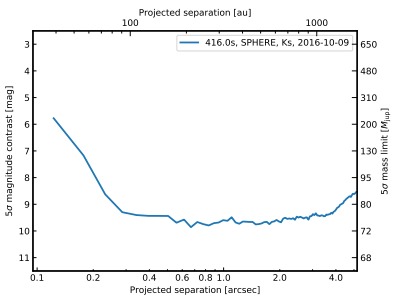

(w) WASP-73

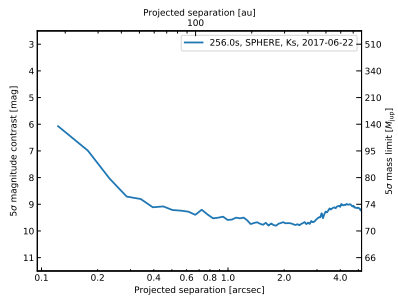

(x) WASP-74

Figure 2.12 (continued).

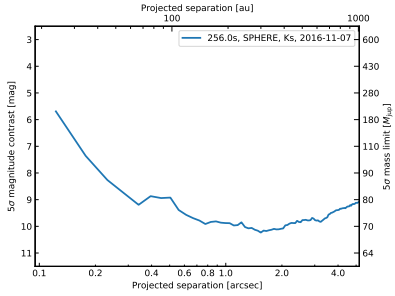

(y) WASP-76

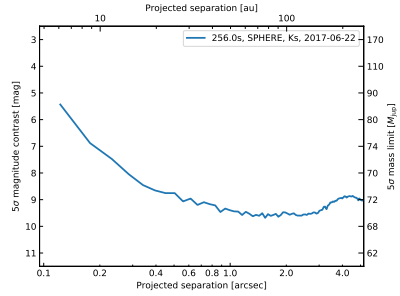

(z) WASP-80

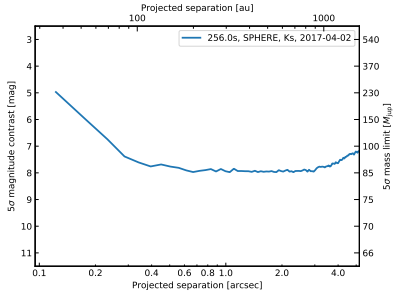

(aa) WASP-87

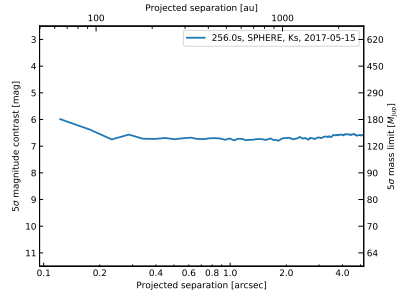

(ab) WASP-88

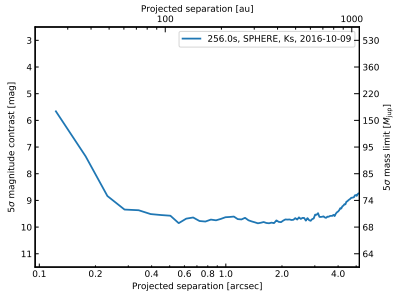

(ac) WASP-94

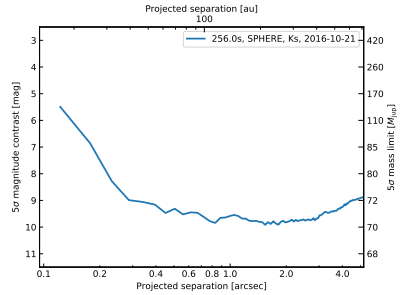

(ad) WASP-95

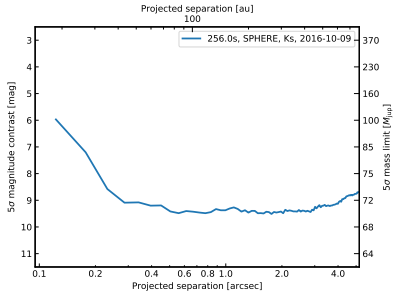

(ae) WASP-97

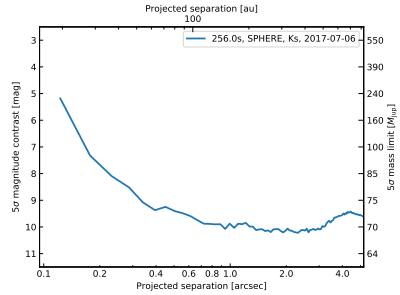

(af) WASP-99

Figure 2.12 (continued).

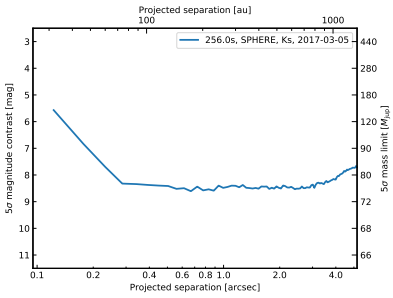

(ag) WASP-108

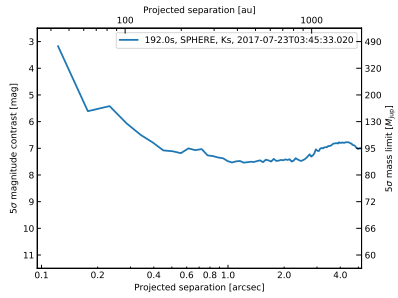

(ah) WASP-109

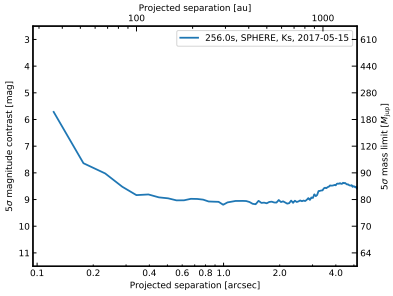

(ai) WASP-111

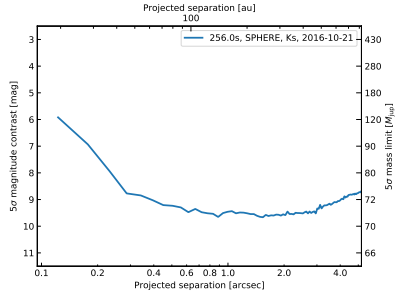

(aj) WASP-117

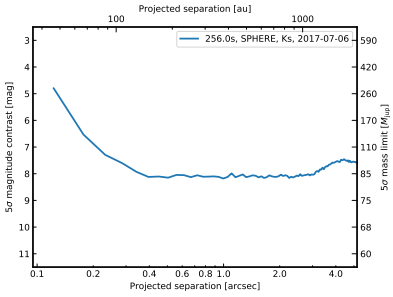

(ak) WASP-118

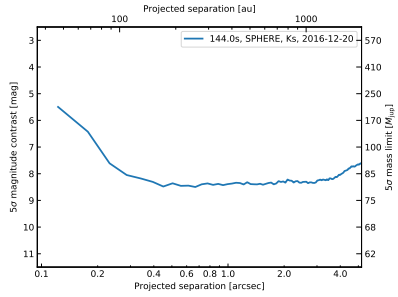

(al) WASP-120

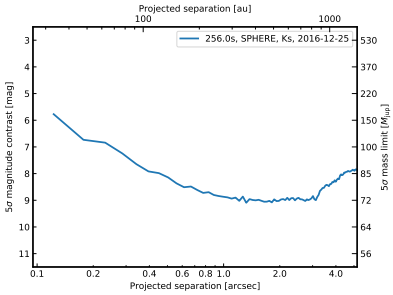

(am) WASP-121

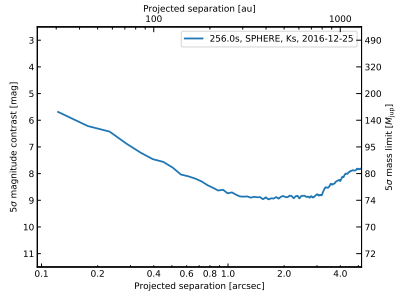

(an) WASP-122

Figure 2.12 (continued).

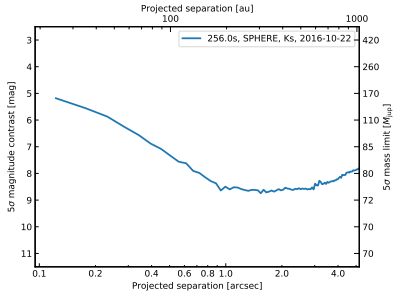

(ao) WASP-123

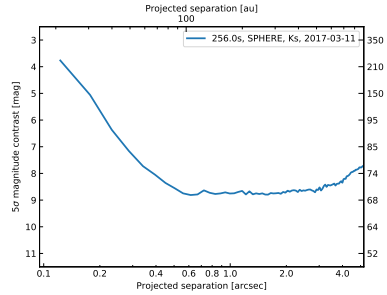

(ap) WASP-130

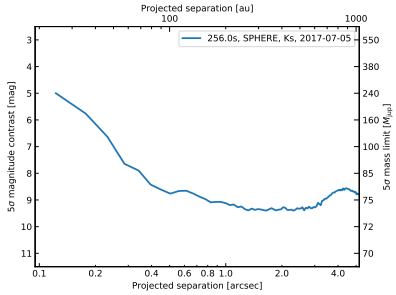

(aq) WASP-131

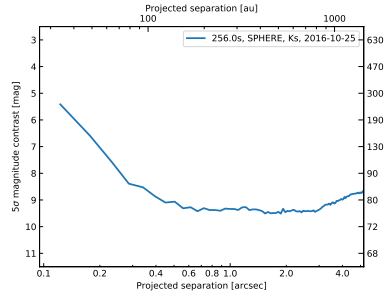

(ar) WASP-136

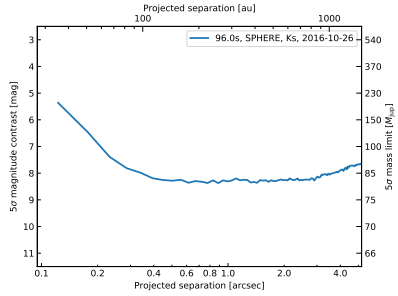

(as) WASP-137

Figure 2.12 (continued).

Chapter 3

Discovery of a directly imaged disk in scattered light around the Sco-Cen member Wray 15-788

Protoplanetary disks are the birth environments of planetary systems. Therefore, the study of young, circumstellar environments is essential to understanding the processes taking place in planet formation and the evolution of planetary systems. We detect and characterize circumstellar disks and potential companions around solar-type, pre-main sequence stars in the Scorpius-Centaurus association (Sco-Cen). As part of our ongoing survey we carried out high-contrast imaging with VLT/SPHERE/IRDIS to obtain polarized and total intensity images of the young (11^{+16}_{-7} Myr old) K3IV star Wray 15-788 within the Lower Centaurus Crux subgroup of Sco-Cen. For the total intensity images, we remove the stellar halo via an approach based on reference star differential imaging in combination with principal component analysis. Both total intensity and polarimetric data resolve a disk around the young, solar-like Sco-Cen member Wray 15-788. Modeling of the stellar spectral energy distribution suggests that this is a protoplanetary disk at a transition stage. We detect a bright outer ring at a projected separation of $\sim$370 mas ($\approx$ 56 au), hints of inner substructures at $\sim$170 mas ($\approx$ 28 au), and a gap in between. Within a position angle range of only $60^\circ < \phi < 240^\circ$, we are confident at the 5σ level that we detect actual scattered light flux from the outer ring of the disk; the remaining part is indistinguishable from background noise. For the detected part of the outer ring we determine a disk inclination of $i = 21^\circ \pm 6^\circ$ and a position angle of $\varphi = 76^\circ \pm 16^\circ$. Furthermore, we find that Wray 15-788 is part of a binary system with the A2V star HD 98363 at a separation of $\sim 50''$ ($\approx$ 6900 au). The detection of only half of the outer ring might be due to shadowing by a misaligned inner disk. A potential substellar companion can cause the misalignment of the inner structures and can be responsible for clearing the detected gap from scattering material. However, we cannot rule out the possibility of a non-detection due to our limited signal-to-noise ratio, combined with brightness azimuthal asymmetry. From our data we can exclude companions more massive than 10 $M_{\rm Jup}$ within the gap at a separation of $\sim$230 mas ($\approx$ 35 au). Additional data are required to characterize the disk's peculiar morphology and to set tighter constraints on the potential perturber's orbital parameters and mass.

Adapted from
A. J. Bohn, M. A. Kenworthy, C. Ginski, M. Benisty, J. de Boer, C. U. Keller, E. E. Mamajek, T. Meshkat, G. A. Muro-Arena, M. J. Pecaut, F. Snik, S. G. Wolff, M. Reggiani
Astronomy & Astrophysics, **624**, A87 (2019)

3.1 Introduction

In the past few years, the second generation of high-contrast imaging instruments such as the Spectro-Polarimetric High-contrast Exoplanet REsearch (SPHERE, Beuzit et al. 2019) instrument and the Gemini Planet Imager (GPI, Macintosh et al. 2015) have resolved and characterized several disks around young, pre-main sequence stars (e.g., Avenhaus et al. 2018; Millar-Blanchaer et al. 2017). These range from warm, gas-rich protoplanetary disks around young stars of ages usually lower than 10 Myr (Andrews et al. 2012) to cold debris disks around more evolved stars where the primordial gas has already dissipated (Matsuyama et al. 2003; Wyatt et al. 2003). Since planets form within protoplanetary disks (Goldreich & Ward 1973), the characterization of circumstellar environments and the search for planetary mass companions is closely related. The study of young stellar systems, therefore, gives us an understanding of the initial conditions of planet formation.

With a mean distance of $\sim$130 pc (de Zeeuw et al. 1999) and an average age of 14 ± 3 Myr (Pecaut & Mamajek 2016), the Scorpius-Centaurus association (Sco-Cen, de Zeeuw et al. 1999) is one of the closest sites of recent star formation to the Sun. Therefore, Sco-Cen is an ideal region when it comes to the search for young, luminous planets or protoplanetary and early debris disks. Pecaut & Mamajek (2016) identified and characterized 156 new K-type star members of Sco-Cen. One object in this sample is the emission-line star Wray 15-788 (2MASS J11175186-6402056, Hen 3-632), which is located in the Lower Centaurus-Crux (LCC) subgroup of Sco-Cen (Mamajek et al. 2013a; Pecaut & Mamajek 2016). It was discovered as an Hα emission object by Wray (1966) and was confirmed within the study of southern emission line stars by Henize (1976). The star is of spectral type K3IVe, has a mass of $1.2\,M_{\odot}$ (Pecaut & Mamajek 2016), and a distance of 139.7 ± 0.5 pc (Gaia Collaboration et al. 2018). In addition, Pecaut & Mamajek (2016) determined an age of 4 Myr, which is likely an underestimate. A more accurate age may be obtained by using evolutionary models that include magnetic fields (Feiden 2016) as presented in Section 3.5.1 of this work. Table 3.1 summarizes the most important stellar parameters of Wray 15-788.

In Section 3.2 we describe the SPHERE data we obtained on Wray 15-788 and Section 3.3 explains our applied data reduction techniques. Thereafter, we present our observational results in Section 3.4 and an analysis of these data is given in Section 3.5. Furthermore, we show the association of Wray 15-788 as a comoving companion to the main sequence star HD 98363 and derive new estimates for ages and masses of both objects. A model of the stellar spectral energy distribution (SED) is also presented in Section 3.5. Finally, we discuss our results in Section 3.6 and present the conclusions of the article in Section 3.7.

3.2 Observations

All our observations were performed with SPHERE, which is mounted on the Nasmyth platform of Unit 3 telescope (UT3) at ESO's VLT. To obtain diffraction limited data, SPHERE is assisted by the SAXO extreme adaptive optics system (Fusco et al. 2006; Petit et al. 2014). In particular, we made use of the infrared dual-band imager and spectrograph (IRDIS; Dohlen et al. 2008), which was operated in both dual-polarization imaging (DPI; Langlois et al. 2014) and classical imaging (CI; Vi-

Table 3.1: Stellar parameters of Wray 15-788 and HD 98363.

Parameter	Value		Reference(s)
	Wray 15-788	HD 98363	
Right Ascension (J2000)	11:17:51.87	11:17:58.14	(1)
Declination (J2000)	-64:02:05.60	-64:02:33.35	(1)
Spectral Type	K3IVe	A2V	(2,3)
Mass [$M_\odot$]	$1.26^{+0.07}_{-0.22}$	$1.92^{+0.08}_{-0.08}$	(2,4)
Effective Temperature [K]	$4\,549^{+225}_{-215}$	$8\,830^{+331}_{-319}$	(2,4)
Luminosity [$L_\odot$]	$0.91^{+0.07}_{-0.06}$	$14.96^{+1.44}_{-1.32}$	(2,4)
Age[a] [Myr]	11^{+16}_{-7}	11^{+16}_{-7}	(2,4)
Parallax [mas]	7.159 ± 0.027	7.215 ± 0.034	(1)
Distance [pc]	139.126 ± 0.52	138.044 ± 0.66	(1,5)
Proper motion (RA) [mas]	-28.583 ± 0.042	-28.491 ± 0.053	(1)
Proper motion (Dec) [mas]	-1.411 ± 0.040	-0.795 ± 0.051	(1)
V [mag]	11.89 ± 0.08	7.85 ± 0.01	(2,6,7)
$B - V$ [mag]	1.11 ± 0.09	0.18 ± 0.01	(2,6,7)
J [mag]	9.39 ± 0.02	7.53 ± 0.02	(2,8)
H [mag]	8.59 ± 0.04	7.48 ± 0.03	(2,8)
K_s [mag]	8.18 ± 0.03	7.50 ± 0.02	(2,8)
$W1$ [mag]	7.75 ± 0.02	7.36 ± 0.03	(2,9)
$W2$ [mag]	7.49 ± 0.02	7.43 ± 0.02	(2,9)
$W3$ [mag]	6.42 ± 0.02	6.93 ± 0.02	(2,9)
$W4$ [mag]	3.88 ± 0.02	4.64 ± 0.02	(2,9)

Notes. [(a)] The primary, HD 98363, has a most likely age of 11 Myr, but since the error bars of the primary overlap the main sequence in the Hertzsprung-Russell diagram, the 95% confidence range of 22 Myr to 480 Myr does not contain the mode. Given its membership in Sco-Cen, this is not a useful age constraint. The secondary, Wray 15-788, is in a stage of evolution where we can place meaningful limits on the age, so we adopt the system age as that of the secondary, 11 Myr with 95% CL range of 11^{+16}_{-7} *Myr*.

References. (1) Gaia Collaboration et al. (2018); (2) Pecaut & Mamajek (2016); (3) Houk & Cowley (1975); (4) Section 3.5.1 of this work; (5) Bailer-Jones et al. (2018); (6) Henden et al. (2012); (7) Høg et al. (2000); (8) Cutri et al. (2012a); (9) Cutri et al. (2012b)

Table 3.2: Observations of Wray 15-788 carried out with SPHERE/IRDIS.

Observation date (yyyy-mm-dd)	Mode[a]	Filter	NDIT×DIT[b] (1×s)	$\Delta\pi^c$ (°)	$\langle\omega\rangle^d$ ($''$)	$\langle X\rangle^e$	$\langle\tau_0\rangle^f$ (ms)
2018-05-14	CI	H	4×32	0.86	0.86	1.30	2.55
2018-05-14	CI	K_s	4×32	0.87	0.85	1.30	2.15
2018-06-05	DPI	H	4×64	-	0.99	1.30	1.48

Notes. [(a)] Observation mode is either classical imaging (CI) or dual-polarization imaging (DPI). [(b)] NDIT describes the number of dithering positions and DIT is the detector integration time per dithering position. [(c)] $\Delta\pi$ describes the amount of field rotation during the observation, if it is carried out in pupil-stabilized mode (only valid for CI observations). [(d)] $\langle\omega\rangle$ denotes the average seeing conditions during the observation. [(e)] $\langle X\rangle$ denotes the average airmass during the observation. [(f)] $\langle\tau_0\rangle$ denotes the average coherence time during the observation.

gan et al. 2010) modes to obtain high-contrast polarized and total intensity images of the system. A detailed description of the observations is presented in Table 3.2.

3.2.1 Classical imaging

The CI observations (PI: M. A. Kenworthy) were obtained on May 14, 2018, within a larger program looking for planetary mass companions around solar-type stars in Sco-Cen (Bohn et al. in prep). The target was observed in good weather conditions with two broadband filters in the H and K_s band (Filter IDs: `BB_H`, `BB_Ks`) for 128 s each. The central wavelengths of the filters are λ_c^H=1625.5 nm and $\lambda_c^{K_s}$=2181.3 nm with bandwidths of $\Delta\lambda^H$=291.0 nm and $\Delta\lambda^{K_s}$=313.5 nm, respectively. To reduce the effect of bad detector pixels, a dither pattern on a 2×2 grid with 1pixel spacing was applied during the observation. Additionally, an apodized pupil Lyot coronagraph (Soummer 2005; Carbillet et al. 2011; Guerri et al. 2011) with a diameter of 185 mas (Coronagraph ID: `N_ALC_YJH_S`) was used to block the central flux of the star. The observations were carried out in pupil-stabilized mode, but the amount of field rotation during the observation was less than 1°. To model the thermal sky and instrument background, an additional exposure with the science setup was taken at an offset sky position without any source. Center frames were obtained, for which a sinusoidal pattern was applied to the deformable mirror in order to create four calibration spots around the target's position behind the coronagraphic mask. In addition, we obtained unsaturated, non-coronagraphic flux frames of the star with a neutral density filter (Filter ID: `ND_1.0`) in place to avoid saturation of the detector.

3.2.2 Dual-polarization imaging

The DPI observation (PI: M. Benisty) was carried out on the night of June 5, 2018, under very poor weather conditions. We obtained one polarimetric cycle, which consists of one image for each of the four half-wave plate positions (0°, 45°, 22.5°, and 67.5°) with an exposure time of 64 s each. Furthermore, we applied the same coronagraph and broadband filter in H band as was used for the CI observations. In a similar manner as described before, we also obtained additional center and sky

frames for the DPI observation. The DPI cycle was conducted in field-stabilized mode.

3.3 Data reduction

Both CI and DPI data were reduced by a personal processing pipeline based on the new release of the PynPoint package (Stolker et al. 2019). This included basic image processing steps such as flat fielding and sky subtraction for both CI and DPI data. Furthermore, a simple bad pixel correction was applied by a 5σ box filtering algorithm (based on the IDL routine of Varosi & Gezari 1993).

3.3.1 Classical imaging

The dithering offsets of the science images to the center frame were registered and all frames were aligned accordingly. Afterwards, the aligned science images were centered with respect to the star's position behind the coronagraph. This position was determined as the center of the four calibration spots within the additionally obtained center frame (see Langlois et al. 2013). Because IRDIS was operated in CI mode, we obtained two copies of the coronagraphic stellar point spread function (PSF) simultaneously for each exposure (see Dohlen et al. 2008). To compensate for bad pixel introduced noise, we averaged the two centered PSFs from both detector sides for each individual exposure. Finally, we removed the stellar halo and instrumental artifacts by an approach based on reference star differential imaging (RDI, Smith & Terrile 1984; Lafrenière et al. 2007a). Within a larger survey for planets around solar-type stars (PI: M. A. Kenworthy), in Sco-Cen we observed 26 and 12 stars in H and K_s band, respectively. A detailed list of these reference stars and the observing conditions is presented in Appendix 3.A. The stars are very similar to Wray 15-788 in terms of spectral type, mass, age, distance, position on sky, and apparent magnitude. Furthermore, they were observed with exactly the same observational setup as for Wray 15-788. Therefore, we created a library from these reference targets, on which we applied principal component analysis (PCA; Amara & Quanz 2012; Soummer et al. 2012). Thereafter, the PSF of Wray 15-788 in each science frame was modeled as linear combination of the first m principal components (PCs) from the reference library (RDI+PCA; e.g., Choquet et al. 2014). These PSF-models were subtracted from the science images, the residuals were de-rotated according to their parallactic angle and median combined. For characterization of disks at low inclination, this technique has proven superior to algorithms based on angular differential imaging (Marois et al. 2006a), which leads to undesirable self-subtraction effects from radial symmetric parts of the disk (Choquet et al. 2014). An additional constant rotation of $135\overset{\circ}{.}99$ in the counterclockwise direction was applied to correct for the instrument's offset angle included to align the pupil with the Lyot stop[1]. We used the general astrometric solution for IRDIS with a plate scale of 12.251 ± 0.009 mas per pixel and 12.265 ± 0.009 mas per pixel for H and K_s band, respectively, as well as a true north correction of $-1\overset{\circ}{.}75 \pm 0\overset{\circ}{.}08$ according to Maire et al. (2016).

[1]This value is obtained from the latest version of the instrument manual: `https://www.eso.org/sci/facilities/paranal/instruments/sphere/doc.html`

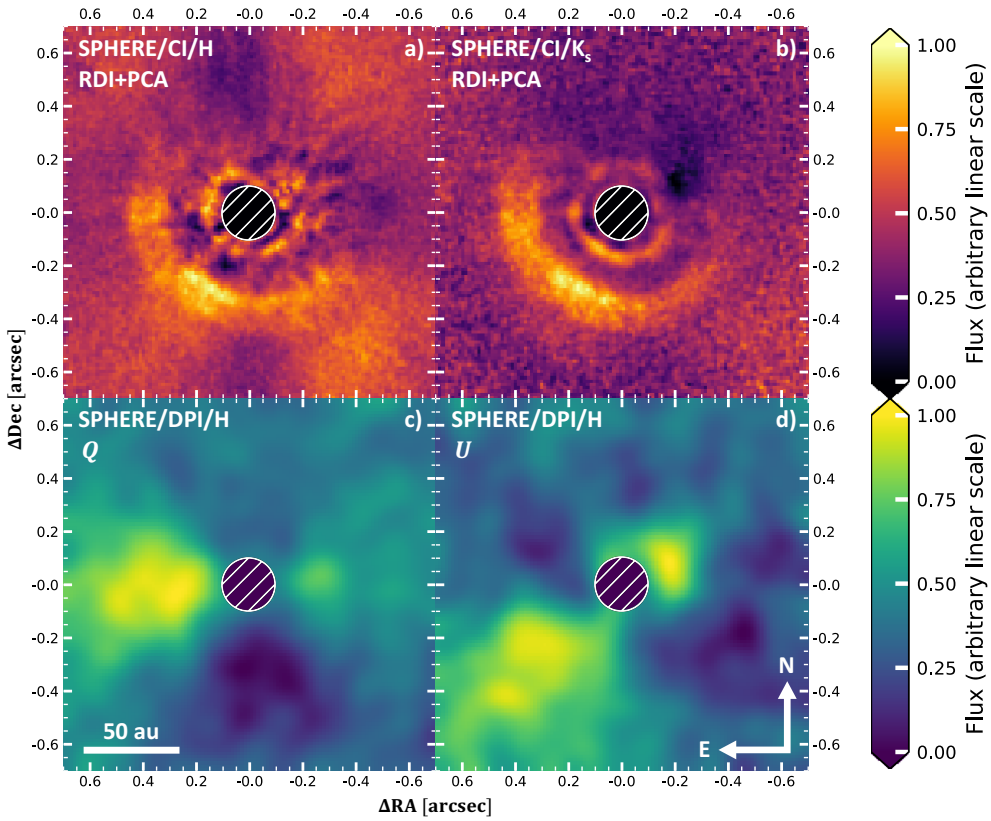

Figure 3.1: Reduced SPHERE images of Wray 15-788. All frames show the same region on the sky with a field of view of approximately $1\farcs39 \times 1\farcs39$. The star is positioned in the center of each image. An artificial mask with a diameter of ∼196 mas is applied to obscure the coronagraph and leaking flux close to it. The images are scaled with r^2 according to the deprojected separation of the disk to star in the center of the image. The scaling is corrected for an inclination of 21° and a position angle of 76°, as derived in Section 3.5.3. In each image north is up and east is left. An arbitrary linear color scale is applied, which is normalized to the maximum flux in each frame. Images **a** and **b** show the results obtained with SPHERE in CI mode applying a broad H- and K_s-band filter, respectively. The stellar point spread function was reconstructed by a fit of 20 principal components obtained from a library of reference stars. In the bottom panel we present the results obtained from SPHERE DPI data in H band. Images **c** and **d** show the Stokes Q and U parameters for linear polarization, respectively. Both polarimetric results are smoothed with a Gaussian kernel having a FWHM of ∼50 mas. This is equivalent to the theoretical SPHERE FWHM in H band.

3.3.2 Dual-polarization imaging

The reduction of the DPI data was carried out following the description given in Ginski et al. (2016b).

3.4 Observational results

The results of our data reduction are presented in Figure 3.1. For both CI and DPI,

an artificial mask with a diameter of ∼196 mas is applied to hide the innermost parts of the images that are obscured by the coronagraphic mask and polluted by leaking flux around it. Furthermore, each pixel is scaled by the squared, deprojected radial separation to the image center to account for intensity loss in scattered light and to highlight features of the disk. For a correct deprojection we use an inclination of 21° and a position angle of 76° following our disk fitting results presented in Section 3.5.3.

3.4.1 CI data

In frame **a** and **b** of Figure 3.1 we present the SPHERE/CI results in H and K_s band, respectively. We modeled the stellar PSFs with 20 PCs[2] from our reference library and subtracted these models afterwards. A bright disk that shows several features is detected in both filters. The most prominent are the following:

(i) *Ring A*: a bright outer arc at an average projected separation of ∼370 mas that is brightest southeast of the star and indistinguishable from background noise in the northwest;

(ii) *Ring B*: a tentative circular inner ring at an average projected separation of ∼170 mas;

(iii) a gap in between the two rings.

An annotated image of the disk, in which the main features are highlighted, is presented in Figure 3.2. All these detected features of the disk are analyzed in depth in Section 3.5.3, and discussed in Section 3.6.

3.4.2 DPI data

In frames **c** and **d** of Figure 3.1 we present Stokes Q and U parameters of the SPHERE/DPI data. To increase the signal-to-noise ratio in the poor quality observations, we smoothed the images with a Gaussian kernel that has a full width at half maximum (FWHM) of ∼50 mas. This corresponds to the diffraction limited size of the SPHERE PSF in H band. Both polarimetric results reveal a strong butterfly-like pattern, approximately centered at the star's position behind the coronagraph. This agrees with what we expect of azimuthal linear polarization of light scattered by a circumstellar disk. The positive flux extends down to the artificial mask that we have applied in the image center. However, this does not necessarily mean that we receive scattered light flux from all separations down to the mask's radial separation of ∼98 mas, due to the poor weather conditions and the previously performed smoothing. Furthermore, an excess of flux in the southeastern part compared to the northwestern part of the disk is detected in the Q and U images, which agrees very well with the shape of *ring A* that we detect in the CI results. Moreover, the scattered light flux in the DPI result seems to extend farther out compared to the distinct shape of *ring A* in the CI results. Whether this extended structure is real or just caused by the applied smoothing and due to the poor weather conditions during the observation will be analyzed in Section 3.5.3.

[2]We optimized the number of fitted principal components in order to achieve the best contrast inside the possible disk gap at a projected separation of ∼220 mas.

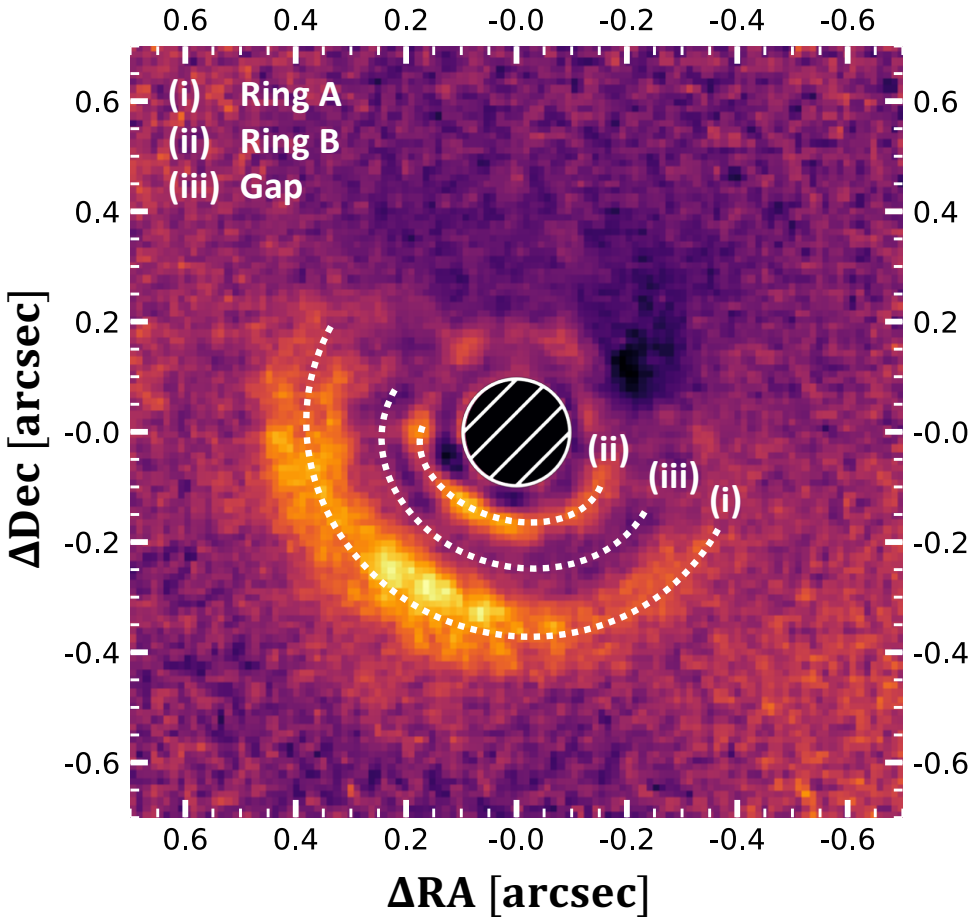

Figure 3.2: Annotated version of Figure 3.1 **b**. The discussed features of the disk are highlighted.

3.5 Analysis

3.5.1 Association of Wray 15-788 with HD 98363

In our investigation we discovered that Wray 15-788 is part of a multiple system with the A2V star HD 98363 (HIP 55188). HD 98363 is a main sequence star of spectral type A2V (Houk & Cowley 1975), and de Zeeuw et al. (1999) had identified it as a member of LCC based on Hipparcos astrometry. Tetzlaff et al. (2011) estimated an isochronal age of 13.0 ± 3.7 Myr to HD 98363 and constrained a mass of $2.0 \pm 0.1\,M_{\odot}$. Considering binarity with Wray-15-788, our aim is to derive new estimates for these parameters. All the important stellar properties are listed in Table 3.1.

Our companionship analysis is based on parallaxes and proper motions from Gaia DR2 (ICRS, epoch 2015.5, Gaia Collaboration et al. 2018), which are listed in Table 3.1 as well. The calculated separation of the binary is $49\farcs64974 \pm 0.05$ mas and the distances agree within 1.08 ± 0.84 parsec, statistically consistent with these two stars being co-distant. The differential velocity in the plane of the sky between the two stars is 0.623 ± 0.462 mas/year. An estimate of the orbital period of the binary

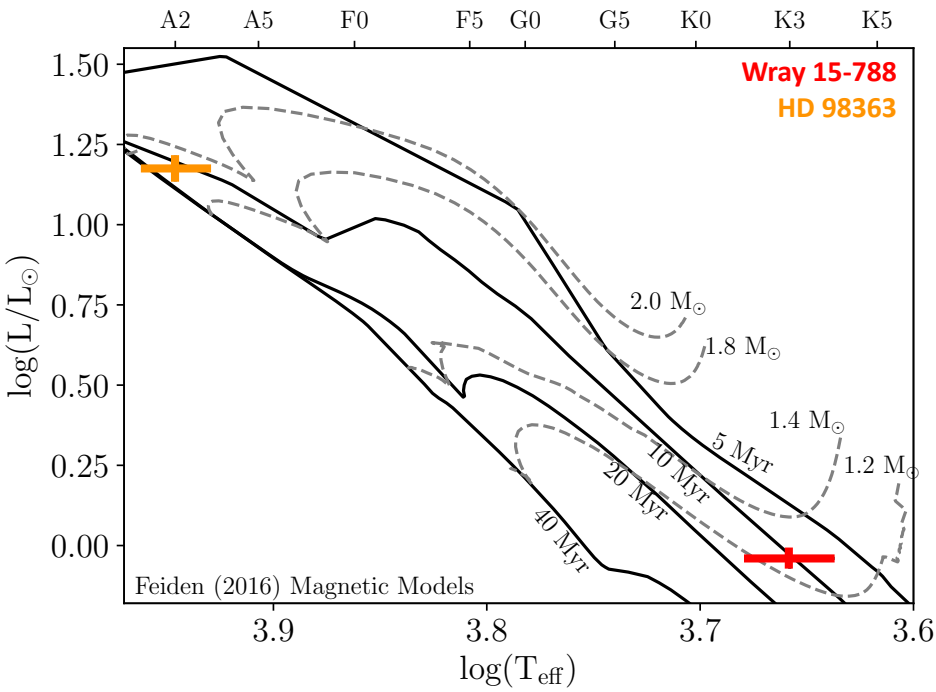

Figure 3.3: Hertzsprung-Russell diagram for the binary system of Wray 15-788 and HD 98363. We plot pre-main sequence tracks and isochrones according to Feiden (2016) to constrain masses and ages of the companions.

with a separation of 6900 au is around 330 kyr, with a circular orbital velocity of 0.63 km/s, which is 0.001 mas/year. This is marginally consistent with the differential velocity of the two stars above. So, Wray 15-788 is actually HD 98363 B: a stellar companion to HD 98363.

Furthermore, Chen et al. (2012) detected a debris disk around HD 98363 based on 24 µm and 70 µm photometry from *Spitzer* MIPS (Werner et al. 2004; Rieke et al. 2004). Moór et al. (2017) reported a non-detection of CO with an upper limit of 0.036 ,Jy km/s on the integrated line flux of ^{12}CO J=2–1. This gas-poor debris disk around HD 98363 is especially interesting due to our finding of a disk around Wray 15-788. A discussion of this special binary system with two hosts of circumstellar disks is presented in Section 3.6.3.

To derive consistent masses and ages of the binary system we analyzed the two stars within an Hertzsprung-Russell diagram, as presented in Figure 3.3. We estimated the masses and ages using Feiden/Dartmouth tracks (Feiden 2016). These models include magnetism below 1.7 $M_\odot$ and yield a consistent age for the Upper Scorpius subgroup of Sco-Cen (Feiden 2016). Therefore, they define a good basis for an analysis of our two LCC objects. Using a flat age and Maschberger (2013) initial mass function as priors, we obtain masses of $1.26^{+0.07}_{-0.22}\,M_\odot$ and $1.92^{+0.08}_{-0.08}\,M_\odot$ for Wray 15-788 and HD 98363, respectively. Furthermore, we obtain an age of 11^{+16}_{-7} Myr for the two companions, apparent in Figure 3.3.

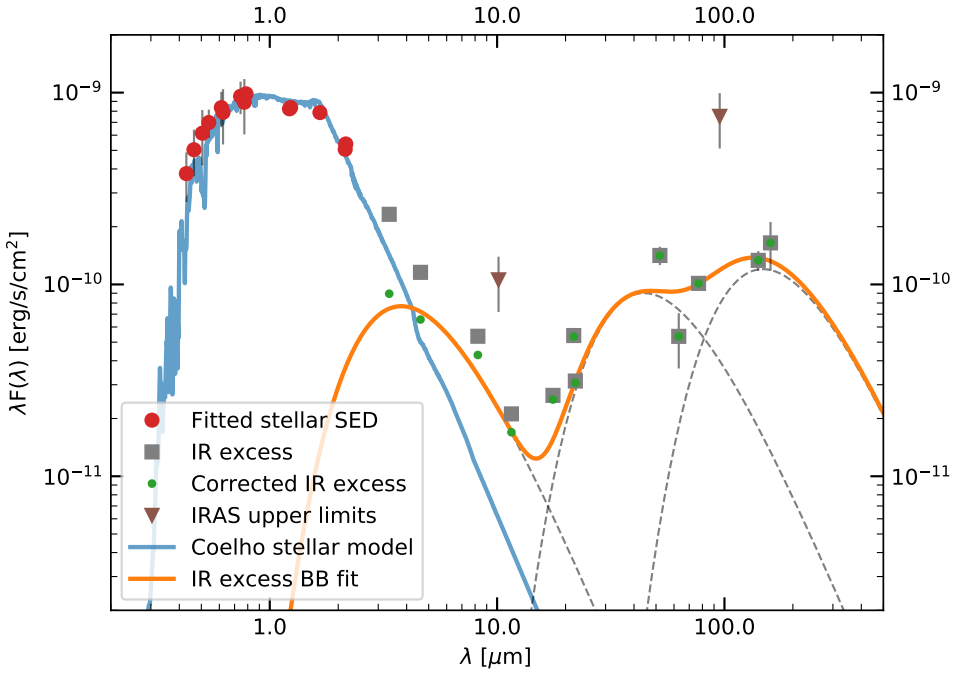

Figure 3.4: De-reddened spectral energy distribution of Wray 15-788. The blue curve shows a Coelho stellar model (Coelho 2014) with $T_{\rm eff} = 4250\,$K, $\log(g) = 4.5$, [Fe/H] =0, [α/Fe]=0, and $A_V = 0.74$ that is fitted to the red data points from the *APASS*, *Gaia*, *2MASS*, and *DENIS* photometry. The gray squares denote flux measurements from *WISE*, *IRAS*, *AKARI/FIS*, and *AKARI/IRC*, and the brown triangles provide upper limits from *IRAS*. Three blackbodies with $T_{\rm dust,1} = 969\,$K, $T_{\rm dust,2} = 83\,$K, and $T_{\rm dust,3} = 25\,$K were simultaneously fitted to the green data points that denote the object's far-infrared excess, corrected for stellar contamination. The individual blackbody functions are indicated by the dashed gray lines, whereas their sum is presented by the solid orange curve.

3.5.2 SED modeling

We obtained the available SED of Wray 15-788 presented in Figure 3.4. It is rather well sampled by photometry from *APASS* (Henden & Munari 2014), *Gaia* (Gaia Collaboration et al. 2018), *2MASS* (Cutri et al. 2012a), and *DENIS* (Epchtein et al. 1997) for wavelengths up to approximately 2 µm; however, we only have a few data points from *WISE* (Cutri et al. 2012b), *IRAS* (Neugebauer et al. 1984), *AKARI/FIS* (Murakami et al. 2007; Kawada et al. 2007), and *AKARI/IRC* (Murakami et al. 2007; Ishihara et al. 2010), and additional upper limits from *IRAS* for wavelengths longer than this. In particular, there is no data available beyond 160 µm.

To evaluate whether the system is a potential gas-rich protoplanetary disk, we aimed to derive the fractional infrared luminosity

$$f = \frac{L_{\rm IR}}{L_*}\,, \tag{3.1}$$

where $L_{\rm IR}$ and L_* denote the bolometric luminosities of the infrared excess and the star, respectively. To get accurate estimates of both bolometric luminosities, we fitted the stellar spectrum and the infrared contribution to the SED due to circumstellar material individually with a suitable model.

Analyzing the SED with VOSA (Bayo et al. 2008) indicates an infrared excess for wavelengths longer than $W1$ ($\lambda_{\rm c}^{W1}$=3.35 µm). Thus, we only used the data points at wavelengths shorter than this to fit the spectrum of the star. For this purpose we applied a Coelho stellar model (Coelho 2014) that depends on effective temperature $T_{\rm eff}$, surface gravity $\log(g)$, and the metallicity parameters [Fe/H] and [α/Fe] of the star. Furthermore, we assumed a total extinction A_V in the range of 0.5 mag ¡ A_V ¡1.5 mag, in agreement with $A_V = 0.88 \pm 0.18$ mag as determined by Pecaut & Mamajek (2016) for Wray 15-788. The χ^2 fit yields a template stellar spectrum with $T_{\rm eff} = 4250$ K, $\log(g) = 4.5$, [Fe/H] = 0, [α/Fe] = 0, and $A_V = 0.74$, which is represented by the blue line in Figure 3.4. These model parameters agree very well with the stellar properties of Wray 15-788 determined by Pecaut & Mamajek (2016) and within the scope of this work as presented in Section 3.5.1. The red points in Figure 3.4 show the fitted photometric data points from *APASS*, *Gaia*, *2MASS*, and *DENIS*, for which a de-reddening according to the best fit stellar model was applied. The gray squares and brown triangles represent the infrared flux of the system and upper limits to it, respectively.

To determine $L_{\rm IR}$ we focused on the excess at wavelengths longer than 2 µm. First, we corrected the available data points for the contamination by stellar flux using the best fit Coelho stellar model that we had found for the star. The corrected data is presented by the green dots in Figure 3.4. To model the infrared SED of circumstellar material around Wray 15-788 we used three individual blackbodies: one to account for a hot, inner component at wavelengths between 2 µm and 10 µm, and two additional blackbodies to characterize the colder, outer parts of the disk. The corrected data was fitted by the sum of these blackbody functions using a Levenberg–Marquardt non-linear least-squares solver (Levenberg 1944; Marquardt 1963) and taking the inverse of each data point's uncertainty as corresponding numerical weight. This yields a best fit result with effective blackbody temperatures of 969 K, 83 K, and 25 K. The individual blackbodies are indicated by the gray dashed lines in Figure 3.4 and their sum is represented by the solid orange curve.

Integrating the stellar model and the fit of the infrared excess over the entire spectral range yields a fractional infrared luminosity of $f \gtrsim 0.27$. Due to the incomplete SED for wavelengths longer than 160 µm this value has to be interpreted as a lower threshold.

3.5.3 Imaging data

Both classical and dual-polarimetric imaging results confirm a resolved, asymmetrical, disk-like structure around Wray 15-788. Consequently, we tried to quantify the reliability of the features detected in Figure 3.1.

Ring A

Ring A of the disk is detected with SPHERE/CI in the H and K_s bands, and the butterfly patterns in Stokes Q and U frames from SPHERE/DPI are a strong confirmation of a scattering, disk-like structure around Wray 15-788. Due to the higher

Table 3.3: Ellipse fit parameters.

Parameter	Explanation
$(\delta x, \delta y)$	Center offset from the star position
a	Semimajor axis
b	Semiminor axis
φ	Position angle of the semimajor axis

signal-to-noise ratio of the disk detection, we restricted our subsequent analyses to the the K_s-band data.

Disk fitting To determine the inclination of the disk, we fitted *ring A* by an elliptical aperture. For this purpose, we used the SPHERE/CI K_s-band result (see Figure 3.1 **b**).

We smoothed the images with a Gaussian kernel having a FWHM of 55 mas, which corresponds to the theoretical size of the instrument's PSF in K_s band. To focus the fit only on the actual signal of the disk, an inner and outer mask were placed around *ring A*. The mask's inner and outer radii were set to 0.″31 and 0.″47, respectively. Afterwards, we split the image in 100 azimuthal slices, centered at the star's position. Within each slice, we determined the pixel of maximum flux. In order to reject background signal we set a lower threshold that corresponds to the median flux at the pixel's separation to the star. Finally, an ellipse was fitted to the remaining pixels of maximum flux by a linear least-squares algorithm according to the implementation of Fitzgibbon et al. (1999). We used a model of an arbitrary, two-dimensional ellipse with five free parameters δx, δy, a, b, φ. The meaning of these parameters is explained in Table 3.3. The disk inclination i can consequently be calculated as

$$i = \arccos\left(\frac{b}{a}\right) . \tag{3.2}$$

To assess an estimate of the uncertainties on our best fit parameters we assumed that the locations of the initial positions used for the fit are uncertain to the FWHM that was applied for smoothing. Therefore, we randomly sampled the initial positions around the previously used values within a box with the size of the FWHM. We used a flat prior in the x and y directions, and repeated the fitting procedure 10^6 times. We obtain symmetric posterior distributions of the ellipse parameters and use the standard deviation as an estimate for the statistical uncertainties of the fit parameters.

The best fit values and corresponding uncertainties of the ellipse parameters are presented in Table 3.4. The fitting yields a disk inclination of $i = 21^\circ \pm 6^\circ$ and a position angle of $\varphi = 76^\circ \pm 16^\circ$. These constraints are rather loose due to the low inclination of the system and because the data points used for the fit sample less than half of an ellipse. Additional high-quality data is required to confine this parameter space.

Disk signal-to-noise ratio estimation As presented in Figure 3.1, the azimuthal brightness profile of *ring A* varies widely. Starting north of the star, the disk flux

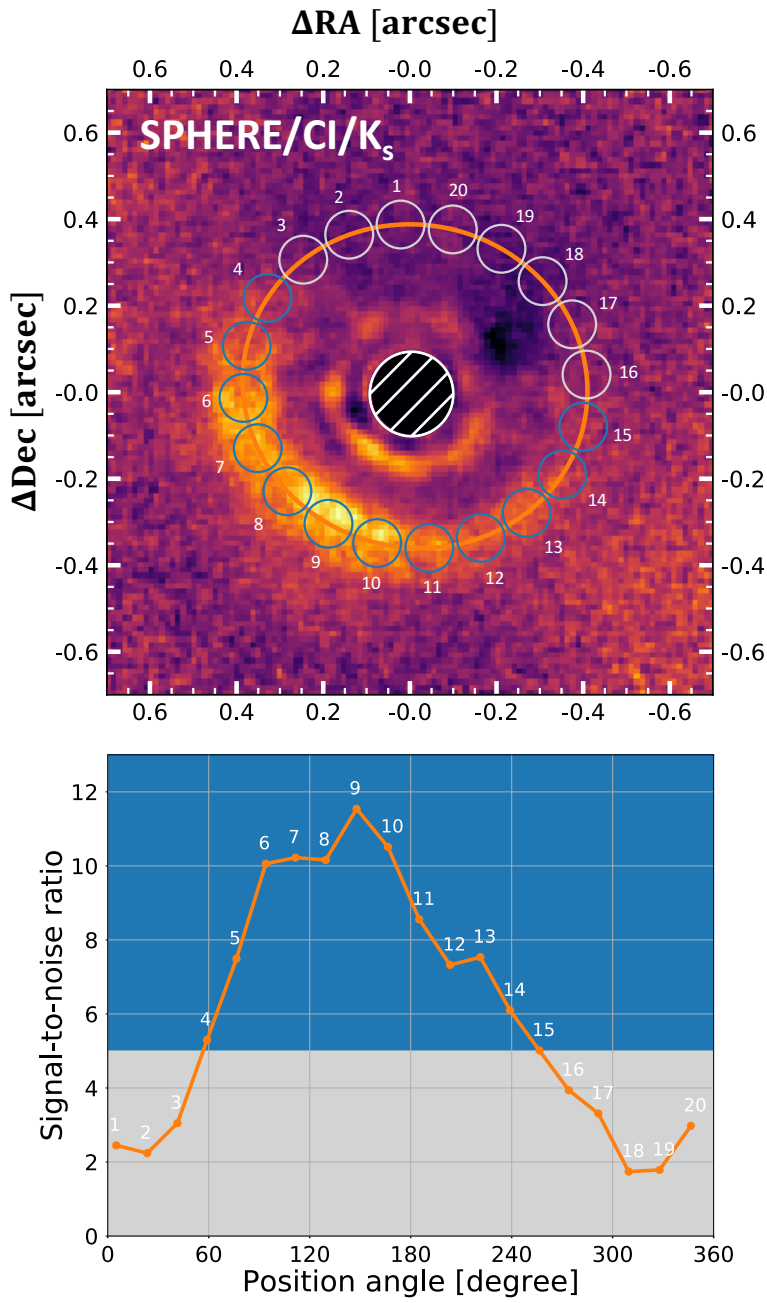

Figure 3.5: Signal-to-noise ratio measurements of the disk flux of Wray 15-788. *Top*: Signal-to-noise ratio measurements in circular apertures around the best fit ellipse (orange line) for the K_s-band data from Section 3.5.3. The blue apertures contain flux of *ring A* according to the applied 5σ criterion, whereas the gray apertures reside within the background dominated regime. *Bottom*: Signal-to-noise ratio within the circular apertures from the top panel, sorted by position angle. The gray and blue areas mark the regimes below and above the 5σ threshold to distinguish background and disk apertures, respectively.

Table 3.4: Best fit parameters of the ellipse fitting.

Parameter	Best fit value
δx [pix][a]	0.96 ± 1.17
δy [pix]	1.12 ± 2.01
a [pix]	32.56 ± 0.81
b [pix]	30.39 ± 2.12
φ [$^\circ$]	76 ± 16
i [$^\circ$]	21 ± 6

Notes. [(a)] To convert pixels to projected separations in mas the results must be multiplied with the pixel scale of the detector, which is 12.265 ± 0.009 mas per pixel in K_s band.

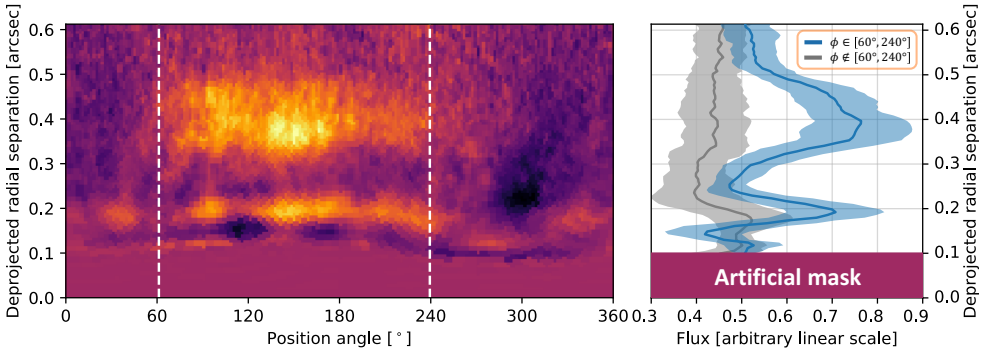

Figure 3.6: Polar projection of the disk around Wray 15-788. *Left panel*: Polar projection of the SPHERE/CI result in K_s band. The image is corrected for the offset and the inclination of the best fit ellipse to *ring A*. The white dashed lines indicate the range of position angles in which we detect scattered light flux from *ring A* with a signal-to-noise ratio higher than 5. *Right panel*: Radial brightness profile of the disk and background noise. The blue curve shows the averaged disk signal for position angles in the range of $60^\circ \leq \phi \leq 240^\circ$ and the gray curve represents the average noise over all remaining position angles. The envelopes indicate the corresponding standard deviations.

increases with increasing position angle ϕ. The maximum intensity of this ring is located southeast of the star. Thereafter, the flux decreases with increasing position angle until the disk signal cannot be distinguished from the background noise.

We aimed to determine a range of position angles in which we have a significant detection of scattered light flux from *ring A*. Therefore, we used the best fit ellipse that we had derived earlier and distributed evenly spaced circular apertures along it, as indicated in Figure 3.5. We measured the mean flux and standard deviation inside each individual circular aperture. The average flux values μ_i provide an estimate of the signal at the position angle of the corresponding aperture. To get an estimate of the background noise, we performed a sigma clipping on the array of aperture fluxes. For the clipping we ran five iterations with no lower threshold and an upper threshold of 1σ to exclude strong contamination by disk flux. After this selection, we calculated the average of the remaining standard deviations for estimating the background noise σ_{bg}. The signal-to noise ratio (S/N) of each individual aperture is calculated as

$$(\mathrm{S/N})_i = \frac{\mu_i}{\sigma_{\mathrm{bg}}}. \tag{3.3}$$

We applied an arbitrary threshold of $(\mathrm{S/N})_i > 5$ for the selection of disk apertures and rejection of background signal. This selection criterion, however, agrees very well with the range of position angles, where the disk signal can still be distinguished from background noise by visual inspection (see Figure 3.1 b).

The bottom panel of Figure 3.5 shows the measured S/N inside each aperture and compares the values to the applied threshold criterion. Data points in the blue regime of the plot refer to apertures above the threshold, and are therefore considered to indicate a detection of scattered light flux from *ring A*. The gray regime, however, represents apertures that are dominated by background noise. This color scheme coincides with the colors chosen for the circular apertures in the top panel of the figure. Considering these blue apertures, we derive a range of $60^\circ \lesssim \phi \lesssim 240^\circ$ in which we are confident at the 5σ level to detect scattered light flux of the disk.

Furthermore, we create an inclination-corrected polar projection of the SPHERE classical imaging results in K_s band as presented in the left panel of Figure 3.6. Averaging over the position angles within the derived range of $60^\circ \lesssim \phi \lesssim 240^\circ$ (white dashed lines) yields the radial brightness profile presented by the blue curve in the right panel of Figure 3.6. The gray curve presents the average over the remaining range of position angles in which we do not detect significant disk signal. From these profiles, it becomes clear that we resolve both the gap and *ring A*. The latter even shows some hints for substructures as the averaged flux does not decrease as steeply in the radially outward direction as it does towards the inward gap. Even beyond deprojected separations of $0\farcs5$ the average flux of the disk signal is significantly higher than the average background noise. This is a strong confirmation for scattering material beyond the sharp edge of *ring A*, which was already implied by the DPI data presented in Figure 3.1 **c** and **d**.

Additionally, the polar deprojection allowed us to estimate physical separations of the disk features that we have detected: *Ring A* has its peak of scattered light intensity at $\sim$56 au, the scattered light flux is lowest inside the gap at $\sim$35 au, and *ring B* has a separation of $\sim$28 au.

Ring B

To quantify the significance of the detected inner substructure from the SPHERE imagery, we investigated the polar projection presented in the left panel of Figure 3.6. Between the two white dashed lines at a deprojected separation of $\sim$0.″2, *ring B* appears to be partly parallel to the resolved *ring A* and even has a similar azimuthal brightness distribution. Therefore, it is possible that we detect parts of an inner substructure with similar scattering properties. In the remaining range of position angles, however, the flux received from *ring B* is significantly smaller and its deprojected radial separation varies strongly. This is an indication for a symmetrical, probably non-astrophysical residual around the coronagraph that gets distorted by the inclination correction that we perform to create Figure 3.6.

To test this hypothesis, we compared our result to data from our reference library, obtained with the same observational setup. These data were reduced analogously to the approach we describe in Section 3.3. For each target we applied RDI in combination with PCA and we fitted 20 components for modeling the stellar PSF. All residuals were averaged individually for both filters and to enhance the comparability to our previous results from Figure 3.1, we applied the same radial scaling and masking of the innermost region. However, we did not perform any de-rotation of the images. Because all data was obtained in pupil stabilized mode, this approach ensures proper alignment of potential instrumental artifacts. These reference images in H and K_s band are presented in Figure 3.7.

We detect some features close to the coronagraph in both reference images. The H-band data shows a rather unstructured speckle pattern similar to the science result in that filter (compare to Figure 3.1 **a**), while the K_s-band reference residuals reveal a faint inner ring at the same projected radial separation of $\sim$170 mas, but *ring B* that we detect around Wray 15-788 is significantly brighter in the southeast than the residuals from the reference library. Northwest of the star, however, the intensity of *ring B* is equal for Wray 15-788 and the reference stars. This is consolidating our claim that we actually detect the scattered light flux of an inner substructure southwest of the star. To quantify this observation, we performed photometry in circular apertures distributed alongside *ring B* as indicated in the top panel of Figure 3.8. We chose a radial separation of $\sim$170 mas to the star and each aperture has a radius of $\sim$25 mas, which corresponds to the measured width of *ring B*. These measurements were performed for both filter combinations and the corresponding reference results. We determine the average flux and standard deviation per aperture and plot these as a function of position angle as presented in the bottom panel of Figure 3.8. In H band no strong differences between the flux around Wray 15-788 and the reference image can be detected; instead, we observe a significant peak in K_s-band. Within a range of position angles of $120^\circ \lesssim \phi \lesssim 240^\circ$ the flux measured in the apertures on *ring B* around Wray 15-788 is greater than the flux from the reference image within the same range of position angles. The determined angular interval lies within the interval where we detect *ring A* with a S/N greater than 5. This strengthens the claim that we actually detect parts of a inner substructure around Wray 15-788. Because we do not spatially resolve these structures, we cannot make an accurate estimate of its inclination.

Even though Figure 3.6 implies the detection of another gap interior to *ring B*, we do not trust this feature, because it is placed very close to the inner working

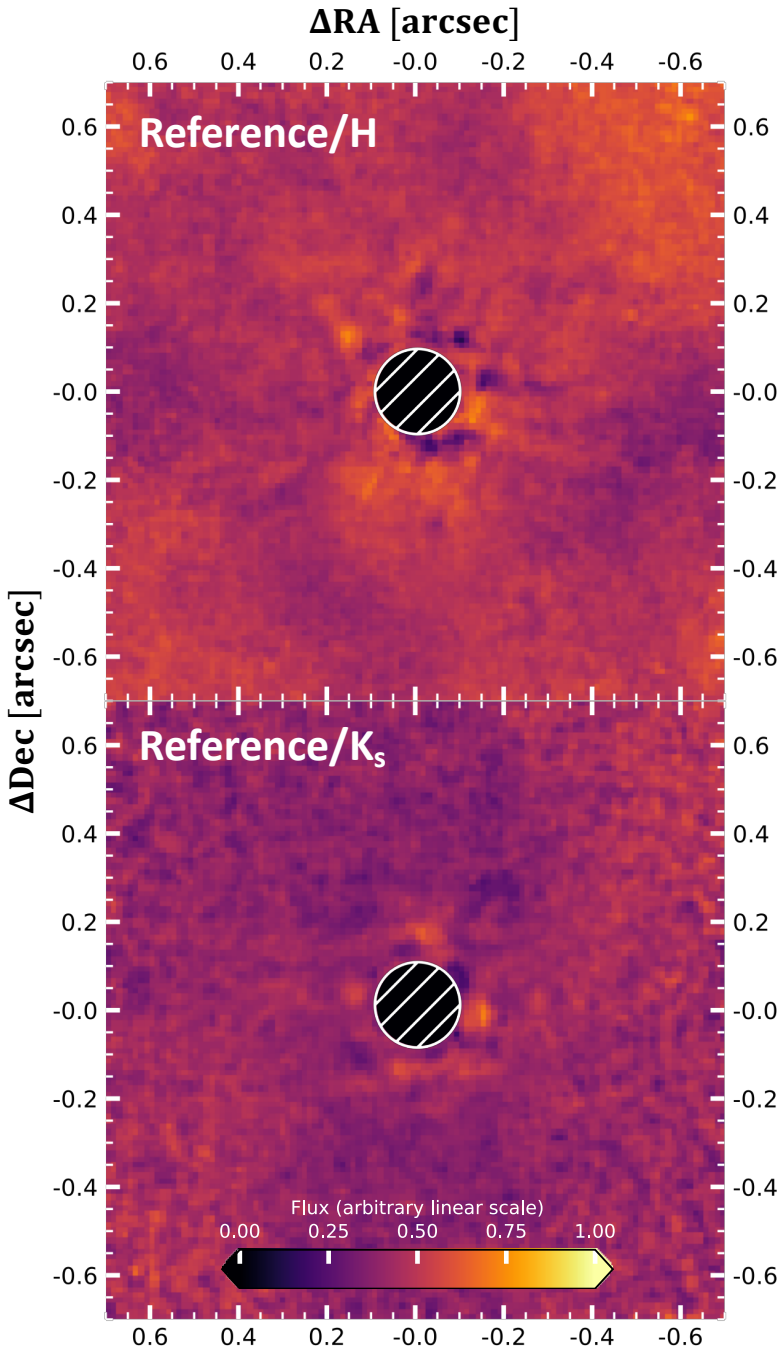

Figure 3.7: Comparison to average images obtained from reduced reference library targets I. Combined data products in H band (*top*) and K_s band (*bottom*).

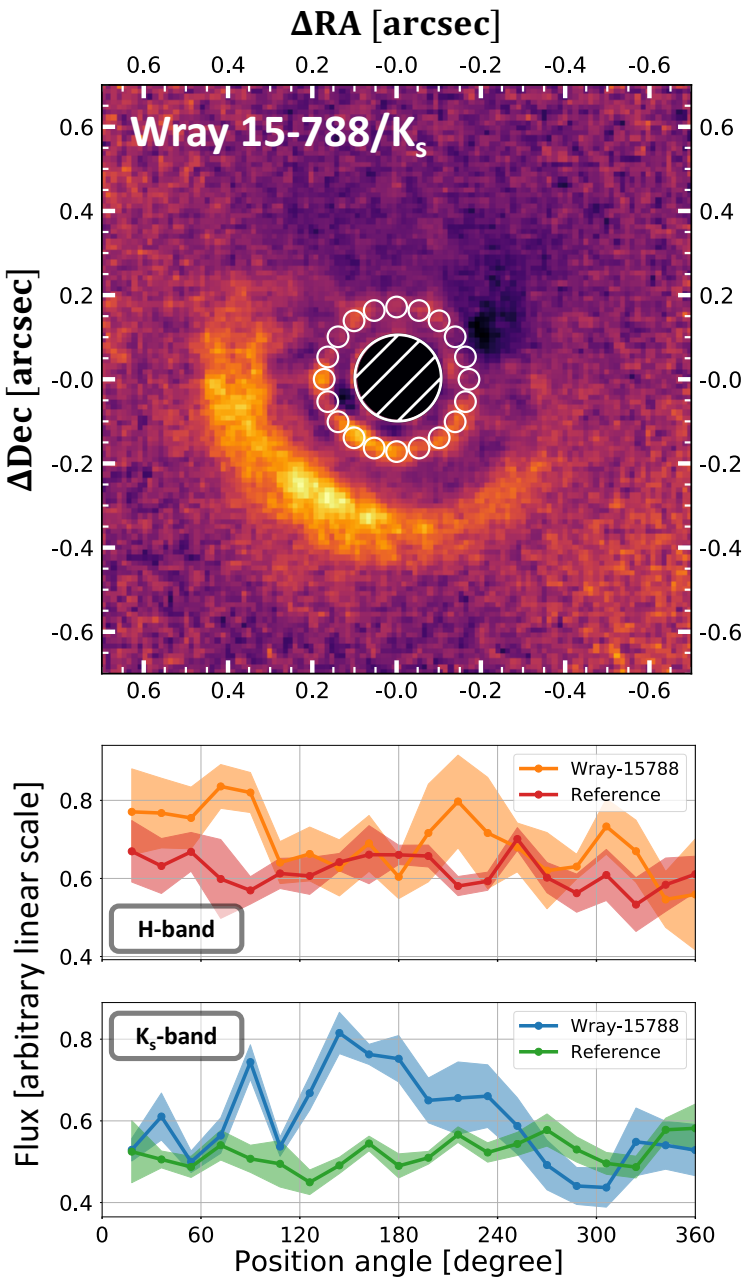

Figure 3.8: Comparison to average images obtained from reduced reference library targets II. *Top*: Locations of the flux apertures that are distributed alongside *ring B* (white circles). *Bottom*: Flux measurements in the apertures from the top panel as a function of position angle. The solid lines correspond to the average flux per aperture. The envelope indicates the corresponding standard deviation.

angle (IWA) of the coronagraph of 100 mas (Wilby et al. in prep.). For this reason we consider it to be an artifact caused by our post-processing strategy.

Gap

For the CI results we detect a significant decrease in flux interior to *ring A*. Depending on the position angle, this radial gradient is steepest at a projected separation of ∼250 mas. We do not recover this drop in scattered light surface brightness from the polarimetric dataset, but there are several factors that can explain this behavior (e.g., non-optimal weather conditions or smoothing with a Gaussian kernel). Furthermore, we can conclude from the polar deprojection of the disk in Figure 3.6 that we are able to spatially resolve this radial drop in intensity. Because we detect this decrease in scattered light flux even in data processed without proper subtraction of the stellar PSF by RDI+PCA (see Appendix 3.B.1), we conclude that it is a real phenomenon. Possible explanations for this very certain dip in surface brightness are either a shadowed region or a physical cavity within the disk.

Detection limits

To derive mass limits of an undetected companion to Wray 15-788, we calculated 5σ contrast curves using the standard routine of the PynPoint package (Stolker et al. 2019). Artificial companions were obtained from the non-coronagraphic flux images that we had taken alongside our science observations. They were scaled to correct for the difference in exposure times and the attenuation of a neutral density filter. The injection was performed for six evenly spaced azimuthal directions and radial separations ranging from $0\farcs15$ to $1''$ with a step size of 20 mas. We present the 5σ detection limits for both CI filters in Figure 3.9. Close to the star, we applied a correction to account for small sample statistics according to Mawet et al. (2014). The conversion from magnitude contrast to a detectable mass threshold was performed using AMES-Cond[3] atmospheric models of 11 Myr old substellar objects (Allard et al. 2001; Baraffe et al. 2003). We indicate the position of the two rings and the gap in blue and gray, respectively. Because the structures are not detected face-on, there are small spatial overlaps between rings and the gap. At the center of the gap we are sensitive to companions as massive as 10 $M_{\rm Jup}$ and 15 $M_{\rm Jup}$ in H and K_s band, respectively. At separations larger than $1''$, we can rule out companions more massive than 4 $M_{\rm Jup}$. We did not apply any correction for reddening and extinction by interstellar matter or disk material in our analysis.

3.6 Discussion

3.6.1 SED analysis

Pecaut & Mamajek (2016) classify Wray 15-788 as a potential host of a protoplanetary disk based on two criteria: (i) the Hα emission as an indicator of accretion from a gas-rich disk and (ii) the presence of an infrared excess in its SED indicative of dust grains. The EW(Hα) threshold for accretion from Barrado y Navascués & Martín (2003) for a K3 star is 4.1 Å; the measured EW(Hα) from Pecaut & Mamajek (2016)

[3]The latest version of these models were obtained from `https://www.phoenix.ens-lyon.fr/Grids/AMES-Cond`

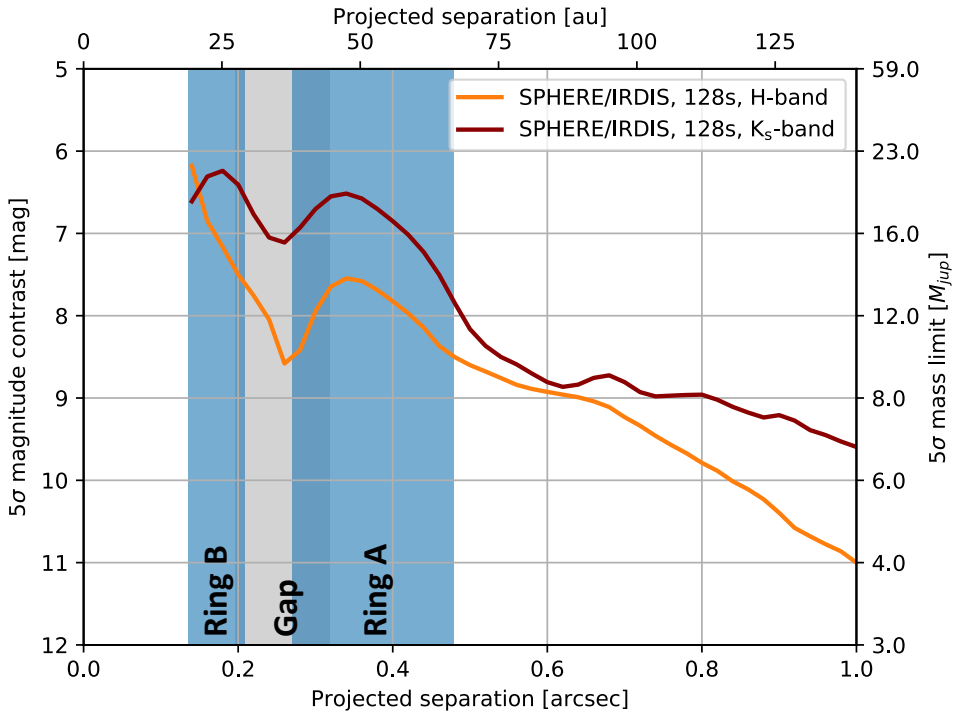

Figure 3.9: Magnitude and mass limits (5σ) up to $1''$ around Wray 15-788. The positions of the two rings and the gap are indicated in blue and gray, respectively. The magnitude contrast was converted to an upper mass limit by AMES-Cond models for 11 Myr old objects. Inside the gap we are sensitive to companions as massive as 10 M_{Jup} (H band) and 15 M_{Jup} (K_s band).

is 10.3 Å. The full width at 10% max of the line is 430 km/s (Pecaut, private communication 2018), which exceeds the empirical criterion for accretion of 270 km/s (White & Basri 2003), and thus is consistent with ongoing accretion. Furthermore, Pecaut & Mamajek (2016) derive the extent of the infrared excess by determining the K_s–$W3$ and K_s–$W4$ colors from *2MASS* (Henden et al. 2012) and *WISE* (Cutri et al. 2012b) magnitudes (see Table 3.1). According to the empirical threshold determined by Luhman & Mamajek (2012), a protoplanetary disk is expected to have excesses exceeding K_s–$W3$ ¿ 1.5 and K_s–$W4$ ¿ 3.2. With K_s–$W3 = 1.76 \pm 0.04$ and K_s–$W4 = 4.3 \pm 0.04$, Wray 15-788 clearly meets these criteria.

The conclusion that Wray 15-788 hosts a protoplanetary disk is clearly supported by the analysis of the object's SED presented in Section 3.5.2. Comparison of the derived fractional infrared luminosity $f \gtrsim 0.27$ with empirical thresholds of Dominik et al. (2003) and Lagrange et al. (2000), strongly imposes that Wray 15-788 harbors a gas-rich protoplanetary disk rather than a debris disk where most of the gas has already dissipated. Usual fractional infrared luminosities of the latter category are in all known cases indeed smaller than 10^{-2}. So, Wray 15-788 exceeds this threshold by more than one order of magnitude.

Furthermore, the fit of the flux at wavelengths longer than 2 µm as presented in Figure 3.4 clearly illustrates that the infrared SED of the system cannot be de-

scribed by a single belt model alone. The excess at near-infrared wavelengths ($2\,\mu m < \lambda < 10\,\mu m$) modeled by a blackbody with an effective temperature of 969 K strongly indicates the presence of a hot, inner component of the disk around the star (e.g., Tilling et al. 2012). Based on the high effective temperature, this inner component must be located close to the dust sublimation radius, and therefore definitely interior to the IWA of the applied coronagraph. Thus, we can rule out with high confidence that *ring B*, as potentiality detected in the imaging data, is equivalent to this hot inner component of the disk. Comparing the SPHERE imagery with the object's SED suggests that *ring A* and *B* are represented by the infrared excess at wavelengths longer than 10 µm.

Around 10 µm there is an apparent dip in the SED that is followed by a positive gradient towards longer wavelengths. These characteristics of the SED impose a physical, dust depleted cavity inside the disk that is enclosed by an extended, colder component of disk material. For these reasons we conclude that Wray 15-788 hosts a protoplanetary disk at a transition stage (Strom et al. 1989; Furlan et al. 2009).

3.6.2 Disk morphology

The disk around Wray15-788 appears highly asymmetric with flux only detected on the southeastern side. Because we can detect this asymmetry in the DPI data as well, and even in the CI data processed without proper subtraction of the stellar PSF, we can rule out that this appearance is an artifact of our post-processing. These alternative reductions are presented in Appendix 3.B. Due to the low inclination of the disk, our observation probes only a limited range of scattering angles, which should not be significantly smaller than $\sim 50^\circ$. In this range of scattering angles the scattering phase functions of typical disks are flat (see Hughes et al. 2018, for an extensive overview). Thus, we should receive scattered light from all azimuthal positions of the disk. This is indeed true even for slightly more inclined debris and gas-rich disks, such as HD 181327 ($i \approx 32^\circ$; e.g., Soummer et al. 2012), PDS 66 ($i \approx 32^\circ$; e.g., Schneider et al. 2014; Wolff et al. 2016), V4046 Sgr ($i \approx 34^\circ$; e.g., Rapson et al. 2015), or HD 100453 ($i \approx 38^\circ$; e.g., Benisty et al. 2017). For PDS 66, Wolff et al. (2016) measure contrasts in scattered light brightness of 2.1 and 1.6 for H and $K1$ band, respectively, between the near and far sides of the disk. Adopting this contrast ratio for Wray 15-788 shows that we should detect the far side of the disk (northwestern part) at a S/N higher than 5, because the near side (southeastern part) is detected at a S/N of approximately 12. As presented in Figure 3.5, this is obviously not the case. Although we cannot fully rule out the possibility that the asymmetry is caused by a larger contrast ratio between the near and far sides of the disk so that the S/N in the northwest drops below our detection ability, it seems unlikely that the apparent morphology is caused by scattering phase function effects.

We can thus conclude that the asymmetry is either caused by a strong azimuthal variation in surface density or scale height of the disk, or that a shadow is cast on *ring A* by unresolved disk structures interior to the structures we detect in our SPHERE observations. Azimuthal variations in surface density are regularly observed at longer (millimeter) wavelengths with ALMA, for example around HD 142527 (Pérez et al. 2014) or V1247 Ori (Kraus et al. 2017). These azimuthal asymmetries are hypothesized to originate from pressure bumps in the gas that trap large, millimeter-sized dust particles in the disk midplane. With SPHERE/IRDIS, however, we trace small, micron-sized dust particles at the disk surface which are much less affected by

particle trapping in the disk (see, e.g., Pinilla et al. 2016). It is thus unlikely that we would observe an extreme asymmetry in scattered light. This effect can indeed be observed, for example for the HD 142527 transition disk where the strong azimuthal asymmetry in large dust grains is not visible in scattered light (Avenhaus et al. 2014, Casassus et al. 2015).

This leaves us with the hypothesis that the northwestern side of the visible disk structure is possibly shadowed by an unresolved part of the disk at separations not probed by the SPHERE observations. This can be the case if the inner part of the disk is misaligned with respect to the visible structures. For example, according to Price et al. (2018), a (sub)stellar companion may cause this misalignment of an inner disk. Such a misalignement can produce a variety of features from sharp, dark lanes, as observed in the disks around HD 142527 (Avenhaus et al. 2014), HD 100453 (Benisty et al. 2017), or HD 135344B (Stolker et al. 2016), to broader wedges, as reported for PDS 66 (Wolff et al. 2016) or TW Hya (Debes et al. 2017). Recently, Benisty et al. (2018) showed scattered light images of the circumstellar disk around HD 143006 in which, analogously to the current case, approximately half of the outer ring is shadowed by inner disk structures and is thus not detected in scattered light. As presented in Section 3.5.2, the analysis of the object's SED strongly indicates the presence of a hot inner component of the disk, just as required for the proposed shadowing scenario. However, the absence of narrow lanes implies that if present, the shadowing must be due to a very small misalignment. To confirm this hypothesis, however, deeper data is required (e.g., a time series that could show the rotation of the shadowed regions around the star).

3.6.3 Comparison with HD 98363

As studied by Chen et al. (2012) and Moór et al. (2017), the primary star HD 98363 hosts a gas-poor debris disk. The detected disk around Wray 15-788, however, rather seems to be a gas-rich protoplanetary disk.

This brings up interesting questions about the evolution of the systems. Assuming both formed at approximately the same time and with similar initial conditions, it is peculiar that the disk around HD 98363 is already more evolved compared to the one around Wray 15-788. As studied by Ribas et al. (2015), there seems to be a trend of decreasing protoplanetary disk lifetimes with increasing mass of the star. In their empirical study, however, they only compare the evolutionary stages of disks around stars above and below $2\,M_{\odot}$. Because both Wray 15-788 and HD 98363 fall into the latter category, their conclusions cannot directly be applied to our sample. Another explanation for the different nature of the disks around the two stars might be the presence of multiple planetary companions around Wray 15-788. These companions can act as traps for dust particles leading to a radial segregation of different sized dust particles as studied by Pinilla et al. (2015). To further explore possible scenarios, additional data on Wray 15-788 is necessary.

3.7 Conclusions

For the first time, we resolved a transition disk around young K3IV star Wray 15-788 in scattered light with both SPHERE/CI and SPHERE/DPI data. SED analysis suggests that the star hosts a hot inner disk located interior to the IWA of the presented

imaging data. An excess at wavelengths longer than 10 µm indicates additional disk material at larger separations from the star. In agreement with this far-infrared SED, we identified an arc at a projected separation of ∼370 mas and a potential inner ring at ∼170 mas in the SPHERE data. These two features are separated by a resolved region of significantly reduced flux. From the outer arc, which is detected above 5σ within a range of position angles of $60^\circ \lesssim \phi \lesssim 240^\circ$, we determined a disk inclination of $i = 21^\circ \pm 6^\circ$ and a position angle of $\varphi = 76^\circ \pm 16^\circ$. Correction for this inclination places the outer ring, the gap, and the inner substructures from the imaging data at approximate physical separations of 56 au, 35 au, and 28 au, respectively.

Although we detected the disk at low inclination, large parts of the the outer ring remain hidden below the background noise. This peculiar appearance may be caused by a shadow that is cast from unresolved inner substructures that are misaligned with respect to the outer material. This scenario is in very good agreement with the SED of Wray 15-788, which shows clear evidence of an inner disk with an effective temperature of 969 K. The misalignment of this inner disk may be caused by an undetected substellar companion. From our 5σ detection thresholds we derive an upper mass limit of $10\,M_{\rm Jup}$ for a companion inside the detected gap. At projected separations larger than $1''$ we can rule out companions more massive than $4\,M_{\rm Jup}$; however, we cannot rule out the possibility that half of the disk is faint in the northwest and that our S/N is not high enough to detect it.

Furthermore, we found Wray 15-788 to be companion to the A2V star HD 98363. Therefore, Wray 15-788 is actually HD 98363 B at a separation of $\sim 50''$ (≈ 6900 au) to the primary. Even though both objects have the same age of 11^{+16}_{-7} Myr, the primary hosts a debris disk where most of the primordial gas has already dissipated, whereas we are confident to detect a less evolved protoplanetary disk around Wray 15-788. Possible undetected companions may be responsible for trapping the dust, leading to the different kind of disks within the binary system of HD 98363 and Wray 15-788.

Further, deeper observations need to be conducted to better understand the disk's peculiar morphology and to find possible planetary-mass companions. To confirm the detection of an inner ring and to constrain the inclination of the disk, a deeper, polarimetric observation is necessary. Additional constraints to the disk's composition, the presence of gas, and the sizes of its dust grains can be set with submillimeter observations making use of the Atacama Large Millimeter/submillimeter Array (ALMA).

3.A Reference star library

To remove both stellar halo and instrumental artifacts in the data on Wray 15-788 obtained with SPHERE in CI mode, we made use of an approach based on RDI in combination with PCA. The stars used for our reference library are all young, K-type star members of LCC subgroup of Sco-Cen. We list the names and corresponding observational parameters in Table 3.5. We observed 26 and 12 reference stars (PI: M. A. Kenworthy) in H and K_s band, respectively. The same observational setup as for the science data on Wray 15-788 was used.

Table 3.5: Observations of reference stars carried out with SPHERE/IRDIS. All data were obtained in classical imaging mode.

Target (2MASS ID)	Observation date (yyyy-mm-dd)	Filter[a]	NDIT×DIT[b] (1×s)	$\langle\omega\rangle$[c] ($''$)	$\langle X\rangle$[d]	$\langle\tau_0\rangle$[e] (ms)
J11272881-3952572	2017-04-18	H	4×32	1.51	1.10	1.40
J11320835-5803199	2017-06-17	H	4×32	0.67	1.47	2.90
J11445217-6438548	2018-05-14	H	4×32	0.73	1.31	2.38
J11445217-6438548	2018-05-14	K_s	4×32	0.78	1.31	2.60
J12065276-5044463	2017-04-02	H	3×32	1.24	1.12	1.50
J12090225-5120410	2018-05-15	H	4×32	0.86	1.12	2.70
J12090225-5120410	2018-05-15	K_s	4×32	0.70	1.12	2.90
J12101065-4855476	2017-04-18	H	4×32	1.71	1.15	1.40
J12123577-5520273	2017-06-17	H	4×32	0.77	2.41	2.80
J12185802-5737191	2017-06-17	H	2×32	0.72	1.22	2.70
J12220430-4841248	2017-04-18	H	3×32	1.82	1.17	1.40
J12234012-5616325	2017-06-17	H	4×32	0.63	1.73	3.45
J12393796-5731406	2017-06-17	H	4×32	0.64	1.77	3.83
J12404664-5211046	2018-04-30	H	4×32	0.75	1.13	7.05
J12404664-5211046	2018-04-30	K_s	4×32	0.87	1.13	7.10
J12454884-5410583	2018-04-30	H	4×32	0.71	1.15	6.93
J12454884-5410583	2018-04-30	K_s	4×32	0.66	1.15	8.98
J12480778-4439167	2017-06-17	H	4×32	0.90	1.34	2.75
J13055087-5304181	2018-07-04	H	4×32	0.82	1.14	1.95
J13055087-5304181	2018-07-04	K_s	4×32	0.93	1.14	2.03
J13064012-5159386	2018-04-30	H	4×32	0.56	1.13	8.15
J13064012-5159386	2018-04-30	K_s	4×32	0.56	1.13	9.88
J13065439-4541313	2018-04-08	H	4×32	0.46	1.09	5.65
J13065439-4541313	2018-04-08	K_s	4×32	0.55	1.09	4.68
J13095880-4527388	2018-05-01	H	4×32	1.08	1.07	2.70
J13095880-4527388	2018-05-01	K_s	4×32	1.03	1.07	2.45
J13103245-4817036	2018-05-01	H	4×32	1.03	1.10	3.30
J13103245-4817036	2018-05-01	K_s	4×32	0.87	1.10	4.40
J13121764-5508258	2018-05-15	H	4×32	0.62	1.16	2.50
J13121764-5508258	2018-05-15	K_s	4×32	0.62	1.16	3.00
J13174687-4456534	2018-05-28	H	4×32	0.70	1.07	4.33
J13174687-4456534	2018-05-28	K_s	4×32	0.67	1.07	4.15
J13233587-4718467	2017-04-02	H	4×32	1.68	1.21	1.40
J13334410-6359345	2017-07-05	H	4×32	1.06	1.53	3.05
J13354082-4818124	2017-04-02	H	4×32	1.06	1.30	2.08
J13380596-4344564	2017-04-02	H	4×32	1.05	1.33	2.40
J13455599-5222255	2018-04-28	H	4×32	0.64	1.13	6.35
J13455599-5222255	2018-04-28	K_s	4×32	0.65	1.13	6.03

Notes. [a] A broadband filter in either H- or K_s-band was applied. [b] NDIT describes the number of dithering positions and DIT is the detector integration time per dithering position. [c] $\langle\omega\rangle$ denotes the average seeing conditions during the observation. [d] $\langle X\rangle$ denotes the average airmass during the observation. [e] $\langle\tau_0\rangle$ denotes the average coherence time during the observation.

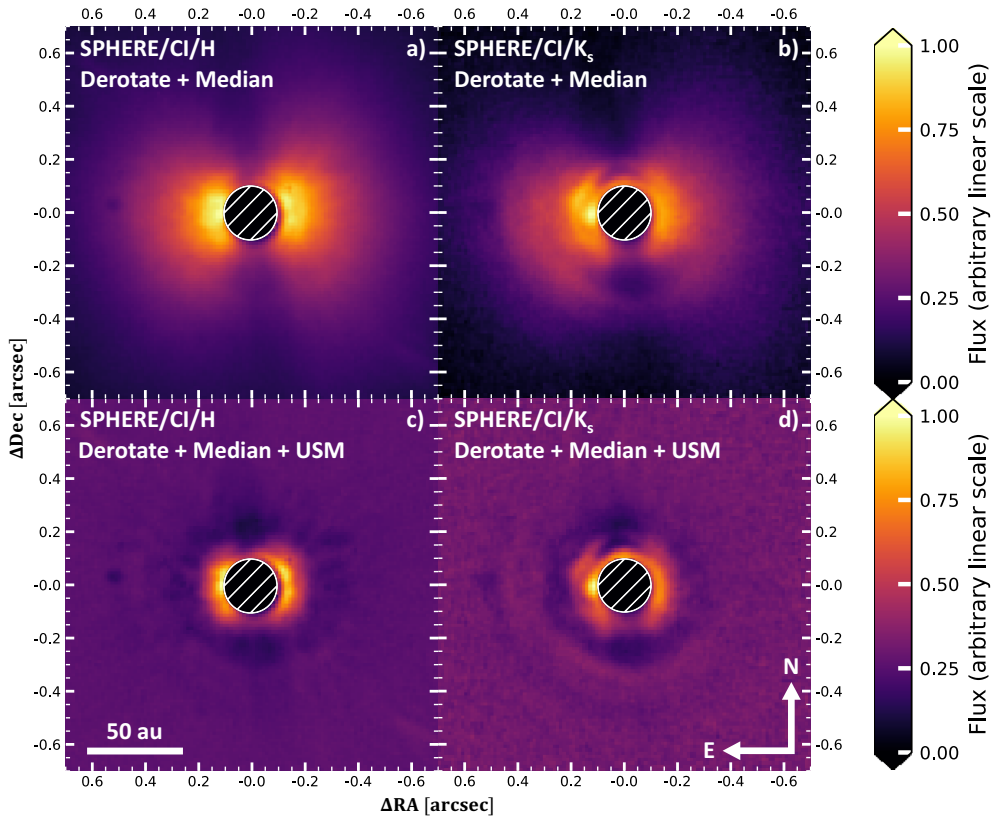

Figure 3.10: Other reductions of SPHERE classical imaging data on Wray 15-788. The images were normalized to the maximum in each frame and arbitrarily, linearly scaled. No subtraction of the stellar point-spread function (PSF) was performed. For all images north is up and east is left. Images **a** and **b** show the de-rotated and median combined image stack of science frames in H and K_s band, respectively. Frames **c** and **d** represent the same image as above, but an additional unsharp mask (USM) is applied (Gaussian kernel with full width at half maximum equal to PSF size).

3.B Other reduction strategies

In addition to the results presented in section 3.4, we apply other data reduction strategies for both SPHERE/CI and SPHERE/DPI data. In this way we can test the stability of the detected disk's appearance and morphology.

3.B.1 CI data

Figure 3.10 shows the individual analysis of the dataset on Wray 15-788. We did not subtract any PSF model, but only de-rotated the images to have north pointing up and east towards the left. The median combined image of the four exposures is presented. In frames **a** and **b** we show this result for H and K_s band, respectively. There is no obvious detection of the disk in H band; instead, the outer ring and the gap are marginally visible in the K_s-band result. Furthermore, the brightness asymmetry

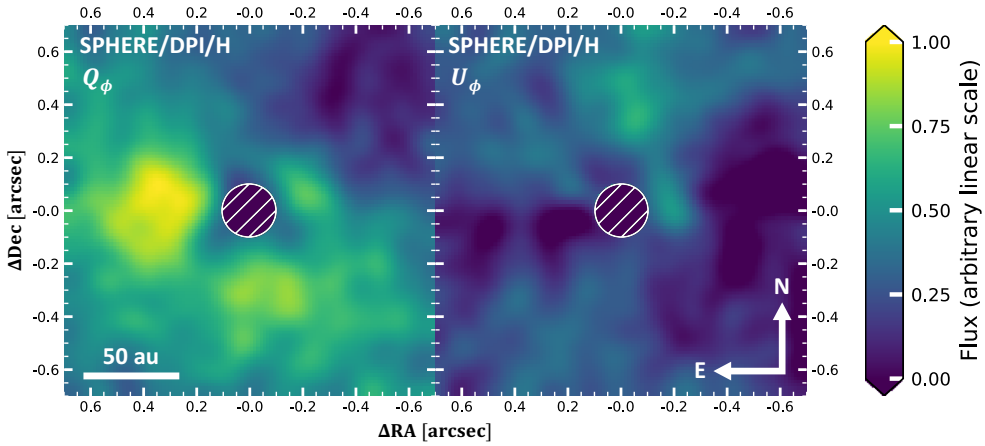

Figure 3.11: Other reductions of SPHERE dual-polarimetric imaging data on Wray 15-788. We present the azimuthal Stokes parameters Q_ϕ and U_ϕ in the left and right panel, respectively. Both images are scaled with r^2 and normalized with respect to the minimum and maximum flux in the Q_ϕ frame. In both frames north is up and east is left.

from northwest towards the southeastern part can be marginally recovered as well. To obtain the results presented in frames **c** and **d** of Figure 3.10, we also applied an unsharp mask to the results from the top panel of the figure. For unsharp masking, we used a Gaussian kernel with a FWHM of the instrumental PSF size of 50 mas and 55 mas in H band and in K_s band, respectively. Due to this high-pass filtering we are able to detect some structures of the outer ring in both filters. Also, the gap of the disk is highlighted.

3.B.2 DPI data

In addition to the linear Stokes parameters Q and U, we derived their azimuthal analogs Q_ϕ and U_ϕ according to Schmid et al. (2006) as

$$Q_\phi = Q\cos(2\phi) + U\sin(2\phi)\,, \tag{3.4}$$
$$U_\phi = Q\cos(2\phi) - U\sin(2\phi)\,, \tag{3.5}$$

where ϕ denotes the position angle as defined before. By construction, $Q_\phi > 0$ refers to a polarization direction azimuthally oriented around the star. This is what we expect from stellar flux being recorded on the detector after a single scattering event at the dust grains of the disk. A negative value of Q_ϕ, however, represents a polarization vector radially aligned to the star. The U_ϕ image can be used as a measure of an upper limit on the noise inside the Q_ϕ frame.

We present the azimuthal Stokes vectors in Figure 3.11. The images are smoothed with a Gaussian kernel having a FWHM of the PSF size and are scaled with the squared radial distance to the image center. Both frames are normalized to the minimum and maximum value of the Q_ϕ image.

In the Q_ϕ image, we detect a clear indication of azimuthally polarized flux southeast of the star. This agrees very well with our other observations from section 3.4. However, due to the non-optimal observing conditions the noise level is rather high,

as seen in the U_ϕ frame. Therefore, the data is not suited to study the morphology of the disk or to quantitatively compare it to the CI results presented in the top panel of Figure 3.1.

Chapter 4

Detection of a wide orbit planetary mass companion to a solar-type Sco-Cen member

The Young Suns Exoplanet Survey (YSES) consists of a homogeneous sample of 70 young, solar-mass stars located in the Lower Centaurus-Crux subgroup of the Scorpius-Centaurus association with an average age of 15 ± 3 Myr. We report the detection of a co-moving companion around the K3IV star YSES 1 (TYC 8998-760-1, 2MASSJ13251211-6456207) that is located at a distance of 94.6 ± 0.3 pc using SPHERE/IRDIS on the VLT. Spectroscopic observations with VLT/X-SHOOTER constrain the mass of the star to $1.00 \pm 0.02\,M_{\odot}$ and an age of 16.7 ± 1.4 Myr. The companion YSES 1b (TYC 8998-760-1 b) is detected at a projected separation of $1.71''$, which implies a projected physical separation of 162 au. Photometric measurements ranging from Y to M band provide a mass estimate of $14 \pm 3\,M_{\rm jup}$ by comparison to BT-Settl and AMES-dusty isochrones, corresponding to a mass ratio of $q = 0.013 \pm 0.003$ with respect to the primary. We rule out additional companions to YSES 1 that are more massive than $12\,M_{\rm jup}$ and farther than 12 au away from the host. Future polarimetric and spectroscopic observations of this system with ground and space based observatories will facilitate testing of formation and evolution scenarios shaping the architecture of the circumstellar environment around this 'young Sun'.

Adapted from
A. J. Bohn, M. A. Kenworthy, C. Ginski, C. F. Manara, M. J. Pecaut, J. de Boer, C. U. Keller, E. E. Mamajek, T. Meshkat, M. Reggiani, K. O. Todorov, and F. Snik
Monthly Notices of the Royal Astronomical Society, **492**, 431–443 (2020)

4.1 Introduction

With the advent of extreme adaptive optics (AO) assisted, high-contrast imaging instruments at the current generation of 8-m class telescopes, the search and characterization of directly imaged extra-solar planets has gained momentum. The large scale guaranteed time observing campaigns that are currently carried out with these instruments such as the Gemini Planet Imager Exoplanet Survey (GPIES; Macintosh et al. 2014) or the SpHere INfrared survey for Exoplanets (SHINE; Chauvin et al. 2017b), can constrain the occurrence rates of gas giant companions in wide orbits (Nielsen et al. 2019). In addition to these ongoing statistical evaluations, both surveys have already produced many high-impact results by new detections of giant companions (e.g. Macintosh et al. 2015; Chauvin et al. 2017b; Keppler et al. 2018) as well as spectral and orbital characterizations of established members among almost twenty directly imaged extra-solar planets (e.g. Galicher et al. 2014; Wang et al. 2016, 2018; Greenbaum et al. 2018; Samland et al. 2017; Chauvin et al. 2018; Müller et al. 2018; Cheetham et al. 2019; Lagrange et al. 2019).

Most of these directly imaged companions, however, are detected around stars that are more massive than the Sun. To obtain a statistically significant estimate on the occurrence rates of giant sub-stellar companions on wide orbits around solar-type stars, we started the Young Suns Exoplanet Survey (YSES; Bohn et al. in prep.). YSES targets a homogeneous sample of 70 young, solar-type stars located in the Lower-Centaurus Crux subgroup of the Scorpius-Centaurus association (Sco-Cen; de Zeeuw et al. 1999). Based on common kinematics and activity signatures, all YSES targets have been confirmed by Pecaut & Mamajek (2016) as members of the LCC; Gaia DR2 parallaxes and proper motions corroborate this membership status (Gaia Collaboration et al. 2018). In addition to the small range of stellar masses, the YSES targets are homogeneous in terms of stellar ages and distances. This enables self-consistent reference star differential imaging (RDI; Smith & Terrile 1984; Lafrenière et al. 2007a) to increase the contrast performance at close separations (Bohn et al. 2021) and minimizes uncertainties on the properties of identified companions due to poorly constrained system ages.

One star within our sample is YSES 1 (TYC 8998-760-1, 2MASSJ13251211-6456207) at a distance of 94.6 ± 0.3 pc (Bailer-Jones et al. 2018; Gaia Collaboration et al. 2018). Based on new observations of the system we revised the main stellar properties (Section 4.4.1) as summarized in Table 4.1.

In Section 4.2 of this article we describe the observations that we carried out on YSES 1 and in Section 4.3 we explain our data reduction strategies. In Section 4.4 we illustrate how we detect a co-moving planetary mass companion around YSES 1 and in Section 4.5 we discuss the derived properties of this companion. The conclusions of the article are presented in Section 4.6.

4.2 Observations

Our observations of the system can be classified by two categories: (i) medium-resolution spectrographic observations of the host with VLT/X-SHOOTER and (ii) high-contrast imaging data collected with VLT/SPHERE and VLT/NACO. Whereas the former data aims for a precise characterization of the host star, the latter ob-

Table 4.1: Stellar properties of YSES 1.

Parameter	Value	Reference(s)
Main identifier	YSES 1	
TYCHO ID	TYC 8998-760-1	(1)
2MASS ID	J13251211-6456207	(2)
Right Ascension (J2000)	13:25:12.13	(3)
Declination (J2000)	-64:56:20.69	(3)
Spectral Type	K3IV	(4,5)
Mass [$M_\odot$]	1.00 ± 0.02	(5)
$T_{\rm eff}$ [K]	4573 ± 10	(5)
$\log(L/L_\odot)$ [dex]	-0.339 ± 0.016	(5)
Age [Myr]	16.7 ± 1.4	(5)
Parallax [mas]	10.540 ± 0.031	(3)
Distance [pc]	94.6 ± 0.3	(6)
Proper motion (RA) [mas / yr]	-40.898 ± 0.045	(3)
Proper motion (Dec) [mas / yr]	-17.788 ± 0.043	(3)
B [mag]	11.94	(7)
V [mag]	11.13	(7)
R [mag]	10.61	(7)
J [mag]	9.07	(2)
H [mag]	8.56	(2)
$K_{\rm s}$ [mag]	8.39	(2)
$W1$ [mag]	8.37	(8)
$W2$ [mag]	8.38	(8)
$W3$ [mag]	8.32	(8)
$W4$ [mag]	> 8.43	(8)

References. (1) Høg et al. (2000); (2) Cutri et al. (2012a); (3) Gaia Collaboration et al. (2018); (4) Pecaut & Mamajek (2016); (5) Section 4.4.1 of this work; (6) Bailer-Jones et al. (2018); (7) Zacharias et al. (2005); (8) Cutri et al. (2012b)

servations facilitate an accurate astrometric and photometric characterization of the companion around YSES 1.

4.2.1 X-SHOOTER

We observed YSES 1 with X-SHOOTER (Vernet et al. 2011) on the night of May 23, 2019, in excellent atmospheric conditions with an average seeing of 0.″54 (PI: A. Bohn; ESO ID: 2103.C-5012(A)). X-SHOOTER was operated in SLT mode providing medium resolution spectra from $300 - 2500$ nm. We chose slit widths of 0.″8, 0.″4, and 0.″4 with corresponding exposure times of 210 s, 120 s, and 3×80 s for UVB, VIS, and NIR[1] subsystems, respectively. Applying two nodding cycles along the slit for background subtraction at NIR wavelengths, yielded total integration times of 840 s, 480 s, and 960 s for the three subsystems. For flux calibration we took additional spectra with a wide slit configuration of $5''$ and exposure times of 15 s, 60 s and 4×15 s for UVB, VIS, and NIR arm, respectively.

4.2.2 SPHERE

The first part of our high-contrast imaging observations were carried out with the SPHERE instrument (Beuzit et al. 2019), mounted at the Naysmith platform of Unit 3 telescope (UT3) at ESO's VLT. SPHERE is assisted by the SAXO extreme AO system (Fusco et al. 2006) to deliver diffraction limited imaging data. We used the infrared dual-band imager and spectrograph (IRDIS; Dohlen et al. 2008) in classical imaging (CI) and dual-band imaging (DBI; Vigan et al. 2010) modes. To block the stellar flux and to enable longer exposure times we used SPHERE's apodized Lyot coronagraph (Soummer 2005). We obtained additional center frames by applying a sinusoidal pattern to the instrument's deformable mirror to determine the position of the star behind the coronagraph. This creates four waffle spots around the star that can be used for precise centering[2]. For photometric calibration we took additional flux images by offsetting the stellar point spread function (PSF) from the coronagraphic mask and used a neutral density filter to avoid saturation of the detector. All observations were carried out in pupil tracking mode to enable post-processing based on RDI within the scope of the survey (Bohn et al. in prep.).

We took short first epoch observations (Night: July 5, 2017; PI: M. Kenworthy; ESO ID: 099.C-0698(A)) applying a broadband filter in J and H band[3]. For second epoch observations (Night: March 17, 2019; PI: A. Bohn; ESO ID: 0103.C-0371(A)), we scheduled a long sequence using the instrument's integral field spectrograph (IFS; Claudi et al. 2008) in extended mode in combination with IRDIS/CI in K_s band. The IFS provides low resolution spectra with a resolving power of $R = 30$ ranging from Y to H band for the innermost field of view ($1.''73 \times 1.''73$) around the star. Due to degrading weather conditions the observation was terminated after 384 s. In this aborted sequence, however, we detected a co-moving companion that was located outside the IFS's field of view. We thus rearranged the observational setup aiming

[1] The individual integration time for the NIR arm was 80 s and each exposure is composed of 3 sub-integrations (NDIT).

[2] See description in the latest version of the SPHERE manual: `https://www.eso.org/sci/facilities/paranal/instruments/sphere/doc.html`

[3] All filter profiles can be found at `https://www.eso.org/sci/facilities/paranal/instruments/sphere/inst/filters.html`

Table 4.2: High-contrast observations of YSES 1.

Observation date (yyyy-mm-dd)	Instrument	Mode[a]	Filter	FWHM[b] (mas)	NEXP×NDIT×DIT[c] (1×1×s)	$\Delta\pi$[d] (°)	$\langle\omega\rangle$[e] (″)	$\langle X\rangle$[f]	$\langle\tau_0\rangle$[g] (ms)
2017-07-05	SPHERE	CI	J	46.7	4×2×32	1.11	1.12	1.54	3.15
2017-07-05	SPHERE	CI	H	52.3	4×1×32	0.50	1.22	1.52	2.90
2019-03-17	SPHERE	CI	K_s	64.2	6×2×32	2.26	1.11	1.31	3.15
2019-03-23	SPHERE	DBI	$Y23$	37.2 / 37.9	4×3×64	3.84	0.41	1.38	9.30
2019-03-23	SPHERE	DBI	$J23$	40.1 / 41.8	4×3×64	3.72	0.40	1.41	10.75
2019-03-23	SPHERE	DBI	$H23$	47.5 / 49.5	4×3×64	3.60	0.43	1.44	10.83
2019-03-23	SPHERE	DBI	$K12$	60.2 / 63.6	4×3×64	3.45	0.53	1.49	8.75
2019-05-18	NACO	CI	L'	125.0	30×600×0.2	22.99	0.88	1.32	2.32
2019-06-03	NACO	CI	M'	131.6	112×900×0.045	50.15	0.78	1.33	3.69

Notes. [a] The applied mode is either classical imaging (CI) with a broadband filter or dual-band imaging (DBI) with two intermediate band filters simultaneously. [b] FWHM denotes the full width at half maximum that we measure from the average of the non-coronagraphic flux images that are collected for each filter. For NACO data these are equivalent to the science exposures of the star. [c] NEXP describes the number of exposures, NDIT is the number of sub-integrations per exposure and DIT is the detector integration time of an individual sub-integration. [d] $\Delta\pi$ denotes the amount of parallactic rotation during the observation. [e] $\langle\omega\rangle$ denotes the average seeing during the observation. [f] $\langle X\rangle$ denotes the average airmass during the observation. [g] $\langle\tau_0\rangle$ denotes the average coherence time during the observation.

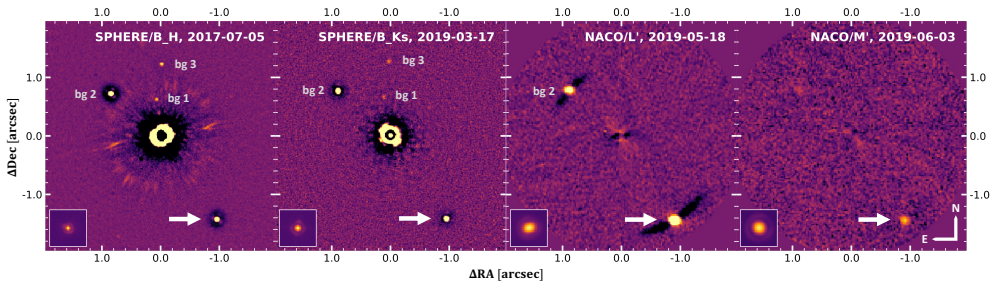

Figure 4.1: Reduced imaging data on YSES 1. We present four different epochs on the target that were collected in H, K_s, L', and M' band, respectively. For the SPHERE data, an unsharp mask is applied; the NACO results are reduced with ADI and the main principal component subtracted. All images are presented with an arbitrary logarithmic color scale to highlight off-axis point sources. Proper motion analysis proves that all objects north of the star are background (bg) contaminants, while the object south-west of YSES 1 (highlighted by the white arrow) is co-moving with its host. This claim is supported by the very red color of this object compared to the other point sources in the field. In the lower left of the each figure we present the reduced non-coronagraphic flux image at the same spatial scale and field orientation. For all images north points up and east towards the left.

for optimal photometric characterization of this companion. These second epoch observations were obtained on the night of March 23, 2019, integrating for 768 s with each of the $Y23$, $J23$, $H23$, and $K12$ DBI filter combinations. A detailed description of the observations, applied filters, and weather conditions is presented in Table 4.2.

4.2.3 NACO

To constrain the thermal infrared spectral energy distribution (SED) of the companion, we took additional L' and M' band data (PI: A. Bohn; ESO ID: 2103.C-5012(B)) with VLT/NACO (Lenzen et al. 2003; Rousset et al. 2003). A summary of the observational parameters is presented in Table 4.2. The instrument was operated in pupil-stabilized imaging mode and the detector readout was performed in cube mode to store each individual sub-integration. As the star is faint at the observed wavelengths, no coronagraph was used. We chose integrations times of 0.2 s and 0.045 s for the observations in L' and M' band, respectively, resulting in 3600 s and 4536 s total time on target. In both configurations the science frames are unsaturated and the individual pixel counts are in the linear regime of the detector, so no additional flux calibration frames were required.

4.3 Data reduction

4.3.1 X-SHOOTER data

The X-SHOOTER data were reduced using the ESO pipeline (Modigliani et al. 2010) v3.2.0 run through the Reflex workflow. The pipeline includes bias and flat-field correction, wavelength calibration, spectrum rectification, flux calibration using a standard star observed in the same night, and spectrum extraction. As described in Section 4.2, the target was observed with a set of wide slits of 5″, which have no slit

losses, and another set of narrower slits providing higher spectral resolution. After the standard pipeline flux calibration, the data obtained with the wider slits shows good agreement in the flux between the three arms. The spectra obtained with the narrower slits show a lower flux than the ones with the wide slits by a factor $\sim$1.7, 2.7, and 2.5 in the three arms, respectively. The narrower slit spectra were adjusted in flux by this ratio in the UVB and NIR arms, and by a wavelength dependent ratio in the VIS arm to match the wide slit spectra. This final flux calibrated spectrum is in good agreement with previous non-simultaneous photometry. The spectra were corrected for telluric absorption using the MOLECFIT tool (Smette et al. 2015; Kausch et al. 2015).

4.3.2 SPHERE data

The SPHERE data were reduced with a custom processing pipeline based on the latest version of the PynPoint package (version 0.8.1; Stolker et al. 2019). This includes flatfielding, sky subtraction, and bad pixel correction by replacing bad pixels with the average value in a 5×5 pixels sized box around the corresponding location. We corrected for the instrumental anamorphic distortion in y direction according to the description in the SPHERE manual. For the data obtained in CI mode, we averaged both detector PSFs per exposure to minimize the effect of bad pixels. Since the companion is not contaminated by stellar flux, we did not perform any advanced PSF subtraction. We simply derotated the individual frames according to the parallactic rotation of the field and the static instrumental offset angle of $135\overset{\circ}{.}99$ required for correct alignment of pupil and Lyot stop, and we used the standard astrometric solution for IRDIS (Maire et al. 2016). This provides a general true north correction of $-1\overset{\circ}{.}75 \pm 0\overset{\circ}{.}08$ and plate scales in the range of 12.283 ± 0.01 mas per pixel and 12.250 ± 0.01 mas per pixel depending on the applied filter.

4.3.3 NACO data

For reduction of the NACO data, we used the same framework as applied for SPHERE including flatfielding, dark subtraction, and bad pixel correction. There is a high readout noise that decreases exponentially throughout the cube, so we removed the first 5 frames of each cube. The background subtraction was performed by an approach based on principal component analysis (PCA) as described in Hunziker et al. (2018) making use of the three distinct dither positions on the detector. We masked a region of $0\overset{''}{.}55$ around the star and fitted 60 principal components to model sky and instrumental background. After subtraction of this model, we aligned the stellar PSFs by applying a cross-correlation in the Fourier domain (Guizar-Sicairos et al. 2008) and centered the aligned images by fitting a two-dimensional Gaussian function to the average of the stack. Frame selection algorithms then reject all frames which deviate by more than 2σ from the median flux within (i) a background annulus with inner and outer radii of $1\overset{''}{.}6$ and $1\overset{''}{.}9$ and (ii) an aperture with the size of the average PSF FWHM, resulting in 10.45% and 10.05% of our L' and M' band data being removed from the subsequent analysis. All frames were derotated according to their parallactic angle and median combined. As we have a sufficient amount of parallactic rotation for both datasets, we tested angular differential imaging (ADI; Marois et al. 2006a) techniques for further analysis steps as described in the following Section. For astrometric calibration of the results we adapted a plate scale of

27.20 ± 0.06 mas per pixel and a true north correction of $0.^{\circ}486 \pm 0.^{\circ}180$ according to Musso Barcucci et al. (2019) and Launhardt et al. (2020).

4.4 Results and analysis

Our first epoch observation with SPHERE reveals 16 off-axis point sources around YSES 1 within the IRDIS field of view ($11.''0 \times 12.''5$). We present the innermost $2''$ $\times 2''$ for several epochs and wavelengths in Figure 4.1. All point sources in the field of view are consistent with background sources at 5σ significance with the exception of the point source south-west of the star (highlighted by the white arrow) which has a proper motion consistent with being a co-moving companion (see analysis in Section 4.4.2). This hypothesis is strongly supported by the very red color of this object in comparison to the other sources in the field of view in Figure 4.1. In order to constrain the properties of this companion, the properties of the host star – especially its age – need to be determined first.

4.4.1 Stellar properties

We used two approaches to determine the stellar properties of the host star. In both cases we assumed an object distance of 94.6 ± 0.3 pc based on the Gaia DR2 parallax (Gaia Collaboration et al. 2018; Bailer-Jones et al. 2018). Our first method was based on the X-SHOOTER spectrum and follows the analysis described in Manara et al. (2013b). We performed a χ^2 fit of the full spectrum using a library of empirical photospheric templates of pre-main sequence stars presented by Manara et al. (2013a, 2017). The best fit is obtained using the template of the K4 star RXJ1538.6-3916 with an extinction of $A_V = 0.0$ mag. This converts to an effective temperature of 4590 ± 50 K and a luminosity of $\log(L/L_{\odot}) = -0.33 \pm 0.10$ dex. Comparison against isochronal tracks of Baraffe et al. (2015) – hereafter B15 – provides a stellar mass of $1.01 \pm 0.08\,M_{\odot}$ and an age of 15 ± 5 Myr. We derived an independent age estimate of the system based on the Lithium-absorption equivalent width of 360 ± 20 mÅ as measured in the X-SHOOTER spectrum. As presented in panel (a) of Figure 4.2, this provides an age estimate of 17 ± 1 Myr when compared to the B15 tracks. The Lithium abundances of the isochrones were converted to Lithium-absorption equivalent widths adopting an initial lithium abundance of 3.28 ± 0.05 (Lodders et al. 2009) and using the tables presented in Soderblom et al. (1993).

An additional check for the stellar properties is by using the photometry. To constrain the stellar properties of YSES 1 we used existing photometry measurements from Tycho-2 (Høg et al. 2000), APASS (Henden & Munari 2014), Gaia (Gaia Collaboration et al. 2018), 2MASS (Cutri et al. 2012a), and WISE (Cutri et al. 2012b) catalogues. Consistent with our previous results, we assumed a negligible extinction and fitted a grid of BT-Settl models (Baraffe et al. 2015) with the abundances from Caffau et al. (2011) to the data. This fit provides an effective temperature of 4573 ± 10 K and a luminosity of $\log(L/L_{\odot}) = -0.339 \pm 0.016$ dex. Comparison to the B15 pre-main sequence isochrones plotted in an Hertzsprung-Russell (HR) diagram as presented in panel (b) of Figure 4.2, results in a stellar mass of $1.00 \pm 0.02\,M_{\odot}$ and a system age of 16.3 ± 1.9 Myr.

The derived stellar properties for both methods are consistent within their uncertainties. In Table 4.1 we cite the more precise mass, temperature and luminosity

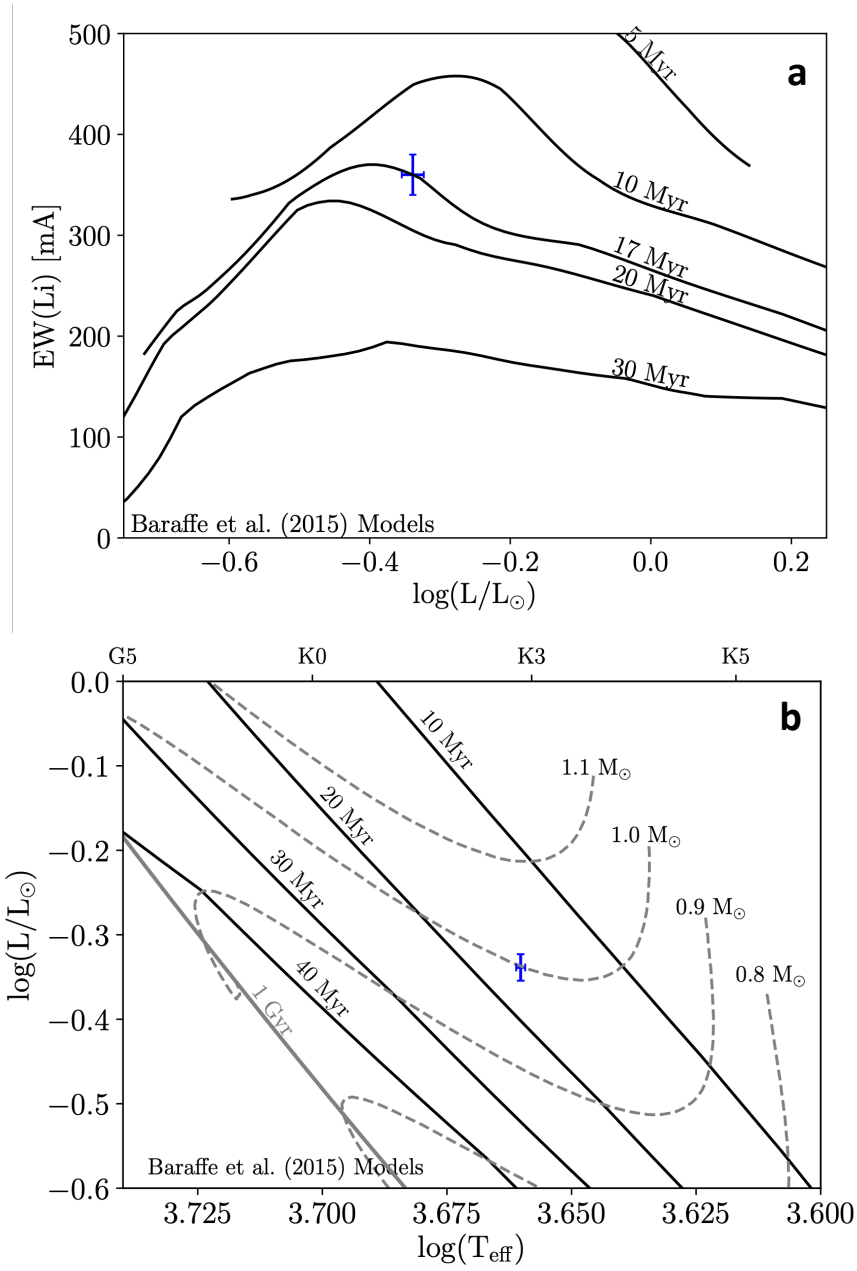

Figure 4.2: Stellar properties of YSES 1. *Panel (a)*: Baraffe et al. (2015) isochrones plotted for the Lithium-absorption equivalent width that we measure in the X-SHOOTER spectrum. *Panel (b)*: Hertzsprung-Russell diagram using the effective temperature that is constrained by fitting BT-Settl models to Tycho-2, APASS, Gaia, 2MASS, and WISE photometry. The isochronal tracks from Baraffe et al. (2015) are used to determine the stellar mass and age.

estimates for YSES 1. As the determined effective temperature suggests a spectral type of K3 instead of K4 when comparing it to the scale presented in Pecaut & Mamajek (2013), we adopt the former for our final classification. For the age of the system, we apply the average of 16.7 ± 1.4 Myr based on our Lithium-absorption and HR diagram analysis. This estimate is in good agreement with the average age of LCC of 15 ± 3 Myr as determined by Pecaut & Mamajek (2016).

To accurately characterize the companion around YSES 1, we determined the magnitudes of the primary in the applied SPHERE and NACO filters. For all wavelengths shorter than 2500 nm (i.e. all SPHERE filters) we measured these fluxes directly from our calibrated X-SHOOTER spectrum. To assess the stellar magnitudes in L' and M' bands, we used the BT-Settl model instead that we have previously fitted to the available photometric data. The results of this analysis are presented in Table 4.4.

4.4.2 Companion properties

We extracted astrometry and magnitude contrasts of the companion for all epochs using the `SimplexMinimizationModule` of PynPoint as described in Stolker et al. (2019). This injects a negative artificial companion into each individual science frame aiming to iteratively minimize the curvature in the final image around the position of the companion using a simplex-based Nelder-Mead algorithm (Nelder & Mead 1965). For the SPHERE data we obtained this template PSF from the non-coronagraphic flux images and for the NACO data this negative artificial companion was modeled from the unsaturated stellar PSF of the science data itself. For the latter case we have an individual template for each science frame that directly accounts for the different PSF shapes due to wind effects or varying AO performance. As the parallactic rotation of the SPHERE datasets is not sufficient to perform ADI-based post-processing strategies, we derotated and median combined the images. For both NACO datasets, we performed ADI+PCA (Amara & Quanz 2012; Soummer et al. 2012) and subtracted one principal component from the images. We then applied a Gaussian filter with a kernel size equivalent to the pixel scale to smooth pixel to pixel variations before evaluating the curvature in the residual image in an aperture with a radius of one FWHM around the companion.

When studying the residuals after the minimization, it became clear that this analysis method is non-optimal for determining the companion's astrometry and photometry in the SPHERE data. Whereas in the NACO data the residuals around the companion agree with the average background noise at the same radial separation, the minimization does not provide similarly smooth results for the SPHERE data. We attribute this to the different shapes of flux and companion PSFs collected under differing atmospheric conditions.

We therefore proceeded with aperture photometry to extract the magnitude contrast of the companion in the SPHERE data and the astrometry was calibrated by a two-dimensional Gaussian fit, instead. We chose circular apertures with a radius equivalent to the average FWHM measured in the flux images, and used identical apertures around the position of the companion that was determined by the Gaussian fit. For an accurate estimate of the background noise at this position, we placed several apertures at the same radial separation from the primary. The average flux within these background apertures was subtracted from the measured flux of the companion. As a sanity check, we applied this aperture photometry approach also

Table 4.3: Astrometry of YSES 1b.

Epoch (yyyy-mm-dd)	Filter	Separation ($''$)	PA ($^\circ$)
2017-07-05	H	1.715 ± 0.004	212.1 ± 0.2
2019-03-17	K_s	1.706 ± 0.008	212.0 ± 0.3
2019-03-23	$Y2$	1.712 ± 0.003	212.0 ± 0.1
2019-03-23	$Y3$	1.714 ± 0.003	212.0 ± 0.1
2019-03-23	$J2$	1.711 ± 0.003	212.0 ± 0.1
2019-03-23	$J3$	1.711 ± 0.003	212.0 ± 0.1
2019-03-23	$H2$	1.711 ± 0.003	212.0 ± 0.1
2019-03-23	$H3$	1.711 ± 0.003	212.0 ± 0.1
2019-03-23	$K1$	1.710 ± 0.003	212.0 ± 0.1
2019-03-23	$K2$	1.709 ± 0.003	212.0 ± 0.1
2019-05-18	L'	1.708 ± 0.005	212.6 ± 0.2
2019-06-03	M'	1.713 ± 0.012	212.4 ± 0.4

to the NACO data. The resulting astrometry and photometry of this analysis is consistent with the previously derived values within their uncertainties.

Astrometric analysis

The astrometry of the companion for several epochs and filters is presented in Table 4.3. As the companion is visible in a single exposure, we extracted its radial separation and position angle directly in the reduced center frames to achieve highest astrometric accuracy. In these frames we can simultaneously fit the position of the companion and the star behind the coronagraph using the four waffle spots. We thus do not include the J band measurements in Table 4.3, as these data were collected without any center frames.

The extracted radial separations and position angles of YSES 1b are mostly consistent within their corresponding uncertainties. Only in the NACO data we measure a systematically larger position angle compared to the SPHERE astrometry. This systematic effect has the same magnitude as the applied true north correction of $0\overset{\circ}{.}486 \pm 0\overset{\circ}{.}180$ adapted from Musso Barcucci et al. (2019). Due to the very consistent SPHERE measurements it is thus likely that this correction factor – which Musso Barcucci et al. (2019) present for reference epochs from 2016 to 2018 – is not valid for our NACO data collected in 2019. This marginal inconsistency, however, does not affect the further companionship assessments of the object.

Analysis towards common proper motion shows that YSES 1b is clearly co-moving with its host. As visualized in Figure 4.3, the relative position of the companion is incompatible with a stationary background object at a significance considerably greater than 5σ. A similar study was performed for the 15 remaining point sources detected around YSES 1. As presented in Appendix 4.A their astrometry is highly consistent with background contaminants, instead.

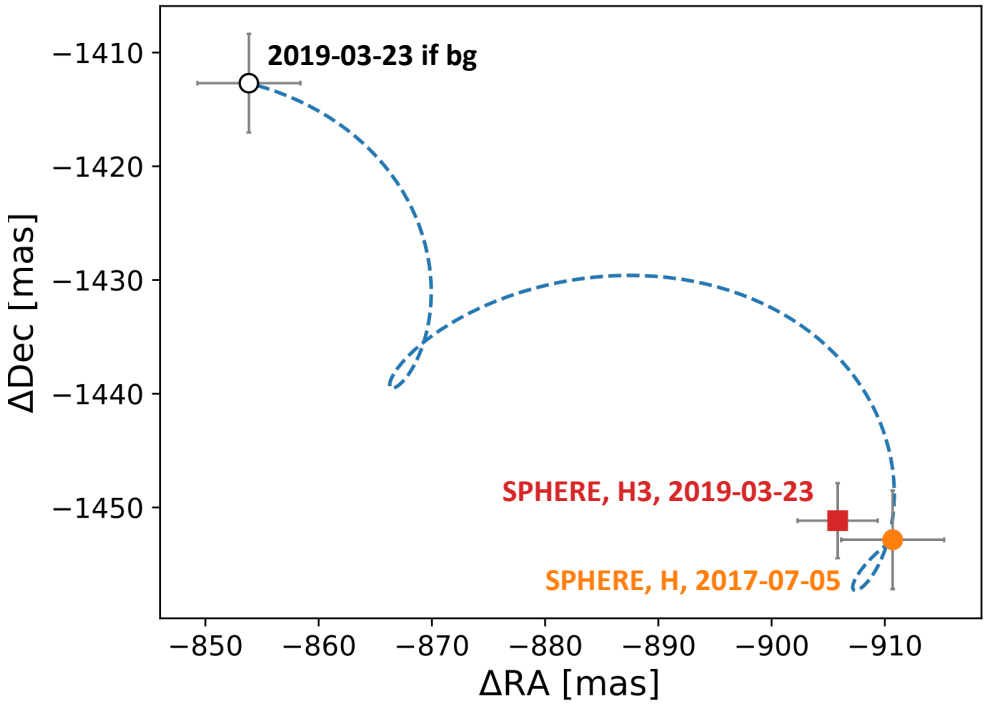

Figure 4.3: Proper motion plot of the companion south-west of YSES 1. The coordinates are relative offsets to the primary and the blue dashed line represents the trajectory of a static background (bg) object.

Photometric analysis

We present the magnitude contrasts of the companion for all filters in Table 4.4. The SPHERE broadband photometry is rather inconsistent with the dual band measurements, especially in H and K_s band. This is mainly caused by the very variable observing conditions during these observations. During the SPHERE H band observations seeing and coherence time between flux and science images degraded from 1.″08 to 1.″22 and 3.2 ms to 2.9 ms, respectively. In K_s band the conditions were even worse as the seeing increased from 0.″74 to 1.″11 and the coherence time dropped from 4.5 ms to 3.5 ms between flux and science exposures. Due to these very unstable atmospheric conditions the AO performance was highly variable during these sequences. Although these fluctuations in flux are included in our statistical uncertainties, the degrading AO performance naturally causes an underestimation of the companion's flux in the science images, leading to an overestimation of the derived magnitude contrast. Without any additional knowledge of the actual AO performance, it is however not straightforward to correct for this effect. In our further analysis we thus focus on the results originating from the SPHERE DBI observations that were obtained in more stable weather conditions (see Table 4.2). These variable weather conditions, however, do not affect the astrometric measurements on YSES 1b that we present in Section 4.4.2. As the companion's position angle and separation is directly extracted from the SPHERE center frames, our accuracy is only limited

Table 4.4: Photometry of YSES 1b and its host.

Filter	Magnitude star (mag)	ΔMag (mag)	Flux companion ($\mathrm{erg\,s^{-1}\,cm^{-2}\,\mu m^{-1}}$)
Y2	9.47	7.56 ± 0.21	$(0.97 \pm 0.19) \times 10^{-12}$
Y3	9.36	7.31 ± 0.16	$(1.13 \pm 0.16) \times 10^{-12}$
J2	9.13	7.14 ± 0.08	$(1.16 \pm 0.08) \times 10^{-12}$
J3	8.92	6.81 ± 0.07	$(1.37 \pm 0.08) \times 10^{-12}$
H2	8.46	6.65 ± 0.08	$(1.04 \pm 0.07) \times 10^{-12}$
H3	8.36	6.42 ± 0.07	$(1.12 \pm 0.07) \times 10^{-12}$
K1	8.31	6.13 ± 0.04	$(0.77 \pm 0.03) \times 10^{-12}$
K2	8.28	5.79 ± 0.04	$(0.88 \pm 0.03) \times 10^{-12}$
J	9.02	6.71 ± 0.38	$(1.59 \pm 0.55) \times 10^{-12}$
H	8.44	7.43 ± 0.38	$(0.48 \pm 0.17) \times 10^{-12}$
K_s	8.29	6.41 ± 0.14	$(0.54 \pm 0.07) \times 10^{-12}$
L′	8.27	5.03 ± 0.08	$(0.26 \pm 0.02) \times 10^{-12}$
M′	8.36	4.72 ± 0.20	$(0.16 \pm 0.03) \times 10^{-12}$

by the precision of the Gaussian fits to the waffle spots and the companion's PSF in these individual frames.

To model the companion's SED we converted the apparent magnitudes to physical fluxes using VOSA (Bayo et al. 2008). These measurements are presented in Table 4.4 and visualized as red squares in Figure 4.4. To characterise the companion, we fitted a grid of BT-Settl models (Allard et al. 2012) to the photometric data by a linear least squares approach. In agreement with our characterization of the primary we assumed a negligible extinction and focused on solar metallicity models. We constrained our input parameter space to effective temperatures between 1200 K and 2500 K and surface gravities in the range of 3.0 dex to 5.5 dex with step sizes of 100 K and 0.5 dex, respectively. The flux for each model was integrated over the photometric band passes of the applied filters and we determined the scaling that minimizes the Euclidean norm of the residual vector. We compared the resulting residuals for all models from the grid and chose the one that yielded the minimum residual as the best fit. This is provided by a model with an effective temperature of 1700 K and a surface gravity of $\log(g) = 3.5$ dex as presented by the blue curve in Figure 4.4.

To evaluate the the impact of the photometric uncertainties on the resulting best fit model, we repeated the fitting procedure 10^5 times, drawing the fitted fluxes from a Gaussian distribution centered around the actual data point and using the uncertainty as standard deviation of the sampling. In Figure 4.4, we show 200 randomly selected best fit models from this Monte Carlo approach as indicated by the grey curves. The posterior distributions for the best-fit parameters are presented in Figure 4.5. This procedure provides estimates of $T_{\mathrm{eff}} = 1727^{+172}_{-127}$ K, $\log(g) = 3.91^{+1.59}_{-0.41}$, $R = 3.0^{+0.2}_{-0.7}\,R_{\mathrm{jup}}$, and $\log(L/L_\odot) = -3.17^{+0.05}_{-0.05}$ dex for the companion's effective temperature, surface gravity, radius, and luminosity, respectively. The uncertainties of these values are determined as the 2.5 and 97.5 percentiles of the corresponding

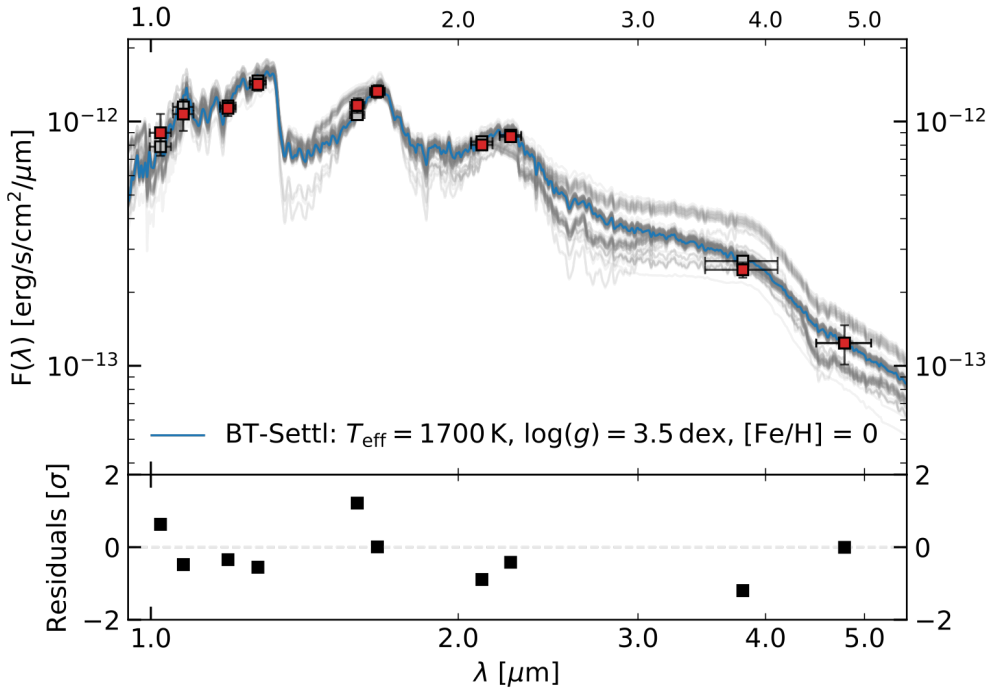

Figure 4.4: Best-fit result to the spectral energy distribution of YSES 1b. *Top panel*: The red squares represent the flux measurements from SPHERE DBI and NACO L' and M' imaging. The blue line represents the best-fit BT-Settl model (Allard et al. 2012) to the data with $T_{\rm eff} = 1700\,$K, $\log(g) = 3.50\,$dex, and solar metallicity and the grey curves represent 200 randomly drawn best-fit models from a Monte Carlo fitting procedure. The flux of the best-fit model, evaluated at the applied filters, is visualized by the grey squares. The uncertainties in wavelength direction represent the widths of the corresponding filters. *Bottom panel*: Residuals of data and best-fit model.

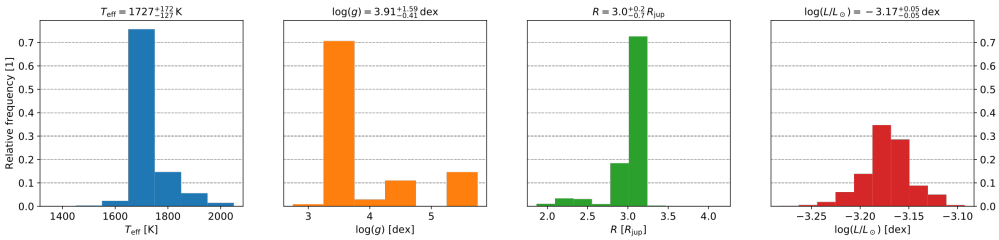

Figure 4.5: Posterior distributions of best-fit parameters. The fit is repeated 10^5 times, drawing each fitted data point from a Gaussian distribution with a standard deviation that is equivalent to the uncertainty.

posterior distributions. Both radius and luminosity depend on the distance to the system, which is constrained by Gaia DR2 astrometry. The radius estimate arises from the scaling factor that needs to be applied to the model and the luminosity is obtained by integrating the resulting model over the entire wavelength range. We note that the predicted radius is larger than the usual value of $\sim 1\,R_{\rm jup}$ that is associated with gas giant planets and brown dwarfs (e.g., Chabrier et al. 2009). This unexpected property is discussed in Section 4.5.1.

Companion mass

To convert the derived photometric properties of the companion to a mass, we used BT-Settl isochrones (Allard et al. 2012) that we evaluated at the derived system age of 16.7±1.4 Myr. As we only fitted photometric data that does not resolve any lines or molecular features, the object's surface gravity is not strongly constrained from our analysis. We base our mass estimate on the better constrained effective temperature and luminosity of the companion instead. Comparing these values to BT-Settl isochrones yields masses of $12.1^{+1.7}_{-1.6}\,M_{\rm jup}$ and $15.7^{+1.0}_{-0.4}\,M_{\rm jup}$ for measured temperature and luminosity, respectively. We obtained similar mass estimates when using the AMES-dusty isochrones (Allard et al. 2001; Chabrier et al. 2000) instead of the the BT-Settl models.

To test these results, we converted the absolute magnitudes of the companion to mass estimates using the BT-Settl isochones evaluated at the corresponding band passes[4]. For the SPHERE data this gives values consistent with our previous mass estimates in the range of $14\,M_{\rm jup}$ to $16\,M_{\rm jup}$. In the thermal infrared we obtain masses of approximately $18\,M_{\rm jup}$ and $25\,M_{\rm jup}$ for the absolute L' and M' magnitudes. This gradient towards longer wavelengths is usual for sub-stellar companions, as these are often redder than the predictions from the models (Janson et al. 2019).

We additionally determined the spectral type of the companion following the analysis demonstrated in Janson et al. (2019). This analysis was performed analogously to the SED fit described before; it was however confined to the SPHERE photometry, because the input models only support this wavelength coverage. Using the empirical spectra for M-L dwarfs of Luhman et al. (2017) we derive a best-fit spectral type of L0. This is equivalent to the spectral type derived for HIP 79098 (AB)b (Janson et al. 2019), which is indeed an ideal object for comparison, as it is also located in Sco-Cen – though in the Upper Scorpius sub-group instead of LCC – with an estimated age of 10 ± 3 Myr. The absolute magnitudes for the companion around YSES 1 are approximately 1.5 mag fainter than the values derived for HIP 79098 (AB)b, supporting the theory that YSES 1b is less massive than the object of this comparison, for which Janson et al. (2019) derive a mass range of $16 - 25\,M_{\rm jup}$.

To verify the derived properties, we compared the color of YSES 1b to that of known sub-stellar companions of similar spectral type. Based on the NIRSPEC Brown Dwarf Spectroscopic Survey (McLean et al. 2003, 2007), the IRTF Spectral library (Rayner et al. 2009; Cushing et al. 2005), and the L and T dwarf data archive (Knapp et al. 2004; Golimowski et al. 2004; Chiu et al. 2006), we compiled a sample of M, L, and T dwarfs. The spectra of these objects were evaluated at the bandpasses of the SPHERE $H2$ and $K1$ filters that we chose for the color analysis. To determine the absolute magnitudes of these field dwarfs we used distance measure-

[4]The models were downloaded from `http://perso.ens-lyon.fr/france.allard/`.

ments provided by Gaia DR2 (Gaia Collaboration et al. 2018; Bailer-Jones et al. 2018), the Brown Dwarf Kinematics Project (Faherty et al. 2009), and the Pan-STARRS1 3π Survey (Best et al. 2018). Targets without any parallax measurement were discarded from the sample. In addition to these field objects, we compared the color of YSES 1b to photometric measurements[5] of confirmed sub-stellar companions (based on data from Cheetham et al. 2019; Janson et al. 2019; Lafrenière et al. 2008; Chauvin et al. 2005; Currie et al. 2013; Bonnefoy et al. 2011; Keppler et al. 2018; Müller et al. 2018; Chauvin et al. 2017a; Zurlo et al. 2016). The results of this analysis are presented in a color-magnitude diagram in Figure 4.6. YSES 1b is located at the transition between late M and early L-type dwarfs, which is in very good agreement with the previously assigned spectral type of L0. As observed for many other young, directly imaged L-type companions, YSES 1b is considerably redder than the sequence of evolved field dwarfs of similar spectral type. This appearance is associated with lower surface gravities of these young objects in comparison to their field counterparts (e.g., Gizis et al. 2015; Janson et al. 2019).

All our analyses, therefore, indicate that the detected companion is sub-stellar in nature. Accounting for the spread among the various methods used to infer the object's mass, we adopt a conservative estimate of $14 \pm 3\,M_{\rm jup}$, yielding a mass ratio of $q = 0.013 \pm 0.003$ between primary and companion. We conclude that YSES 1b is a sub-stellar companion to YSES 1 at the boundary between giant planets and low mass brown dwarfs. Further studies at higher spectral resolution are required to confine this parameter space and to test the planetary nature of the object.

4.4.3 Detection limits

To assess our sensitivity to further companions in the system, we determined the contrast limits for each of the datasets. For the SPHERE data, which do not provide a large amount of parallactic rotation, we did not perform any PSF subtraction. Instead we determined the contrast in the derotated and median combined images by measuring the standard deviation of the residual flux in concentric annuli around the star. To exclude flux of candidate companions that might distort these noise measurements, we performed a 3σ clipping of the flux values inside the annuli, before calculating the standard deviation of the remaining pixels. The annuli have widths of the FWHM at the corresponding wavelength and we evaluate the statistics at radial separations between $0\farcs1$ and $5\farcs5$ with a step size of 50 mas. With these noise terms and the peak flux of the PSF in the corresponding median flux image, we derived the 5σ contrast curves for the SPHERE data, presented in the top panel of Figure 4.7. Due to the poor weather conditions and shorter integration times, we neglect the SPHERE broadband imaging data for this analysis.

The NACO data was analysed with the `ContrastCurveModule` of PynPoint. For both L' and M' data we injected artificial planets into the data and fitted one principal component for PSF subtraction before de-rotation. The planets were injected at six equidistantly distributed angles with radial separations increasing from $0\farcs2$ to $2\farcs0$ and a step size of 100 mas. The magnitude of the injected planets was optimized so that these are detected at 5σ significance applying an additional correction for small sample statistics at small angular separations (Mawet et al. 2014). To obtain the final

[5]For companions that have not been observed with the identical combination of SPHERE $H2$ and $K1$ dual band filters, we based the presented magnitudes and colors on the corresponding broadband photometry, instead.

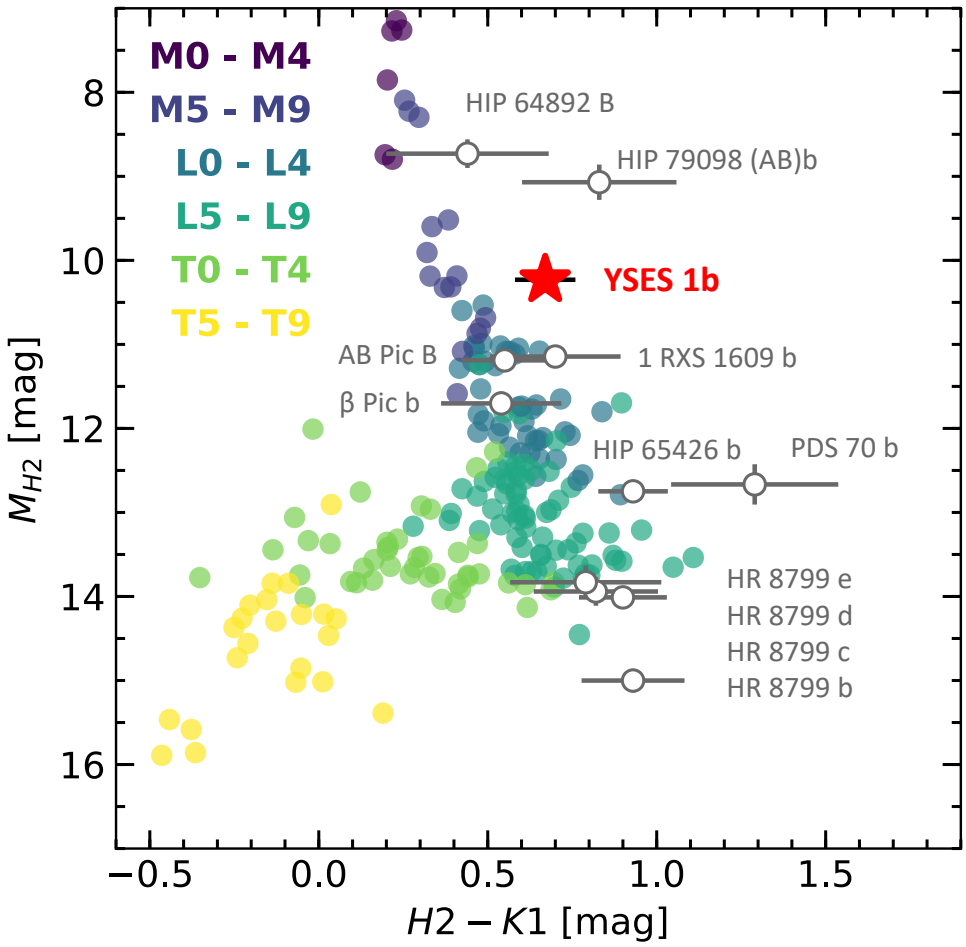

Figure 4.6: Color-magnitude diagram for YSES 1b. The filled circles indicate the color-magnitude evolution of M, L and T field dwarfs, whereas the white markers indicate companions that were directly imaged around young stars. YSES 1b – highlighted by the red star – is located at the transition stage between late M and early L dwarfs and is considerably redder than the corresponding evolved counterparts of similar spectral type.

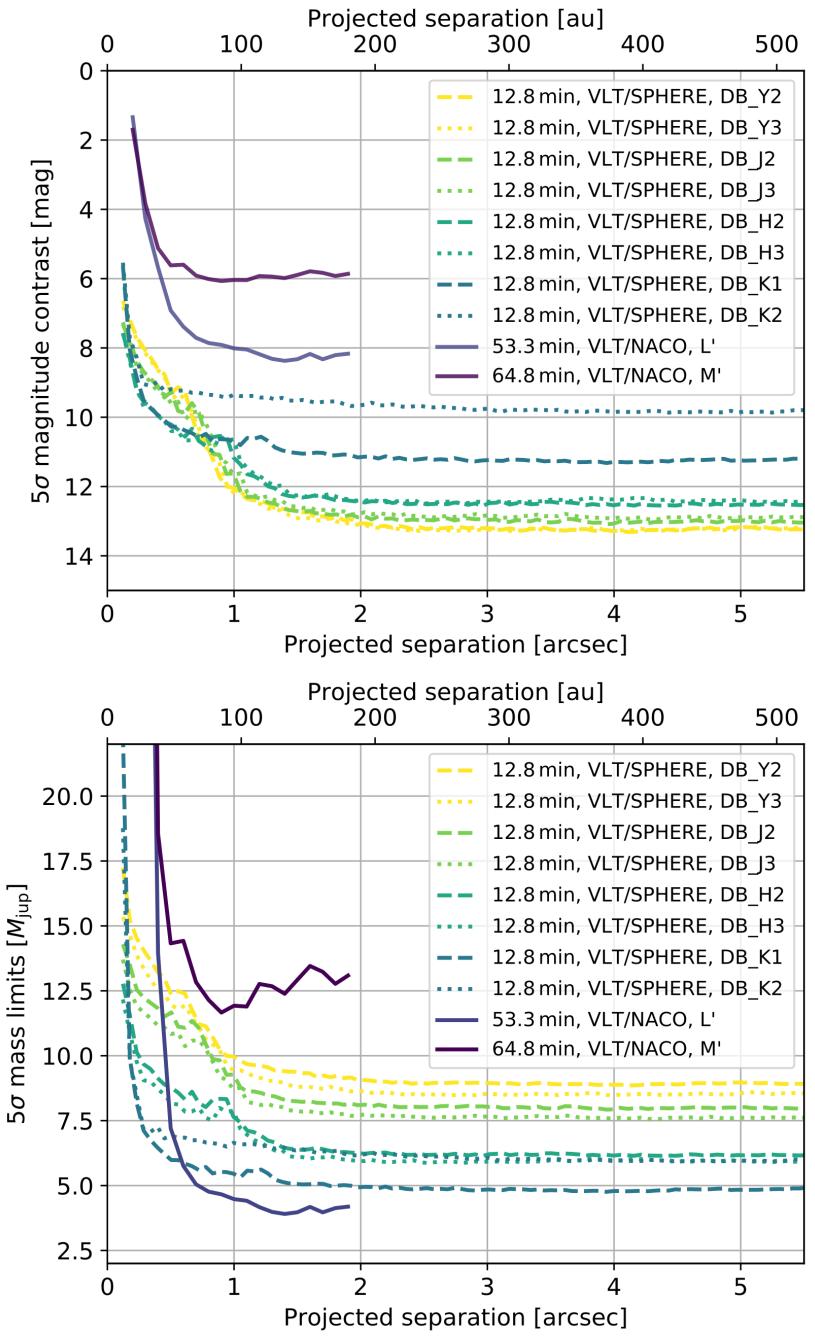

Figure 4.7: Detection limits for SPHERE/DBI and NACO datasets. *Upper panel*: Magnitude contrast as a function of angular separation. *Lower panel*: Mass limits as a function of angular separation. The magnitude contrast is converted to masses via AMES-dusty (Allard et al. 2001; Chabrier et al. 2000) models.

contrast curves as presented in the top panel of Figure 4.7 we averaged the data along the azimuthal dimension.

To convert the derived magnitude contrasts to detectable planetary masses we used the AMES-dusty models (Allard et al. 2001; Chabrier et al. 2000) and evaluated the isochrones at a system age of 16.7 Myr. The SPHERE observations provide the best performance for small angular separations. The $H2$ data rules out any additional companions more massive than $12\,M_{\rm jup}$ for separations larger than 120 mas. This is equivalent to ruling out additional stellar or brown dwarf companions separated farther than 12 au from YSES 1. For angular separations larger than $0\farcs5$ up to approximately $2''$, NACO L' band imaging yields the tightest constraints for additional companions in the system. For separations in the range of $1''$ to $2''$ we can rule out additional companions that are more massive than approximately $4\,M_{\rm jup}$. Farther out, the $H2$ background limit is approximately $5\,M_{\rm jup}$.

Due to deeper integrations in the SPHERE observations collected on the night of March 23, 2019, we detect additional point sources to the 16 objects that were found in the first epoch data from July 5, 2017. The contrasts of these objects are above the derived detection limits. Statistical evaluation based on the first epochs already indicates a very high fraction of background contaminants in the IRDIS field of view around YSES 1; as we do not have additional data to test the proper motion of these new candidate companions we cannot entirely rule out the possibility that these are co-moving with YSES 1.

4.5 Discussion

4.5.1 Companion properties

Whilst effective temperature, surface gravity and luminosity of YSES 1b that we have derived in Section 4.4.2 seem to agree with general properties of similar low-mass companions (e.g., Bonnefoy et al. 2013; Chauvin et al. 2017a) the radius estimate of $R = 3.0^{+0.2}_{-0.7}\,R_{\rm jup}$ is larger than expected from these analogous systems. Empirical data suggest an almost constant radius of approximately $1\,R_{\rm jup}$ for planets in the range of $1\,M_{\rm jup}$ up to stellar masses (e.g., Chabrier et al. 2009) – but these relations are derived from field populations of sub-stellar objects. Their young, gravitationally bound counterparts tend to be inflated instead as these are still contracting (Baraffe et al. 2015). This leads to earlier spectral types, lower surface gravities, and larger radii of young companions in comparison to field objects of the same mass (Asensio-Torres et al. 2019). Furthermore, the constraints that are imposed on the radius are only very weak. The lower bound from the Monte Carlo analysis already implies that smaller radii are not ruled out by our best-fit models. As the masses that are derived from effective temperature, luminosity, individual photometry, and spectral type are all in very good agreement, it is unlikely that the object is not a low-mass companion to YSES 1.

Another possible explanation for the radius anomaly might be given by the scenario that YSES 1b is an unresolved binary with two components of near equal brightness. To test this hypothesis, we repeated the SED modeling, allowing for two objects contributing to the observed photometry. The best-fit result is obtained by binary components with effective temperatures of 1700 K and 1800 K and corresponding radii of $1.6\,R_{\rm jup}$ and $2.1\,R_{\rm jup}$. These results are in better agreement with potential radii of inflated, young sub-stellar objects (Baraffe et al. 2015). As the

PSF of YSES 1b is azimuthally symmetric, this potential binary pair of nearly equal brightness would have to be unresolved in our data. Applying the FWHM for our observations at highest angular resolution in Y2 band (see Table 4.2) implies that a binary companion must have a angular separation smaller than 37.2 mas to be unresolved in the data. At the distance of this system this translates to a physical separation smaller than 3.5 au, which lies well within the Hill sphere of a secondary with a mass of approximately 14 $M_{\rm jup}$. Although this hypothesis might explain the large radius that we find for YSES 1b, additional data of the companion is required to thoroughly test this scenario of binarity. An infra-red medium resolution spectrum of the companion would thus be very valuable for confirming this hypothesis.

4.5.2 Comparison to other directly imaged sub-stellar companions

Although tens of low-mass, sub-stellar companions have been directly imaged, the majority of the host stars are either more massive than the Sun (e.g., Lagrange et al. 2010; Marois et al. 2008; Rameau et al. 2013; Chauvin et al. 2017a; Carson et al. 2013; Janson et al. 2019), are located at the lower end of the stellar mass distribution (e.g., Luhman et al. 2005; Delorme et al. 2013; Artigau et al. 2015; Béjar et al. 2008; Luhman et al. 2009; Rebolo et al. 1998; Kraus et al. 2014; Bowler et al. 2013; Gauza et al. 2015; Naud et al. 2014; Itoh et al. 2005), or of sub-stellar nature themselves (e.g., Todorov et al. 2010; Gelino et al. 2011; Liu et al. 2012). The sample of planetary mass companions that are unambiguously confirmed around solar-type stars is still small, containing PDS 70 b and c (Keppler et al. 2018; Haffert et al. 2019), 2M 2236+4751 b (Bowler et al. 2017), AB Pic b (Chauvin et al. 2005), 1RXS 1609 b (Lafrenière et al. 2008), HN Peg b (Luhman et al. 2007), CT Cha b (Schmidt et al. 2008), HD 203030 b Metchev & Hillenbrand (2006), and GJ 504 b Kuzuhara et al. (2013). This selection was compiled[6] applying conservative mass thresholds in the range of 0.6 $M_{\odot}$ to 1.4 $M_{\odot}$ for host stars to be considered solar type. In Figure 4.8, we visualize the properties of YSES 1b among this sample of directly imaged sub-stellar companions around solar-mass stars. To estimate the semi-major axis of the object, we use the projected separation of 162 au that we derived earlier. This value is thus a lower limit of the actual semi-major axis, as it is the case for many directly imaged companions on wide orbits.

From Figure 4.8 it is apparent that YSES 1 is among the youngest systems with a directly imaged sub-stellar companion around a solar-mass host star. Its mass ratio q is one of the smallest within the sample, only surpassed by HD 203030 b, GJ 504 b, and both planets around PDS 70. The distance at which it is detected is interesting as it is well separated from the host. This facilitates long-term monitoring and spectroscopic characterization of the companion with both ground and space based missions. Near infrared observations towards the photometric variability of the object would help to constrain its rotation period and potential cloud coverage (e.g Yang et al. 2016); additional spectroscopic data will allow to constrain the mass of YSES 1b and to determine molecular abundances in its atmosphere (e.g., Hoeijmakers et al. 2018b).

[6]For this analysis we used the `http://exoplanet.eu/` database (Schneider et al. 2011)

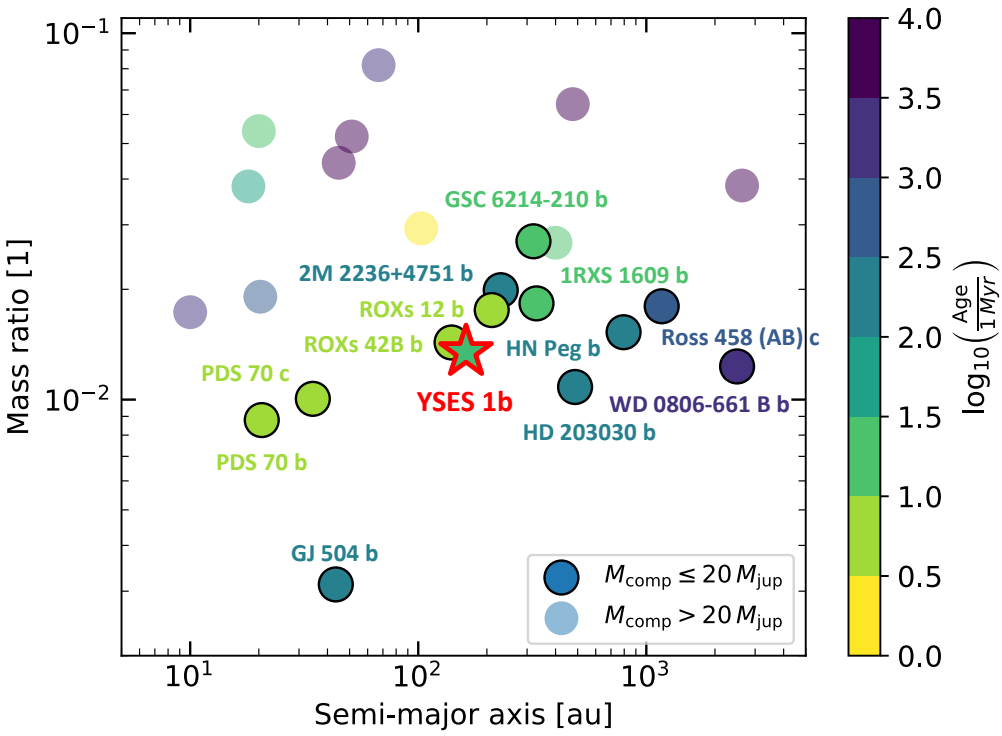

Figure 4.8: Directly imaged sub-stellar companions around solar-mass stars. For the sample selection we chose host stars with masses in the range of $0.6\,M_{\odot}$ and $1.4\,M_{\odot}$ We present the mass ratio q between companion and primary as a function of radial separation to the host. The color indicates the age of the corresponding system.

4.5.3 Formation scenarios

The origin of giant planetary-mass companions at large separations from their host stars is a highly debated topic. Studies by Kroupa (2001) and Chabrier (2003) argue that these objects can form in situ and represent the lower mass limit of multiple star formation via fragmentation processes in the collapsing protostellar cloud. If the companion has formed via the core accretion channel (Pollack et al. 1996; Alibert et al. 2005; Dodson-Robinson et al. 2009; Lambrechts & Johansen 2012) or via gravitational instabilities of the protoplanetary disc (Boss 1997; Rafikov 2005; Durisen et al. 2007; Kratter et al. 2010; Boss 2011) this must have happened closer to the star and after formation, the protoplanet needs to be scattered to the large separation at which it is observed. For regions with a high number density of stars such as Sco-Cen, also capture of another low-mass member of the association needs to be considered as a potential pathway of producing wide orbit companions (e.g., Varvoglis et al. 2012; Goulinski & Ribak 2018). YSES 1b is an ideal candidate to test potential scenarios of (i) formation closer to the host and scattering to its current location, (ii) in-situ formation, and (iii) capture of a low mass Sco-Cen member.

Scenario (i) requires a third component in the system in addition to host star and companion. This component has to be more massive than the companion to scatter

the protoplanet off the system to its current location. Even though the detection limits of our high-contrast observations rule out additional companions that are more massive than 12 $M_{\rm jup}$ for projected separations that are larger than 12 au, this does not rule out a binary companion in a close orbit around YSES 1. To constrain the parameter space of a close, massive companion in the system, reflex motion measurements of the host star are required. This analysis could be performed by combining our high-contrast imaging data with additional radial velocity observations of the system as for instance presented by Boehle et al. (2019). High-precision astrometry provided by future data releases of the Gaia mission (Gaia Collaboration et al. 2016) will be valuable to identifying potential close-in binaries.

One way to discriminate between the three potential formation scenarios is provided by a precise determination of YSES 1b's orbit. This can be achieved by monitoring of the relative astrometric offset between primary and secondary in combination with additional radial velocity measurements. The primary's radial velocity is measured by Gaia as $12.8 \pm 1.4\,\mathrm{kms}^{-1}$ and for the companion – as it is reasonably far separated from the host – this will be accessible by medium resolution spectroscopy. Polarimetric observations of the target and detection of a potential circumstellar or even circumplanetary disc around either of the components would impose further constraints on the orbital dynamics of the system.

With the currently available data it is not possible to unambiguously identify the mechanism that shaped the appearance of the young solar system around YSES 1, but with future observations as outlined in the previous paragraphs, it should be possible to discern which is the most likely scenario that shaped the architecture of this young, solar-like system.

4.6 Conclusion

After the discovery of a shadowed protoplanetary disc at transition stage around Wray 15-788 (Bohn et al. 2019), we report the detection of a first planetary mass companion within the scope of YSES. The companion is found around the K3IV star YSES 1, located in the LCC subgroup of Sco-Cen. Using X-SHOOTER and archival photometric data, we determine a mass of $1.00 \pm 0.02\,M_{\odot}$, an effective temperature of 4573 ± 10 K, a luminosity of $\log(L/L_{\odot}) = -0.339 \pm 0.016$ dex, and an age of 16.7 ± 1.4 Myr for the primary. The companion is detected at a projected separation of approximately 1.″7 which translates to a projected physical separation of 162 au at the distance of the system. Fitting the companion's photometry with BT-Settl models provides an effective temperature of $T_{\rm eff} = 1727^{+172}_{-127}$ K, a surface gravity of $\log(g) = 3.91^{+1.59}_{-0.41}$, a radius of $R = 3.0^{+0.2}_{-0.7}\,R_{\rm jup}$, and a luminosity of $\log(L/L_{\odot}) = -3.17^{+0.05}_{-0.05}$ dex. At the age of the system we adopt a mass estimate of $14 \pm 3\,M_{\rm jup}$, which is equivalent to a mass ratio of $q = 0.013 \pm 0.03$ between primary and secondary. YSES 1b is among the youngest and least massive companions that are directly detected around solar-type stars. The large radius we have derived suggests that the companion is either inflated, or is an unresolved binary in a spatially unresolved orbit with a semi-major axis smaller than 3.5 au. From our high-contrast imaging data we can exclude any additional companions in the system with masses larger than 12 $M_{\rm jup}$ at separations larger than 12 au. This discovery opens many pathways for future ground and space-based characterization of this solar-like environment at a very early stage of its evolution.

4.A Proper motion analysis of other point sources

In our first epoch data, we detect 16 point sources around YSES 1. All these candidate companions are re-detected in our deeper second epoch data from March 23, 2019. We analyzed the relative motion of all these object towards common proper motion with the primary. As presented in Figure 4.9 all candidate companions but YSES 1b have to be considered background contaminants, as their relative positions are not compatible with a bound companion. In most cases our measurements agree well with the predicted trajectory of a static background object. Small deviations from this prediction indicate an intrinsic non-zero proper motion of the object, instead.

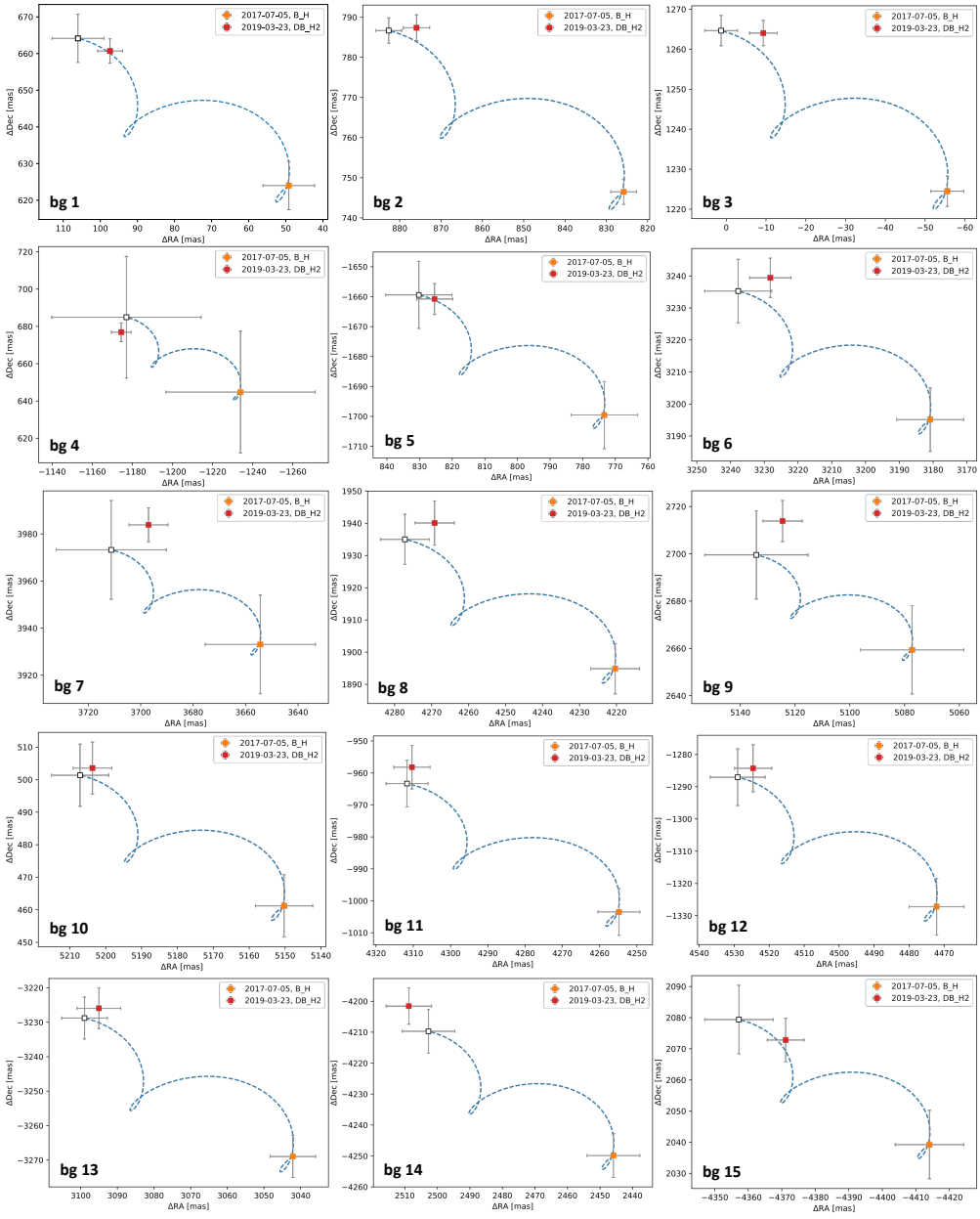

Figure 4.9: Proper motion analysis of other candidate companions around YSES 1. The coordinates are relative offsets to the primary and the blue dashed line represents the trajectory of a static background (bg) object. The white marker along that trajectory indicates the expected relative position of a static background object for the second epoch data.

Chapter 5

Two directly imaged, wide-orbit giant planets around the young, solar analog YSES 1

Even though tens of directly imaged companions have been discovered in the past decades, the number of directly confirmed multiplanet systems is still small. Dynamical analysis of these systems imposes important constraints on formation mechanisms of these wide-orbit companions. As part of the Young Suns Exoplanet Survey (YSES) we report the detection of a second planetary-mass companion around the 17 Myr-old, solar-type star YSES 1 (TYC 8998-760-1) that is located in the Lower Centaurus Crux subgroup of the Scorpius–Centaurus association. The companion has a projected physical separation of 320 au and several individual photometric measurements from 1.1 to 3.8 microns constrain a companion mass of $6 \pm 1\,M_{\rm Jup}$, which is equivalent to a mass ratio of $q = 0.57 \pm 0.10\%$ with respect to the primary. With the previously detected $14 \pm 3\,M_{\rm Jup}$ companion that is orbiting the primary at 160 au, YSES 1 is the first directly imaged multiplanet system that is detected around a young, solar analog. We show that circular orbits are stable, but that mildly eccentric orbits for either/both components ($e > 0.1$) are chaotic on Gyr timescales, implying in-situ formation or a very specific ejection by an unseen third companion. Due to the wide separations of the companions YSES 1 is an excellent system for spectroscopic and photometric follow-up with space-based observatories such as the James Webb Space Telescope.

Adapted from
Alexander J. Bohn, Matthew A. Kenworthy, Christian Ginski, Steven Rieder, Eric E. Mamajek, Tiffany Meshkat, Mark J. Pecaut, Maddalena Reggiani, Jozua de Boer, Christoph U. Keller, Frans Snik, and John Southworth
The Astrophysical Journal Letters, **898**, L16 (2020)

5.1 Introduction

Driven by the installation of extreme adaptive-optics (AO) assisted imagers such as the Gemini Planet Imager (GPI; Macintosh et al. 2014) and the Spectro-Polarimetric High-contrast Exoplanet REsearch (SPHERE; Beuzit et al. 2019) instrument, the number of directly imaged extrasolar planets has been increasing continuously over the past years. Even though several substellar companions have been identified and characterized with these instruments (e.g. Macintosh et al. 2015; Galicher et al. 2014; Chauvin et al. 2017a; Keppler et al. 2018; Müller et al. 2018; Janson et al. 2019; Mesa et al. 2019b), only two systems have been detected so far that show unambiguous evidence for the presence of more than one directly imaged companion: one of these multiplanet systems is HR 8799 – an approximately 30 Myr-old star of spectral class A5 that is harboring four giant planets at orbits with semi-major axes ranging from 15 au to 70 au (Marois et al. 2008, 2010; Wang et al. 2018). The other one is PDS 70, which is a K7-type star at an age of approximately 5.4 Myr that is hosting at least two accreting protoplanets inside the gap of a transitional disk that is surrounding this pre-main-sequence star (Keppler et al. 2018; Müller et al. 2018; Haffert et al. 2019). These multiplanet systems are intriguing laboratories to study dynamical interactions and scattering events between several planetary-mass companions, which is is crucial for understanding the formation and dynamical evolution of planetary systems (e.g. Morbidelli 2018).

To obtain a statistically significant census of wide-orbit companions to solar-type stars we launched the Young Suns Exoplanet Survey (YSES; Bohn et al. 2020a) targeting a homogeneous sample of 70 solar-mass pre-main-sequence stars in the Lower Centaurus Crux subgroup of the Scorpius–Centaurus association (Sco–Cen; de Zeeuw et al. 1999; Pecaut & Mamajek 2016). Within the scope of this survey, we already detected a self-shadowed transition disk around Wray 15-788 (Bohn et al. 2019) as part of a stellar binary with the debris disk host HD 98363 (Chen et al. 2012; Moór et al. 2017; Hom et al. 2020). Most recent was the announcement of a $14 \pm 3\,M_{\mathrm{Jup}}$ companion that is orbiting the solar analog YSES 1 (TYC 8998-760-1, 2MASSJ13251211–6456207) at a projected separation of 160 au (Bohn et al. 2020a). The primary is a 16.7 ± 1.4 Myr-old K3IV star with a mass of $1.00 \pm 0.02\,M_{\odot}$, located at a distance of 94.6 ± 0.3 pc (Bailer-Jones et al. 2018; Gaia Collaboration et al. 2018). We refer to Table 1 of Bohn et al. (2020a) for further information on the host star.

In this article we present new data on this system and report the detection of a second, farther separated, yet lower-mass companion to this young solar analog. Section 5.2 outlines the observations that we acquired on YSES 1 and how the data were reduced. In Section 5.3 we present the results of this analysis and study the properties of this gas giant companion. Our conclusions and further prospects on characterization of this intriguing multiplanet system are presented in Section 5.4.

5.2 Observations and data reduction

On the night of 2020 February 16 we acquired data on YSES 1 with SPHERE/IRDIS (Dohlen et al. 2008) which was operated in dual-polarization imaging mode (DPI; de Boer et al. 2020; van Holstein et al. 2020) with the instrument derotator switched off (PI: A. Bohn). SPHERE is mounted at the Very Large Telescope (VLT) of the European Southern Observatory (ESO) and it is supported by the SAXO extreme AO system

(Fusco et al. 2006) to provide Strehl ratios better than 90 % in H band. Within the scope of this work we only used the total intensity frames of the DPI dataset that are created by adding the left and right sides of the IRDIS detector. Furthermore, we used parts of the observations presented in Bohn et al. (2020a) that were collected with NACO (Lenzen et al. 2003; Rousset et al. 2003) and SPHERE/IRDIS in classical and dual-band imaging modes (Vigan et al. 2010). A detailed description of all observations, applied filters, and weather conditions is presented in Appendix 5.A.

The data reduction was performed as described in Bohn et al. (2020a) using a custom processing pipeline based on version 0.8.1 of PynPoint (Stolker et al. 2019) that includes dark and flat calibration, bad pixel cleaning, and subtraction of the sky and instrument background. A more detailed description is presented in Appendix 5.B.

5.3 Results and analysis

We report the detection of a second, very red companion to YSES 1 which we will refer to as YSES 1c (TYC 8998-760-1 c) henceforth. A compilation of both confirmed companions around this young, solar analog in several SPHERE and NACO bandpasses is presented in Figure 5.1. YSES 1c was detected with a signal-to-noise ratio greater than 5 from $Y3$ to L' band and we did not detect any significant flux at the expected position in the $Y2$ and M' filters. A detailed analysis of the detection significance for the individual bandpasses and nights is presented in Appendix 5.C.

5.3.1 Astrometric analysis

The main confirmation of the companionship was performed by common proper motion analysis. Because both companions are well separated from the PSF halo of the primary and no PSF subtraction was performed, we extracted the astrometry in the final images with a two-dimensional Gaussian fit. In the H band data collected on the night of 2017 July 5, we detected YSES 1c at a separation of $3\farcs369 \pm 0\farcs033$ and a position angle of $221\fdg1 \pm 0\fdg6$ with respect to the primary[1]. From the $K1$ band data – which provides the highest signal-to-noise ratio of the companion on the night of 2019 March 23 – we derived a separation of $3\farcs377 \pm 0\farcs005$ and position angle of $221\fdg2 \pm 0\fdg1$ east of north. For the H band data from 2020 February 16, a separation of $3\farcs380 \pm 0\farcs006$ and a position angle of $221\fdg3 \pm 0\fdg1$ were measured. These measurements imply a projected physical separation of approximately 320 au at the distance of the system.

This proper motion analysis is visualized in Figure 5.2. The primary has a parallax of 10.54 ± 0.03 mas and proper motions of $\mu_\alpha = -40.90 \pm 0.04\,\mathrm{mas\,yr^{-1}}$ and $\mu_\delta = -17.79 \pm 0.04\,\mathrm{mas\,yr^{-1}}$ based on Gaia DR2 (Gaia Collaboration et al. 2018). In the top panel we present the additional astrometric measurement of the confirmed comoving companion YSES 1b which was detected at a separation of $1\farcs708 \pm 0\farcs003$ and a position angle of $212\fdg1 \pm 0\fdg1$ on the night of 2020 February 16. The bottom panel displays the relative astrometric offsets that we measured for background contaminants within the SPHERE/IRDIS field of view. Whereas YSES 1b shows no

[1]The uncertainties of these measurements are much larger than the usual astrometric precision of SPHERE. This is attributed to the nonoptimal AO performance caused by poor atmospheric conditions with an average seeing of $1\farcs22$ and a coherence time of 2.9 ms, resulting in a smeared PSF and limited astrometric accuracy (see Appendix 5.C).

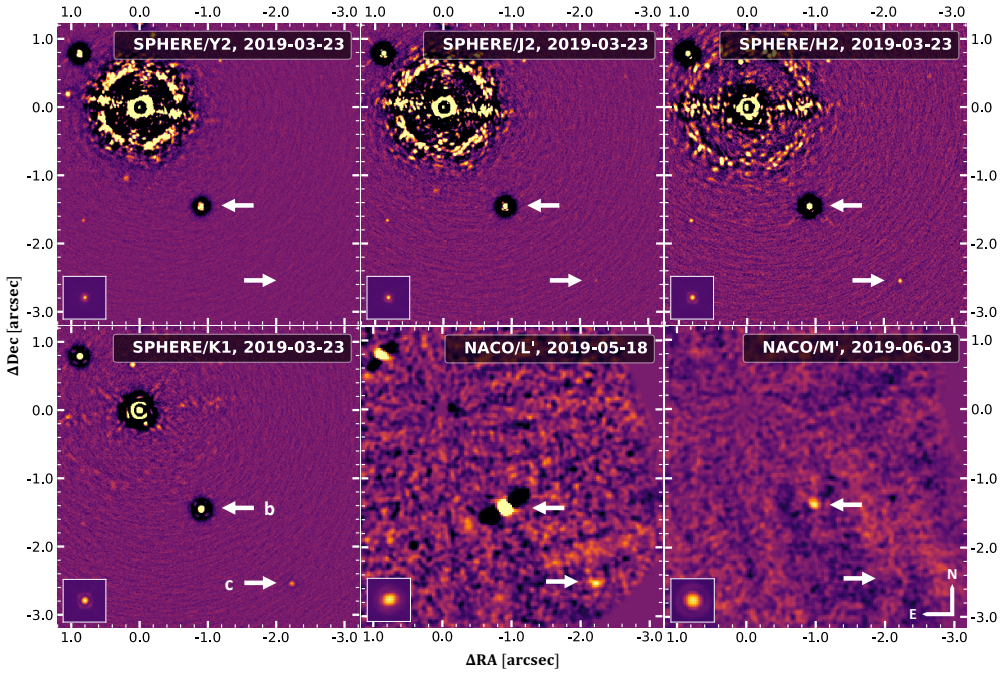

Figure 5.1: Two planetary-mass companions around YSES 1. We present the reduced data for several SPHERE and NACO filters. The white arrows indicate the positions of the confirmed, planetary-mass companions YSES 1b and c as labeled in the bottom left panel. All other objects in the field of view are background contaminants confirmed by proper motion analysis. To highlight off-axis point sources an unsharp mask is applied to the SPHERE data and we smoothed pixel-to-pixel variations in the NACO data with a Gaussian kernel. All images are displayed with an arbitrary logarithmic color scale. The primary is in the upper left of each panel setting the origin of the coordinate system that represents the differential offsets in R.A. and decl. In the lower left of each panel, we present the noncoronagraphic flux PSF as a reference for the corresponding filter. In all frames, north points up and east is to the left.

relative motion with respect to the primary within the measurement uncertainties, the background data points clearly follow the expected trajectory of a static object at infinity as indicated by the blue dashed line. Minor deviations from this trajectory indicate intrinsic nonzero proper motions of these background objects, the measured motions, however, clearly disfavor any bound orbits for these contaminants. As presented in the top right of Figure 5.2, the relative proper motion of YSES 1c is highly inconsistent with the expected movement of a static background object. Analogously to YSES 1b (top left) its relative motion with respect to the primary is close to zero within the provided uncertainties and the measurements from 2017 July 5 and 2019 March 23 are significantly distinct from the cloud of background objects for the corresponding reference epochs. This is in good agreement with the infinitesimal amount of orbital motion expected for an object at a projected physical separation of 320 au.

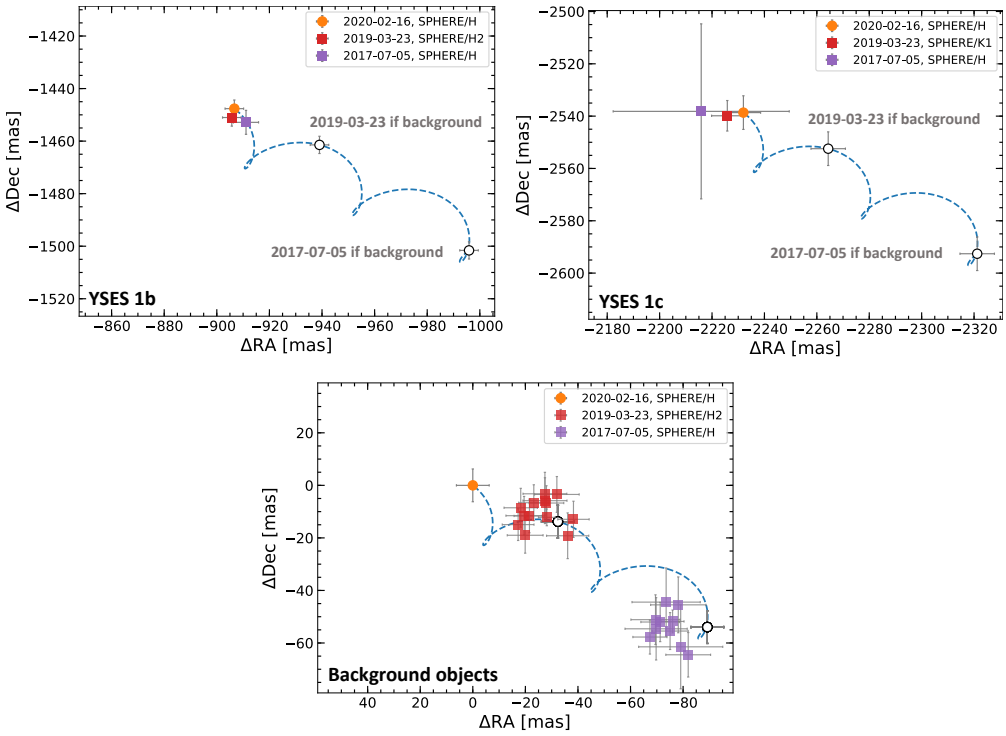

Figure 5.2: Multiepoch proper motion assessments of YSES 1b, c, and confirmed background objects. The colored markers represent the extracted relative astrometry of objects in the SPHERE field of view. The blue, dashed line represents the trajectory of a static background object and the white circles indicate the expected position of such an object, evaluated at the epochs indicated in the top and middle panels. Whereas the origin of the coordinate system is located at the position of the star for the comoving companions (top panels), we present the relative offsets to reference epoch 2020 February 26 for confirmed background objects (bottom panel). The field of view sizes of the plots and the relative positions of the background trajectories are identical for all three panels, so that individual measurements of companions and background objects can be compared amongst each other.

5.3.2 Photometric analysis

To corroborate the companion status and to further characterize YSES 1c, we analyzed its spectral energy distribution (SED) that we constructed from the SPHERE and NACO detections ranging from $Y3$ to L' band. The $Y2$ and M' data imposed additional upper limits to the SED. As described in Bohn et al. (2020a) we extracted the companion flux in the SPHERE filters by aperture photometry, choosing an aperture size equivalent to the PSF FWHM of the corresponding filter. The magnitude contrast with respect to the primary is evaluated using the noncoronagraphic flux images that were acquired alongside the observations. As we performed a PCA-based PSF subtraction for the reduction of the NACO L' data, we extracted the magnitude of the companion by injection of negative artificial companions that were generated from the unsaturated stellar PSF in each individual frame. This analysis was performed with the `SimplexMinimizationModule` of PynPoint that is iteratively minimizing the

Table 5.1: Photometry of YSES 1c and Its Host.

Filter	Magnitude star (mag)	ΔMag (mag)	Flux companion ($\mathrm{erg\,s^{-1}\,cm^{-2}\,\mu m^{-1}}$)
Y2	9.47	> 13.22	$< 0.49 \times 10^{-14}$
Y3	9.36	13.01 ± 0.31	$(0.56 \pm 0.16) \times 10^{-14}$
J2	9.13	12.68 ± 0.22	$(0.69 \pm 0.14) \times 10^{-14}$
J3	8.92	12.25 ± 0.15	$(0.95 \pm 0.13) \times 10^{-14}$
H2	8.46	11.32 ± 0.08	$(1.57 \pm 0.11) \times 10^{-14}$
H	8.44	11.25 ± 0.23	$(1.62 \pm 0.34) \times 10^{-14}$
H3	8.36	10.96 ± 0.06	$(2.04 \pm 0.12) \times 10^{-14}$
K1	8.31	10.03 ± 0.04	$(2.21 \pm 0.09) \times 10^{-14}$
K2	8.28	9.57 ± 0.09	$(2.67 \pm 0.51) \times 10^{-14}$
L′	8.27	8.02 ± 0.21	$(1.58 \pm 0.30) \times 10^{-14}$
M′	8.36	> 4.45	$< 15.83 \times 10^{-14}$

Notes. We present 5σ upper limits of the companion flux in the $Y2$ and M' bands. The broadband H data is reported for the night of 2020 February 16, which is superior to the data collected on 2017 July 5 due to the longer integration time and better weather conditions.

absolute value norm within a circular aperture around the estimated position of the companion (Wertz et al. 2017) using a simplex-based Nelder–Mead optimization algorithm (Nelder & Mead 1965). The upper limits for $Y3$ and M' bands were calculated as the 5σ detection limits at the position of the companion. The extracted flux values are presented in Table 5.1 and visualized in Figure 5.3.

To assess the planetary parameters of YSES 1c we fitted the photometric data points with a grid of BT-Settl models (Allard et al. 2012) that we evaluated in the corresponding bandpasses. We restricted this analysis to models with effective temperatures from 500 K to 2000 K and surface gravities ranging from 3.5 dex to 5.5 dex with grid spacings of 100 K and 0.5 dex, respectively. In accordance with Sco–Cen membership, only models with solar metallicity were considered for this analysis. Furthermore, we assumed a negligible extinction in agreement with SED modeling of the primary as described in Bohn et al. (2020a). To facilitate model evaluation at intermediate temperatures and surface gravities we linearly interpolated the original data grid.

The planetary properties were inferred by a Bayesian parameter study using the affine-invariant Markov chain Monte Carlo (MCMC) ensemble sampler implemented in the `emcee` python module (Foreman-Mackey et al. 2013). The fitted parameters were the companion's effective temperature T_{eff}, surface gravity $\log(g)$, and radius R. Due to the negligible uncertainties in system parallax, we set the distance to a fixed value of 94.6 pc. The planet luminosity for any realization of T_{eff}, $\log(g)$, and R was inferred from the integrated flux of the corresponding BT-Settl model, considering the previously fixed system distance. Our MCMC implementation used uniform priors for each of the input parameters, sampling T_{eff} and $\log(g)$ over the full range of interpolated BT-Settl models and allowing for planet radii between $0.5\,R_{\mathrm{Jup}}$ and

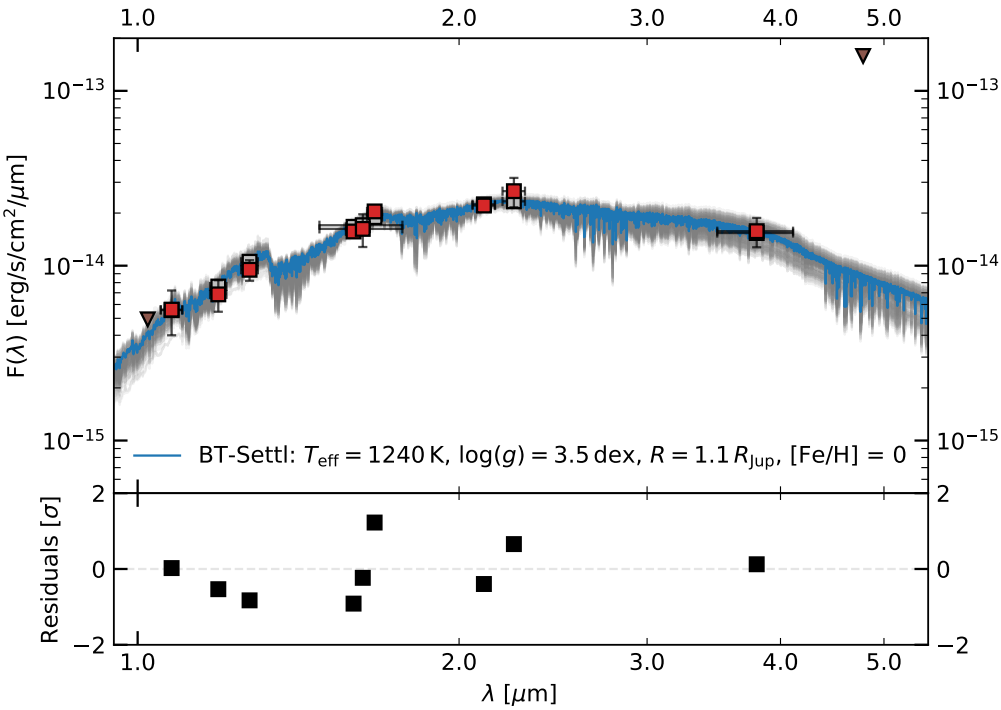

Figure 5.3: SED of YSES 1. The red squares indicate the photometric measurements we extracted from SPHERE and NACO data and the brown triangles are 5σ upper limits for bandpasses with a nondetection of the companion. The blue line represents the median of the posterior distributions from our MCMC fitting routine and the gray squares indicate the evaluation of this model in the SPHERE and NACO bandpasses. We show 100 randomly drawn models from our MCMC posterior distribution (gray curves) and in the bottom panel the residuals of the posterior-median model and the measured photometry are plotted.

$5\,R_{\rm Jup}$. We used a Gaussian likelihood function for the measured photometry of the companion and additionally required that the likelihood decreases to zero in case the flux in Y or M' bands exceeds the corresponding $5\,\sigma$ limits. We set up an MCMC sampler with 100 walkers and 10,000 steps each for the SED fit of the companion. Based on the derived autocorrelation times of approximately 100 iterations, we discarded the first 500 steps of the chains as burn-in phase and continued using only every twentieth step of the remaining data, which resulted in 47,500 individual posterior samples.

The SED of YSES 1c and resulting models from our MCMC fitting procedure are presented in Figure 5.3. From this analysis we derived estimates of $T_{\rm eff} = 1240^{+160}_{-170}$ K, $\log(g) = 3.51^{+0.02}_{-0.01}$ dex, $R_{\rm p} = 1.1^{+0.6}_{-0.3}\,R_{\rm Jup}$, and $\log(L/L_\odot) = -4.65^{+0.05}_{-0.08}$ as the 95 % confidence intervals around the median of the posterior distributions[2]. The uncertainties derived for the surface gravity appear underestimated, as photometric measurements alone cannot precisely constrain this parameter. We thus adopted the spacing of the original model grid of 0.5 dex as the reported uncertainty

[2]The full posterior distributions of this analysis and the correlations between the fitted parameters are presented in Appendix 5.D.

in the planet's surface gravity henceforth. Future measurements at higher spectral resolution are required though to place tighter constraints to this parameter.

To convert the derived properties to a planetary mass, we evaluated effective temperature and luminosity individually with BT-Settl isochrones at the system age of 16.7 ± 1.4 Myr. This yielded masses of $7.0^{+2.1}_{-1.9}\,M_{\rm Jup}$ and $5.5^{+0.6}_{-0.7}\,M_{\rm Jup}$ for both parameters, respectively. The planet luminosity is usually less model dependent than the derived effective temperature (e.g., Bonnefoy et al. 2016), which is apparent in the uncertainties of both mass estimates. We thus adopted a final mass estimate of $6 \pm 1\,M_{\rm Jup}$ for YSES 1c as the weighted average of both measurements. This is equivalent to a mass ratio of $q = 0.57 \pm 0.10\,\%$ with respect to the primary. Fitting the Y to K band data with several empirical spectra of substellar objects from Chiu et al. (2006) showed best compatibility with a spectral type of L7.5.

We further evaluated the colors of both companions with respect to field brown dwarfs and known directly imaged companions. This analysis is presented within the color-magnitude diagram in Figure 5.4. To compile the sample of field M, L, and T dwarfs we used data provided by the NIRSPEC Brown Dwarf Spectroscopic Survey (McLean et al. 2003, 2007), the IRTF Spectral library (Rayner et al. 2009; Cushing et al. 2005), the L and T dwarf data archive Knapp et al. (2004); Golimowski et al. (2004); Chiu et al. (2006), and the SpeX Prism Libraries (Burgasser et al. 2010; Gelino & Burgasser 2010; Burgasser 2007; Siegler et al. 2007; Reid et al. 2006; Kirkpatrick et al. 2006; Cruz et al. 2004; Burgasser & McElwain 2006; McElwain & Burgasser 2006; Sheppard & Cushing 2009; Looper et al. 2007; Burgasser et al. 2008; Looper et al. 2010; Muench et al. 2007; Dhital et al. 2011; Kirkpatrick et al. 2010; Burgasser et al. 2004), using distances from Gaia DR2 (Gaia Collaboration et al. 2018; Bailer-Jones et al. 2018), the Brown Dwarf Kinematics Project (Faherty et al. 2009), and the Pan-STARRS1 3π Survey (Best et al. 2018). The photometry of the directly imaged companions were adopted from Chauvin et al. (2005); Lafrenière et al. (2008); Bonnefoy et al. (2011); Currie et al. (2013); Zurlo et al. (2016); Samland et al. (2017); Chauvin et al. (2017b); Keppler et al. (2018); Müller et al. (2018); Cheetham et al. (2019); Janson et al. (2019). YSES 1b and c are both considerably redder than the evolutionary sequence of field brown dwarfs, which is another strong indicator of their youth and low surface gravity. YSES 1c is located close to the L/T transition but substantially redder than field dwarf equivalents of similar spectral type. Indeed, it is the reddest object among the directly imaged, substellar companions that are presented in Figure 5.4.

5.3.3 Dynamical stability

We model the system using `Rebound` and the `WHFast` integrator (Rein & Liu 2012; Rein & Tamayo 2015). We assume semi-major axes of planets b and c to be 160 and 320 au respectively, and we place both planets at apastron. For various values of the eccentricity of the planets we then calculate the chaos indicator as the mean exponential growth factor of nearby orbits (MEGNO; Cincotta et al. 2003; Rein & Tamayo 2016) for the system, integrating it for its current lifetime and up to 1 Gyr to check its long-term stability. We find that for orbits with low eccentricity ($e \lessapprox 0.1$) for both planets, the system is stable on gigayear timescales. For larger eccentricities, the system is chaotic and likely to experience dynamical interaction between the planets, implying that either the planets formed in-situ or that they were ejected from the system by an unseen third companion.

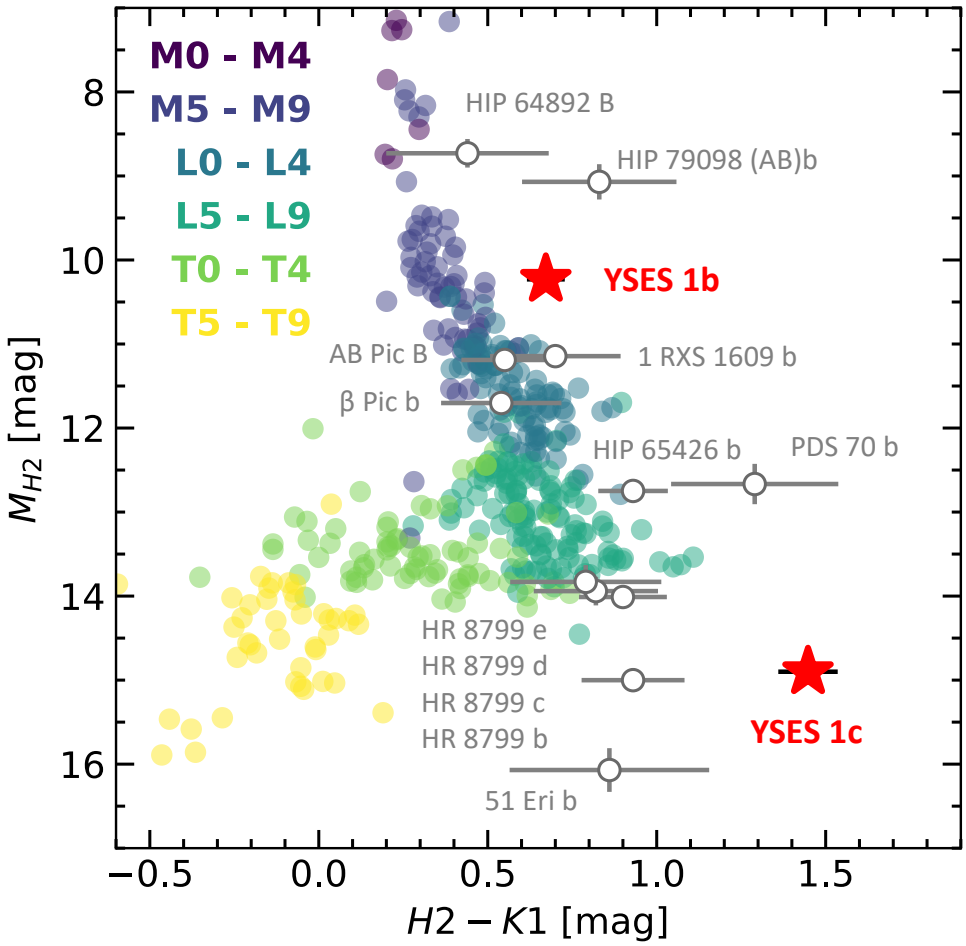

Figure 5.4: Color–magnitude diagram for YSES 1b and c. The two objects of interest are highlighted by the red stars. The colored, filled circles indicate the evolutionary sequence of field dwarfs of spectral class M to T and the white circles represent confirmed directly imaged companions.

5.4 Conclusions

We report the detection of YSES 1c: a second, planetary-mass companion to the solar-type Sco–Cen member YSES 1, making this the first directly imaged system around a star of approximately 1 $M_\odot$. From the astrometry of the object, we derived a projected physical separation of 320 au. SED analysis of broadband photometric data sampled from Y to L' band constrains an effective temperature of $T_{\rm eff} = 1240^{+160}_{-170}$ K, a surface gravity $\log(g) = 3.5 \pm 0.5$ dex, a planet radius of $R_{\rm p} = 1.1^{+0.6}_{-0.3}\,R_{\rm Jup}$, a luminosity of $\log(L/L_\odot) = -4.65^{+0.05}_{-0.08}$, and a spectral type of L7.5. Evaluation of BT-Settl isochrones at the system age of 16.7 ± 1.4 Myr yielded a planet mass of $6 \pm 1\,M_{\rm Jup}$, which is consistent with a mass ratio of $q = 0.57 \pm 0.10$ % with regard to the primary. This is in very good agreement with the color-magnitude analysis of the system that ranks YSES 1c as an object that is close to the L/T transition, yet much redder than field objects of the same spectral type. Comparison to other well-characterized, substellar companions shows that YSES 1c is indeed the reddest among these objects. Using dynamical modeling of the system, we find that the system is stable on gigayear timescales only for near-circular orbits, with eccentric orbits becoming chaotic on timescales comparable to the system's lifetime.

YSES 1 is a prime system to further study the dynamical and chemical properties of two coeval, gravitationally bound, gas giant planets. Continuous astrometric monitoring will constrain the orbital solutions for both companions and thus enable testing of potential formation scenarios. Due to the wide separations of both companions, contaminating flux from the primary is negligible, so spectral characterization at high resolution is easily accessible to determine rotational periods and molecular abundances in the planetary atmospheres (e.g. Snellen et al. 2014). Multi-wavelength photometric variability monitoring with space-based observatories such as the Hubble space telescope (e.g. Zhou et al. 2016; Biller et al. 2018) and the James Webb Space Telescope (JWST) will facilitate studies of the vertical cloud structures in these Jovian companions. Even mid-infrared spectroscopy with JWST/MIRI will be feasible to provide benchmark spectra for theoretical atmosphere models of young, substellar companions at wavelengths longer than 5 microns.

5.A Observational setup and conditions

The setup that was used for each observation and the weather conditions during data collection are presented in Table 5.2.

5.B Data reduction

5.B.1 SPHERE data

As both companions are located outside the stellar PSF halo, we did not perform any advanced post-processing for the SPHERE data: all frames were centered and derotated accounting for the parallactic rotation of the field. We used the standard astrometric calibration for SPHERE/IRDIS with a true north offset of $-1\overset{\circ}{.}75 \pm 0\overset{\circ}{.}08$ and plate scales varying from 12.250 ± 0.010 mas per pixel to 12.283 ± 0.010 mas per pixel for the applied filters as described in Maire et al. (2016).

Table 5.2: High-contrast observations of YSES 1.

Observation date (yyyy-mm-dd)	Instrument	Mode[a]	Filter	FWHM[b] (mas)	NEXP×NDIT×DIT[c] (1×1×s)	$\Delta\pi^d$ (°)	$\langle\omega\rangle^e$ ($''$)	$\langle X\rangle^f$	$\langle\tau_0\rangle^g$ (ms)
2017-07-05	SPHERE	CI	H	52.3	4×1×32	0.50	1.22	1.52	2.90
2019-03-23	SPHERE	DBI	$Y23$	37.2 / 37.9	4×3×64	3.84	0.41	1.38	9.30
2019-03-23	SPHERE	DBI	$J23$	40.1 / 41.8	4×3×64	3.72	0.40	1.41	10.75
2019-03-23	SPHERE	DBI	$H23$	47.5 / 49.5	4×3×64	3.60	0.43	1.44	10.83
2019-03-23	SPHERE	DBI	$K12$	60.2 / 63.6	4×3×64	3.45	0.53	1.49	8.75
2019-05-18	NACO	CI	L'	125.0	30×600×0.2	22.99	0.88	1.32	2.32
2019-06-03	NACO	CI	M'	131.6	112×900×0.045	50.15	0.78	1.33	3.69
2020-02-16	SPHERE	DPI	H	50.5	16×4×32	13.05	0.67	1.32	9.15

Notes. [a] The applied mode is either classical imaging (CI) with a broadband filter, dual-band imaging (DBI) with two intermediate band filters simultaneously, or dual-polarization imaging (DPI). [b] FWHM denotes the full width at half maximum that we measure from the average of the noncoronagraphic flux images that are collected for each filter. For NACO data these are equivalent to the science exposures of the star. [c] NEXP describes the number of exposures, NDIT is the number of subintegrations per exposure and DIT is the detector integration time of an individual subintegration. [d] $\Delta\pi$ denotes the amount of parallactic rotation during the observation. [e] $\langle\omega\rangle$, denotes the average seeing during the observation. [f] $\langle X\rangle$, denotes the average airmass during the observation. [g] $\langle\tau_0\rangle$, denotes the average coherence time during the observation.

5.B.2 NACO data

As the NACO observations were optimized for the characterization of YSES 1b, we had to reject large fractions of the original datasets as described in Table 5.2, because YSES 1c was located outside the detector window for these frames. After additional frame selection to reject frames with bad AO correction, approximately 30 % and 15 % of the full data was remaining for L' and M' data, respectively. As the amount of parallactic rotation in the data was sufficient, we performed a PSF subtraction based on principal component analysis (PCA; Amara & Quanz 2012; Soummer et al. 2012). For both L' and M' data, we fitted and subtracted one principal component from the images. This was optimizing the signal-to-noise ratio of YSES 1c for the L' data and it provided the best upper limit for the M' data at the position of the companion.

5.C Signal-to-noise assessment

To assess the significance of the detection of YSES 1c for each individual epoch and filter, we measured the signal-to-noise ratio of the companion in the processed images. We evaluated the signal flux in a circular aperture placed at the previously determined position of the companion for the corresponding filter (see Section 5.3.1). For bandpasses in which the companion is not detected (i.e. $Y2$ band on the night of 2019 March 23 and M' band on the night of 2019 June 3), we used the astrometric position of the $K1$ data from 2019 March 23 instead. The aperture radius was chosen as the FWHM of the unsaturated flux PSF of the corresponding filter as reported in Table 5.2. To measure the noise, we distributed circular apertures of the same size radially around the star at the same radial separation as the companion. We calculated the integrated flux within each of the background apertures and subtracted the average of these measurements from the integrated signal flux in the science aperture. The noise was computed as the standard deviation of the integrated fluxes from the background apertures, following the description of Mawet et al. (2014). The resulting signal-to-noise ratios are presented in Figure 5.5. Besides nondetections in the $Y2$ and the M' data, we measure the flux of YSES 1c with a signal-to-noise ratio greater than 5.

5.D Posterior distributions of SED fit

We present the full parameter space of posterior samples from our SED fit of YSES 1c in Figure 5.6. Due to the linear interpolation of the model grid prior to the MCMC fitting routine, each parameter is sampled continuously within the predefined intervals. The upper three panels of the corner plot show the correlations between the three input parameters $T_{\rm eff}$, $\log(g)$, and R. Furthermore, we present the corresponding planet luminosities that are derived from these input parameters and the system distance in the bottom panel of the figure. The posterior distributions show two families of solutions with effective temperatures of approximately 1225 K and 1375 K and associated planet radii of 1.2 $R_{\rm Jup}$ and 0.8 $R_{\rm Jup}$, respectively. Even though the latter family of solutions is slightly disfavored due to the corresponding planet radius of 0.8 $R_{\rm Jup}$ – which is smaller than theoretical predictions and empirical constraints for an object of this age and mass (e.g., Chabrier et al. 2009; Mordasini et al. 2012) –

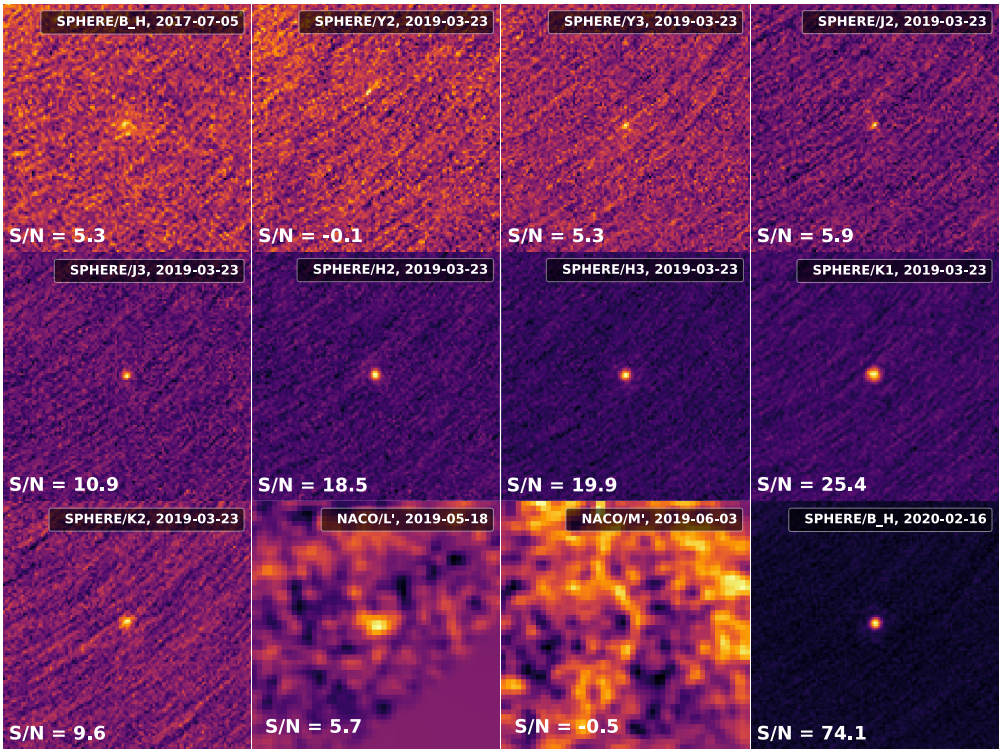

Figure 5.5: Signal-to-noise ratio assessment of YSES 1c. We show a cutout of the final images for all filters and epochs. The signal-to-noise ratios of the companion were measured with aperture photometry and the resulting values are presented in the lower left of each panel. Each image is presented on an individual linear color scale that is normalized with respect to the maximum and minimum flux value within the image cutout.

we report the 95 % confidence intervals around the medians of the distributions as a conservative estimate of the planetary properties. This estimate can certainly be refined by future studies at higher spectral resolution.

5.E Dynamical modeling

In Figures 5.7 and 5.8, we show the MEGNO values for systems after simulating them for 17 Myr and 1 Gyr, respectively (see subsection 5.3.3). A MEGNO value > 2 indicates a chaotic system, for which we cannot accurately predict the orbits on these timescales.

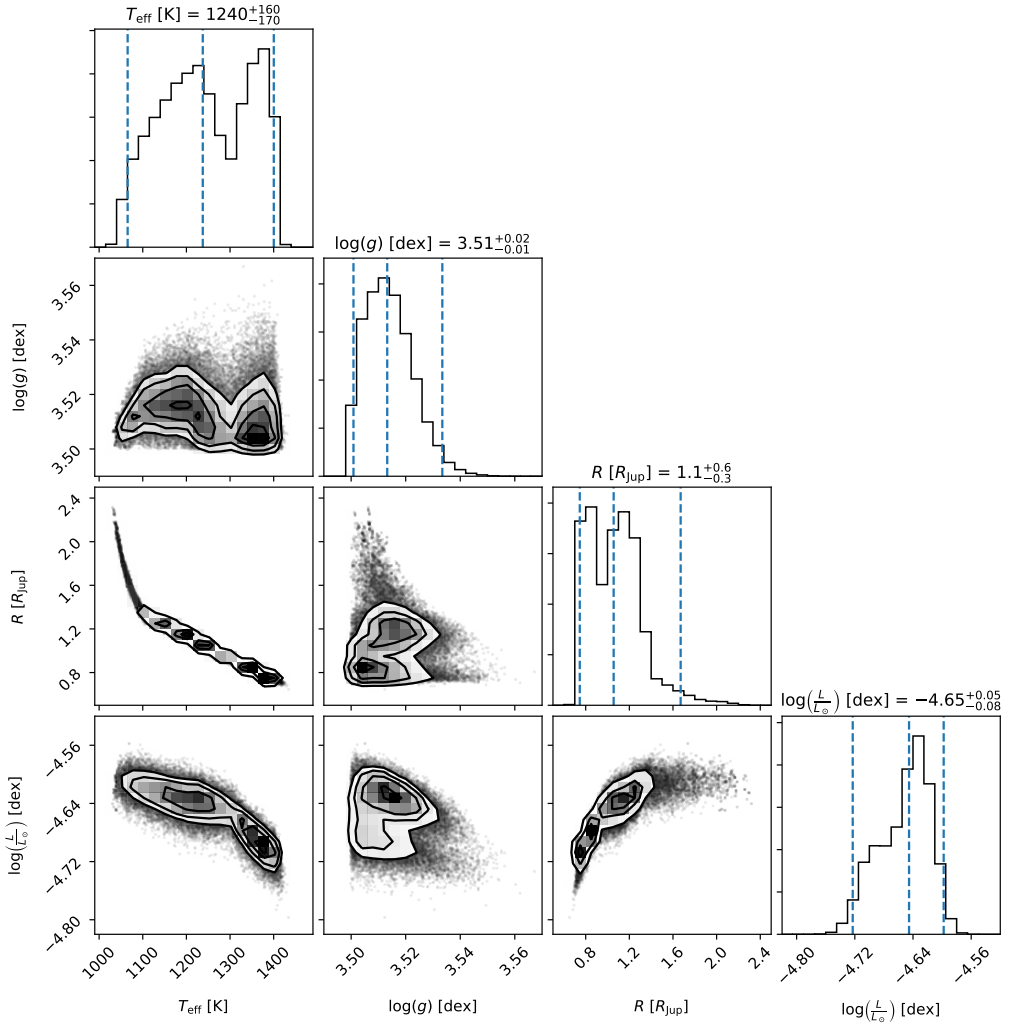

Figure 5.6: Posterior distributions of the MCMC fitting procedure to the photometric SED of YSES 1c. The input parameters of the fit were effective temperature $T_{\rm eff}$, surface gravity $\log(g)$, and object radius R. We further show the resulting planet luminosities that can be derived from the three input parameters and the system distance. The dashed blue lines in the marginalized distributions present the 2.5 %, 50 %, and 97.5 % quantiles and the title of the corresponding diagram indicates the 95 % confidence interval around the median, derived from these quantities.

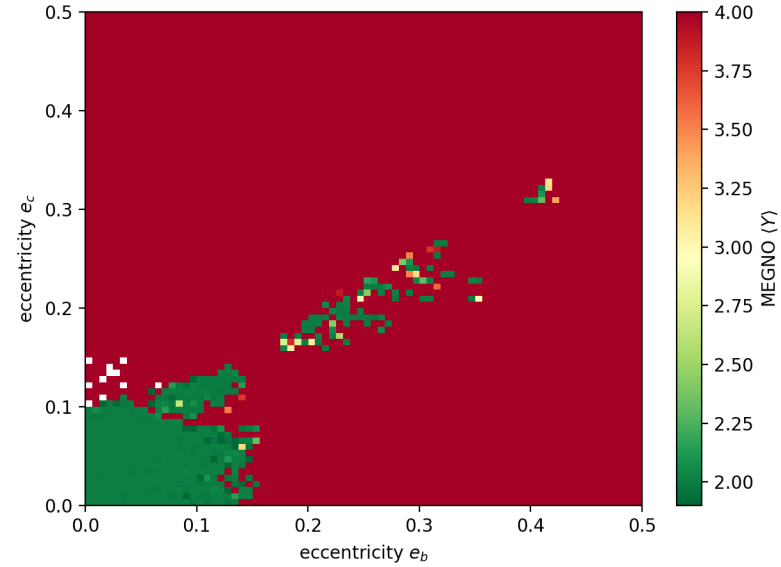

Figure 5.7: System stability analysis I. MEGNO value for the system after 17 Myr, for different eccentricities of planets b and c. A value > 2 indicates a chaotic system.

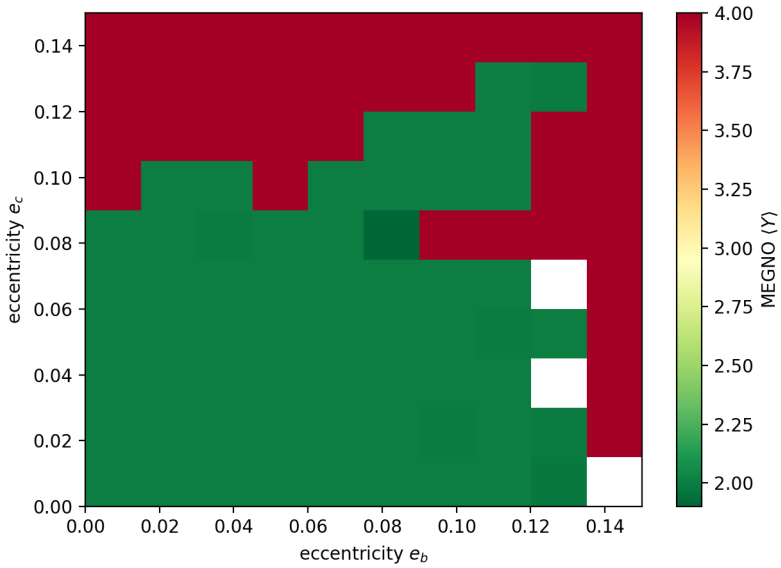

Figure 5.8: System stability analysis II. As Figure 5.7, but on a 1 Gyr timescale. We have not plotted orbits with $e > 0.15$, as they are all chaotic on this timescale.

Chapter 6

Discovery of a directly imaged planet to the young solar analog YSES 2

To understand the origin and formation pathway of wide-orbit gas giant planets, it is necessary to expand the limited sample of these objects. The mass of exoplanets derived with spectrophotometry, however, varies strongly as a function of the age of the system and the mass of the primary star. By selecting stars with similar ages and masses, the Young Suns Exoplanet Survey (YSES) aims to detect and characterize planetary-mass companions to solar-type host stars in the Scorpius-Centaurus association. Our survey is carried out with VLT/SPHERE with short exposure sequences on the order of 5 min per star per filter. The subtraction of the stellar point spread function (PSF) is based on reference star differential imaging (RDI) using the other targets (with similar colors and magnitudes) in the survey in combination with principal component analysis. Two astrometric epochs that are separated by more than one year are used to confirm co-moving companions by proper motion analysis. We report the discovery of YSES 2b, a co-moving, planetary-mass companion to the K1 star YSES 2 (TYC 8984-2245-1, 2MASS J11275535-6626046). The primary has a Gaia EDR3 distance of 110 pc, and we derive a revised mass of 1.1 $M_\odot$ and an age of approximately 14 Myr. We detect the companion in two observing epochs southwest of the star at a position angle of 205° and with a separation of $\sim 1''.05$, which translates to a minimum physical separation of 115 au at the distance of the system. Photometric measurements in the H and K_s bands are indicative of a late L spectral type, similar to the innermost planets around HR 8799. We derive a photometric planet mass of $6.3^{+1.6}_{-0.9}\,M_{\rm Jup}$ using AMES-COND and AMES-dusty evolutionary models; this mass corresponds to a mass ratio of $q = (0.5 \pm 0.1)\,\%$ with the primary. This is the lowest mass ratio of a direct imaging planet around a solar-type star to date. We discuss potential formation mechanisms and find that the current position of the planet is compatible with formation by disk gravitational instability, but its mass is lower than expected from numerical simulations. Formation via core accretion must have occurred closer to the star, yet we do not find evidence that supports the required outward migration, such as via scattering off another undiscovered companion in the system. We can exclude additional companions with masses greater than 13 $M_{\rm Jup}$ in the full field of view of the detector ($0''.15 < \rho < 5''.50$), at $0''.5$ we can rule out further objects that are more massive than 6 $M_{\rm Jup}$, and for projected separations $\rho > 2''$ we are sensitive to planets with masses as low as 2 $M_{\rm Jup}$.

YSES 2b is an ideal target for follow-up observations to further the understanding of the physical and chemical formation mechanisms of wide-orbit Jovian planets. The YSES strategy of short snapshot observations ($\leq$ 5 min) and PSF subtraction based on a large reference library proves to be extremely efficient and should be considered for future direct imaging surveys.

Adapted from
Alexander J. Bohn, Christian Ginski, Matthew A. Kenworthy, Eric E. Mamajek, Mark J. Pecaut, Markus Mugrauer, Nikolaus Vogt, Christian Adam, Tiffany Meshkat, Maddalena Reggiani, and Frans Snik
Astronomy & Astrophysics, **648**, A73 (2021)

6.1 Introduction

Despite several remarkable exoplanet and brown dwarf discoveries by high-contrast imaging at high angular resolution in the past few years (e.g., Marois et al. 2008; Schmidt et al. 2008; Marois et al. 2010; Lagrange et al. 2010; Rameau et al. 2013; Bailey et al. 2014; Macintosh et al. 2015; Chauvin et al. 2017a; Keppler et al. 2018; Haffert et al. 2019; Janson et al. 2019; Bohn et al. 2020a,b), there is an ongoing debate regarding the formation mechanisms that create these super-Jovian gas giants with semi-major axes greater than 10 au. It is unclear whether these companions have a star-like origin from a collapsing molecular cloud that is broken up into fragments, creating planetary-mass objects similar to a stellar binary (Kroupa 2001; Chabrier 2003), or through formation in a circumstellar disk instead. The classical bottom-up framework postulates formation via core accretion by coagulation of small dust grains into planetary embryos (Pollack et al. 1996; Alibert et al. 2005; Dodson-Robinson et al. 2009; Lambrechts & Johansen 2012). These evolve either via collisions or pebble accretion (Johansen & Lacerda 2010; Ormel & Klahr 2010) into planetary cores that are massive enough to accrete a gaseous envelope and to open a gap in the disk (Paardekooper & Mellema 2004). In the corresponding top-down scenario, planetary cores can be created by gravitational instabilities leading to the collapse of dense regions in the protoplanetary disk (Boss 1997; Rafikov 2005; Durisen et al. 2007; Kratter et al. 2010; Boss 2011; Kratter & Lodato 2016).

To study this question for the underlying planet formation mechanisms from a statistical point of view, several direct imaging surveys have been conducted (e.g., Vigan et al. 2012; Galicher et al. 2016; Bowler 2016; Vigan et al. 2017). Synthetic planet populations that represent each of the potential formation channels can be compared to the observational results from surveys and place constraints on the efficiency of the corresponding formation pathway (e.g., Mordasini et al. 2009a,b; Forgan & Rice 2013; Forgan et al. 2018). The two largest surveys were carried out with two of the most advanced adaptive-optics assisted, high-contrast imagers available: the Spectro-Polarimetric High- contrast Exoplanet REsearch (SPHERE; Beuzit et al. 2019) instrument at the 8.2 m ESO/VLT and the Gemini Planet Imager (GPI; Macintosh et al. 2014) at the 8.1 m Gemini South telescope. The preliminary statistical analysis of the first 300 stars from the Gemini PLanet Imager Exoplanet Survey (GPIES; Nielsen et al. 2019) concludes that giant planets between 10 au and 100 au that have masses smaller than 13 M_{Jup} favorably form via core accretion mechanisms, whereas brown dwarf companions in the same separation range but with masses from 13 M_{Jup} to 80 M_{Jup} seem to be predominantly created by disk instabilities. This finding is supported by the analysis of the first 150 stars observed within the scope of the SpHere INfrared survey for Exoplanets (SHINE; Vigan et al. 2020), which additionally hypothesizes that companions with masses between 1 M_{Jup} and 75 M_{Jup} are likely to originate from bottom-up formation scenarios around B and A type stars, whilst objects of the same mass around M-type stars are consistent with simulated populations from top-down mechanisms. For the intermediate masses of F-, G-, and K-type stars, the observed detections can be explained by a combination of both formalisms. A statistical meta-analysis on the distribution of wide-orbit companion eccentricities carried out by Bowler et al. (2020) provides supporting evidence for two distinct formation channels shaping the populations of giant planets ($2\,M_{\mathrm{Jup}} < M < 15\,M_{\mathrm{Jup}}$) and brown dwarfs ($15\,M_{\mathrm{Jup}} < M < 75\,M_{\mathrm{Jup}}$).

Most of these statistical evaluations are affected by the small number of actual substellar companions that were detected in the preceding imaging surveys. To expand the sample size for solar-mass host stars, we started the Young Suns Exoplanet Survey (YSES; Bohn et al. 2020a, Bohn et al. in prep.) that is observing a homogeneous sample of 70 ∼15 Myr-old, K-type stars in the Lower Centaurus Crux (LCC) subgroup of the Scorpius-Centaurus association (Sco-Cen; de Zeeuw et al. 1999). All stars have masses close to 1 $M_\odot$ and the proximity (average parallactic distance $\langle D \rangle = 114 \pm 17$; Gaia Collaboration et al. 2021) and youth of the LCC facilitate the direct imaging search of giant, self-luminous substellar companions around these stars.

In this article we report the detection of a new exoplanet that was discovered within the scope of our survey. As this is already the second planetary system discovered by YSES, we introduce a new stellar identifier that is based on our survey acronym. The details of this new designation are described in Section 6.2. In Section 6.3 we describe our observations and data reduction methods. We discuss previous observations on the host star and reassess its main parameters in Section 6.4. The results of our high-contrast imaging observations are presented and analyzed in Section 6.5. We discuss potential formation mechanisms of this newly detected exoplanet in Section 6.6 and we present our conclusions in Section 6.7.

6.2 Nomenclature of YSES planets

Owing to the recent success of YSES, we decided to introduce a dedicated catalog that will be used for star-planet systems discovered within the scope of our survey. The YSES acronym has been verified by the IAU Commission B2 Working Group on Designations and was added to the Simbad database (Wenger et al. 2000).[1] The nomenclature of planet hosts from our survey is YSES NNN and planets that are associated with these stars will be named YSES NNNa, accordingly. Following these guidelines, we assigned the host star of the intriguing multi-planet system that was discovered around TYC 8998-760-1 the new primary identifier YSES 1 (Bohn et al. 2020a,b). The planets formerly known as TYC 8998-760-1 b and TYC 8998-760-1 c, will be named YSES 1b and YSES 1c, henceforth. Further planetary systems discovered by our survey will receive designated YSES identifiers followed by ascending integer identifications (IDs). Hence, the new companion discovered within the scope of this paper will be referred to as YSES 2b, orbiting its Sun-like host YSES 2.

6.3 Observations and data reduction

We observed YSES 2 (TYC 8984-2245-1, 2MASS J11275535-6626046) as part of YSES on the nights of 2018 April 30 (PI: Kenworthy) and 2020 December 8 (PI: Vogt) with SPHERE (mounted at the Nasmyth platform of Unit Telescope 3 of the ESO Very Large Telescope). We used the IRDIS camera (Dohlen et al. 2008) in classical imaging mode, applying a broadband filter in the H and K_s bands during the first and second nights, respectively. The observations were carried out in pupil stabilized imaging mode and an apodized Lyot coronagraph was used to block the flux of the primary star (Soummer 2005; Martinez et al. 2009; Carbillet et al. 2011). In addition to the

[1] Database entry available at: `http://cds.u-strasbg.fr/cgi-bin/Dic-Simbad?/18721212`

science frames, we obtained center frames, with a sinusoidal pattern applied to the deformable mirror that creates a waffle pattern to locate the position of the star behind the coronagraphic mask; sky frames of an offset position with no adaptive optics (AO) correction and without any source in the field of view, to subtract the instrument and thermal background; and non-coronagraphic images of the star that are used for photometric reference of point sources detected in the science images. This last category of non-coronagraphic flux images was obtained with an additional neutral density filter in the optical path to record an unsaturated stellar point spread function (PSF) in the linear readout regime of the detector. This neutral density filter (filter ID: ND_1.0) provided an attenuation of 7.9 and 6.9 across the H and K_s bandpasses, respectively. A detailed description of the observing setup and the weather conditions can be found in Appendix 6.A.

The data reduction was performed with `PynPoint` (version 0.8.1; Stolker et al. 2019) and included basic processing steps such as dark and flat calibration, bad pixel cleaning, sky subtraction, and correction for the instrumental distortion along the vertical axis of the detector. To remove the stellar halo that is affecting approximately the innermost $1\farcs2$ around the coronagraph, we utilized an approach based on reference star differential imaging (RDI; Smith & Terrile 1984) in combination with principal component analysis (PCA; Amara & Quanz 2012; Soummer et al. 2012). As the parallactic rotation of our YSES observations is usually less than a few degrees, classical PSF subtraction schemes, such as angular differential imaging (ADI; Marois et al. 2006a), perform much worse compared to this reference library approach. This method of combined RDI plus PCA was already successfully employed to recover circumstellar disks in archival HST data (e.g., Choquet et al. 2014) and within the scope of our survey for the discovery of a transition disk around the YSES target Wray 15-788 (Bohn et al. 2019).

Owing to the same location on sky, similar distances, and spectral types, all YSES targets exhibit very similar magnitudes in the red part of the optical spectrum (where the wavefront sensor of SPHERE is operating) and at the near-infrared wavelengths of our scientific observations. This facilitates comparable AO corrections amongst all our YSES observations, and the resulting images compose an excellent reference library to perform RDI. The reference targets that were used for our library PSF subtraction are listed in Appendix 6.B. We modeled the stellar PSF with 50 principal components that were obtained from our full reference library. After the PSF subtraction, the frames were de-rotated according to their parallactic angles and median combined.

For the astrometric calibration we used the standard instrumental solution as presented by Maire et al. (2016) with a wavelength independent true north offset of $-1\fdg75 \pm 0\fdg08$ and plate scales of $(12.251 \pm 0.010)\,\mathrm{mas\,px^{-1}}$ and $(12.265 \pm 0.010)\,\mathrm{mas\,px^{-1}}$ in the H and K_s band, respectively.

6.4 Stellar properties

We briefly summarize previous literature characterizing YSES 2 in Section 6.4.1 and compile the stellar properties of YSES 2 in Table 6.1. In Section 6.4.2 and Section 6.4.3, we derive updated stellar parameters for YSES 2, more importantly, including stellar mass and age.

6.4.1 Previous studies

YSES 2 was first identified as a young star in the Search for Associations Containing Young stars (SACY) survey (Torres et al. 2006) of optical counterparts to the ROSAT All-Sky Survey (RASS) X-ray sources (Voges et al. 1999). Torres et al. (2006) reported the star to be a Li-rich (EW[Li I λ6707] = 367 mÅ) K1V(e) star with filled-in Hα, showing fast rotation ($v \sin i$ = 19.3 km s^{-1}) and radial velocity 15.8 $\pm$ 1.0 km s^{-1}. Based on its position, proper motion, and youth indicators, Preibisch & Mamajek (2008) included the star in a list of new members of the LCC subgroup of the Sco-Cen OB association (their Table 4), and provided initial estimates of isochronal age (16 Myr), mass (1.1 $M_\odot$), and fractional X-ray luminosity ($\log(L_X/L_{bol})$ = -3.2). Preibisch & Mamajek (2008) also predicted a kinematic distance of 109 pc (based on the proper motion and space velocity of LCC), which compares remarkably well to the Gaia EDR3 parallactic distance (ϖ = 9.1537 $\pm$ 0.0118 mas, D = 109.25 $\pm$ 0.14 pc; Gaia Collaboration et al. 2021). Kiraga (2012) reported the star to be a variable in the All Sky Automatic Survey (ASAS; IDed as ASAS J112755-6625.9) showing high amplitude (0.093 mag in V) and rapid rotation ($P_{\rm rot}$ = 2.7325 d), which is consistent with the observed saturated X-ray emission (and right near the median rotation period for Sco-Cen pre-main-sequence stars of $\langle P_{\rm rot} \rangle \simeq$ 2.4 d; Mellon et al. 2017). Pecaut & Mamajek (2016) include the star in their age analysis of pre-main-sequence K stars across Sco-Cen, estimating an age of 23 Myr and a mass of 1.0 $M_\odot$. The star has subsequently appeared in multiple LCC membership lists (Gagné et al. 2018; Goldman et al. 2018; Damiani et al. 2019). The status of this star as a pre-main-sequence member of LCC is strongly corroborated by a 99.9 % membership probability from the BANYAN Σ algorithm (Gagné et al. 2018) applied to the available *Gaia* astrometry and radial velocities (Gaia Collaboration et al. 2018, 2021).

6.4.2 Spectral analysis of YSES 2

To check the previously published spectral properties of YSES 2, we examined two archival UVES spectra from the ESO archive taken on UT 2007 May 2 (Program 079.C-0556(A); PI Torres). The UVES spectra at resolution R = 40,000 were convolved to lower resolution R = 3,000 and compared to the grid of MK spectral standards from Pecaut & Mamajek (2016). The blue spectrum, 3280 Å– 4560 Å, is consistent with K0V, but the red spectrum, 4730 Å– 6840 Å, appears to be K2V. The Hα line exhibits marginal emission, similar to the filled-in emission reported by Torres et al. (2006). Hence, we infer a temperature type of K1$\pm$1 and confirm the type K1V(e) published by Torres et al. (2006). From the original spectra, we independently measure the equivalent width of the Li I λ6707 feature to be 364 $\pm$ 5 mÅ, by simultaneously fitting Voigt profiles to the Li I feature and Fe I blend nearby (see, e.g., Soderblom et al. 1993). This is in good agreement with the 367 mÅ reported by Torres et al. (2006). The assigned luminosity class that we adapted from Torres et al. (2006) does not necessarily imply that YSES 2 is on the main sequence rather than being a pre-main-sequence star. Even though the luminosity and gravity indicators used by Torres et al. (2006) were more in line with main-sequence dwarfs than subgiant or giant standard stars, more persuasive indicators such as the HRD position, Li absorption, X-ray emission, and the confirmed LCC membership clearly favor the pre-main-sequence evolutionary stage.

Table 6.1: Stellar properties of YSES 2.

Parameter	Value	Ref.
Main identifier	YSES 2	(1)
TYCHO ID	TYC 8984-2245-1	(2)
2MASS ID	J11275535-6626046	(3)
GAIA EDR3 ID	5236792880333011968	(4)
α (J2000) [hh mm ss.sss]	11 27 55.355	(4)
δ (J2000) [dd mm ss.ss]	-66 26 04.50	(4)
Spectral Type	K1V(e)	(5)
ϖ [mas]	9.1537 ± 0.0118	(4)
D [pc]	109.25 ± 0.14	(7)
$\mu_{\alpha*}$ [mas yr^{-1}]	-34.025 ± 0.013	(4)
μ_δ [mas yr^{-1}]	2.319 ± 0.011	(4)
$v_{\rm rad}$ [km s^{-1}]	13.41 ± 0.17	(5)
B [mag]	11.819 ± 0.010	(8)
V [mag]	10.860 ± 0.017	(8)
G [mag]	10.525 ± 0.003	(4)
I [mag]	9.773 ± 0.044	(9)
J [mag]	9.006 ± 0.026	(3)
H [mag]	8.484 ± 0.029	(3)
$K_{\rm s}$ [mag]	8.358 ± 0.029	(3)
$W1$ [mag]	8.323 ± 0.014	(10)
$W2$ [mag]	8.351 ± 0.008	(10)
$W3$ [mag]	8.258 ± 0.019	(11)
$W4$ [mag]	7.929 ± 0.118	(11)
P_{rot} [day]	2.7325	(9)
$v \sin i$ [km s^{-1}]	19.3 ± 0.5	(5)
log(L_X/L_{bol}) [dex]	-3.07 ± 0.23	(9)
EW(Li I λ6707) [mÅ]	364 ± 0.05	(6)
EW(Hα) [mÅ]	0.0	(5)
U [km s^{-1}]	-10.10 ± 0.08	(7)
V [km s^{-1}]	-18.93 ± 0.12	(7)
W [km s^{-1}]	-5.60 ± 0.09	(7)
A_V [mag]	$0.06^{+0.03}_{-0.04}$	(6)
$T_{\rm eff}$ [K]	4749 ± 40	(6)
$m_{\rm bol}$ [mag]	10.396 ± 0.015	(6)
$M_{\rm bol}$ [mag]	5.204 ± 0.016	(6)
log $(L/L_\odot)$ [dex]	-0.1854 ± 0.0063	(6)
R [$R_\odot$]	1.193 ± 0.022	(6)
Mass [$M_\odot$]	1.10 ± 0.03	(6)
Age [Myr]	13.9 ± 2.3	(6)

References. (1) This paper, see Section 6.2; (2) Høg et al. (2000); (3) Cutri et al. (2003); (4) Gaia Collaboration et al. (2021), and *Gaia* EDR3 and DR2 ID #s are the same; (5) Torres et al. (2006); (6) this paper, see Section 6.4.3; (7) distance and heliocentric Galactic Cartesian velocity calculated using Gaia EDR3 values (D = 1/ϖ); (8) Henden et al. (2016); (9) Kiraga (2012); (10) Eisenhardt et al. (2020); (11) Cutri & et al. (2014).

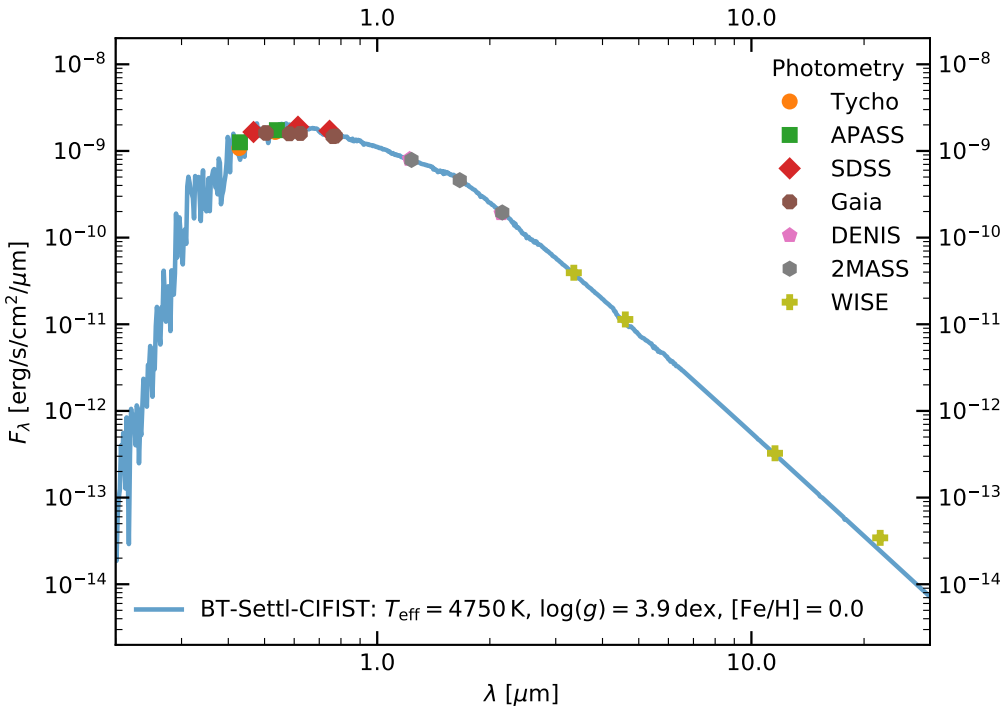

Figure 6.1: Spectral energy distribution of YSES 2. The colored markers indicate the archival photometric measurements of the star and the blue curve presents our best-fit BT-Settl-CIFIST model to the data. The uncertainties of the photometric measurements are too small to be visualized in the figure.

6.4.3 Updated stellar parameters

Using the VOSA spectral energy distribution (SED) analyzer (Bayo et al. 2008),[2] we fit synthetic stellar spectra to the observed visible and infrared photometry for YSES 2. For priors, we constrained the reddening to be E($B-V$) = 0.016 ± 0.017 mag based on the STILISM 3D reddening maps (Lallement et al. 2019) and searched for best-fit synthetic spectra in the range 3000 K $< T_{\rm eff} <$ 6000 K, 3.5 dex $<$ log g $<$ 4.5 dex, and metallicities -0.5 $<$ [Fe/H] $<$ 0.5 and [α/Fe] = 0.0. A Bayesian fit using the BT-Settl-CIFIST models using 22 photometric points yielded the following parameters: A_V = 0.06 (0.02-0.09; 68%CL; 0.00-0.11; 95%CL), $T_{\rm eff}$ = 4749 K (4709-4789 K; 68%CL; 4700-4900 K; 95%CL), log g = 3.9 dex (3.5-4.5 dex), [Fe/H] = 0.0. We present the results of this SED fit in Figure 6.1.

The best-fit bolometric flux is $f_{\rm bol} = (1.7490 \pm 0.0248) \times 10^{-9}$ erg s^{-1} cm^{-2}, which on the IAU 2015 scale of apparent bolometric magnitudes translates to $m_{\rm bol} = 10.396 \pm 0.015$ mag. Adopting the Gaia EDR3 parallax, this translates to an absolute bolometric magnitude $M_{\rm Bol} = 5.204 \pm 0.016$ mag and a bolometric luminosity log($L/L_\odot$) = -0.1854 ± 0.0063. This is considerably more accurate than previous estimates of log($L/L_\odot$) = -0.06 (Preibisch & Mamajek 2008) and log($L/L_\odot$) = -0.265 ± 0.075 (Pecaut & Mamajek 2016)), and benefits from a very precise distance,

[2]Online available at: `http://svo2.cab.inta-csic.es/theory/vosa/index.php`

well-constrained extinction from 3D reddening maps, and integrating synthetic SEDs using 22 photometric data points. Combining this improved luminosity estimate with the improved $T_{\rm eff}$ from the SED fitting ($T_{\rm eff}$ = 4749 ± 40 K) yields a good estimate of the radius of the star ($1.193 \pm 0.022\,R_\odot$). A comparison against evolutionary tracks from Baraffe et al. (2015) provided an updated stellar mass of (1.10 ± 0.03) $M_\odot$ and an age of (13.9 ± 2.3) Myr. Furthermore we note that the SED of the star showed no signs of infrared excess through to the WISE-4 band (22 µm). The 2MASS-WISE colors (K_s-$W1$ = -0.035 ± 0.032 mag, K_s-$W2$ = -0.007 ± 0.030 mag, K_s-$W3$ = 0.100 ± 0.035 mag, K_s-$W4$ = 0.429 ± 0.122 mag) can be compared to the mean for K1 pre-main-sequence stars from Pecaut & Mamajek (2013) (K_s-$W1$ = 0.09 mag, K_s-$W2$ = 0.06 mag, K_s-$W3$ = 0.10 mag, K_s-$W4$ = 0.18 mag), and show a significant hint of IR excess. The K_s-$W4$ color is marginally red (2σ excess), perhaps hinting at a debris disk (common among non-accreting pre-main-sequence Sco-Cen stars), but there is no corroborating evidence to further support this.

We searched for common proper motion stellar or substellar companions for YSES 2. Assuming a mass of 1.0 $M_\odot$, the tidal radius of YSES 2 is ∼1.35 pc (projected radius ∼0°.71 or ∼2560″; Mamajek et al. 2013b), that is, bound companions would be expected to lie projected within this radius. Surveying the lists of Sco-Cen candidates and pre-main-sequence stars from the Gaia DR2 catalogs of Goldman et al. (2018), Zari et al. (2018), and Damiani et al. (2019) with parallactic distances of <140 pc shows only a couple of likely LCC siblings within 1° of YSES 2: the poorly studied classical T Tauri star Wray 15-813 at 2845″ (D = 101 pc) (Pereira et al. 2003) and uncharacterized candidate pre-main-sequence object 2MASS J11375287-6631197 (D = 104 pc). A query of the recently released Gaia EDR3 catalog searching for comoving, co-distant objects (with generous selection range of proper motions in α and δ within ±5 mas yr^{-1}, and parallax ±2 mas of YSES 2) yields zero candidate companions within 1°. Thus far, YSES 2 appears to be a stellar singleton.

6.5 Observational results and analysis

In Section 6.5.1 we show that our observations reveal a co-moving companion to YSES 2. The reduced images for both epochs are presented in Figure 6.2. Our photometric analysis in Section 6.5.2 indicates that this companion has a mass that is significantly lower than the deuterium burning limit of $\sim 13\,M_{\rm Jup}$. We refer to this newly identified planet as YSES 2b henceforth. In Section 6.5.3 we present the detection and mass limits of our acquired data.

6.5.1 Companion astrometry

We extracted the companion astrometry and photometry by the injection of negative artificial companions (e.g., Lagrange et al. 2010; Bonnefoy et al. 2011). A detailed description of our method is presented in Appendix 6.C. The extracted astrometry is listed in Table 6.2. As visualized in the proper motion plot in Figure 6.3 the companion is clearly incompatible with the calculated trajectory of a static background object at 14σ significance. The relative astrometric motion with respect to the primary is consistent with a comoving companion. This conclusion is further confirmed by a similar analysis of other point sources within the detector field of view. As presented in Appendix 6.D, all additional off-axis point sources are consistent with being non-moving background contaminants. We thus conclude that

Table 6.2: Astrometry, photometry, and derived masses of YSES 2b.

Observation date	Filter	Separation	Position angle	ΔMag	M_{abs}	Photometric mass	
						COND	Dusty
(yyyy-mm-dd)		(mas)	(°)	(mag)	(mag)	(M_{Jup})	(M_{Jup})
2018-04-30	H	1057 ± 3	205.3 ± 0.2	10.37 ± 0.11	13.57 ± 0.11	5.3 ± 0.5	8.0 ± 0.7
2020-12-08	K_s	1053 ± 5	205.2 ± 0.2	9.55 ± 0.11	12.71 ± 0.11	6.1 ± 0.6	6.4 ± 0.6

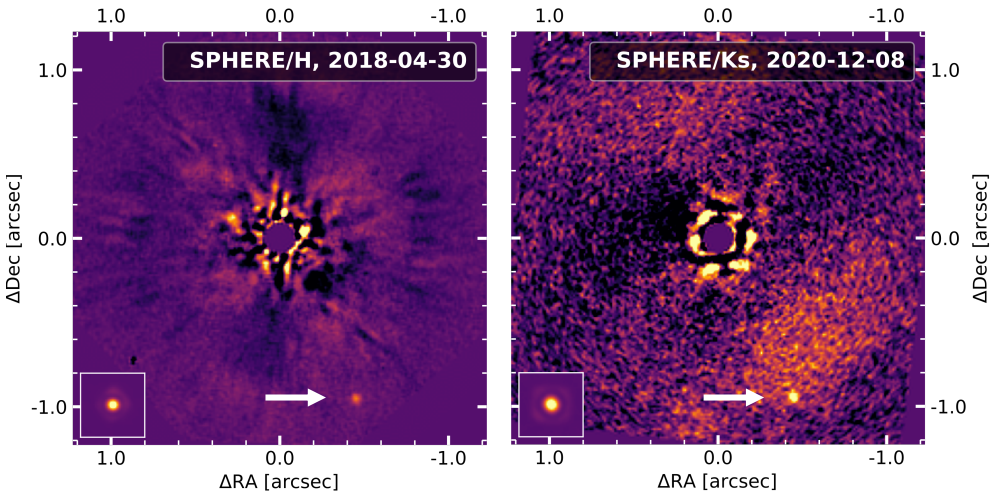

Figure 6.2: Multi-epoch observations of YSES 2 and its planetary-mass companion. Final data products of the SPHERE observations collected in the H band (left panel) and K_s band (right panel) are presented. For both filters, the stellar PSF is modeled by 50 principal components that were derived from a reference library of YSES targets. These PSF models were subtracted and the residuals rotated such that north points up and east toward the left. In the presented images the median of these de-rotated residuals is shown. For the K_s band data, uncorrected residuals of a wind-driven halo are detected that extend from the northeast to southwest. The planet YSES 2b is highlighted by white arrows. The primary is located at the origin of the coordinate system and we artificially masked the inner region up to the radial extent of the coronagraphic mask of 100 mas. To assess the spatial extent of the instrumental PSF, the median combination of the non-coronagraphic flux images of the primary star are shown in the lower left of each panel. The intensity of each flux image is rescaled to match the maximum and minimum counts in the corresponding residual science image, and we display both images with the same spatial and color scales.

YSES 2b is a gravitationally bound companion to its solar-mass host star. From our astrometric measurements we derived a projected physical separation of approximately 115 au. Future astrometric measurements are required to derive meaningful constraints to the orbital parameters of this wide-orbit planet.

6.5.2 Companion photometry

We present the photometry of the companion in Figure 6.4 in a color-magnitude diagram. The corresponding numerical values are reported in Table 6.2. YSES 2b is consistent with a late L to early T spectral type when comparing it to colors of field brown dwarfs from the NIRSPEC Brown Dwarf Spectroscopic Survey (McLean et al. 2003, 2007), the IRTF spectral library (Rayner et al. 2009; Cushing et al. 2005), the L and T dwarf data archive Knapp et al. (2004); Golimowski et al. (2004); Chiu et al. (2006), and the SpeX Prism Libraries (Burgasser et al. 2010; Gelino & Burgasser 2010; Burgasser 2007; Siegler et al. 2007; Reid et al. 2006; Kirkpatrick et al. 2006; Cruz et al. 2004; Burgasser & McElwain 2006; McElwain & Burgasser 2006; Sheppard & Cushing 2009; Looper et al. 2007; Burgasser et al. 2008; Looper et al. 2010; Muench et al. 2007; Dhital et al. 2011; Kirkpatrick et al. 2010; Burgasser et al. 2004). Object distances were

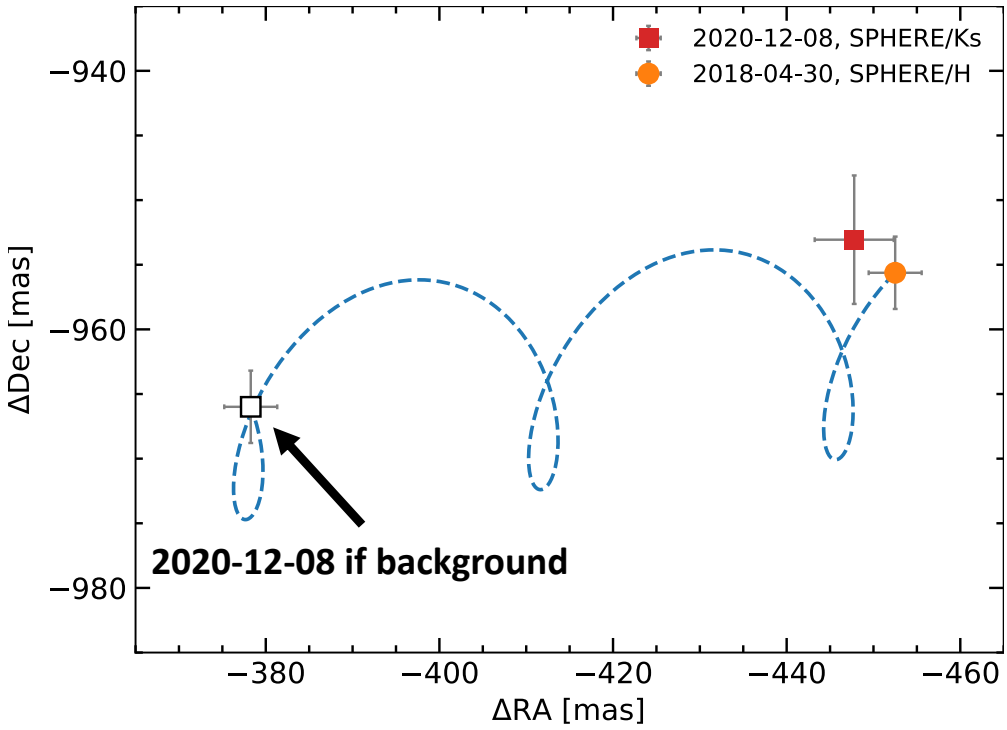

Figure 6.3: Proper motion plot for YSES 2b. The colored markers represent the relative astrometry with respect to the primary star measured for our two observational epochs. The blue trajectory indicates the simulated motion of a static background object at infinity and the white marker is the theoretical position of such an object at our second observational epoch.

derived from Gaia EDR3 (Gaia Collaboration et al. 2021), the Brown Dwarf Kinematics Project (Faherty et al. 2009), and the Pan-STARRS1 3π Survey (Best et al. 2018). In color-magnitude space, YSES 2b is very close to the innermost three planets of the HR 8799 multi-planetary system (Marois et al. 2008, 2010). These three planets are classified as mid to late L type dwarfs (e.g., Greenbaum et al. 2018), which agrees well with the sequence evolution of the adjacent field brown dwarfs from L to T spectral types.[3] A similar spectral type in this domain, therefore, seems very likely for YSES 2b, requiring confirmation by measurements at higher spectral resolution. Whereas the masses of the spectrally similar trio of HR 8799 c, d, and e are in the range 7-12 $M_{\rm Jup}$ (Wang et al. 2018; Marois et al. 2008, 2010), it is likely that YSES 2b has an even lower mass as the system age of (13.9 ± 2.3) Myr is significantly younger than the age of HR 8799, which is claimed to be member of the Columba association with an age of 30–50 Myr (Zuckerman et al. 2011; Bell et al. 2015). This is supported by the AMES-COND and AMES-dusty models (Allard et al. 2001; Chabrier et al. 2000) that we present in Figure 6.4 for a system age of 13.9 Myr. An individual evaluation of these isochrones yielded masses from 5.3 $M_{\rm Jup}$ to 8.0 $M_{\rm Jup}$ as presented in

[3]We would like to note that the planets around HR 8799, although closely located to the sequence of field brown dwarfs in the selected SPHERE filters as presented in the color-magnitude diagram in Figure 6.4, can have near-infrared colors in different passbands that are significantly distinct from those of their field dwarf analogs (e.g., Currie et al. 2011).

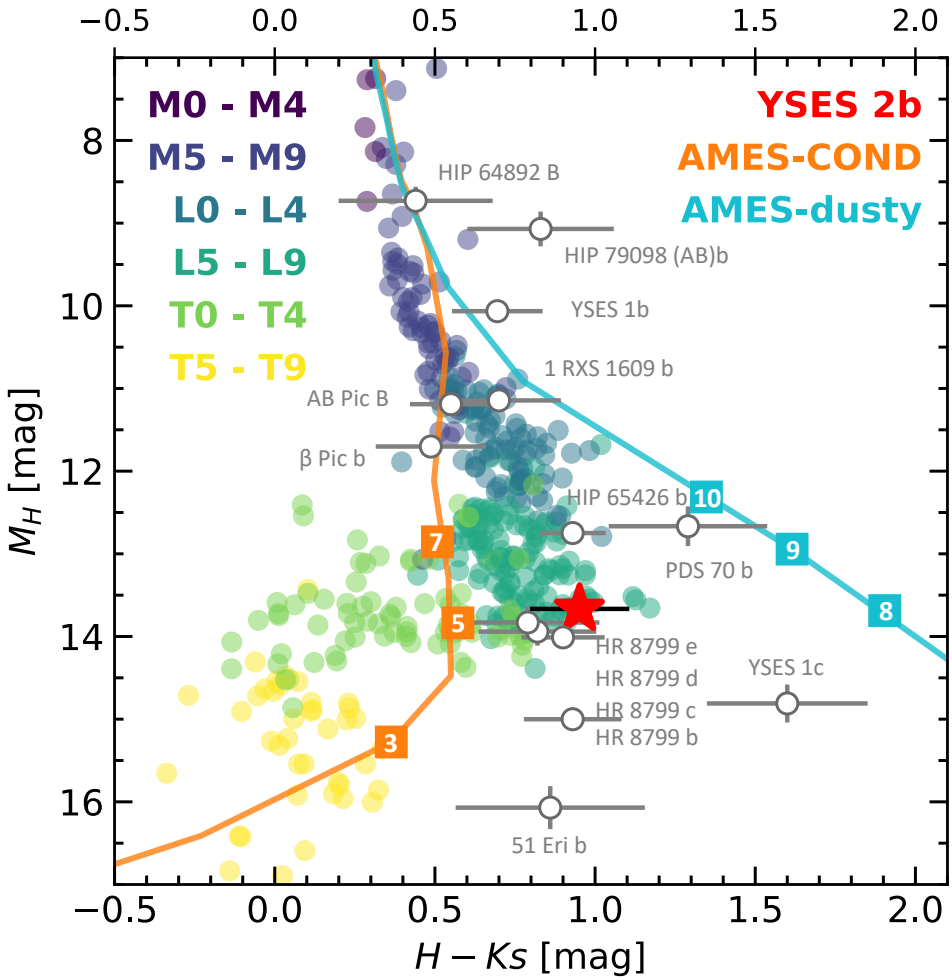

Figure 6.4: Color-magnitude diagram for YSES 2b. The colored markers show the sequence of field brown dwarfs with various spectral types from M to late T. The white markers represent known directly imaged companions that are usually younger than the presented field objects. YSES 2b is highlighted by the red star. We further show AMES-COND and AMES-dusty evolutionary models that were evaluated at a system age of 13.9 Myr (solid lines). The markers along the line indicate the equivalent object masses in M_{Jup}.

Table 6.2. The uncertainties originate from the errors in the system age and planet magnitude that were propagated by a bootstrapping approach with 1,000 randomly drawn samples from Gaussian distributions around both parameters. When combining the posterior distributions for the different models and filters we derived a final mass estimate of $6.3^{+1.6}_{-0.9}\,M_{\rm Jup}$ as the 68% confidence interval around the median of the sample. This estimate is based on broadband photometric measurements alone; further spectral coverage of the planetary SED will be important to constrain its effective temperature, luminosity, surface gravity, and mass.

6.5.3 Detection limits

To derive upper mass limits for additional companions in the system, we calculated the detection limits of our datasets. As a baseline, we evaluated the contrast in the image that was obtained by de-rotating and median combining the individual exposures without any PSF subtraction. This image covers the full field of view of the SPHERE/IRDIS detector up to an angular separation of 5.″5. We evaluated the contrast directly in the final image using aperture photometry. The chosen aperture size was one full width at half maximum (FWHM) of the unsaturated stellar PSF as measured in the flux images (see Table 6.3 in Appendix 6.A). The signal flux was measured as the sum over the full circular aperture within the mean combined flux image and scaled for the flux difference with the science frames owing to the shorter exposure times and the applied neutral density filters. For several radial positions that were equidistantly sampled from 0.″15 to 5.″50 in steps of 0.″05, we measured the noise as the standard deviation of the integrated flux within apertures that were distributed around the star at the same radial separation (excluding the signal aperture itself). We applied a sigma clipping with an upper bound of 3σ to the integrated fluxes of the noise apertures before calculating the standard deviation to discard apertures that were polluted by flux of off-axis point sources (see the full frame image in Figure 6.6 in Appendix 6.D). A correction for small sample statistics as described in Mawet et al. (2014) was considered in these noise calculations. We reiterated this analysis for six uniformly spaced position angles and present the azimuthally averaged results as two-dimensional contrast curves in Figure 6.5. The solid yellow lines represent the 5σ raw contrast in the H and K_s bands that was obtained without any PSF subtraction.

For the innermost region around the star ($< 1.''2$), the sensitivity was additionally assessed considering our PSF subtraction by RDI plus PCA. We used the `ContrastCurveModule` from `PynPoint` version 0.6.0[4] that utilizes the same aperture photometry framework and metric to evaluate the contrast for several positions that were distributed around the star in the residual images. For each position, the module injects an artificial companion, whose detection significance is evaluated after the PSF subtraction with RDI combind with PCA. In this framework, the signal aperture is directly placed on top of the position at which the artificial companion has been injected, and the noise apertures are azimuthally distributed around the primary star

[4]As mentioned before, version 0.8.1 of `PynPoint` was used for all remaining analysis steps. The modules of both versions are compatible; only the implementation of some algorithms changed throughout the development process. This affects the `ContrastCurveModule`, which follows the iterative process described in this paragraph for release version 0.6.0. We prefer this implementation over the solution presented in `PynPoint` version 0.8.1, which calculates one attenuation factor per position that is based on the single injection of an artificial companion with a user-defined signal-to-noise ratio.

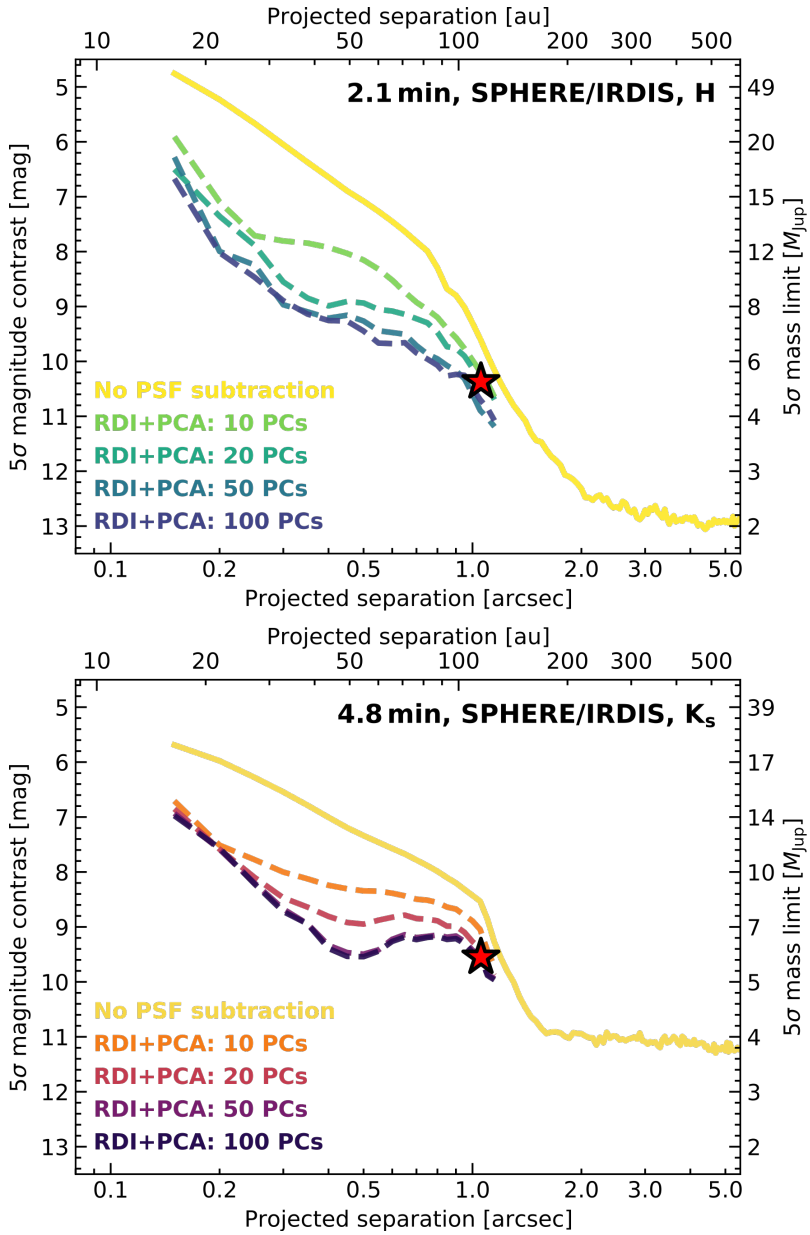

Figure 6.5: 5σ detection limits of our SPHERE/IRDIS observations in the H (upper panel) and K_s bands (lower panel). On the left axis the magnitude contrast with respect to the primary star is reported, and the absolute magnitudes are converted to detectable planet masses with AMES-COND models as indicated on the right axis; this scale varies between the H and K_s bands. The solid yellow lines represent the limits when no PSF subtraction is performed. The dashed lines indicate the sensitivity, when a PSF subtraction with RDI plus PCA is performed. The red star highlights the contrast of YSES 2b that we detect at $\sim 5\sigma$ significance in both filters after PSF subtraction with more than 50 principal components.

as described before, yet excluding the signal aperture itself. The companion template was obtained as the median combination of the non-coronagraphic flux images that was scaled for the difference in exposure time and the attenuation due to the applied neutral density filter. From an initial magnitude contrast of 8 mag, the flux of the injected companion was adjusted and the post-processing was performed iteratively until the artificial companion was retrieved at 5σ detection significance in the final image product. These limiting magnitude contrasts were stored for each of the injection positions. For the calculation of the final contrast curves with RDI plus PCA, we used a radial sampling in the range 0.″15-1.″20 with a spatial resolution of 0.″05, and six position angles that were equidistantly sampled in polar space. Again, the contrast as a function of radial separation was obtained by azimuthal averaging of the various position angles. We considered several numbers of principal components to model the stellar PSF as indicated by the sequentially colored, dashed lines in Figure 6.5. The detectable planet masses that correspond to the calculated magnitude contrasts were derived by evaluation of AMES-COND models at the system age of 13.9 Myr (see right axes of Figure 6.5).

The contrast performance close the star improves for an increasing number of principal components. This differential gain in contrast ceases for $\sim$50 subtracted components and the contrast for 100 principal components does not change significantly compared to the curve generated for half as many components. This justifies our previously selected value of 50 principal components that were used for our PSF subtraction with RDI plus PCA. This amount of components is equivalent to 19 % and 30 % of the reference libraries in the H and K_s bands, which are composed of 269 and 164 individual frames, respectively. In the H band we observe a contrast improvement of more than two magnitudes at an angular separation of 0.″2. This corresponds to an increase in planet detection sensitivity by more than 45 $M_{\rm Jup}$ at this close separation. The contrast improvement in the H band is maximized at an angular separation of $\sim$0.″3, where RDI plus PCA provides detection limits that are approximately three magnitudes deeper than our raw data. At angular separations larger than 1″ the contrast improvement decreases as the flux contribution of the stellar PSF becomes negligible. At separations $\geq$ 2″ we reach a fundamental noise floor that is mainly composed of residual sky background and detector read out noise. The K_s band contrast behaves very similar to the detection limits in the H band and the RDI plus PCA reduction scheme can provide a maximum gain of up to 2.5 mag at an angular separation of $\sim$0.″4. The overall improvement for separations $<$ 1″ is marginally worse compared to the H band data and the contribution of the asymmetric wind-driven halo is clearly visible for separations in the range 0.″5-1.″2. Combining the data from the H and K_s bands allows us to exclude stellar and brown dwarf companions around YSES 2 with masses $>$ 13 $M_{\rm Jup}$ for angular separations that are larger than 0.″15. At 0.″5 we are sensitive to objects that are more massive than 6 $M_{\rm Jup}$ and for angular separations that are larger than 2″ we can even rule out planets with masses as low as 2 $M_{\rm Jup}$.

This demonstrates, impressively, how a large reference library can help to significantly improve the contrast performance at small angular separations $<$ 1.″2. Especially for datasets with little parallactic rotation, RDI plus PCA should be considered as a default PSF subtraction strategy. This conclusion is also supported by first results from the star-hopping mode that was recently implemented at VLT/SPHERE

(Wahhaj et al. 2021). As visualized by the red stars in Figure 6.5, RDI plus PCA is required to detect YSES 2b at 5σ significance in both the H and K_s band data.

6.6 Discussion

The newly discovered planetary companion to YSES 2 is among the lowest mass direct imaging companions known to date. The only objects of similar low mass are 51 Eri b (Macintosh et al. 2015), HD 95086 b (Rameau et al. 2013), HR8799 b (Marois et al. 2008), PDS 70 b and c, (Keppler et al. 2018; Haffert et al. 2019; Wang et al. 2020; Stolker et al. 2020b), and YSES 1c (Bohn et al. 2020b). Of these, only YSES 1c is located around a solar-mass star. Within the uncertainties, the mass of YSES 2b is the same as YSES 1c, which we previously discovered in our survey. Given our mass estimate for the planet, the mass ratio of YSES 2b to its host star is $q = 0.54^{+0.13}_{-0.08}$ %. This value is comparable, but slightly lower than the $q = 0.57 \pm 0.10$ % derived for YSES 1c. The mass ratio is the lowest among direct imaging companions to solar-type stars.[5]

The in situ formation of super-Jovian planets at tens or hundreds of Astronomical Units is challenging. We recently discussed possible formation scenarios for such objects in the context of the YSES 1 system in Bohn et al. (2020a). In our previous study we considered scattering or planet capturing events to explain the current large separation of YSES 1b. However, dynamic scattering by a third body in the system is expected to produce high eccentricities, inconsistent with orbital stability of both planetary components in the YSES 1 system (Bohn et al. 2020b).[6] The new detection of YSES 2b in our small survey sample of 70 solar-type systems in Sco-Cen makes the hypothesis that we see captured free-floating planets unlikely. Goulinski & Ribak (2018) find with numerical simulations that only $\sim$0.1% of solar-type stars in the Galactic thin disk should capture a free-floating planet in their lifetime. YSES 2b in principle might have formed in situ via disk gravitational instability. Boss (2011) find that they can produce 1-5 $M_{\rm Jup}$ planets between 30 au and 70 au with eccentricities as high as 0.35. If YSES 2b is on an eccentric orbit it may explain its current projected separation of 110 au. Kratter et al. (2010) conversely find with their hydrodynamic simulations that planets formed via disk instability need to be at large separations outside of the 40 au to 70 au range to not accumulate too much mass and remain in the planetary regime. This hypothesis that gravitationally instabilities predominantly create brown dwarf and stellar companions is supported by other theoretical studies (e.g., Zhu et al. 2012; Forgan & Rice 2013). Spatially resolved observations of gas-rich planet forming disks in the last few years have shown that radial substructures, which are thought to be caused by perturbing planets, are nearly ubiquitous (see, e.g., Garufi et al. 2018 for an overview, observed in scattered light). These structures can, in a growing number of cases, be traced out to tens or hundreds of Astronomical Units (e.g., ALMA Partnership et al. 2015; Ginski et al. 2016a; de Boer et al. 2016; van Terwisga et al. 2018). Recently it was found that these substructures are already present in proto-stellar disks as young as $\sim$0.1 Myr (Sheehan et al. 2020; Sheehan 2020), suggesting that planet formation sets in early and operates on short

[5] See Bohn et al. (2020a) for an overview of mass ratios of direct imaging companions to solar-type stars.

[6] We, however, note that in some cases high eccentricities are inferred for substellar companions, for example, the brown dwarf companion to the young solar analog PZ Tel (Mugrauer et al. 2012; Ginski et al. 2014).

timescales. Despite this abundance of substructures observed in young, circumstellar environments, it is unlikely that all these protoplanetary disks are gravitationally unstable and support planet formation via this channel (e.g., Kratter & Lodato 2016). Conversely, we expect that the timescale to form a planet via core accretion at the current location of YSES 2b would be too long, given the system age and that the gas-rich disk in the system has already dissipated (e.g., Haisch et al. 2001).

Even though capturing scenarios are considered unlikely for YSES 2b, we cannot confidently conclude whether its formation via either top-down or bottom-up scenarios is more likely: whereas a mass of 6.3 $M_{\rm Jup}$ is rather low for an object to originate from gravitational disk instabilities, core accretion would favor a formation at closer separations to the star. More data are thus required to explore the origin of this wide-orbit Jovian giant. Promising methods to evaluate the likelihood of either formation scenario are by characterization measurements of the planetary atmosphere, continuous orbital monitoring to constrain especially its eccentricity, and deeper searches for additional companions in the system.

To identify the formation channel of YSES 2b via atmospheric characterization, we can utilize the framework postulated by Öberg et al. (2011), who argued that elemental abundances in the planetary atmosphere (and especially the C/O ratio) are directly linked to its natal environment in the planet-forming disk. Different ice lines in the protoplanetary disk and the associated freeze out of the corresponding molecular species alter molecular abundance ratios as a function of radial separation from the host star, making this atmospheric quantity a promising indicator of the natal environment and formation channel of a planet. The chemical and dynamical evolution of the disk can alter these initial abundances and should be considered in the analysis (e.g., Ali-Dib et al. 2014; Mordasini et al. 2016; Eistrup et al. 2016, 2018). Gravity Collaboration et al. (2020) utilized this framework to study β Pic b and proposed its formation through core accretion, with strong planetesimal enrichment based on its subsolar C/O abundance ratio. If YSES 2b formed via disk gravitational instability, then we expect this object to have similar elemental abundances as the primary star in the system, while formation by core accretion should lead to an overabundance of heavy elements due to pebble accretion. YSES 2b, along with other planet mass objects detected by direct imaging, provides an ideal test case for future detailed atmospheric characterization.

We can further continue to monitor the separation and position angle of YSES 2b with respect to the primary star to derive orbital solutions for the planet (e.g., Wang et al. 2018). In particular, the VLTI/GRAVITY instrument (Gravity Collaboration et al. 2017) will be extremely useful for this purpose, as it facilitates an unprecedented astrometric precision down to sub-milliarcsecond scales (e.g., Gravity Collaboration et al. 2019; Wang et al. 2021). These astrometry measurements could be complemented by VLT/CRIRES$^+$ data to constrain the radial velocity of the planet and to obtain three-dimensional information about its orbital motion (e.g., Schwarz et al. 2016). The eccentricity of the planet might provide hints regarding the likelihood of a potential migration of the companion, which would be an indicator of formation via core accretion at closer separation to the star. If this migration was caused by scattering off another, so far undetected companion to the primary star, a deep imaging campaign is required to search for evidence of such an additional component to the planetary system. At the moment, we cannot provide conclusive evidence for the most likely formation scenario of YSES 2b based on the available

data; but future observations might be able to shed light on the origin of this Jovian gas giant.

Even though the second epoch observations of YSES are not concluded yet and candidate companions to ∼45 stars of our sample need to be confirmed or rejected, our survey has already discovered three planetary-mass companions amongst 70 young, Sun-like stars. This high planet-detection rate is in stark contrast to previous surveys that were targeting Sun-like stars at closer distances than the LCC (e.g., Kasper et al. 2007; Biller et al. 2013; Galicher et al. 2016), which discovered mostly stellar and brown dwarf companions. These preliminary statistical results from YSES tentatively indicate that despite the farther distance, Sco-Cen and especially LCC are more favorable than moving groups in the immediate solar neighborhood for the detection of young planets briefly after their formation. Many of the moving groups that were targeted in these aforementioned surveys are significantly older than LCC (15 ± 3 Myr), such as the Tucana-Horologium moving group (45 ± 4 Myr Bell et al. 2015), the AB Dor moving group (149^{+51}_{-19} Myr; Bell et al. 2015), or the Hercules-Lyra association (257 ± 46 Myr; Eisenbeiss et al. 2013). As a consequence of the decreasing luminosity of objects below the deuterium burning limit with increasing age (e.g., Burrows et al. 1997), it is natural that the sensitivity to Jovian planets is worse around members of these associations compared to significantly younger host stars. Yet some of these closer moving groups have ages comparable to that of LCC – such as the TW Hya association (10 ± 3 Myr) or the β Pic moving group (24 ± 3 Myr; Bell et al. 2015) – and should provide even better planet-detection sensitivities owing to their much closer distances. However, before speculating about potential reasons for this tentative overabundance of planetary-mass companions to our YSES targets, it is necessary to finish the second epoch observations of the survey and to derive reliable occurrence rates of planetary-mass companions to Sun-like stars in Sco-Cen.

6.7 Conclusions

We report the detection of a new directly imaged planet to the solar-mass primary YSES 2 that was discovered within the scope of YSES. Reassessment of the stellar parameters provided an effective temperature of $T_{\rm eff} = (4749 \pm 40)$ K, a luminosity of $\log(L/L_\odot) = -0.1854 \pm 0.0063$, a mass of $(1.10 \pm 0.03)\,M_\odot$, and a system age of (13.9 ± 2.3) Myr.

We detect YSES 2b in two consecutive epochs collected on 2018 April 30 and 2020 December 18 with VLT/SPHERE. The companion has a projected separation of approximately 1″.05, which translates to a physical minimum distance of ∼115 au with respect to the primary star. Photometric measurements in the H and K_s bands constrain a planet mass of $6.3^{+1.6}_{-0.9}\,M_{\rm Jup}$ according to AMES-COND and AMES-dusty evolutionary models. This mass estimate is supported by the position of the object in color-magnitude space, where it is located amongst the mid to late L type field brown dwarfs and close to HR 8799 c, d, and e. The slightly higher mass estimates of these exoplanets on the order of 7–12 $M_{\rm Jup}$ are consistent with the older system age of HR 8799 of 30–50 Myr.

The mass and separation of YSES 2b are inconsistent with planet populations for most in situ formation scenarios: whereas disk instabilities predominantly create companions above the deuterium burning limit at a separation of 110 au, core-accretion mechanisms are not efficient enough to form a planet of $6.3\,M_{\rm Jup}$ this

widely separated from the primary star. So, the new companion might be either at the low-mass end of potential in situ formation outcomes from top-down scenarios, or it formed via core accretion at closer separation to the star and migrated to its current location. Atmospheric characterization measurements of molecular abundance ratios, orbital monitoring, and evaluation of the eccentricity of the planet, or a deep search for additional companions in the system, might help to evaluate the likelihood of these potential formation pathways. While we cannot rule out scattering or capture scenarios, we point out that the former require an (as of yet) third undetected body in the system, while the latter are unlikely given numerical simulations. YSES 2b is an important addition to the sparsely populated group of wide-orbit gas giant companions. Owing to the moderate separation with respect to the primary star, spectroscopic observations with JWST, VLT/ERIS, or VLTI/GRAVITY will be easily available. These data will be important to further constrain the properties of this Jovian companion. Measurements of molecular abundance ratios such as C/O or its orbital eccentricity might even facilitate hypotheses regarding the most likely formation mechanism for this wide-orbit gas giant planet.

Our data rule out brown dwarf and stellar companions with $M > 13\,M_{\rm Jup}$ in the SPHERE/IRDIS field of view for angular separations $> 0\farcs15$ and at $0\farcs5$ we can exclude objects that are more massive than $6\,M_{\rm Jup}$. At separations that are larger than $2''$ we are even sensitive to planets with masses as low as $2\,M_{\rm Jup}$. In general, the applied PSF subtraction scheme based on RDI plus PCA is extremely successful and provides substantial contrast improvements (> 1 mag) for separations that are smaller than $1''$. In the H band, the PSF subtraction enhances our sensitivity by more than $45\,M_{\rm Jup}$ at $0\farcs2$, and the greatest contrast improvement of $\sim$3 mag is achieved at an angular separation of $0\farcs3$. Our YSES strategy with short snapshot observations of ≤ 5 min combined with a large reference library for PSF subtraction is certainly a promising approach to image planetary-mass companions to young, Sun-like stars in Sco-Cen. With three newly discovered planetary-mass companions in less than 40 h of allocated telescope time the survey efficiency is unprecedented and the mission concept can certainly be applied to future high-contrast imaging studies targeting different samples of pre-main-sequence stars.

6.A Observational conditions and setup

We present the observational setup and the weather conditions for our SPHERE observations in Table 6.3.

6.B Reference library

The reference libraries were compiled from the full amount of YSES data that were collected under ESO IDs 099.C-0698(A) (PI: Kenworthy), 0101.C-0153(A) (PI: Kenworthy), 0101.C-0341(A) (PI: Bohn), and 106.20X2.001 (PI: Vogt). We used RDI in the innermost region of the images $< 1\farcs2$, where the stellar halo was dominating the received flux. We deselected all targets with obvious point sources or extended structures in this region because these signals are not part of the stellar PSF and would therefore deteriorate the quality of our model created by PCA. The remaining targets, their observation epochs, and observing conditions that were used as a reference library for the H and K_s band data are listed in Tables 6.4 and 6.5, respectively.

Table 6.3: SPHERE observations of YSES 2.

Observation date (yyyy-mm-dd)	Filter	FWHM[a] (mas)	NEXP×NDIT×DIT[b] (1×1×s)	$\Delta\pi$[c] (°)	$\langle\omega\rangle$[d] ($''$)	$\langle X\rangle$[e]	$\langle\tau_0\rangle$[f] (ms)
2018-04-30	H	50.5	4×1×32	0.98	0.87	1.343	6.25
2020-12-08	K_s	61.7	1×18×16	1.37	0.55	1.52	4.30

Notes. [(a)] Full width at half maximum measured for the non-coronagraphic stellar PSF. [(b)] NEXP describes the number of exposures, NDIT is the number of subintegrations per exposure, and DIT is the detector integration time of an individual subintegration. [(c)] $\Delta\pi$ describes the amount of field rotation during the observation, if it is carried out in pupil-stabilized mode (only valid for CI observations). [(d)] $\langle X\rangle$ denotes the average airmass during the observation. [(e)] $\langle\omega\rangle$ denotes the average seeing conditions during the observation. [(f)] $\langle\tau_0\rangle$ denotes the average coherence time during the observation.

In the H band we have 269 individual reference frames and in the K_s band we have 164.

6.C Extraction of companion astrometry and photometry

We extracted the astrometry and photometry of the companion with `PynPoint`'s `SimplexMinimizationModule`. This injects an artificial planet into the data prior to the stellar PSF subtraction with RDI plus PCA. The planet template PSF is obtained from the unsaturated, non-coronagraphic flux images that were taken alongside the observations. The methods injects the artificial planet into the data at the approximate position and magnitude of the real point source, considering the parallactic rotation during the observing sequence. The PSF subtraction is performed using the same library as before (see Appendix 6.B), we smooth the image with a Gaussian kernel with a FWHM of 12 mas (which corresponds to the size of a detector pixel) to reduce pixel-to-pixel variations, and we evaluate the residuals in an aperture with a diameter of $\sim 0\farcs25$ around the injection position. We choose the image curvature, which is represented by the determinant of the Hessian matrix as function of merit, which we aim to minimize by varying the input separation, position angle, and magnitude contrast of our artificial companion. We do not use the absolute value norm as presented by Wertz et al. (2017) as an objective to the minimization because this would not consider large-scale features in the residual image that are not correctly modeled by our PSF subtraction approach. Such a feature is for instance the asymmetric wind driven halo (Cantalloube et al. 2018) that is apparent in the K_s band data in the northeastern to southwestern direction (see right panel of Figure 6.2). This uncorrected stellar flux contributes to the planet signal and minimization of the absolute value norm around the planet position would certainly overestimate its flux and perhaps even compromise its astrometry. Planet separation, position angle, and magnitude contrast are optimized simultaneously by a Nelder-Mead simplex minimization algorithm (Nelder & Mead 1965).

Owing to the optimization process our final values for the planetary astrometry and photometry do not exhibit any intrinsic uncertainties. To derive the systematic uncertainties of our injection and minimization approach, we follow the analysis described by Stolker et al. (2020a), using the cube in which the optimized negative planet is injected such that no companion signal remains in the data. For 24 position angles that are equidistantly distributed in polar space we inject positive artificial companions into the data using the same magnitude contrast and the same radial separation as previously determined for our companion. We extract the astrometry and photometry of these artificial companions with the same method as described before and we evaluate the deviations from the injection position and flux. The standard deviation along the 24 distinct positions is utilized as uncertainty of our extraction method. These are combined with additional astrometric uncertainties originating from the detector plate scale, the true north offset, and the centering accuracy of 2.5 mas (see SPHERE manual) to derive the final value of planet separation and position angle as presented in Table 6.2. For the companion photometry, we add uncertainties due to the variation of the unsaturated stellar PSF throughout the sequence of flux measurements and we account for transmissivity variations of the neutral density filter across the broadband filter that was used for our observations (either the H or K_s band).

Table 6.4: Reference library for the data reduction in H band.

Target (2MASS ID)	Observation date (yyyy-mm-dd)	NEXP×NDIT×DIT[a] (1×1×s)	$\langle\omega\rangle^b$ ($''$)	$\langle X\rangle^c$	$\langle\tau_0\rangle^d$ (ms)
J11272881-3952572	2017-04-18	4×1×32	1.51	1.10	1.40
J11320835-5803199	2017-06-17	4×1×32	0.67	1.47	2.90
J11445217-6438548	2018-05-14	4×1×32	0.72	1.31	2.38
J11454278-5739285	2018-06-04	4×1×32	0.70	1.19	2.80
J11454278-5739285	2019-01-13	4×1×32	1.14	1.62	3.83
J12065276-5044463	2017-04-02	3×1×32	1.24	1.11	1.50
J12090225-5120410	2018-05-15	4×1×32	0.86	1.12	2.70
J12090225-5120410	2019-12-14	12×2×32	0.63	1.51	7.75
J12101065-4855476	2017-04-18	4×1×32	1.71	1.15	1.40
J12113142-5816533	2018-12-22	3×2×32	1.46	1.47	2.13
J12113142-5816533	2019-02-18	4×2×32	0.45	1.23	14.30
J12160114-5614068	2018-12-27	4×2×32	0.41	1.45	11.88
J12164023-7007361	2018-12-23	3×1×32	0.98	1.59	2.93
J12164023-7007361	2019-02-15	4×1×32	0.54	1.63	11.20
J12185802-5737191	2017-06-17	2×1×32	0.72	1.22	2.70
J12195938-5018404	2018-12-30	4×1×32	0.53	1.62	8.00
J12210499-7116493	2019-01-12	4×2×32	0.80	1.53	4.25
J12220430-4841248	2017-04-18	3×1×32	1.82	1.17	1.40
J12234012-5616325	2017-06-17	4×1×32	0.62	1.72	3.45
J12264842-5215070	2018-12-30	4×1×32	0.40	1.38	8.20
J12302957-5222269	2018-12-30	4×1×32	0.38	1.33	9.85
J12333381-5714066	2019-01-01	4×1×32	0.76	1.37	7.03
J12333381-5714066	2019-01-14	4×1×32	1.26	1.21	2.45
J12361767-5042421	2018-12-30	4×1×32	0.51	1.59	4.68
J12361767-5042421	2019-12-18	16×2×32	1.14	1.57	3.07
J12374883-5209463	2018-12-30	4×1×32	0.41	1.50	7.30
J12383556-5916438	2019-01-03	4×1×32	0.52	1.59	13.90
J12383556-5916438	2019-01-12	4×1×32	0.79	1.26	4.25
J12393796-5731406	2017-06-17	4×1×32	0.64	1.77	3.83
J12404664-5211046	2018-04-30	4×1×32	0.74	1.13	7.05
J12442412-5855216	2017-06-17	4×3×32	0.71	1.37	2.67
J12454884-5410583	2018-04-30	4×1×32	0.71	1.15	6.92
J12480778-4439167	2017-06-17	4×2×32	0.90	1.34	2.75
J12505143-5156353	2019-01-12	4×1×32	1.14	1.32	3.75
J12510556-5253121	2019-01-08	4×1×32	0.58	1.68	3.90
J13015069-5304581	2019-01-08	4×1×32	0.55	1.60	3.95
J13055087-5304181	2018-06-11	4×1×32	0.82	1.14	1.95
J13055087-5304181	2018-07-04	4×1×32	1.73	1.14	1.70
J13064012-5159386	2018-04-30	4×1×32	0.56	1.13	8.15
J13065439-4541313	2018-04-08	4×1×32	0.46	1.09	5.65
J13095880-4527388	2018-05-01	4×1×32	1.08	1.07	2.70
J13103245-4817036	2018-05-01	4×1×32	1.03	1.09	3.30
J13121764-5508258	2017-08-31	4×1×32	0.68	2.22	4.42
J13121764-5508258	2018-05-15	4×1×32	0.62	1.16	2.50
J13174687-4456534	2018-05-28	4×1×32	0.70	1.07	4.33

Table 6.4 (continued).

Target (2MASS ID)	Observation date (yyyy-mm-dd)	NEXP×NDIT×DIT[a] (1×1×s)	$\langle\omega\rangle^b$ ($''$)	$\langle X\rangle^c$	$\langle\tau_0\rangle^d$ (ms)
J13334410-6359345	2017-07-05	4×1×32	1.06	1.53	3.05
J13343188-4209305	2017-04-02	4×1×32	1.14	1.21	1.70
J13354082-4818124	2017-04-02	4×1×32	1.06	1.30	2.08
J13380596-4344564	2017-04-02	4×1×32	1.05	1.32	2.40
J13455599-5222255	2018-04-28	4×1×32	0.64	1.13	6.35

Notes. [(a)] NEXP describes the number of exposures, NDIT is the number of subintegrations per exposure, and DIT is the detector integration time of an individual subintegration. [(b)] $\langle X\rangle$ denotes the average airmass during the observation. [(c)] $\langle\omega\rangle$ denotes the average seeing conditions during the observation. [(d)] $\langle\tau_0\rangle$ denotes the average coherence time during the observation.

6.D Astrometric analysis of background objects

In addition to YSES 2b, there are four candidate companions (CCs) in the SPHERE field of view that we could identify in both observational epochs. These CCs are presented in Figure 6.6, in which we show the de-rotated data from the night of 2020 December 12. No PSF subtraction with RDI is performed, instead we just applied an unsharp mask with a Gaussian kernel size of 5 pixels. YSES 2b can easily be identified in this image product as well. For the remaining CCs, we present the relative astrometric offsets between both observational epochs in the proper motion diagram in Figure 6.7. The relative motions of CCs 2–5 are clearly compatible with stationary background objects, and co-movement can be ruled out for all of them.

Table 6.5: Reference library for the data reduction in K_s band.

Target (2MASS ID)	Observation date (yyyy-mm-dd)	NEXP×NDIT×DIT[a] (1×1×s)	$\langle\omega\rangle^b$ ($''$)	$\langle X\rangle^c$	$\langle\tau_0\rangle^d$ (ms)
J11445217-6438548	2018-05-14	4×1×32	0.77	1.31	2.60
J11454278-5739285	2019-01-13	4×1×32	1.18	1.59	3.58
J12090225-5120410	2018-05-15	4×1×32	0.70	1.12	2.90
J12113142-5816533	2018-12-22	4×2×32	1.38	1.44	2.05
J12113142-5816533	2019-02-18	4×2×32	0.45	1.22	15.00
J12160114-5614068	2018-12-27	4×2×32	0.47	1.42	10.27
J12164023-7007361	2018-12-23	4×1×32	1.06	1.58	3.43
J12164023-7007361	2019-02-15	4×1×32	0.57	1.61	10.75
J12195938-5018404	2018-12-30	4×1×32	0.55	1.59	9.00
J12210499-7116493	2019-01-12	4×2×32	0.82	1.52	4.40
J12264842-5215070	2018-12-30	4×1×32	0.41	1.36	9.20
J12302957-5222269	2018-12-30	4×1×32	0.45	1.32	7.48
J12333381-5714066	2019-01-01	4×1×32	0.80	1.36	6.25
J12333381-5714066	2019-01-14	4×1×32	1.24	1.21	2.30
J12333381-5714066	2020-12-10	1×20×16	0.58	1.76	5.50
J12361767-5042421	2018-12-30	4×1×32	0.47	1.56	6.22
J12374883-5209463	2018-12-30	4×1×32	0.46	1.48	6.95
J12383556-5916438	2019-01-03	4×1×32	0.46	1.56	12.47
J12383556-5916438	2019-01-12	4×1×32	0.94	1.26	3.45
J12404664-5211046	2018-04-30	4×1×32	0.87	1.13	7.10
J12454884-5410583	2018-04-30	4×1×32	0.66	1.15	8.97
J12505143-5156353	2019-01-12	4×1×32	1.03	1.31	4.10
J12510556-5253121	2019-01-08	4×1×32	0.52	1.65	3.98
J13015069-5304581	2019-01-08	4×1×32	0.49	1.58	4.80
J13055087-5304181	2018-06-11	4×1×32	0.93	1.14	2.02
J13055087-5304181	2018-07-04	4×1×32	1.73	1.14	1.70
J13064012-5159386	2018-04-30	4×1×32	0.56	1.13	9.88
J13065439-4541313	2018-04-08	4×1×32	0.55	1.09	4.68
J13095880-4527388	2018-05-01	4×1×32	1.03	1.07	2.45
J13103245-4817036	2018-05-01	4×1×32	0.87	1.10	4.40
J13121764-5508258	2018-05-15	4×1×32	0.62	1.16	3.00
J13174687-4456534	2018-05-28	4×1×32	0.67	1.07	4.15
J13455599-5222255	2018-04-28	4×1×32	0.65	1.13	6.03

Notes. [a] NEXP describes the number of exposures, NDIT is the number of subintegrations per exposure, and DIT is the detector integration time of an individual subintegration. [b] $\langle X\rangle$ denotes the average airmass during the observation. [c] $\langle\omega\rangle$ denotes the average seeing conditions during the observation. [d] $\langle\tau_0\rangle$ denotes the average coherence time during the observation.

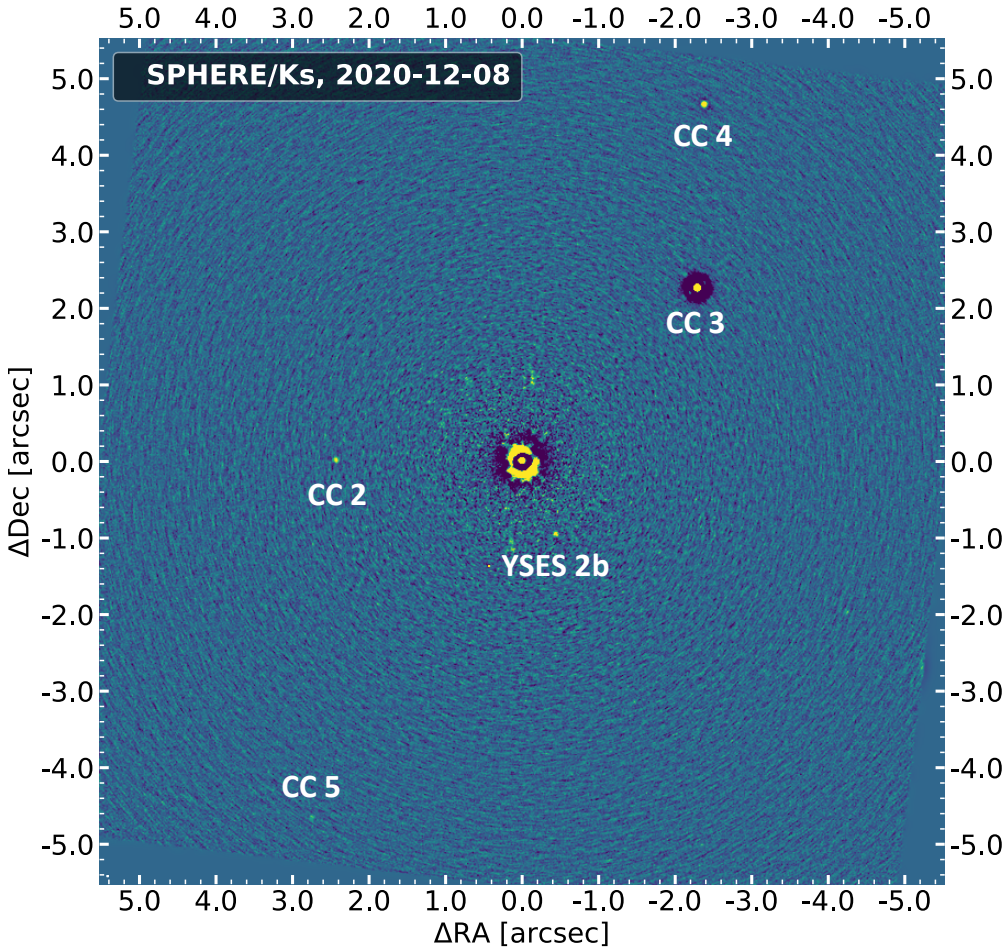

Figure 6.6: Reduced SPHERE data for the full IRDIS field of view. The images are de-rotated and median combined; an unsharp mask is applied to remove the stellar halo. Four additional companion candidates to YSES 2b are identified in the field of view. The image is presented at an arbitrary logarithmic color scale to highlight the off-axis point sources.

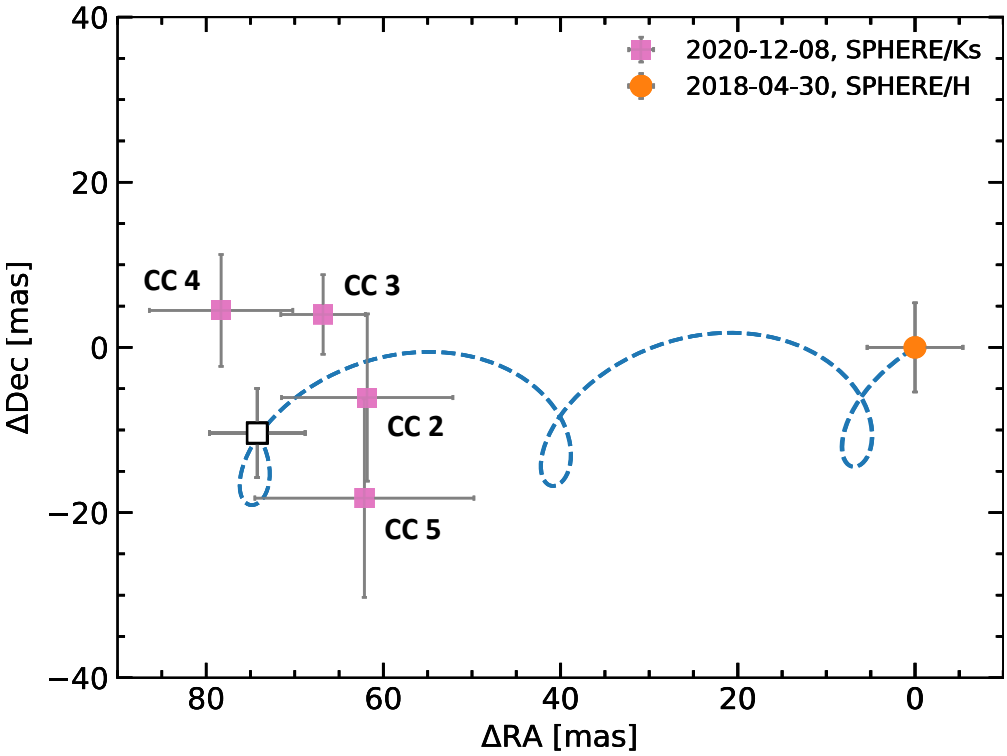

Figure 6.7: Proper motion plot for background objects in the SPHERE/IRDIS field of view. The pink markers indicate the relative astrometric offsets to the first observational epoch that is plotted at the origin of the coordinate system (orange marker). The blue trajectory represents the simulated motion of a static background object at infinity and the white marker shows the relative positional offset of such an object at the time of our second observation.

Chapter 7

Outlook

The main objective of my future work will certainly be the conclusion of YSES. First and foremost, this means collecting all remaining second epoch observations for 44 stars from our sample that host unconfirmed candidate companions. As soon as these data have been collected, we can derive a meaningful occurrence rate of extra-solar giant planets to young, Sun-like stars. The new planet detections from YSES and our sensitivity limits will then be combined in a final statistical survey paper. Comparison to model predictions based on the various formation mechanisms will enable us to probe the formation pathways of giant Jovian companion to Sun-like stars, similar to Nielsen et al. (2019) and Vigan et al. (2020). Never has this problem be approached on a sample that was as homogeneous and that contained as many stars of $1\,M_{\odot}$. Therefore, our results will have vital implications for gas giant formation in solar-like environments.

Besides, each detected planetary-mass companion will foster an abundance of follow-up characterization measurements. This will allow to test the framework proposed by Öberg et al. (2011) on a large and statistical significant sample of giant companions for the first time. We will begin to systematically probe molecular abundance ratios in exoplanet atmospheres, enabling analyses as to whether this quantity is indeed a reliable tracer of planetary birthplaces. Additional isotopologue measurements might be helpful to support hypotheses based on molecular abundance ratios alone. Especially VLT/CRIRES^{+}, VLT/ERIS, VLTI/GRAVITY, and JWST will play crucial roles in obtaining these measurements.

Future direct imaging surveys (perhaps inspired by the YSES approach and strategy) will certainly continue to expand the sample of gas giant wide-orbit planets. A potential successor program of YSES could be designed as described in the following section.

7.1 LEGACYS: The Large Extrasolar Giant planet Abundance Census around Young Suns

By construction, the YSES sample is representing only a short time frame of the pre-main-sequence evolution of planetary systems. To test several formation scenarios of early, solar-like environments, the logical next step is to extend the sample towards the temporal dimension without altering the previously fixed constraint on the host star masses. Planet occurrence rates and semi-major axis evolution as a function of

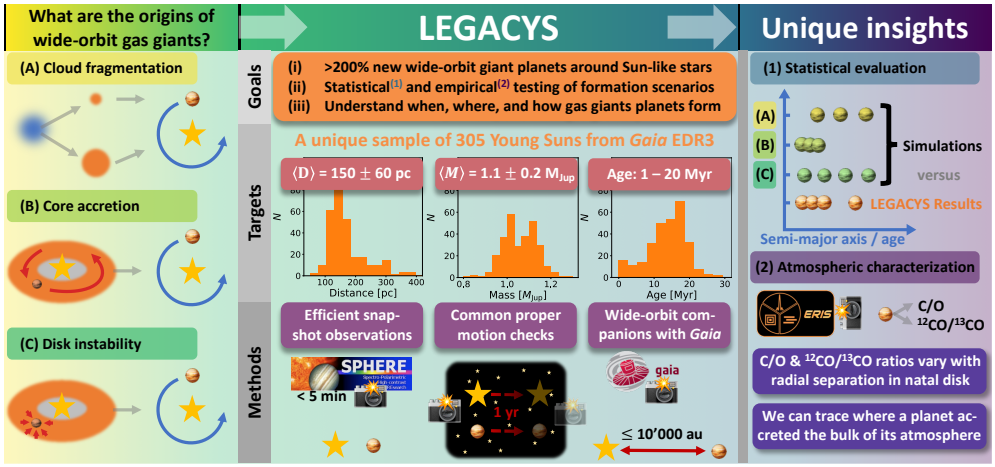

Figure 7.1: Schematic overview of the LEGACYS project.

stellar age are great tracers of different formation scenarios: scenario (B) -– in which the planets form close to the host star and migrate outwards driven by scattering processes — imposes a positive correlation of planet separations and increasing system ages, whereas a flat distribution of semi-major axes versus time is expected for the in-situ formation mechanisms (A,C).

LEGACYS aims to shed light on the enigmatic origins of wide-orbit gas-giant planets in young solar systems by observing a homogeneous sample of 305 solar-mass pre-main sequence stars to detect and characterize wide-orbit companions to these young, solar analogs (see Figure 7.1). This survey will

(i) more than triple the small sample size of directly imaged gas-giant planets to Sun-like hosts to

(ii) facilitate statistical analyses regarding the occurrence rates of these objects as a function of time without diluting effects due to varying host star masses (see Chapter 1.3.1) and to

(iii) enable atmospheric characterization of a significant sample of wide-orbit Jovian companions (see Chapter 1.3.2),

(iv) and thus, foster accurate testing of different formation scenarios by exploring the full spatial, temporal, and chemical parameter space of our sample for the first time (right panel of Figure 7.1).

The survey strategy is summarized in the carton presented in Figure 7.1. It relies on an unbiased sample of young, solar-type stars with various ages, compiled from the pre-main sequence star catalog compiled by Zari et al. (2018). These targets are members of various young associations representing different ages of early pre-main sequence evolution: Scorpius-Centaurus – with its sub-groups Upper Scorpius (10 ± 3 Myr), Upper Centaurus Lupus (16 ± 2 Myr), and LCC (15 ± 3 Myr) – Lupus ($1 - 3$ Myr), Taurus (~ 1 Myr), and Corona Australis ($1 - 3$ Myr). As presented in Figure 7.2, the LEGACYS sample comprises the closest and largest selection of young, solar-mass stars to our Sun, complementary to the parameter space probed by other

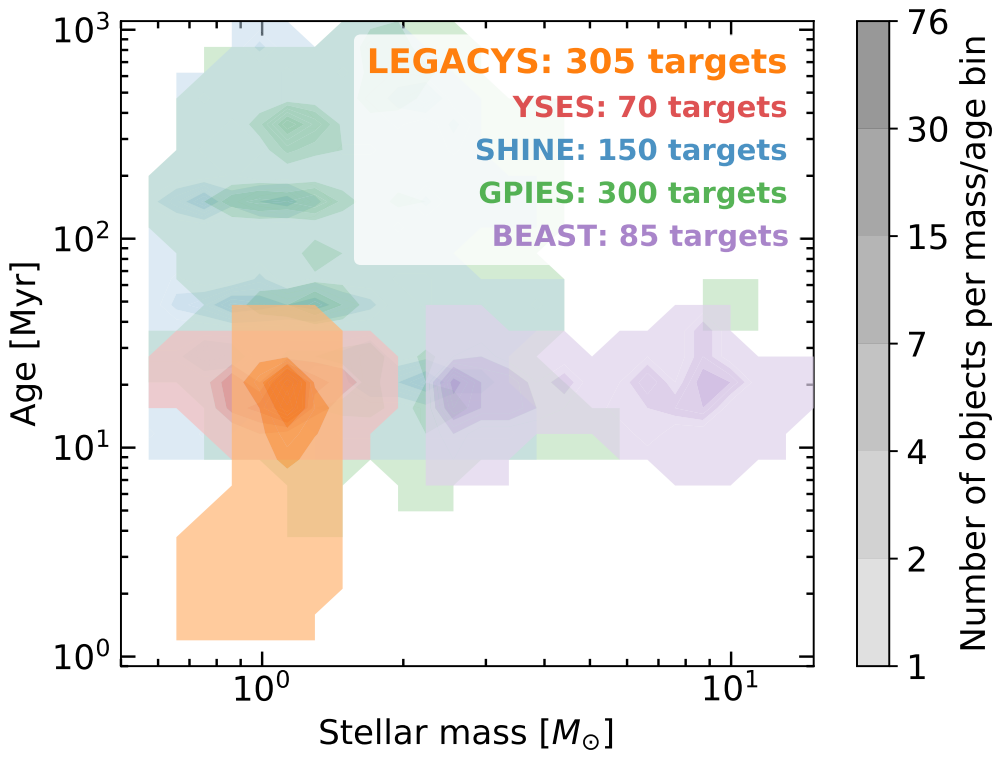

Figure 7.2: Comparison of the LEGACYS sample to previous direct imaging surveys. LEGACYS is expanding the YSES sample towards the temporal dimension and targeting the largest selection of young, Sun-like stars amongst all surveys. For each survey, the different shades of color represent the number densities of target stars in this mass-age diagram.

direct imaging campaigns. These targets can be observed in a similar snapshot approach as applied for YSES; data reduction would be performed by RDI with an even larger reference library of similar targets. With an abundance of new detections of wide-orbit, planetary-mass companions, this new survey will have an unparalleled legacy value and will provide a temporally-resolved insight into the initial stages of planetary systems for the first time. Studying the entire pre-main-sequence evolution of solar-like environments and comparing the observed occurrence rates to simulated planet populations will provide vital implications for the efficiency of the underlying planet formation mechanisms. YSES and perhaps LEGACYS will be crucial to constrain the underlying formation pathways of wide-orbit Jovian gas giants to solar-type host stars, and these surveys will perfectly complement the results of other large programs such as SHINE, GPIES, and BEAST.

7.2 Our place in the Universe

The observations of the past years have shown that planetary systems are ubiquitous with various architectures either similar or vastly different from our Solar System. Based on this plethora of exoplanets, it is likely that one of these worlds will exhibit favorable conditions to develop something that can be considered as *life*. As

humanity has learned to accept their own mediocrity throughout the past centuries, it would not be surprising if we learned one day that there is life outside of Earth. Recent estimates of $\eta_\oplus$ – defined as the occurrence rate of Earth-sized rocky planets that reside in the habitable zones of their host star – can be quite inconsistent and vary from $\eta_\oplus = 0.064$ (Silburt et al. 2015) to $\eta_\oplus = 0.35$ (Barbato et al. 2018). Yet they are usually significantly larger than zero. Even if the probability that an individual terrestrial planet in the habitable zone facilitates favorable conditions for life to emerge is tiny, this small likelihood should be compensated by the huge number of stars in the Universe.

Of course, this does not necessarily mean that this extraterrestrial life will actually be located in our Galactic neighborhood; and even if it is, it is still unclear if we will be able to actually detect it. However, the recent progress in exoplanetary sciences provided promising results, and especially future observatories such as the ELTs, LUVOIR, HabEx, and LIFE will play a crucial part in finding an answer to this most ancient question of humankind.

Bibliography

ALMA Partnership et al., 2015, ApJ, 808, L3

Absil O., Bakker E. J., Schoeller M., Gondoin P. A., 2004, in Traub W. A., ed., Society of Photo-Optical Instrumentation Engineers (SPIE) Conference Series Vol. 5491, New Frontiers in Stellar Interferometry. p. 1320, doi:10.1117/12.549311

Adams E. R., Dupree A. K., Kulesa C., McCarthy D., 2013, AJ, 146, 9

Ali-Dib M., Mousis O., Petit J.-M., Lunine J. I., 2014, ApJ, 785, 125

Alibert Y., Mordasini C., Benz W., Winisdoerffer C., 2005, A&A, 434, 343

Allard F., Hauschildt P. H., Alexander D. R., Tamanai A., Schweitzer A., 2001, ApJ, 556, 357

Allard F., Homeier D., Freytag B., 2012, Philosophical Transactions of the Royal Society of London Series A, 370, 2765

Amara A., Quanz S. P., 2012, MNRAS, 427, 948

Anderson D. R., et al., 2011, ApJ, 726, L19

Anderson D. R., et al., 2014a, arXiv e-prints, p. arXiv:1410.3449

Anderson D. R., et al., 2014b, MNRAS, 445, 1114

Anderson D. R., et al., 2018, arXiv e-prints, p. arXiv:1812.09264

Andrews S. M., Williams J. P., 2007, ApJ, 659, 705

Andrews S. M., et al., 2012, ApJ, 744, 162

Andrews S. M., et al., 2018, ApJ, 869, L41

Anglada-Escudé G., et al., 2016, Nature, 536, 437

Ansdell M., et al., 2016, ApJ, 828, 46

Artigau É., Gagné J., Faherty J., Malo L., Naud M.-E., Doyon R., Lafrenière D., Beletsky Y., 2015, The Astrophysical Journal, 806, 254

Asensio-Torres R., et al., 2019, A&A, 622, A42

Astropy Collaboration et al., 2013, A&A, 558, A33

Astropy Collaboration et al., 2018, AJ, 156, 123

Auvergne M., et al., 2009, A&A, 506, 411

Avenhaus H., Quanz S. P., Schmid H. M., Meyer M. R., Garufi A., Wolf S., Dominik C., 2014, ApJ, 781, 87

Avenhaus H., et al., 2018, ApJ, 863, 44

Babcock H. W., 1953, PASP, 65, 229

Bailer-Jones C. A. L., Rybizki J., Fouesneau M., Mantelet G., Andrae R., 2018, AJ, 156, 58

Bailey V., et al., 2014, ApJ, 780, L4

Bakos G., Noyes R. W., Kovács G., Stanek K. Z., Sasselov D. D., Domsa I., 2004, PASP, 116, 266

Baraffe I., Chabrier G., Barman T. S., Allard F., Hauschildt P. H., 2003, A&A, 402, 701

Baraffe I., Homeier D., Allard F., Chabrier G., 2015, A&A, 577, A42

Baranne A., et al., 1996, A&AS, 119, 373

Barbato D., Bonomo A. S., Sozzetti A., Morbidelli R., 2018, arXiv e-prints, p. arXiv:1811.08249

Barbieri M., et al., 2007, A&A, 476, L13

Barclay T., Quintana E. V., Raymond S. N., Penny M. T., 2017, ApJ, 841, 86

Barman T. S., Macintosh B., Konopacky Q. M., Marois C., 2011, ApJ, 733, 65

Barrado y Navascués D., Martín E. L., 2003, AJ, 126, 2997

Batygin K., 2012, Nature, 491, 418

Batygin K., Brown M. E., 2016, AJ, 151, 22

Batygin K., Bodenheimer P. H., Laughlin G. P., 2016, ApJ, 829, 114

Bayo A., Rodrigo C., Barrado Y Navascués D., Solano E., Gutiérrez R., Morales-Calderón M., Allard F., 2008, A&A, 492, 277

Béjar V. J. S., Zapatero Osorio M. R., Pérez-Garrido A., Álvarez C., Martín E. L., Rebolo R., Villó-Pérez I., Díaz-Sánchez A., 2008, The Astrophysical Journal, 673, L185

Bell C. P. M., Mamajek E. E., Naylor T., 2015, MNRAS, 454, 593

Benedict G. F., et al., 2006, AJ, 132, 2206

Benisty M., et al., 2017, A&A, 597, A42

Benisty M., et al., 2018, A&A, 619, A171

Bennett D. P., Anderson J., Bond I. A., Udalski A., Gould A., 2006, ApJ, 647, L171

Bergfors C., et al., 2013, MNRAS, 428, 182

Bernardakis G. N., 1893, Quaestiones Naturales. Teubner

Best W. M. J., et al., 2018, ApJS, 234, 1

Beuzit J. L., et al., 2019, A&A, 631, A155

Biller B. A., Bonnefoy M., 2018, Exoplanet Atmosphere Measurements from Direct Imaging. p. 101, doi:10.1007/978-3-319-55333-7˙101

Biller B. A., et al., 2013, ApJ, 777, 160

Biller B. A., et al., 2018, AJ, 155, 95

Biller B. A., et al., 2021, MNRAS, 503, 743

Bodenheimer P., Hubickyj O., Lissauer J. J., 2000, Icarus, 143, 2

Boehle A., Quanz S. P., Lovis C., Ségransan D., Udry S., Apai D., 2019, A&A, 630, A50

Bohn A. J., et al., 2019, A&A, 624, A87

Bohn A. J., et al., 2020a, MNRAS, 492, 431

Bohn A. J., et al., 2020b, ApJ, 898, L16

Bohn A. J., et al., 2021, A&A, 648, A

Boley A. C., Granados Contreras A. P., Gladman B., 2016, ApJ, 817, L17

Bond I. A., et al., 2004, ApJ, 606, L155

Bonnefoy M., et al., 2011, A&A, 528, L15

Bonnefoy M., et al., 2013, A&A, 555, A107

Bonnefoy M., et al., 2016, A&A, 587, A58

Borucki W. J., Summers A. L., 1984, Icarus, 58, 121

Borucki W. J., et al., 2010, Science, 327, 977

Boss A. P., 1997, Science, 276, 1836

Boss A. P., 2011, ApJ, 731, 74

Bouchy F., et al., 2010, A&A, 519, A98

Bowler B. P., 2016, PASP, 128, 102001

Bowler B. P., Liu M. C., Shkolnik E. L., Dupuy T. J., 2013, The Astrophysical Journal, 774, 55

Bowler B. P., et al., 2017, The Astronomical Journal, 153, 18

Bowler B. P., Blunt S. C., Nielsen E. L., 2020, AJ, 159, 63

Bradley L., et al., 2016, Photutils: Photometry tools (ascl:1609.011)

Brandl B. R., et al., 2014, in Ramsay S. K., McLean I. S., Takami H., eds, Society of Photo-Optical Instrumentation Engineers (SPIE) Conference Series Vol. 9147, Ground-based and Airborne Instrumentation for Astronomy V. p. 914721 (arXiv:1409.3087), doi:10.1117/12.2056468

Brown T. M., 2001, ApJ, 553, 1006

Brown T. M., 2003, ApJ, 593, L125

Brown D. J. A., et al., 2017, MNRAS, 464, 810

Burgasser A. J., 2007, ApJ, 659, 655

Burgasser A. J., McElwain M. W., 2006, AJ, 131, 1007

Burgasser A. J., Marley M. S., Ackerman A. S., Saumon D., Lodders K., Dahn C. C., Harris H. C., Kirkpatrick J. D., 2002, ApJ, 571, L151

Burgasser A. J., McElwain M. W., Kirkpatrick J. D., Cruz K. L., Tinney C. G., Reid I. N., 2004, AJ, 127, 2856

Burgasser A. J., Liu M. C., Ireland M. J., Cruz K. L., Dupuy T. J., 2008, ApJ, 681, 579

Burgasser A. J., Cruz K. L., Cushing M., Gelino C. R., Looper D. L., Faherty J. K., Kirkpatrick J. D., Reid I. N., 2010, ApJ, 710, 1142

Burnet J., 1903, Platonis Opera. Oxford University Press

Burrows A., et al., 1997, ApJ, 491, 856

Butler R. P., Marcy G. W., Williams E., Hauser H., Shirts P., 1997, ApJ, 474, L115

Caffau E., Ludwig H. G., Steffen M., Freytag B., Bonifacio P., 2011, Sol. Phys., 268, 255

Cantalloube F., et al., 2015, A&A, 582, A89

Cantalloube F., et al., 2018, A&A, 620, L10

Cantalloube F., et al., 2020, in Society of Photo-Optical Instrumentation Engineers (SPIE) Conference Series. p. 114485A, doi:10.1117/12.2574803

Carbillet M., et al., 2011, Experimental Astronomy, 30, 39

Carson J., et al., 2013, The Astrophysical Journal, 763, L32

Casassus S., et al., 2015, ApJ, 812, 126

Castelli F., Kurucz R. L., 1994, A&A, 281, 817

Chabrier G., 2003, PASP, 115, 763

Chabrier G., Baraffe I., Allard F., Hauschildt P., 2000, ApJ, 542, 464

Chabrier G., Baraffe I., Leconte J., Gallardo J., Barman T., 2009, in Stempels E., ed., American Institute of Physics Conference Series Vol. 1094, 15th Cambridge Workshop on Cool Stars, Stellar Systems, and the Sun. pp 102–111 (arXiv:0810.5085), doi:10.1063/1.3099078

Charbonneau D., Brown T. M., Latham D. W., Mayor M., 2000, ApJ, 529, L45

Charbonneau D., Brown T. M., Dunham E. W., Latham D. W., Looper D. L., Mandushev G., 2004, in Holt S. S., Deming D., eds, American Institute of Physics Conference Series Vol. 713, The Search for Other Worlds. pp 151–160 (arXiv:astro-ph/0401063), doi:10.1063/1.1774515

Chatterjee S., Ford E. B., Matsumura S., Rasio F. A., 2008, ApJ, 686, 580

Chauvin G., Lagrange A. M., Dumas C., Zuckerman B., Mouillet D., Song I., Beuzit J. L., Lowrance P., 2004, A&A, 425, L29

Chauvin G., et al., 2005, Astronomy and Astrophysics, 438, L29

Chauvin G., et al., 2017a, in SF2A-2017: Proceedings of the Annual meeting of the French Society of Astronomy and Astrophysics. p. Di

Chauvin G., et al., 2017b, Astronomy and Astrophysics, 605, L9

Chauvin G., et al., 2018, A&A, 617, A76

Cheetham A. C., et al., 2019, A&A, 622, A80

Chen C. H., Pecaut M., Mamajek E. E., Su K. Y. L., Bitner M., 2012, ApJ, 756, 133

Chiu K., Fan X., Leggett S. K., Golimowski D. A., Zheng W., Geballe T. R., Schneider D. P., Brinkmann J., 2006, AJ, 131, 2722

Choi J., Dotter A., Conroy C., Cantiello M., Paxton B., Johnson B. D., 2016, ApJ, 823, 102

Choquet E., et al., 2014, in Exploring the Formation and Evolution of Planetary Systems. pp 30–31, doi:10.1017/S1743921313007722

Choquet É., et al., 2016, ApJ, 817, L2

Choquet É., et al., 2017, ApJ, 834, L12

Christiaens V., et al., 2019, MNRAS, 486, 5819

Ciceri S., et al., 2013, A&A, 557, A30

Cincotta P. M., Giordano C. M., Simó C., 2003, Physica D Nonlinear Phenomena, 182, 151

Claudi R. U., et al., 2008, in Ground-based and Airborne Instrumentation for Astronomy II. p. 70143E, doi:10.1117/12.788366

Cocconi G., Morrison P., 1959, Nature, 184, 844

Cochran W. D., Hatzes A. P., 1996, Ap&SS, 241, 43

Codona J. L., Kenworthy M. A., Hinz P. M., Angel J. R. P., Woolf N. J., 2006, in McLean I. S., Iye M., eds, Society of Photo-Optical Instrumentation Engineers (SPIE) Conference Series Vol. 6269, Society of Photo-Optical Instrumentation Engineers (SPIE) Conference Series. p. 62691N, doi:10.1117/12.672727

Coelho P. R. T., 2014, MNRAS, 440, 1027

Collier Cameron A., et al., 2007, MNRAS, 375, 951

Cosentino R., et al., 2012, in Ground-based and Airborne Instrumentation for Astronomy IV. p. 84461V, doi:10.1117/12.925738

Cridland A. J., Pudritz R. E., Alessi M., 2016, MNRAS, 461, 3274

Cruz K. L., Burgasser A. J., Reid I. N., Liebert J., 2004, ApJ, 604, L61

Currie T., et al., 2011, ApJ, 729, 128

Currie T., et al., 2013, ApJ, 776, 15

Cushing M. C., Rayner J. T., Vacca W. D., 2005, ApJ, 623, 1115

Cutri R. M., et al. 2014, VizieR Online Data Catalog, p. II/328

Cutri R. M., et al., 2003, 2MASS All Sky Catalog of point sources.. IPAC

Cutri R. M., et al., 2012a, VizieR Online Data Catalog, p. II/281

Cutri R. M., et al., 2012b, VizieR Online Data Catalog, p. II/311

Daemgen S., Hormuth F., Brandner W., Bergfors C., Janson M., Hippler S., Henning T., 2009, A&A, 498, 567

Dahlqvist C. H., Cantalloube F., Absil O., 2020, A&A, 633, A95

Dahlqvist C. H., Louppe G., Absil O., 2021, A&A, 646, A49

Damasso M., et al., 2020, Science Advances, 6, eaax7467

Damiani F., Prisinzano L., Pillitteri I., Micela G., Sciortino S., 2019, A&A, 623, A112

Davies R., et al., 2018, in Evans C. J., Simard L., Takami H., eds, Society of Photo-Optical Instrumentation Engineers (SPIE) Conference Series Vol. 10702, Ground-based and Airborne Instrumentation for Astronomy VII. p. 1070209 (arXiv:1807.05089), doi:10.1117/12.2311480

Debes J. H., et al., 2017, ApJ, 835, 205

Deeming T. J., 1964, MNRAS, 127, 493

Delorme P., et al., 2013, Astronomy and Astrophysics, 553, L5

Delrez L., et al., 2014, A&A, 563, A143

Delrez L., et al., 2016, MNRAS, 458, 4025

Delrez L., et al., 2018, in Marshall H. K., Spyromilio J., eds, Society of Photo-Optical Instrumentation Engineers (SPIE) Conference Series Vol. 10700, Ground-based and Airborne Telescopes VII. p. 107001I (arXiv:1806.11205), doi:10.1117/12.2312475

Demory B.-O., et al., 2013, ApJ, 776, L25

Dhital S., Burgasser A. J., Looper D. L., Stassun K. G., 2011, AJ, 141, 7

Dietrich J., Ginski C., 2018, A&A, 620, A102

Dodson-Robinson S. E., Veras D., Ford E. B., Beichman C. A., 2009, ApJ, 707, 79

Dohlen K., et al., 2008, in McLean I. S., Casali M. M., eds, Society of Photo-Optical Instrumentation Engineers (SPIE) Conference Series Vol. 7014, Ground-based and Airborne Instrumentation for Astronomy II. p. 70143L, doi:10.1117/12.789786

Dominik C., Dullemond C. P., Waters L. B. F. M., Walch S., 2003, A&A, 398, 607

Dorn R. J., et al., 2014, The Messenger, 156, 7

Dotter A., 2016, ApJS, 222, 8

Drake S., 1957, Discoveries and opinions of Galileo. Doubleday New York

Drake F. D., 1961, Physics Today, 14, 40

Drake F. D., 1979, Cosmic Search, 1, 10

Durisen R. H., Boss A. P., Mayer L., Nelson A. F., Quinn T., Rice W. K. M., 2007, in Reipurth B., Jewitt D., Keil K., eds, Protostars and Planets V. p. 607 (arXiv:astro-ph/0603179)

Dyson F. W., Eddington A. S., Davidson C., 1920, Philosophical Transactions of the Royal Society of London Series A, 220, 291

Eggleton P. P., Kiseleva-Eggleton L., 2001, ApJ, 562, 1012

Einstein A., 1916, Annalen der Physik, 354, 769

Einstein A., 1936, Science, 84, 506

Eisenbeiss T., Ammler-von Eiff M., Roell T., Mugrauer M., Adam C., Neuhäuser R., Schmidt T. O. B., Bedalov A., 2013, A&A, 556, A53

Eisenhardt P. R. M., et al., 2020, ApJS, 247, 69

Eistrup C., Walsh C., van Dishoeck E. F., 2016, A&A, 595, A83

Eistrup C., Walsh C., van Dishoeck E. F., 2018, A&A, 613, A14

Epchtein N., et al., 1997, The Messenger, 87, 27

Evans J. E., Maunder E. W., 1903, MNRAS, 63, 488

Evans D. F., et al., 2016a, A&A, 589, A58

Evans D. F., Southworth J., Smalley B., 2016b, ApJ, 833, L19

Evans D. F., et al., 2018, A&A, 610, A20

Fabrycky D., Tremaine S., 2007, ApJ, 669, 1298

Faedi F., et al., 2013a, MNRAS, 433, 2097

Faedi F., et al., 2013b, A&A, 551, A73

Fagginger Auer F., Portegies Zwart S., 2021, arXiv e-prints, p. arXiv:2101.08033

Faherty J. K., Burgasser A. J., Cruz K. L., Shara M. M., Walter F. M., Gelino C. R., 2009, AJ, 137, 1

Feiden G. A., 2016, A&A, 593, A99

Fienup J. R., 1997, Applied optics, 36, 8352

Fischer D. A., Marcy G. W., Butler R. P., Vogt S. S., Apps K., 1999, PASP, 111, 50

Fitzgibbon A., Pilu M., Fisher R. B., 1999, IEEE Trans. Pattern Anal. Mach. Intell., 21, 476

Flasseur O., Denis L., Thiébaut É., Langlois M., 2018, A&A, 618, A138

Flasseur O., Denis L., Thiébaut É., Langlois M., 2020, A&A, 637, A9

Fontenelle B. L. B. d., 1686, Entretiens sur la pluralité des mondes

Foreman-Mackey D., Hogg D. W., Lang D., Goodman J., 2013, PASP, 125, 306

Forgan D., Rice K., 2013, MNRAS, 432, 3168

Forgan D. H., Hall C., Meru F., Rice W. K. M., 2018, MNRAS, 474, 5036

Fried D. L., 1966, Journal of the Optical Society of America (1917-1983), 56, 1372

Furlan E., et al., 2009, ApJ, 703, 1964

Fusco T., et al., 2006, Optics Express, 14, 7515

Gagné J., et al., 2018, ApJ, 856, 23

Gaia Collaboration et al., 2016, A&A, 595, A1

Gaia Collaboration et al., 2018, A&A, 616, A1

Gaia Collaboration et al., 2021, A&A, 649, A1

Galicher R., et al., 2014, A&A, 565, L4

Galicher R., et al., 2016, A&A, 594, A63

Galicher R., et al., 2018, A&A, 615, A92

Gardner J. P., et al., 2006, Space Sci. Rev., 123, 485

Garufi A., et al., 2018, A&A, 620, A94

Gaudi B. S., et al., 2020, arXiv e-prints, p. arXiv:2001.06683

Gauza B., Béjar V. J. S., Pérez-Garrido A., Zapatero Osorio M. R., Lodieu N., Rebolo R., Pallé E., Nowak G., 2015, The Astrophysical Journal, 804, 96

Gebhard T. D., Bonse M. J., Quanz S. P., Schölkopf B., 2020, arXiv e-prints, p. arXiv:2010.05591

Gelino C. R., Burgasser A. J., 2010, AJ, 140, 110

Gelino C. R., et al., 2011, The Astronomical Journal, 142, 57

Ghezzi L., Montet B. T., Johnson J. A., 2018, ApJ, 860, 109

Gibson N. P., Aigrain S., Barstow J. K., Evans T. M., Fletcher L. N., Irwin P. G. J., 2013, MNRAS, 428, 3680

Gillon M., Jehin E., Magain P., Chantry V., Hutsemékers D., Manfroid J., Queloz D., Udry S., 2011, in European Physical Journal Web of Conferences. p. 06002 (arXiv:1101.5807), doi:10.1051/epjconf/20101106002

Gillon M., et al., 2013, A&A, 552, A82

Gillon M., et al., 2016, Nature, 533, 221

Gillon M., et al., 2017, Nature, 542, 456

Gilmozzi R., Spyromilio J., 2007, The Messenger, 127, 11

Ginski C., Schmidt T. O. B., Mugrauer M., Neuhäuser R., Vogt N., Errmann R., Berndt A., 2014, MNRAS, 444, 2280

Ginski C., et al., 2016a, MNRAS, 457, 2173

Ginski C., et al., 2016b, A&A, 595, A112

Girard J. H., et al., 2020, in Society of Photo-Optical Instrumentation Engineers (SPIE) Conference Series. p. 1144337, doi:10.1117/12.2561736

Girardi L., Groenewegen M. A. T., Hatziminaoglou E., da Costa L., 2005, A&A, 436, 895

Gizis J. E., Allers K. N., Liu M. C., Harris H. C., Faherty J. K., Burgasser A. J., Kirkpatrick J. D., 2015, ApJ, 799, 203

Gladysz S., Christou J. C., 2008, ApJ, 684, 1486

Goldman B., Röser S., Schilbach E., Moór A. C., Henning T., 2018, ApJ, 868, 32

Goldreich P., Ward W. R., 1973, ApJ, 183, 1051

Golimowski D. A., et al., 2004, AJ, 127, 3516

Gomez Gonzalez C. A., Absil O., Absil P. A., Van Droogenbroeck M., Mawet D., Surdej J., 2016, A&A, 589, A54

Gomez Gonzalez C. A., Absil O., Van Droogenbroeck M., 2018, A&A, 613, A71

Goodwin W. W., 1874, Quaestiones Naturales. Little, Brown, and Company

Goulinski N., Ribak E. N., 2018, MNRAS, 473, 1589

Grant M., 1936, Annals of Science, 1, 385

Gravity Collaboration et al., 2017, A&A, 602, A94

Gravity Collaboration et al., 2019, A&A, 623, L11

Gravity Collaboration et al., 2020, A&A, 633, A110

Gray R. O., Kaye A. B., 1999, AJ, 118, 2993

Greenbaum A. Z., et al., 2018, AJ, 155, 226

Grimm S. L., et al., 2018, A&A, 613, A68

Groff T. D., et al., 2015, in Shaklan S., ed., Society of Photo-Optical Instrumentation Engineers (SPIE) Conference Series Vol. 9605, Techniques and Instrumentation for Detection of Exoplanets VII. p. 96051C, doi:10.1117/12.2188465

Guerri G., et al., 2011, Experimental Astronomy, 30, 59

Guizar-Sicairos M., Thurman S. T., Fienup J. R., 2008, Optics letters, 33, 156

Guyon O., 2003, A&A, 404, 379

Haffert S. Y., Bohn A. J., de Boer J., Snellen I. A. G., Brinchmann J., Girard J. H., Keller C. U., Bacon R., 2019, Nature Astronomy, 3, 749

Hagan J. B., Choquet É., Soummer R., Vigan A., 2018, AJ, 155, 179

Haisch Karl E. J., Lada E. A., Lada C. J., 2001, ApJ, 553, L153

Han E., Wang S. X., Wright J. T., Feng Y. K., Zhao M., Fakhouri O., Brown J. I., Hancock C., 2014, PASP, 126, 827

Hardy J. W., 1998, Adaptive Optics for Astronomical Telescopes

Hartman J. D., et al., 2012, AJ, 144, 139

Hartman J. D., et al., 2015, AJ, 150, 197

Hay K. L., et al., 2016, MNRAS, 463, 3276

Hayashi C., 1981, Progress of Theoretical Physics Supplement, 70, 35

Hellier C., et al., 2009, ApJ, 690, L89

Hellier C., et al., 2010, ApJ, 723, L60

Hellier C., et al., 2014, MNRAS, 440, 1982

Hellier C., et al., 2015, AJ, 150, 18

Hellier C., et al., 2017, MNRAS, 465, 3693

Henden A., Munari U., 2014, Contributions of the Astronomical Observatory Skalnate Pleso, 43, 518

Henden A. A., Levine S. E., Terrell D., Smith T. C., Welch D., 2012, Journal of the American Association of Variable Star Observers (JAAVSO), 40, 430

Henden A. A., Templeton M., Terrell D., Smith T. C., Levine S., Welch D., 2016, VizieR Online Data Catalog, p. II/336

Henize K. G., 1976, The Astrophysical Journal Supplement Series, 30, 491

Henry G. W., Marcy G. W., Butler R. P., Vogt S. S., 2000, ApJ, 529, L41

Hoeijmakers H. J., et al., 2018a, Nature, 560, 453

Hoeijmakers H. J., Schwarz H., Snellen I. A. G., de Kok R. J., Bonnefoy M., Chauvin G., Lagrange A. M., Girard J. H., 2018b, A&A, 617, A144

Høg E., et al., 2000, A&A, 355, L27

Hom J., et al., 2020, AJ, 159, 31

Houk N., Cowley A. P., 1975, University of Michigan Catalogue of two-dimensional spectral types for the HD stars. Volume I. Declinations -90° to -53°

Hughes A. M., Duchêne G., Matthews B. C., 2018, ARA&A, 56, 541

Hunter J. D., 2007, Computing in Science and Engineering, 9, 90

Hunziker S., Quanz S. P., Amara A., Meyer M. R., 2018, A&A, 611, A23

Hunziker S., et al., 2020, A&A, 634, A69

Huygens C., Huygens C., 1698, The Celestial Worlds Discover'd, or, Conjectures concerning the Inhabitants, Plants and Productions of the Worlds in the Planets. No. 13, James Knapton

Ishihara D., et al., 2010, A&A, 514, A1

Itoh Y., et al., 2005, The Astrophysical Journal, 620, 984

Janson M., Brandner W., Henning T., 2008, A&A, 478, 597

Janson M., et al., 2019, A&A, 626, A99

Janson M., et al., 2021, A&A, 646, A164

Jehin E., et al., 2011, The Messenger, 145, 2

Johansen A., Lacerda P., 2010, MNRAS, 404, 475

Johnson J. A., Aller K. M., Howard A. W., Crepp J. R., 2010, PASP, 122, 905

Jovanovic N., et al., 2015, PASP, 127, 890

Kasper M., Apai D., Janson M., Brandner W., 2007, A&A, 472, 321

Kausch W., et al., 2015, A&A, 576, A78

Kawada M., et al., 2007, Publications of the Astronomical Society of Japan, 59, S389

Kendall M. G., 1957, Technical report, A course in multivariate analysis

Kenworthy M. A., Codona J. L., Hinz P. M., Angel J. R. P., Heinze A., Sivanandam S., 2007, ApJ, 660, 762

Keppler M., et al., 2018, A&A, 617, A44

Kiefer S., Bohn A. J., Quanz S. P., Kenworthy M. A., Stolker T., subm., A&A

Kiraga M., 2012, Acta Astron., 62, 67

Kirkpatrick J. D., Barman T. S., Burgasser A. J., McGovern M. R., McLean I. S., Tinney C. G., Lowrance P. J., 2006, ApJ, 639, 1120

Kirkpatrick J. D., et al., 2010, ApJS, 190, 100

Kley W., Nelson R. P., 2012, ARA&A, 50, 211

Knapp G. R., et al., 2004, AJ, 127, 3553

Konacki M., Torres G., Jha S., Sasselov D. D., 2003, Nature, 421, 507

Konopacky Q. M., Barman T. S., Macintosh B. A., Marois C., 2013, Science, 339, 1398

Kratter K., Lodato G., 2016, ARA&A, 54, 271

Kratter K. M., Murray-Clay R. A., Youdin A. N., 2010, ApJ, 710, 1375

Kraus A. L., Ireland M. J., Cieza L. A., Hinkley S., Dupuy T. J., Bowler B. P., Liu M. C., 2014, The Astrophysical Journal, 781, 20

Kraus S., et al., 2017, ApJ, 848, L11

Kroupa P., 2001, MNRAS, 322, 231

Kuchner M. J., Seager S., 2005, arXiv e-prints, pp astro–ph/0504214

Kuhn R. B., et al., 2016, MNRAS, 459, 4281

Kuzuhara M., et al., 2013, The Astrophysical Journal, 774, 11

Lafrenière D., Marois C., Doyon R., Nadeau D., Artigau É., 2007a, ApJ, 660, 770

Lafrenière D., et al., 2007b, ApJ, 670, 1367

Lafrenière D., Jayawardhana R., van Kerkwijk M. H., 2008, The Astrophysical Journal, 689, L153

Lagrange A.-M., Backman D. E., Artymowicz P., 2000, Protostars and Planets IV, p. 639

Lagrange A. M., et al., 2009, A&A, 493, L21

Lagrange A. M., et al., 2010, Science, 329, 57

Lagrange A.-M., et al., 2019, A&A, 621, L8

Lai D., Foucart F., Lin D. N. C., 2011, in Sozzetti A., Lattanzi M. G., Boss A. P., eds, IAU Symposium Vol. 276, The Astrophysics of Planetary Systems: Formation, Structure, and Dynamical Evolution. pp 295–299, doi:10.1017/S1743921311020345

Lallement R., Babusiaux C., Vergely J. L., Katz D., Arenou F., Valette B., Hottier C., Capitanio L., 2019, A&A, 625, A135

Lam K. W. F., et al., 2017, A&A, 599, A3

Lamb W. R. M., 1925, Plato in Twelve Volumes. Harvard University Press

Lambrechts M., Johansen A., 2012, A&A, 544, A32

Lammer H., Blanc M., 2018, Space Sci. Rev., 214, 60

Langlois M., Vigan A., Moutou C., Sauvage J.-F., Dohlen K., Costille A., Mouillet D., Le Mignant D., 2013, in Proceedings of the Third AO4ELT Conference. p. 63, doi:10.12839/AO4ELT3.13317

Langlois M., et al., 2014, in Ground-based and Airborne Instrumentation for Astronomy V. p. 91471R, doi:10.1117/12.2055549

Larkin J., et al., 2006, in McLean I. S., Iye M., eds, Society of Photo-Optical Instrumentation Engineers (SPIE) Conference Series Vol. 6269, Society of Photo-Optical Instrumentation Engineers (SPIE) Conference Series. p. 62691A, doi:10.1117/12.672061

Larkin J. E., et al., 2014, in Ramsay S. K., McLean I. S., Takami H., eds, Society of Photo-Optical Instrumentation Engineers (SPIE) Conference Series Vol. 9147, Ground-based and Airborne Instrumentation for Astronomy V. p. 91471K (arXiv:1407.2314), doi:10.1117/12.2056504

Launhardt R., et al., 2020, A&A, 635, A162

Law N. M., et al., 2014, ApJ, 791, 35

Lendl M., et al., 2014, A&A, 568, A81

Lenzen R., et al., 2003, in Iye M., Moorwood A. F. M., eds, Society of Photo-Optical Instrumentation Engineers (SPIE) Conference Series Vol. 4841, Instrument Design and Performance for Optical/Infrared Ground-based Telescopes. pp 944–952, doi:10.1117/12.460044

Levenberg K., 1944, Quarterly of applied mathematics, 2, 164

Lillo-Box J., Barrado D., Bouy H., 2014, A&A, 566, A103

Lin D. N. C., Bodenheimer P., Richardson D. C., 1996, Nature, 380, 606

Lister T. A., et al., 2009, ApJ, 703, 752

Liu M. C., Dupuy T. J., Bowler B. P., Leggett S. K., Best W. M. J., 2012, The Astrophysical Journal, 758, 57

Lodders K., 2004, ApJ, 611, 587

Lodders K., Palme H., Gail H. P., 2009, Landolt-Börnstein, 4B, 712

Looper D. L., Burgasser A. J., Kirkpatrick J. D., Swift B. J., 2007, ApJ, 669, L97

Looper D. L., Bochanski J. J., Burgasser A. J., Mohanty S., Mamajek E. E., Faherty J. K., West A. A., Pitts M. A., 2010, AJ, 140, 1486

Lovejoy A. O., 1936, Cambridge Mas

Lowell P., 1895, Mars

Lowell P., 1906, Mars and its Canals

Luhman K. L., Mamajek E. E., 2012, ApJ, 758, 31

Luhman K. L., Adame L., D'Alessio P., Calvet N., Hartmann L., Megeath S. T., Fazio G. G., 2005, The Astrophysical Journal, 635, L93

Luhman K. L., et al., 2007, The Astrophysical Journal, 654, 570

Luhman K. L., Mamajek E. E., Allen P. R., Muench A. A., Finkbeiner D. P., 2009, The Astrophysical Journal, 691, 1265

Luhman K. L., Mamajek E. E., Shukla S. J., Loutrel N. P., 2017, AJ, 153, 46

Lyot B., 1939, MNRAS, 99, 580

Macintosh B., et al., 2014, Proceedings of the National Academy of Science, 111, 12661

Macintosh B., et al., 2015, Science, 350, 64

Macintosh B., et al., 2018, in Close L. M., Schreiber L., Schmidt D., eds, Society of Photo-Optical Instrumentation Engineers (SPIE) Conference Series Vol. 10703, Adaptive Optics Systems VI. p. 107030K (arXiv:1807.07146), doi:10.1117/12.2314253

Madhusudhan N., 2019, ARA&A, 57, 617

Madhusudhan N., Amin M. A., Kennedy G. M., 2014, ApJ, 794, L12

Maire A. L., et al., 2015, A&A, 576, A133

Maire A.-L., et al., 2016, in Ground-based and Airborne Instrumentation for Astronomy VI. p. 990834, doi:10.1117/12.2233013

Maire A. L., et al., 2020, A&A, 633, L2

Mamajek E. E., Pecaut M. J., Nguyen D. C., Bubar E. J., 2013a, in Protostars and Planets VI Posters.

Mamajek E. E., et al., 2013b, AJ, 146, 154

Manara C. F., et al., 2013a, A&A, 551, A107

Manara C. F., Beccari G., Da Rio N., De Marchi G., Natta A., Ricci L., Robberto M., Testi L., 2013b, A&A, 558, A114

Manara C. F., Frasca A., Alcalá J. M., Natta A., Stelzer B., Testi L., 2017, A&A, 605, A86

Mancini L., et al., 2014, A&A, 562, A126

Mancini L., et al., 2019, MNRAS, 485, 5168

Marois C., Lafrenière D., Doyon R., Macintosh B., Nadeau D., 2006a, ApJ, 641, 556

Marois C., Phillion D. W., Macintosh B., 2006b, in McLean I. S., Iye M., eds, Society of Photo-Optical Instrumentation Engineers (SPIE) Conference Series Vol. 6269, Society of Photo-Optical Instrumentation Engineers (SPIE) Conference Series. p. 62693M (arXiv:astro-ph/0607002), doi:10.1117/12.672263

Marois C., Macintosh B., Barman T., Zuckerman B., Song I., Patience J., Lafrenière D., Doyon R., 2008, Science, 322, 1348

Marois C., Zuckerman B., Konopacky Q. M., Macintosh B., Barman T., 2010, Nature, 468, 1080

Marois C., Correia C., Galicher R., Ingraham P., Macintosh B., Currie T., De Rosa R., 2014, in Marchetti E., Close L. M., Vran J.-P., eds, Society of Photo-Optical Instrumentation Engineers (SPIE) Conference Series Vol. 9148, Adaptive Optics Systems IV. p. 91480U (arXiv:1407.2555), doi:10.1117/12.2055245

Marquardt D. W., 1963, Journal of the society for Industrial and Applied Mathematics, 11, 431

Martin R. G., Livio M., 2012, MNRAS, 425, L6

Martinez P., Dorrer C., Aller Carpentier E., Kasper M., Boccaletti A., Dohlen K., Yaitskova N., 2009, A&A, 495, 363

Maschberger T., 2013, MNRAS, 429, 1725

Matsuyama I., Johnstone D., Hartmann L., 2003, ApJ, 582, 893

Mawet D., Serabyn E., Stapelfeldt K., Crepp J., 2009, ApJ, 702, L47

Mawet D., et al., 2012, in Clampin M. C., Fazio G. G., MacEwen H. A., Oschmann Jacobus M. J., eds, Society of Photo-Optical Instrumentation Engineers (SPIE) Conference Series Vol. 8442, Space Telescopes and Instrumentation 2012: Optical, Infrared, and Millimeter Wave. p. 844204 (arXiv:1207.5481), doi:10.1117/12.927245

Mawet D., et al., 2014, ApJ, 792, 97

Maxted P. F. L., Serenelli A. M., Southworth J., 2015, A&A, 577, A90

Mayor M., Queloz D., 1995, Nature, 378, 355

Mayor M., et al., 2003, The Messenger, 114, 20

McElwain M. W., Burgasser A. J., 2006, AJ, 132, 2074

McLean I. S., McGovern M. R., Burgasser A. J., Kirkpatrick J. D., Prato L., Kim S. S., 2003, ApJ, 596, 561

McLean I. S., Prato L., McGovern M. R., Burgasser A. J., Kirkpatrick J. D., Rice E. L., Kim S. S., 2007, ApJ, 658, 1217

Mellon S. N., Mamajek E. E., Oberst T. E., Pecaut M. J., 2017, ApJ, 844, 66

Mennesson B., et al., 2016, in MacEwen H. A., Fazio G. G., Lystrup M., Batalha N., Siegler N., Tong E. C., eds, Society of Photo-Optical Instrumentation Engineers (SPIE) Conference Series Vol. 9904, Space Telescopes and Instrumentation 2016: Optical, Infrared, and Millimeter Wave. p. 99040L, doi:10.1117/12.2240457

Mesa D., et al., 2019a, MNRAS, 488, 37

Mesa D., et al., 2019b, A&A, 632, A25

Meshkat T., Kenworthy M. A., Quanz S. P., Amara A., 2014, ApJ, 780, 17

Metchev S. A., Hillenbrand L. A., 2006, The Astrophysical Journal, 651, 1166

Millar-Blanchaer M. A., Esposito T. M., Stahl K., Fitzgerald M. P., Perrin M. D., Kalas P., Macintosh B., Graham J. R., 2017, in Society of Photo-Optical Instrumentation Engineers (SPIE) Conference Series. p. 104070V, doi:10.1117/12.2275823

Milli J., Mouillet D., Lagrange A. M., Boccaletti A., Mawet D., Chauvin G., Bonnefoy M., 2012, A&A, 545, A111

Modigliani A., et al., 2010, in Silva D. R., Peck A. B., Soifer B. T., eds, Society of Photo-Optical Instrumentation Engineers (SPIE) Conference Series Vol. 7737, Observatory Operations: Strategies, Processes, and Systems III. p. 773728, doi:10.1117/12.857211

Mollière P., Snellen I. A. G., 2019, A&A, 622, A139

Moór A., et al., 2017, ApJ, 849, 123

Morbidelli A., 2018, Dynamical Evolution of Planetary Systems. p. 145, doi:10.1007/978-3-319-55333-7˙145

Mordasini C., Alibert Y., Benz W., 2009a, A&A, 501, 1139

Mordasini C., Alibert Y., Benz W., Naef D., 2009b, A&A, 501, 1161

Mordasini C., Alibert Y., Georgy C., Dittkrist K. M., Klahr H., Henning T., 2012, A&A, 547, A112

Mordasini C., van Boekel R., Mollière P., Henning T., Benneke B., 2016, ApJ, 832, 41

Morley C. V., Skemer A. J., Miles B. E., Line M. R., Lopez E. D., Brogi M., Freedman R. S., Marley M. S., 2019, ApJ, 882, L29

Močnik T., Hellier C., Anderson D. R., Clark B. J. M., Southworth J., 2017, MNRAS, 469, 1622

Muench A. A., Lada C. J., Luhman K. L., Muzerolle J., Young E., 2007, AJ, 134, 411

Mugrauer M., Röll T., Ginski C., Vogt N., Neuhäuser R., Schmidt T. O. B., 2012, MNRAS, 424, 1714

Müller A., et al., 2018, A&A, 617, L2

Murakami H., et al., 2007, Publications of the Astronomical Society of Japan, 59, S369

Murphy S. J., Bedding T. R., Shibahashi H., 2016, ApJ, 827, L17

Musso Barcucci A., et al., 2019, A&A, 627, A77

Mustill A. J., Davies M. B., Blunt S., Howard A., 2021, arXiv e-prints, p. arXiv:2102.06031

Muterspaugh M. W., et al., 2010, AJ, 140, 1657

Nagasawa M., Ida S., Bessho T., 2008, ApJ, 678, 498

Naud M.-E., et al., 2014, ApJ, 787, 5

Nelder J. A., Mead R., 1965, The computer journal, 7, 308

Nesvorný D., Kipping D. M., Buchhave L. A., Bakos G. Á., Hartman J., Schmitt A. R., 2012, Science, 336, 1133

Neugebauer G., et al., 1984, ApJ, 278, L1

Neveu-VanMalle M., et al., 2014, A&A, 572, A49

Ngo H., et al., 2015, ApJ, 800, 138

Ngo H., et al., 2016, ApJ, 827, 8

Ngo H., et al., 2017, AJ, 153, 242

Nielsen E. L., et al., 2013, ApJ, 776, 4

Nielsen E. L., et al., 2017, AJ, 154, 218

Nielsen E. L., et al., 2019, AJ, 158, 13

Nowak M., et al., 2020, A&A, 642, L2

Öberg K. I., Bergin E. A., 2021, Phys. Rep., 893, 1

Öberg K. I., Murray-Clay R., Bergin E. A., 2011, ApJ, 743, L16

Oliphant T. E., 2006, A guide to NumPy. Vol. 1, Trelgol Publishing USA

Ormel C. W., Klahr H. H., 2010, A&A, 520, A43

Paardekooper S. J., Mellema G., 2004, A&A, 425, L9

Pairet B., Cantalloube F., Gomez Gonzalez C. A., Absil O., Jacques L., 2019, MNRAS, 487, 2262

Pairet B., Cantalloube F., Jacques L., 2021, MNRAS,

Papagiannis M. D., 1985, in Papagiannis M. D., ed., , Vol. 112, The Search for Extraterrestrial Life: Recent Developments. pp 5–11

Paterson A. M., 1971, British Journal for the Philosophy of Science, 22, 207

Pecaut M. J., Mamajek E. E., 2013, ApJS, 208, 9

Pecaut M. J., Mamajek E. E., 2016, MNRAS, 461, 794

Pedregosa F., et al., 2012, arXiv e-prints, p. arXiv:1201.0490

Penny M. T., Gaudi B. S., Kerins E., Rattenbury N. J., Mao S., Robin A. C., Calchi Novati S., 2019, ApJS, 241, 3

Pepe F., et al., 2021, A&A, 645, A96

Pereira C. B., Franco C. S., de Araújo F. X., 2003, A&A, 397, 927

Pérez L. M., Isella A., Carpenter J. M., Chandler C. J., 2014, ApJ, 783, L13

Perryman M., Hartman J., Bakos G. Á., Lindegren L., 2014, ApJ, 797, 14

Peters M. A., et al., 2012, in McLean I. S., Ramsay S. K., Takami H., eds, Society of Photo-Optical Instrumentation Engineers (SPIE) Conference Series Vol. 8446, Ground-based and Airborne Instrumentation for Astronomy IV. p. 84467U (arXiv:1208.3190), doi:10.1117/12.926381

Petigura E. A., et al., 2016, ApJ, 818, 36

Petigura E. A., et al., 2017, AJ, 153, 142

Petigura E. A., et al., 2018, AJ, 156, 89

Petit C., et al., 2014, in Adaptive Optics Systems IV. p. 91480O, doi:10.1117/12.2052847

Pinilla P., de Juan Ovelar M., Ataiee S., Benisty M., Birnstiel T., van Dishoeck E. F., Min M., 2015, A&A, 573, A9

Pinilla P., Klarmann L., Birnstiel T., Benisty M., Dominik C., Dullemond C. P., 2016, A&A, 585, A35

Pinte C., et al., 2018, ApJ, 860, L13

Podolak M., Zucker S., 2004, Meteoritics and Planetary Science, 39, 1859

Pollacco D. L., et al., 2006, PASP, 118, 1407

Pollack J. B., Hubickyj O., Bodenheimer P., Lissauer J. J., Podolak M., Greenzweig Y., 1996, Icarus, 124, 62

Ponnamperuma C., 1964, Science Education in the Space Age: Proceedings [of] a National Conference held in Los Angeles

Preibisch T., Mamajek E., 2008, The Nearest OB Association: Scorpius-Centaurus (Sco OB2). ASP Monograph Publications, p. 235

Price D. J., et al., 2018, MNRAS, 477, 1270

Pudritz R. E., Cridland A. J., Alessi M., 2018, Connecting Planetary Composition with Formation. p. 144, doi:10.1007/978-3-319-55333-7˙144

Pueyo L., et al., 2012, ApJS, 199, 6

Quanz S. P., et al., 2010, ApJ, 722, L49

Quanz S. P., Crossfield I., Meyer M. R., Schmalzl E., Held J., 2015, International Journal of Astrobiology, 14, 279

Quanz S. P., et al., 2019, arXiv e-prints, p. arXiv:1908.01316

Quanz S. P., et al., 2021, arXiv e-prints, p. arXiv:2101.07500

Queloz D., et al., 2010, A&A, 517, L1

Racine R., Walker G. A. H., Nadeau D., Doyon R., Marois C., 1999, PASP, 111, 587

Rafikov R. R., 2005, ApJ, 621, L69

Rafikov R. R., 2011, ApJ, 727, 86

Rameau J., Chauvin G., Lagrange A. M., Thébault P., Milli J., Girard J. H., Bonnefoy M., 2012, A&A, 546, A24

Rameau J., et al., 2013, The Astrophysical Journal, 772, L15

Rameau J., Chauvin G., Lagrange A. M., Maire A. L., Boccaletti A., Bonnefoy M., 2015, A&A, 581, A80

Rapson V. A., Kastner J. H., Andrews S. M., Hines D. C., Macintosh B., Millar-Blanchaer M., Tamura M., 2015, ApJ, 803, L10

Rasio F. A., Ford E. B., 1996, Science, 274, 954

Rauchfuss H., 2008, Chemical evolution and the origin of life. Springer Science & Business Media

Rayner J. T., Cushing M. C., Vacca W. D., 2009, ApJS, 185, 289

Rebolo R., Zapatero Osorio M. R., Madruga S., Bejar V. J. S., Arribas S., Licandro J., 1998, Science, 282, 1309

Reid I. N., Lewitus E., Burgasser A. J., Cruz K. L., 2006, ApJ, 639, 1114

Rein H., Liu S. F., 2012, A&A, 537, A128

Rein H., Tamayo D., 2015, MNRAS, 452, 376

Rein H., Tamayo D., 2016, MNRAS, 459, 2275

Ren B., Pueyo L., Zhu G. B., Debes J., Duchêne G., 2018, ApJ, 852, 104

Ribas Á., Bouy H., Merín B., 2015, A&A, 576, A52

Ribas I., et al., 2018, Nature, 563, 365

Ricker G. R., et al., 2015, Journal of Astronomical Telescopes, Instruments, and Systems, 1, 014003

Rieke G. H., et al., 2004, The Astrophysical Journal Supplement Series, 154, 25

Robinson T. D., Stapelfeldt K. R., Marley M. S., 2016, PASP, 128, 025003

Rouse W. H. D., Smith M. F., 1924, Lucretius: On the Nature of Things. Harvard University Press

Rousset G., et al., 2003, in Wizinowich P. L., Bonaccini D., eds, Society of Photo-Optical Instrumentation Engineers (SPIE) Conference Series Vol. 4839, Adaptive Optical System Technologies II. pp 140–149, doi:10.1117/12.459332

Ruane G., et al., 2018, in Lystrup M., MacEwen H. A., Fazio G. G., Batalha N., Siegler N., Tong E. C., eds, Society of Photo-Optical Instrumentation Engineers (SPIE) Conference Series Vol. 10698, Space Telescopes and Instrumentation 2018: Optical, Infrared, and Millimeter Wave. p. 106982S (arXiv:1807.07042), doi:10.1117/12.2312948

Saar S. H., Butler R. P., Marcy G. W., 1998, ApJ, 498, L153

Sagan C., 1982, Science, 218, 426

Sahlmann J., Lazorenko P. F., Ségransan D., Martín E. L., Queloz D., Mayor M., Udry S., 2013, A&A, 556, A133

Samland M., et al., 2017, A&A, 603, A57

Samland M., Bouwman J., Hogg D. W., Brandner W., Henning T., Janson M., 2021, A&A, 646, A24

Schmid H. M., Joos F., Tschan D., 2006, A&A, 452, 657

Schmidt T. O. B., Neuhäuser R., Seifahrt A., Vogt N., Bedalov A., Helling C., Witte S., Hauschildt P. H., 2008, Astronomy and Astrophysics, 491, 311

Schneider J., Dedieu C., Le Sidaner P., Savalle R., Zolotukhin I., 2011, A&A, 532, A79

Schneider G., et al., 2014, AJ, 148, 59

Schwarz H., Ginski C., de Kok R. J., Snellen I. A. G., Brogi M., Birkby J. L., 2016, A&A, 593, A74

Seager S., 2010, Exoplanets

Selsis F., Kaltenegger L., Paillet J., 2008, Physica Scripta Volume T, 130, 014032

Serenelli A. M., Bergemann M., Ruchti G., Casagrande L., 2013, MNRAS, 429, 3645

Sheehan W., 1988, Planets & perception: telescopic views and interpretations, 1609-1909. University of Arizona Press

Sheehan P., 2020, Nature, 586, 205

Sheehan P. D., Tobin J. J., Federman S., Megeath S. T., Looney L. W., 2020, ApJ, 902, 141

Sheppard S. S., Cushing M. C., 2009, AJ, 137, 304

Shuch H. P., 2011, Searching for Extraterrestrial Intelligence, doi:10.1007/978-3-642-13196-7.

Siegler N., Close L. M., Burgasser A. J., Cruz K. L., Marois C., Macintosh B., Barman T., 2007, AJ, 133, 2320

Silburt A., Gaidos E., Wu Y., 2015, ApJ, 799, 180

Silvotti R., et al., 2007, Nature, 449, 189

Sinukoff E., et al., 2016, ApJ, 827, 78

Smette A., et al., 2015, A&A, 576, A77

Smith B. A., Terrile R. J., 1984, Science, 226, 1421

Smith A. M. S., et al., 2013, A&A, 552, A120

Smith A. M. S., et al., 2017, MNRAS, 464, 2708

Snellen I. A. G., Brandl B. R., de Kok R. J., Brogi M., Birkby J., Schwarz H., 2014, Nature, 509, 63

Snik F., Otten G., Kenworthy M., Miskiewicz M., Escuti M., Packham C., Codona J., 2012, in Navarro R., Cunningham C. R., Prieto E., eds, Society of Photo-Optical Instrumentation Engineers (SPIE) Conference Series Vol. 8450, Modern Technologies in Space- and Ground-based Telescopes and Instrumentation II. p. 84500M (arXiv:1207.2970), doi:10.1117/12.926222

Socrates A., Katz B., Dong S., Tremaine S., 2012, ApJ, 750, 106

Soderblom D. R., Jones B. F., Balachand ran S., Stauffer J. R., Duncan D. K., Fedele S. B., Hudon J. D., 1993, AJ, 106, 1059

Soummer R., 2005, ApJ, 618, L161

Soummer R., Aime C., Falloon P. E., 2003, A&A, 397, 1161

Soummer R., Hagan J. B., Pueyo L., Thormann A., Rajan A., Marois C., 2011, ApJ, 741, 55

Soummer R., Pueyo L., Larkin J., 2012, ApJ, 755, L28

Soummer R., et al., 2014, ApJ, 786, L23

Southworth J., 2011, MNRAS, 417, 2166

Southworth J., 2012, MNRAS, 426, 1291

Southworth J., et al., 2013, MNRAS, 434, 1300

Southworth J., Bohn A. J., Kenworthy M. A., Ginski C., Mancini L., 2020, A&A, 635, A74

Sparks W. B., Ford H. C., 2002, ApJ, 578, 543

Spergel D., et al., 2015, arXiv e-prints, p. arXiv:1503.03757

Stevenson D. J., Lunine J. I., 1988, Icarus, 75, 146

Stolker T., et al., 2016, A&A, 595, A113

Stolker T., Bonse M. J., Quanz S. P., Amara A., Cugno G., Bohn A. J., Boehle A., 2019, A&A, 621, A59

Stolker T., et al., 2020a, A&A, 635, A182

Stolker T., Marleau G. D., Cugno G., Mollière P., Quanz S. P., Todorov K. O., Kühn J., 2020b, A&A, 644, A13

Strom K. M., Strom S. E., Edwards S., Cabrit S., Skrutskie M. F., 1989, AJ, 97, 1451

Sumi T., et al., 2011, Nature, 473, 349

Teague R., Bae J., Bergin E. A., Birnstiel T., Foreman-Mackey D., 2018, ApJ, 860, L12

Tetzlaff N., Neuhäuser R., Hohle M. M., 2011, MNRAS, 410, 190

The LUVOIR Team 2019, arXiv e-prints, p. arXiv:1912.06219

Tilling I., et al., 2012, A&A, 538, A20

Tipler F. J., 1981, QJRAS, 22, 133

Todorov K., Luhman K. L., McLeod K. K., 2010, ApJ, 714, L84

Torres C. A. O., Quast G. R., da Silva L., de La Reza R., Melo C. H. F., Sterzik M., 2006, A&A, 460, 695

Trauger J., Moody D., Krist J., Gordon B., 2016, Journal of Astronomical Telescopes, Instruments, and Systems, 2, 011013

Triaud A. H. M. J., et al., 2013a, A&A, 549, A18

Triaud A. H. M. J., et al., 2013b, A&A, 551, A80

Trilling D. E., Brown R. H., 1998, Nature, 395, 775

Tuomi M., Kotiranta S., Kaasalainen M., 2009, A&A, 494, 769

Turner O. D., et al., 2016, PASP, 128, 064401

Udry S., Santos N. C., 2007, ARA&A, 45, 397

Van Eylen V., et al., 2016, AJ, 152, 143

Van der Walt S., Schönberger J. L., Nunez-Iglesias J., Boulogne F., Warner J. D., Yager N., Gouillart E., Yu T., 2014, PeerJ, 2, e453

Vanderburg A., et al., 2015, ApJ, 800, 59

Vanderburg A., et al., 2020, Nature, 585, 363

Varosi F., Gezari D. Y., 1993, in Astronomical Data Analysis Software and Systems II. p. 393

Varvoglis H., Sgardeli V., Tsiganis K., 2012, Celestial Mechanics and Dynamical Astronomy, 113, 387

Veras D., Crepp J. R., Ford E. B., 2009, ApJ, 696, 1600

Vernet J., et al., 2011, A&A, 536, A105

Vigan A., Moutou C., Langlois M., Allard F., Boccaletti A., Carbillet M., Mouillet D., Smith I., 2010, MNRAS, 407, 71

Vigan A., et al., 2012, A&A, 544, A9

Vigan A., et al., 2017, A&A, 603, A3

Vigan A., et al., 2020, arXiv e-prints, p. arXiv:2007.06573

Virtanen P., et al., 2020, Nature Methods, 17, 261

Voges W., et al., 1999, A&A, 349, 389

Wagner K., et al., 2018, ApJ, 863, L8

Wahhaj Z., et al., 2015, A&A, 581, A24

Wahhaj Z., et al., 2021, A&A, 648, A26

Wang J. J., et al., 2016, AJ, 152, 97

Wang J. J., et al., 2018, AJ, 156, 192

Wang J. J., et al., 2020, AJ, 159, 263

Wang J. J., et al., 2021, AJ, 161, 148

Wenger M., et al., 2000, A&AS, 143, 9

Werner M. W., et al., 2004, The Astrophysical Journal Supplement Series, 154, 1

Wertz O., Absil O., Gómez González C. A., Milli J., Girard J. H., Mawet D., Pueyo L., 2017, A&A, 598, A83

White R. J., Basri G., 2003, ApJ, 582, 1109

Winn J. N., Fabrycky D., Albrecht S., Johnson J. A., 2010, ApJ, 718, L145

Wolff S. G., et al., 2016, ApJ, 818, L15

Wöllert M., Brandner W., 2015, A&A, 579, A129

Wöllert M., Brandner W., Bergfors C., Henning T., 2015, A&A, 575, A23

Wolszczan A., 1994, Science, 264, 538

Wolszczan A., Frail D. A., 1992, Nature, 355, 145

Worden S. P., et al., 2017, Acta Astronautica, 139, 98

Wray J. D., 1966, AJ, 71, 403

Wright J. T., Gaudi B. S., 2013, Exoplanet Detection Methods. p. 489, doi:10.1007/978-94-007-5606-9˙10

Wu Y., Lithwick Y., 2011, ApJ, 735, 109

Wu Y., Murray N., 2003, ApJ, 589, 605

Wyatt M. C., Dent W. R. F., Greaves J. S., 2003, MNRAS, 342, 876

Wyttenbach A., Ehrenreich D., Lovis C., Udry S., Pepe F., 2015, A&A, 577, A62

Yang H., et al., 2016, ApJ, 826, 8

Yates F., 1964, The University Of Chicago Press, Chicago

Zacharias N., Monet D. G., Levine S. E., Urban S. E., Gaume R., Wycoff G. L., 2005, VizieR Online Data Catalog, p. I/297

Zacharias N., Finch C. T., Girard T. M., Henden A., Bartlett J. L., Monet D. G., Zacharias M. I., 2013, AJ, 145, 44

Zari E., Hashemi H., Brown A. G. A., Jardine K., de Zeeuw P. T., 2018, A&A, 620, A172

Zhou Y., Apai D., Schneider G. H., Marley M. S., Showman A. P., 2016, ApJ, 818, 176

Zhu Z., Hartmann L., Nelson R. P., Gammie C. F., 2012, ApJ, 746, 110

Zimmerman N. T., Eldorado Riggs A. J., Jeremy Kasdin N., Carlotti A., Vanderbei R. J., 2016, Journal of Astronomical Telescopes, Instruments, and Systems, 2, 011012

Zuckerman B., Rhee J. H., Song I., Bessell M. S., 2011, ApJ, 732, 61

Zurlo A., et al., 2016, A&A, 587, A57

de Boer J., et al., 2016, A&A, 595, A114

de Boer J., et al., 2020, A&A, 633, A63

de Zeeuw P. T., Hoogerwerf R., de Bruijne J. H. J., Brown A. G. A., Blaauw A., 1999, AJ, 117, 354

van Holstein R. G., et al., 2020, A&A, 633, A64

van Terwisga S. E., et al., 2018, A&A, 616, A88

Summary

How do planetary systems form and evolve? Is our Solar System unique or just one of many others that might even harbor Earth-like planets? And could such Earth-twins perhaps host some forms of life? Questions like these have fascinated humankind for thousands of years, yet we do not have conclusive answers for all of them.

The past 30 years have revolutionized our understanding of planetary systems in our Galaxy. In 1992 the first planet outside our Solar System was discovered: this extra-solar planet (or exoplanet) was a strange world, vastly different from the eight planets that humanity had known before. The star that this planet was found to orbit was markedly different from our Sun. PSR B1257+12, which is the name of this planet hosting star, is a so-called pulsar: a fast-spinning object that marks the endpoint of the evolution of many stars that are more massive than the Sun. But even the first planet that was discovered around a Sun-like star in 1995 is a hostile environment; in fact, it had nothing in common at all with objects that we knew from our Solar System. This exoplanet with the name 51 Peg b is a gas giant like Jupiter, yet located at a much closer separation to its star. With an orbital semi-major axis of merely 5 % of the Earth-Sun distance this planet is even closer to its host star than Mercury is to our Sun. Due to its enormous size and very close orbit, 51 Peg b was the first example of a new class of planetary objects: the so-called hot Jupiters.

From these initial discoveries, an exoplanet revolution emerged in the past decades. Today, we know about 4'500 planets outside our Solar System, and several thousands of new discoveries are predicted for the next few years. Despite this abundance of detected planetary systems, only a small fraction of these planets (about 1 %) could be captured in an image. This small number is due to the major challenges that have to be overcome in order to take such an image. First and foremost, the star is many times brighter than the planet that we want to observe. Second, the separation between both objects as seen on the sky is tiny. An often used analogy is that of a firefly (our model planet) that one wants to image directly next to a giant lighthouse (our star). Naturally, the intensity of the lighthouse outshines the small firefly by several orders of magnitude. Even when just standing a few meters apart, it seems impossible to spot the small firefly with one's bare eyes right next to this massive source of light. But extra-solar planetary systems are usually at much larger distances of several dozens of light years.[1] For our firefly-lighthouse analogy this corresponds to a separation of more than 500 km from which one wants to distinguish both individual components.

Less than two decades ago, the first image of such a planetary-mass object was collected with the Very Large Telescope (VLT) of the European Southern Observatory (ESO). Major advances in optical instrumentation, observing strategies, and data-processing algorithms facilitated the imaging of giant extra-solar planets that are usually widely separated from their

[1] One light year is approximately 9.4×10^{12} km, which is equivalent to 9.4 trillion kilometers.

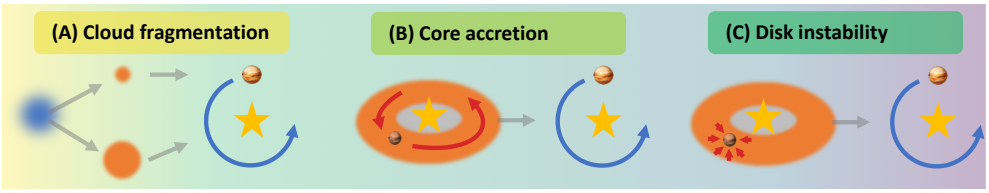

Figure 1: Potential formation mechanisms of wide-orbit gas giant planets.

parent stars. Today, about fifty of these Jovian gas giant planets could be imaged. Most of these have orbital separations that are significantly larger than ten Earth-Sun distances and some are even farther separated from their parent stars than all known bodies in our own Solar System are away from the Sun. The formation mechanisms of these wide orbit super-Jupiters are not understood particularly well. As visualized in Figure 1 there exist three competing theories that might explain this phenomenon.

(A) The cloud fragmentation paradigm postulates the formation of planetary mass objects as a byproduct of stellar formation. A collapsing molecular cloud is split up into fragments and some of these fragments might exhibit masses that are too low to fuse Hydrogen or Deuterium.[2] If these these fragments have masses that are smaller than 13 times the mass of Jupiter, these objects have planetary appearances and properties.

(B) The core-accretion mechanism is thought to be responsible for the formation of all Solar System planets. Young stars are usually surrounded by a massive disk that consists of gas and solids that originate from the initially collapsing molecular cloud. In this framework, small dust grains in this disk can coagulate. Via collision processes these grains can grow to kilometer-sized planetesimals. If these protoplanetary objects grow beyond a critical mass, they start accreting a gaseous envelope as we can see it for Jupiter in our Solar System.

(C) The disk instability scenario predicts that dense regions in a circumstellar stellar disk can collapse under their own gravity. This process can directly from gas giant planets that can accrete additional material from the surrounding disk.

All these potential formation mechanisms have characteristic time scales, planet separations, and companion frequencies. To understand the dominant formation pathway of wide-orbit gas giant planets, it is thus common practice to compare simulated planet populations for each of the scenarios to observational results. However, such an analysis has not been conducted for a large and homogeneous sample of young, Sun-like stars. As this category of stellar hosts might resemble the initial conditions that our early Solar System exhibited, a dedicated study of such a sample is quite intriguing and might even reveal insights into the history and evolution of our own planetary system. For this reason, we initiated the Young Suns Exoplanet Survey (YSES), whose preliminary results are reported in this thesis.

The Young Suns Exoplanet Survey

YSES is observing a unique sample of 70 solar analogs that are located in the Scorpius-Centaurus association. This group of stars is approximately 400 lightyears away from Earth

[2]Planets are objects that cannot produce energy by nuclear fusion in their cores, since their mass is too low to generate the temperatures that are required to ignite this process. Objects that are heavier than approximately 13 times the mass of Jupiter can fuse Deuterium to Helium and are therefore not considered to be planets. Such objects are called brown dwarfs. If the mass of an objects exceeds about 80 times the mass of Jupiter, the internal temperatures get high enough to fuse Hydrogen to Helium, which is the requirement for an objects to be considered a star.

and therefore located in our Galactic neighborhood. All YSES targets are exceptionally young compared to our 4.6-billion-year-old Sun. With an average age of 15 Million years among our sample, we observe these systems just after the phase of planet formation, which is thought to occur within the first few million years of the lifetime of planetary systems. Because planets cool down after their formation, young environments like these are especially well suited to directly detect gas giant companions. We observed all the stars with the Spectro-Polarimetric High-contrast Exoplanet REsearch (SPHERE) instrument that is mounted at Unit Telescope 3 of ESO's VLT. This instrument is one of the most advanced devices to obtain images of extrasolar planets. An extreme adaptive optics system corrects for the blurring effect that is caused by the atmosphere of our own Earth. Such a system is required to obtain sharp images from a telescope with a mirror diameter of 8.2 m. Another device that is used by this instrument is a so-called coronagraph. This opaque mask blocks most of the light from the central star and reveals faint planets that were hidden in the much brighter halo around the star (see for instance Figure 3).

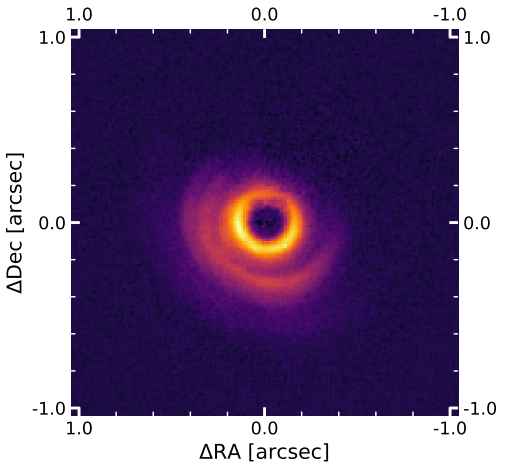

Figure 2: A circumstellar disk around Wray 15-788. Only half of the disk is visible. An additional inner disk might cast a shadow onto the upper right parts of the outer ring. The stellar intensity in the image center is attenuated by a coronagraph.

Even though YSES was designed to image new planets, the first result that originated from our survey was the discovery of a circumstellar disk around Wray 15-788. The extent of this disk is huge: the bright outer ring that can be seen in Figure 2 is more than 50 Earth-Sun distances away from its parent star. Moreover, the appearance of the disk is quite peculiar. It looks like the upper right is hidden in darkness. As this effect cannot be explained by the system geometry that we see in the image, we hypothesized that there is an inner disk that is too small to be resolved in our image. This inner disk is misaligned with respect to the structure that we can see, and therefore it is casting a shadow on some parts of the outer disk. In addition, this misalignment might be caused by a planet that is orbiting the star; yet this hypothesized companion has not been detected so far.

The first planetary system that we discovered as part of our survey received the name YSES 1 (see left panel of Figure 3). This star hosts two gas giant planets at very wide orbits, and it was therefore considered to be the first multi-planet system that was imaged around a Sun-like star. The closer planet YSES 1b has a semi-major axis of at least 160 times the Earth-Sun distance and the outer planet YSES 1c is even 320 times farther away from its host star than the Earth is from the Sun. Also in term of mass both planets surpass Solar System standards. Whereas YSES 1c has a mass of six times the mass of Jupiter, YSES 1b is even fourteen times as heavy as this most massive planet in our Solar System. For that reason it is not entirely clear yet, if YSES 1b is actually a planet or rather a brown dwarf companion. Future observations of this intriguing environment should shed light on this open question. Especially, a thorough characterization of both planetary atmospheres might help to distinguish between the most likely formation scenarios for the planets.

The latest discovery from our survey is YSES 2b, a giant planet that is six times as heavy as Jupiter (see right panel of Figure 3). Again, this planet is detected quite far away from its parent star at a separation of more than 110 times the Earth-Sun distance. It is unclear how YSES 2b has formed, as its mass is lower than usually expected from fragmentation

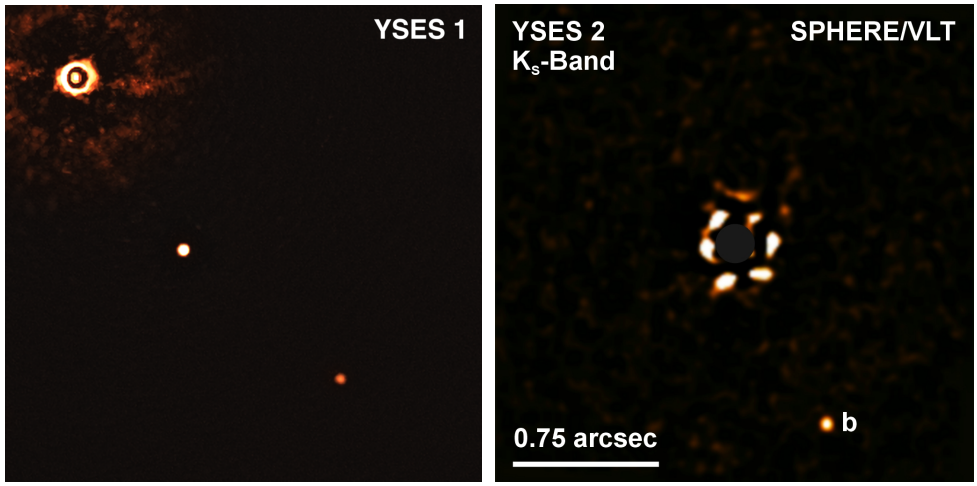

Figure 3: The planetary systems around YSES 1 and YSES 2. *Left panel*: The multi-planet system around YSES 1. The star is located in the upper left of the image and obscured by a coronagraphic mask. Two wide-orbit gas giant planets are detected around this solar analog. The inner and outer planet have a weight of six and fourteen times the mass of Jupiter, respectively. Image credit: ESO/Bohn et al. *Right panel*: The gas giant planet YSES 2b. The star is located at the image center and attenuated by a coronagraph.

processes (A) or gravitational instability mechanisms (C). Besides, it cannot have formed via core accretion (B) at such a large distance from the star. A possible explanation might be another as of yet undiscovered planet around YSES 2. This planet could be located closer to the star. Via gravitational interaction it scattered YSES 2b to its current position. Follow-up observations of this system will help to shed light on this potential scenario.

Future prospects

As some of our YSES observations still need to be carried out, the final statistical analysis of the survey is pending. The occurrence rates of gas giant planets around our target stars will help to constrain the dominant planet formation mechanisms in Sun-like environments. Further atmospheric characterization measurements will provide additional clues regarding the evolutionary history of these solar-like systems. Future observatories such as the James Webb Space Telescope will provide unprecedented insights into the chemical properties of these exoplanet atmospheres, which might be linked to the formation channels of the planets. Especially the new class of giant ground-based observatories such as the Extremely Large Telescope, the Thirty Meter Telescope, and the Giant Magellan Telescope will help to search for additional planets that are located closer to YSES 1, YSES 2, and other stars from our survey sample. These close-in planets are currently out of reach for the present generation of optical telescopes. Driven by the pacey progress in the field of exoplanetary research throughout the last decades that seems to continue for the years to come, we might have a chance to find some answers to the introductory questions – including the detection of life outside our Solar System – perhaps even before the end of this century.

Samenvatting

Hoe ontstaan planetenstelsels en hoe veranderen ze in de tijd? Is ons zonnestelsel uniek of is het een van vele die wellicht aardachtige planeten bevat? En zouden deze aardachtige planeten eventueel leven kunnen herbergen? Dit soort vragen hebben de mensheid al duizenden jaren gefascineerd en toch hebben we geen sluitend antwoord voor een van hen.

De afgelopen 30 jaar heeft een revolutie teweeggebracht in de kennis van planetenstelsels in ons Melkwegstelsel. In 1992 werd de eerste planeet buiten ons zonnestelsel (ook wel exoplaneet) ontdekt: deze exoplaneet is een merkwaardige wereld, met grote verschillen vergeleken met de acht planeten die de mensheid tot dan toe kende. De ster, PSR B1257+12, waar deze planeet omheen draait is aanzienlijk anders dan onze zon. PSR B1257+12 is namelijk een pulsar, een snel-draaiend object dat een overblijfsel is van sterren die veel zwaarder zijn dan de zon. Ook de eerste planeet die draait om een zonachtige ster, ontdekt in 1995, lijkt helemaal niet op een planeet uit ons zonnestelsel. Deze planeet genaamd 51 Pegasi b (afgekort 51 Peg b) is een gasreus net als Jupiter, maar staat veel dichter bij zijn ster. De afstand van de ster tot de planeet is kleiner dan de afstand van Mercurius tot de Zon, slechts 5 % van de afstand van de Zon tot de Aarde. Omdat 51 Peg b zo groot is en zo dichtbij staat, vangt hij veel licht op van de ster. Daardoor is hij erg heet, meer dan 1200 graden Kelvin, en is hij het eerste voorbeeld van een nieuwe klasse van planeten genaamd Hete Jupiters.

Door deze eerste ontdekkingen is in de laatste decennia een exoplaneet revolutie ontstaan. Vandaag de dag zijn er 4500 exoplaneten ontdekt en is er voorspeld dat er in de komende jaren nog duizenden nieuwe planeten gevonden zullen worden. Ondanks de overvloed van gedetecteerde planetenstelsels, is maar een klein aandeel (rond de 1 %) vastgelegd in een afbeelding. Dat dit aandeel zo klein is, komt door de enorme uitdagingen die overwonnen moeten worden om daadwerkelijk zo'n afbeelding te maken. De eerste uitdaging is dat de ster ontzettend veel helderder is dan de planeet die we willen afbeelden. Ten tweede staat de planeet relatief extreem dichtbij de ster. Een veelgebruikte analogie is die van een vuurvlieg (de planeet) die wordt afgebeeld naast een enorme vuurtoren (de ster). De vuurtoren is ordes van grootte helderder dan de vuurvlieg. Zelfs als men meters is verwijderd van de vuurtoren lijkt het onmogelijk om de vuurvlieg met blote ogen te onderscheiden van te onderscheiden van de enorme lichtbron. Exoplaneten staan uiteraard op veel grotere afstanden, meestal op tientallen lichtjaren van de zon.[3] Voor de vuurtoren zou dit betekenen dat we op meer dan 500 km staan en dan proberen de vuurvlieg vast te leggen.

Minder dan twintig jaar geleden is de eerste afbeelding van een exoplaneet gemaakt met de Very Large Telescope (VLT) van de European Southern Observatory (ESO). Grote vooruitgang in optische instrumentatie, waarneemtechnieken, en algoritmen voor dataverwerking maken

[3] Een lichtjaar is ongeveer 9.4×10^{12} km, wat gelijk is aan 9.4 biljoen kilometer.

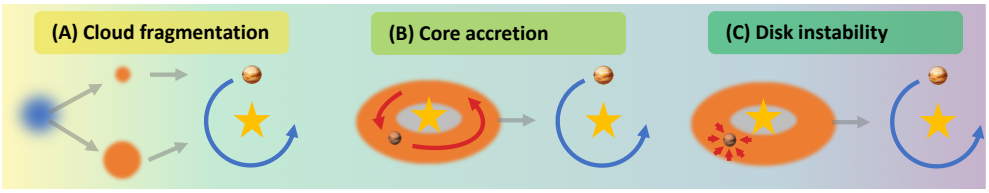

Figuur 4: Mogelijke ontstaansmechanismes van gasreuzen op wijde banen.

het mogelijk om gasreuzen op wijdere banen rond hun ster af te beelden. Tot nu toe zijn er zo'n 50 van deze Joviaanse planeten direct waargenomen. De banen zijn vaak veel groter dan tien keer de afstand van de Aarde tot de Zon, en sommigen staan verder van hun ster dan alle bekende objecten in ons zonnestelsel. Hoe deze grote planeten hebben kunnen vormen zo ver van de ster is nog onzeker. Er zijn momenteel drie verschillende theorieën hierover, die worden uitgelegd in Figuur 4.

(A) Het wolkfragmentatie paradigma stelt dat objecten met een massa van een planeet ontstaan als een bijproduct van stervorming. Een moleculaire wolk die in door de zwaartekracht ineenstort kan in meerdere fragmenten uit elkaar vallen. Sommige van deze fragmenten zullen niet zwaar genoeg zijn voor het fuseren van waterstof of deuterium.[4] Als deze fragmenten minder zwaar zijn dan 13 keer de massa van Jupiter wordt het een planeet.

(B) Het kernaccretie mechanisme wordt beschouwd als het ontstaansmechanisme voor alle planeten in ons zonnestelsel. Jonge sterren worden gewoonlijk omringd door een grote schijf die bestaat uit gas en stof dat is overgebleven uit de ineengestorte moleculaire wolk. In deze schijven klonteren kleine stofdeeltjes samen zodat ze in de loop van de tijd kunnen uitgroeien tot planetesimalen tot wel een kilometer in doorsnee. Als deze planetesimalen groot genoeg zijn zullen ze gas gaan aantrekken en doorgroeien totdat ze een gasreus worden.

(C) Het schijfinstabiliteit scenario voorspelt dat dichte gebieden in de stofschijf zelf ook kunnen instortend door hun eigen zwaartekracht. Dit proces kan in een keer en gasreus vormen die weer materiaal uit de stofschijf aantrekt.

Deze drie potentiele ontstaansmechanismes hebben hun eigen karakteristieke tijdschalen en een verdeling van massa van planeten en planeetbanen. Om te begrijpen welk van deze drie mechanismes het meest gebruikelijke is voor het ontstaan van gasreuzen op grotere afstanden van hun ster, wordt meestal een gesimuleerde planeetpopulatie vergeleken met de waargenomen planeetpopulatie. Tot nu toe is er niet zo'n analyse gedaan voor een groot en homogene selectie van zon-achtige sterren, terwijl deze categorie van sterren juist lijkt op de vroegere condities van ons eigen zonnestelsel. Een toegewijde studie van deze sterren zou daarom inzicht kunnen geven in de geschiedenis en de evolutie van ons eigen zonnestels. Daarom hebben wij de Young Suns Exoplanet Survey (YSES) studie opgezet, waarvan de eerste resultaten worden gepresenteerd in dit proefschrift.

[4]Planeten zijn objecten die geen energie produceren met kernfusie in hun kern omdat hun massa te laag is om de temperatuur te genereren die nodig is voor dit proces. Objecten die zwaarder zijn dan 13 keer de massa van Jupiter kunnen deuterium in helium fuseren en worden daarom niet als planeet beschouwd. Deze objecten heten bruine dwergen. Als een object ongeveer 80 keer zo zwaar is als Jupiter, wordt de interne temperatuur wel hoog genoeg voor kernfusie van waterstof naar helium, waardoor ze kunnen worden beschouwd als ster.

De Young Suns Exoplanet Survey

In de YSES-studie observeren we een unieke groep van 70 zonachtige sterren die horen bij de Scorpius–Centaurus sterassociatie. Deze groep van sterren staat ongeveer 400 lichtjaar van de Aarde en is buitengewoon jong vergeleken met onze 4.6 miljard jaar oude zon. Met een gemiddelde leeftijd van 15 miljoen jaar observeren we de 70 sterren kort na de fase van planeetvorming, waarvan verwacht wordt dat dit in de eerste paar miljoen jaar gebeurt. Kort na de formatie zijn planeten nog heet en dus helder, waardoor ze makkelijker te detecteren zijn. Daarom is deze selectie van sterren ideaal voor het direct waarnemen van gasreuzen. We hebben deze selectie van sterren geobserveerd met het Spectro-Polarimetric High-contrast Exoplanet Research (SPHERE) instrument dat is geïnstalleerd bij de Unit Telescope 3 van ESO's VLT. SPHERE is een van de meest geavanceerde instrumenten om exoplaneten direct af te beelden. Een extreem adaptief optica systeem corrigeert het versmerende effect van de atmosfeer van de Aarde. Zonder dit systeem lukt het niet om een scherpe afbeelding te maken met een telescoop met een diameter van 8.2 meter. Een ander onderdeel van SPHERE is de zogeheten 'coronagraaf'. Dit is een ondoorzichtig masker dat het meeste sterlicht tegen houdt zodat een veel lichtzwakkere planeet, die eerst verstopt zat in de halo van de veel heldere ster, zichtbaar wordt (zie Figuur 6).

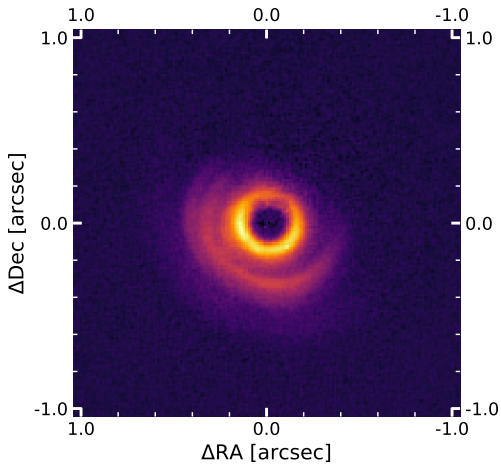

Figuur 5: Een circumstellaire schijf rond de ster Wray 15-788. De helft van deze schijf is maar zichtbaar. Dit zou kunnen komen door een extra schijf die dichterbij staat die het sterlicht blokkeert en een schaduw maakt op de zichtbare schijf. Het sterlicht in het midden van de schijf is enorm verzwakt door een coronagraaf.

Hoewel het doel van de YSES-studie het vinden van nieuwe planeten is, was het eerste resultaat de ontdekking van een circumstellaire schijf rond de ster Wray 15-788. Deze schijf is enorm: de heldere buitenste ring in Figuur 5 staat op meer dan 50 keer de afstand van de Aarde naar de zon van zijn ster. Bovendien ziet de schijf er eigenaardig uit: het lijkt erop alsof een deel van de schijf is gehuld in duisternis. Dit kan niet worden verklaard door de structuur van de schijf zoals te zien in de afbeelding. Daarom stellen wij dat er een extra schijf is die te klein is om te zien, en die scheef staat ten opzichte van de buitenste schijf. Zo'n schijf kan een schaduw werpen op sommige delen van de buitenste schijf, waardoor deze minder of niet meer zichtbaar is. Een binnenste schijf kan scheef gaan staan door de aanwezigheid van een planeet. Deze planeet is echter tot nu toe nog niet gevonden.

Het eerste planetenstelsel dat wij hebben ontdekt met de YSES-studie heeft de naam YSES 1 gekregen (zie het linker paneel van Figuur 6). Om deze ster draaien twee gasreuzen op grote afstand, en dit planetenstelsel is de eerste met meerdere planeten dat direct is waargenomen. De binnenste planeet YSES 1b staat op 160 keer de afstand van de zon tot de aarde, en de buitenste planeet YSES 1c staat zelfs twee keer zo ver weg. Ook in hun massa overtreffen ze de planeten van het zonnestelsel. YSES 1c is ongeveer zes keer zo zwaar als Jupiter, de zwaarste planeet in ons zonnestelsel. YSES 1b is zelfs veertien keer zo zwaar als Jupiter, en daarom is het nog niet zeker of het een bruine dwerg is of een planeet. Verdere waarnemingen van dit stelsel zullen deze vraag kunnen beantwoorden. Bovendien, is het uiterst interessant om de atmosferen van deze planeten te karakteriseren, zodat we wellicht hun ontstaansmechanisme kunnen achterhalen.

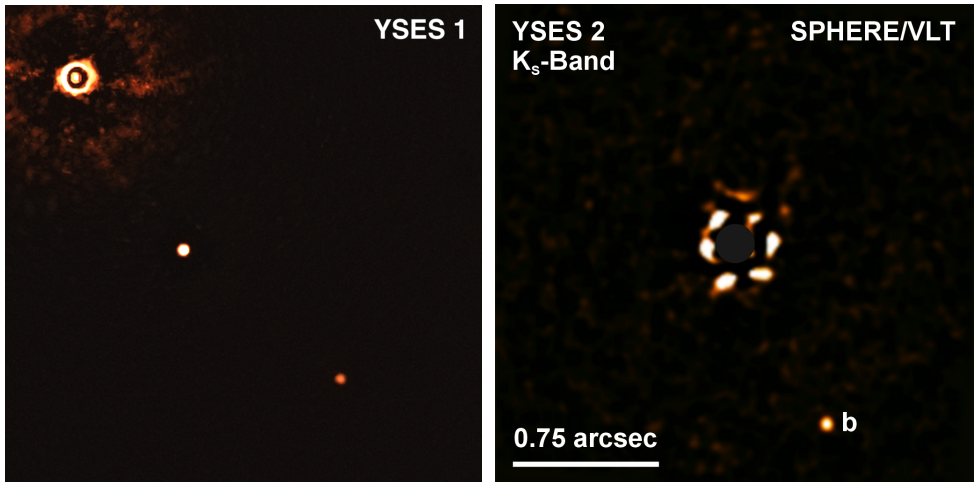

Figuur 6: De planetenstelsels YSES 1 en YSES 2. *Links*: Het planetenstelsel YSES 1 met twee planeten. De ster staat linksboven in de afbeelding en is verduisterd door een coronagraaf. Twee gasreuzen draaien op grote afstand rond deze zon-achtige ster. De binnenste en buitenste planeet hebben een gewicht van respectievelijk zes en veertien keer de massa van Jupiter. Image credit: ESO/Bohn et al. *Rechts*: De gasreus YSES 2b. De ster staat nu in het midden van de afbeelding en is ook verduisterd door een coronagraaf.

De nieuwste ontdekking is YSES 2b, ook een gasreus die op 110 keer de afstand van de zon tot de aarde staat en zes keer zo zwaar is als Jupiter (zie het rechter paneel van Figuur 6). Hoe YSES 2b is ontstaan is nog niet duidelijk omdat de massa beduidend lager is dan je zou verwachten voor het fragmenteren van een gaswolk (A), of voor het schijfinstabiliteit scenario (C). Ook kan het op deze grote afstand niet zijn ontstaan door kernaccretie (B). Het is wel mogelijk dat de planeet dichterbij is ontstaan en door interactie met een andere planeet naar zijn huidige plek is geslingerd. Met eventuele vervolg waarnemingen zou dit scenario beter kunnen worden onderzocht.

Toekomstperspectief

De waarnemingen van de YSES-studie zijn nog niet afgerond, en de uiteindelijke statistische analyse is dus nog niet mogelijk. Het antwoord op de vraag hoe vaak gasreuzen voorkomen rond de sterren die zijn geïncludeerd zal helpen met het bepalen welk ontstaansmechanisme dominant is voor zonachtige sterren. Nieuwe metingen van de atmosfeer van de gevonden planeten zal extra informatie geven over de evolutionaire geschiedenis van deze sterren. Hierbij zullen de toekomstige telescopen, zoals de James Webb Space Telescope, cruciaal zijn. Zij zullen inzicht geven in de chemische eigenschappen van de atmosferen van gasreuzen, wat weer gekoppeld kan worden aan de ontstaansmechanismes van deze planeten. Ook de nieuwe generatie van telescopen op aarde, zoals de Extremely Large Telescope, de Thirty meter telescope, en de Giant Magellan Telescope zullen gebruikt worden om planeten te vinden die dichterbij staan dan de planeten van YSES 1 en YSES 2. Nu zijn deze planeten nog niet detecteerbaar met de huidige generatie van telescopen. Maar als de snelheid van de huidige progressie in het vakgebied van exoplaneten zich doorzet in de komende jaren, hebben we een kans om sommige van de vragen aan het begin van deze samenvatting, inclusief de vraag over het detecteren van leven buiten ons zonnestelsel, te beantwoorden voor het eind van deze eeuw.

Zusammenfassung

Wie entstehen Planetensysteme? Ist unser Sonnensystem einzigartig oder gibt es viele andere solcher Systeme im Universum, die eventuell sogar erdähnliche Planeten beherbergen? Und könnte es auf solchen Erdzwillinge eventuell Leben geben? Seit tausenden von Jahren faszinieren solche Fragen die Menschheit – Fragen, auf welche es bislang meistens jedoch keine endgültige Antwort gibt.

Die letzten 30 Jahre haben unser Verständnis von Planetensystemen grundlegend verändert. Im Jahre 1992 wurde der erste Planet außerhalb unseres Sonnensystems entdeckt. Dieser erste extrasolare Planet (oder auch Exoplanet) ist gänzlich anders als die acht Planeten, welche die Menschheit zuvor gekannt hatte. Auch der Stern, den dieser Planet umkreist, hat nicht viel mit unsere Sonne gemein. PSR B1257+12, der Name dieses Sterns, ist ein sogenannter Pulsar: Ein schnell rotierendes Objekt, welches das Endstadium vieler Sterne darstellt, die schwerer als die Sonne sind. Aber auch der erste Planet, der 1995 um einen sonnenähnlichen Stern herum entdeckt wurde, ist nicht besonders lebensfreundlich. In der Tat unterscheidet sich dieser Planet eklatant von den acht Planeten, die bis anhin aus unserem Sonnensystem bekannt gewesen sind.

Zwar ist dieser Planet mit dem Namen 51 Peg b ein Gasriese wie Jupiter. Allerdings liegt seine Umlaufbahn viel näher um seinen Mutterstern herum. Mit einer großen Halbachse von gerade einmal 5 % der Erde-Sonne-Entfernung ist dieser Exoplanet sogar näher an seinem Mutterstern als Merkur an der Sonne. Aufgrund seiner Größe und der kurzen Umlaufdauer von wenigen Tagen wurde 51 Peg b zum ersten Exemplar einer neuen Gattung von Planeten – die sogenannten heißen Jupiter.

Basierend auf diesen ersten Entdeckungen begann eine Revolution der Exoplanetenforschung. Heutzutage kennen wir ungefähr 4'500 Planeten außerhalb unseres Sonnensystems und viele tausend neue Entdeckungen sind für die nächsten Jahre prognostiziert. Allerdings konnte bislang nur eine kleine Anzahl dieser Planeten direkt abgebildet werden (etwa 1 %). Dies beruht hauptsächlich auf dem großen Kontrast zwischen Stern und Planet. Der Stern ist millionenfach heller als der Planet, der abgelichtet werden soll. Außerdem ist der Abstand zwischen Stern und Exoplanet in der Regel sehr gering. Ein häufig bemühter Vergleich ist der eines kleinen Glühwürmchens, das direkt neben einem hellen Leuchtturm abgebildet werden soll. Selbstverständlich ist Letzterer, welcher den Stern repräsentiert, um ein vielfaches heller als das kleine Glühwürmchen, welches den Planeten darstellt. Selbst in einem Abstand von wenigen Metern scheint es unmöglich, das Glühwürmchen direkt neben dieser gigantischen Lichtquelle mit bloßen Augen zu erkennen. Allerdings sind extrasolare Planetensysteme um ein Vielfaches weiter entfernt.[5] Für den Leuchtturm-Glühwürmchen-Vergleich entspricht dies

[5] Übliche Distanzen sind in der Regel mehrere (hundert) Lichtjahre. Ein Lichtjahr ist eine Strecke von circa 9.4×10^{12} km, was ungefähr 9.4 Billionen Kilometern entspricht.

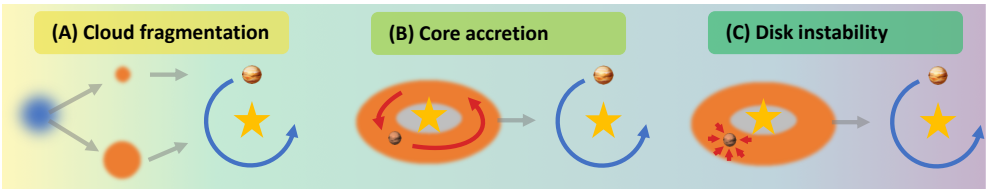

Abbildung 7: Mögliche Szenarien für die Entstehung weiter Gasriesen.

einer Strecke von mehr als 500 km, über die man beide Objekte unterscheiden und abbilden will.

Vor weniger als zwei Jahrzehnten gelang das erste Bild eines solchen planetenähnlichen Objekts mithilfe des Very Large Telescopes (VLT) der Europäischen Südsternwarte (ESO). Gewaltige Fortschritte in Instrumentation, Observationsstrategien und Datenverarbeitungsalgorithmen ermöglichten, dass man große Exoplaneten, die weit von ihren Muttersternen entfernt sind, wirklich abbilden kann. Bis heute gelang dies für etwa 50 jupiterähnliche Gasriesen. Die meisten dieser direkt abgebildeten Exoplaneten sind deutlich weiter von ihrem Mutterstern entfernt als die Erde von der Sonne. Für viele sind diese Abstände sogar noch deutlich größer als für alle bekannten Objekte in unserem Sonnensystem. Insbesondere die Entstehung solcher weiten Gasriesen ist weiterhin unklar. Wie in Abbildung 7 skizziert, gibt es drei konkurrierende Theorien, die diesen Prozess beschreiben können.

(A) Objekte mit Planetenmassen könnten ein Nebenprodukt der Entstehung von Sternen sein. Eine in sich kollabierende molekulare Wolke kann in verschiedene Teile gerissen werden. Manche dieser Fragmente könnten dann Massen aufweisen, die zu gering sind, um Wasserstoff oder Deuterium zu Helium zu fusionieren.[6] Falls diese Fragmente weniger als 13 Jupitermassen wiegen, haben diese Objekte planetare Eigenschaften.

(B) Das Kernwachstumsszenario ist die wahrscheinlichste Erklärung für die Entstehung der Planeten in unserem Sonnensystem. Junge Sterne sind üblicherweise von einer Scheibe aus Gas und Staub umgeben. Durch Kollisionen kleiner Partikel in dieser Scheibe können größere Klumpen entstehen, die zu kilometergroßen Planetesimalen heranwachsen können. Falls solch ein Protoplanet eine kritische Masse überschreitet, kann eine Gasreiche Atmosphäre akkretiert werden, ähnlich der von Jupiter in unserem Sonnensystem.

(C) Die gravitative Scheibeninstabilität postuliert, dass Regionen in circumstellaren Scheiben unter dem Einfluss ihrer Selbstgravitation in sich zusammenfallen können. Dieser Prozess formt große Planeten, die weiteres Material akkretieren können.

All diese möglichen Entstehungsprozesse haben charakteristische Zeitskalen, Planetenumlaufbahnen und -häufigkeiten. Um den wichtigsten Mechanismus für die Entstehung weiter Gasriesen ausmachen zu können, ist es deshalb üblich, simulierte Planetenpopulationen mit Beobachtungsresultaten zu vergleichen. Allerdings wurde eine solche Studie noch nie mit einer großen und homogenen Menge junger, sonnenähnlicher Sterne durchgeführt. Da diese Kategorie von Sternen die Anfangsbedingungen unseres eigenen Sonnensystems widerspiegelt, ist eine solche Studie von großem Interesse. Deshalb starteten wir die Young Suns Exoplanet Survey (YSES), deren vorläufige Ergebnisse in dieser Arbeit präsentiert werden.

[6] Planeten sind Objekte, die nicht in der Lage sind, selbstständig Energie durch nukleare Fusion zu erzeugen. Grund hierfür ist, dass die Masse von Planeten zu gering ist, um im Kern Temperaturen zu erzeugen, die hoch genug sind, um die Fusion in Gang zu setzen. Objekte, die mehr als 13 Mal so schwer sind wie Jupiter, können Deuterium zu Helium fusionieren und sind deswegen keine Planeten mehr. Diese Objekte nennt man Braune Zwerge. Falls ein Objekt eine Masse von 80 Jupitermassen überschreitet, ist die Kerntemperatur hoch genug, um Wasserstoff zu Helium zu fusionieren. Dies ist die notwendige Bedingung, um ein Objekt als Stern bezeichnen zu können.

Die Young Suns Exoplanet Survey

Im Rahmen von YSES beobachteten wir ein einmaliges Sample von 70 sonnenähnlichen Sternen, die sich in der Scorpius-Centaurus Assoziation befinden. Diese Gruppe ist etwa 400 Lichtjahre von der Erde entfernt – ein Katzensprung in astronomischen Distanzen. Alle Sterne von YSES sind sehr jung im Vergleich zu unsere Sonne mit einem Alter von 4,6 Milliarden Jahren. Da die YSES-Sterne lediglich 15 Millionen Jahre alt sind, beobachten wir diese Systeme nur kurze Zeit nach ihrer Entstehung. Auch die Entstehung von Planeten sollte zu diesem Zeitpunkt bereits abgeschlossen sein. Da Planeten nach ihrer Entstehung abkühlen, sind solche jungen Systeme besonders gut geeignet, um nach weiten Gasriesen zu suchen. Wir haben alle Sterne mit dem SPHERE-Instrument beobachtet, welches am Unit Telescope 3 von ESOs VLT angebracht ist. Dieses Instrument ist eines der fortschrittlichsten Geräte zum Abbilden extrasolarer Planeten. Eine interne adaptive Optik korrigiert das Verschwimmen des Sterns, welches durch unsere eigene Atmosphäre verursacht wird. Ein solches System ist erforderlich, um scharfe Bilder mit einem Teleskop aufzunehmen, das einen Spiegeldurchmesser von 8,2 m besitzt. Ein anderes technisches Hilfsmittel ist ein sogenannter Koronograf. Diese undurchsichtige Maske reduziert die Helligkeit des Sterns, wodurch dunkle Planeten um diesen herum sichtbar werden (siehe Abbildung 9).

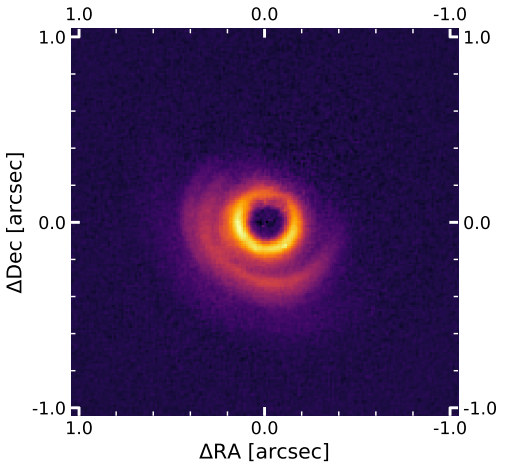

Abbildung 8: Eine circumstellare Scheibe um Wray 15-788 herum. Nur eine Seite der Scheibe ist sichtbar. Eine zusätzliche innere Scheibe könnte einen Schatten auf den äußeren, verborgenen Teil im oberen rechten Bildrand werfen. Die Intensität des Sterns ist mit einem Koronografen abgeschwächt.

Obwohl das Primärziel von YSES die direkte Detektion von Planeten waren, so war das erste Resultat von unserer Studie die Entdeckung einer circumstellaren Scheibe um Wray 15-788 herum. Diese Scheibe ist riesig. Der helle äußere Ring, der in Abbildung 8 zu sehen ist, ist mehr als 50 Mal weiter von seinem Mutterstern entfernt als die Erde von der Sonne. Außerdem sieht die Scheibe sonderbar aus, als wäre die obere rechte Hälfte verborgen. Dies kann nicht mit der Geometrie erklärt werden, die wir in der Abbildung sehen. Deshalb stellten wir die Vermutung auf, dass es eine weitere Scheibe um den Stern herum gibt, die jedoch zu nahe an diesem ist, um sie mit SPHERE auflösen zu können. Falls diese innere Scheibe anders ausgerichtet wäre als die äußere, so könnte dies zu einem Schattenwurf und der beobachteten Verdunklung führen. Diese abweichende Ausrichtung könnte von einem Planeten verursacht werden, der um den Stern kreist. Dieser Planet konnte bislang aber noch nicht gefunden werden.

Das erste Planetensystem, das wir im Rahmen unser Studie entdeckten, erhielt den Namen YSES 1 (siehe linke Seite von Abbildung 9). Diesen Stern umkreisen zwei Gasriesen auf sehr weit entfernten Bahnen. Es war das erste Mehrplanetensystem, das um einen sonnenähnlichen Stern herum abgebildet werden konnte. Der nähere Planet YSES 1b hat eine große Halbachse von mindestens 160 Mal der Erde-Sonne-Entfernung und der äußere Planet YSES 1c ist sogar 320 Mal weiter von seinem Mutterstern entfernt als die Erde von der Sonne. Auch die Masse beider Planeten ist deutlich größer als bei bekannten Objekten in unserem Sonnensystem. YSES 1c ist sechsmal so schwer wie Jupiter, der schwerste Planet in unserem Sonnensystem, und YSES 1b ist sogar 14 Mal so schwer. Daher ist noch ungewiss, ob YSES 1b ein Planet

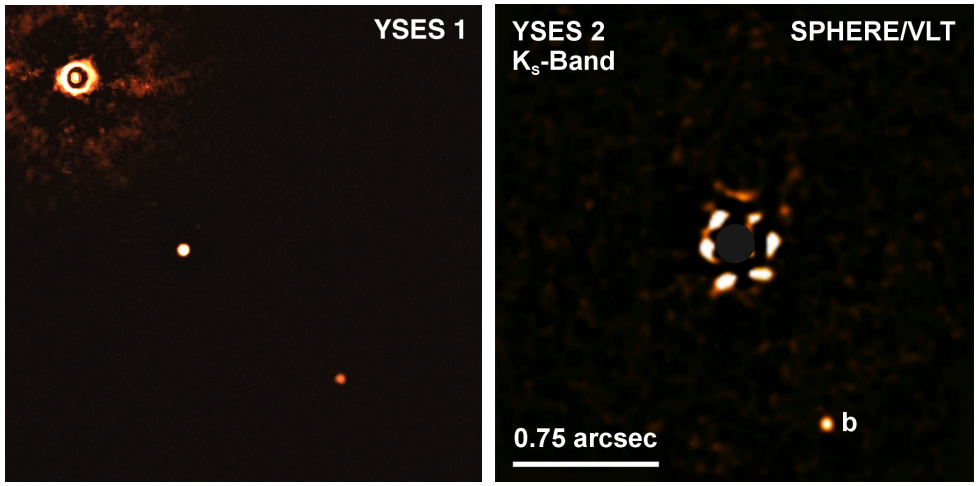

Abbildung 9: Die Planetensysteme YSES 1 und YSES 2. *Linke Seite*: Das Mehrplanetensystem um YSES 1 herum. Der Stern befindet sich oben links und ist hinter einem Koronografen verborgen. Zwei weite Gasriesen kreisen um diesen sonnenähnlichen Stern. Der innere und äußere Planet haben ein Gewicht von 6, beziehungsweise 14 Jupitermassen. Quelle: ESO/Bohn et al. *Rechte Seite*: Der Gasriese YSES 2b. Der Stern ist in der Bildmitte und hinter einem Koronografen verborgen.

oder eher ein Brauner Zwerg ist. Weitere Beobachtungen dieses spannenden Systems sollten dazu beitragen, diese offene Frage zu beantworten. Insbesondere eine detaillierte Charakterisierung der Planetenatmosphären könnte helfen, den wahrscheinlichsten Entstehungsprozess herauszufinden.

Die neueste Entdeckung unsere Studie ist YSES 2b – ein Gasriese, der sechsmal so schwer wie Jupiter ist (siehe rechte Seite von Abbildung 9). Auch dieser Planet ist mit 110 Erde-Sonne-Entfernungen recht weit von seinem Mutterstern entfernt. Es ist unklar, wie YSES 2b entstanden ist. Seine Masse ist niedriger als für Szenarien (A) und (C) postuliert und außerdem kann er nicht durch das Kernwachstumsszenario (B) so weit entfernt vom Stern entstanden sein. Eine mögliche Erklärung könnte ein noch unentdeckter Planet sein. Dieser zusätzliche Planet könnte näher um den Stern kreisen und durch Gravitationswechselwirkungen YSES 2b zu seiner jetzigen Position befördert haben. Weitere Beobachtungen von diesem System sollten helfen, dieses potentielle Szenario zu überprüfen.

Ausblick

Da einige Beobachtungen von YSES immer noch ausgeführt werden müssen, steht die finale statistische Analyse der Studie noch aus. Dadurch sollte sich der wichtigste Entstehungsprozess von weiten Gasriesen um sonnenähnlichen Sterne herum ermitteln lassen. Zukünftige Teleskope so wie das James Webb Space Telescope werden komplett neue Einblicke in die chemischen Eigenschaften dieser Planetenatmosphären generieren. Auch diese könnten Hinweise auf die zugrundeliegenden Entstehungsprozesse liefern. Insbesondere die nächste Generation riesiger, terrestrischer Observatorien, wie zum Beispiel das Extremely Large Telescope, das Thirty Meter Telescope oder das Giant Magellan Telescope, wird einen wichtigen Beitrag zur Suche weiterer Planeten zu den Sternen aus unserer Studie leisten. Aufgrund des raschen Fortschritts bei der Erforschung von Exoplaneten ist es nicht unwahrscheinlich, dass einige Antworten auf die anfänglichen Fragen – inklusive der Entdeckung von Leben außerhalb unseres Sonnensystems – bis zum Ende des 21. Jahrhunderts gefunden werden können.

List of publications

Refereed publications

26. Sutlieff, B. J., **Bohn, A. J.**, Birkby, J. L., Kenworthy, M. A., Morzinski, K. M., Doelman, D. S., Males, J. R., Snik, F., Close, L. M., Hinz, P. M., & Charbonneau, D. (2021) *High-contrast observations of brown dwarf companion HR 2562 B with the vector Apodizing Phase Plate coronagraph*, MNRAS (in press)

25. S. Kiefer, **Bohn, A. J.**, Quanz, S. P., Kenworthy, M., and Stolker, T. (2021), *Spectral and angular differential imaging with SPHERE/IFS. Assessing the performance of various PCA-based PSF subtraction approaches*, A&A (in press), arXiv:2106.05278

24. Zhang, Y., Snellen, I. A. G., **Bohn, A. J.**, Mollière, P., Ginski, C., Hoeijmakers, H. J., Kenworthy, M. A., Mamajek, E. E., Meshkat, T., Reggiani, M., & Snik, F. (2021), *The ^{13}CO-rich atmosphere of a young accreting super-Jupiter*, Nature (in press)

23. Vigan, A., Fontanive, C., Meyer, M., Biller, B., Bonavita, M., Feldt, M., Desidera, S., Marleau, G.-D., Emsenhuber, A., Galicher, R., Rice, K., Forgan, D., Mordasini, C., Gratton, R., Le Coroller, H., Maire, A.-L., Cantalloube, F., Chauvin, G., Cheetham, A., Hagelberg, J., Lagrange, A.-M., Langlois, M., Bonnefoy, M., Beuzit, J.-L., Boccaletti, A., D'Orazi, V., Delorme, P., Dominik, C., Henning, T., Janson, M., Lagadec, E., Lazzoni, C., Ligi, R., Menard, F., Mesa, D., Messina, S., Moutou, C., Müller, A., Perrot, C., Samland, M., Schmid, H. M., Schmidt, T., Sissa, E., Turatto, M., Udry, S., Zurlo, A., Abe, L., Antichi, J., Asensio-Torres, R., Baruffolo, A., Baudoz, P., Baudrand, J., Bazzon, A., Blanchard, P., **Bohn, A. J.**, Brown Sevilla, S., Carbillet, M., Carle, M., Cascone, E., Charton, J., Claudi, R., Costille, A., De Caprio, V., Delboulbé, A., Dohlen, K., Engler, N., Fantinel, D., Feautrier, P., Fusco, T., Gigan, P., Girard, J. H., Giro, E., Gisler, D., Gluck, L., Gry, C., Hubin, N., Hugot, E., Jaquet, M., Kasper, M., Le Mignant, D., Llored, M., Madec, F., Magnard, Y., Martinez, P., Maurel, D., Möller-Nilsson, O., Mouillet, D., Moulin, T., Origné, A., Pavlov, A., Perret, D., Petit, C., Pragt, J., Puget, P., Rabou, P., Ramos, J., Rickman, E. L., Rigal, F., Rochat, S., Roelfsema, R., Rousset, G., Roux, A., Salasnich, B., Sauvage, J.-F., Sevin, A., Soenke, C., Stadler, E., Suarez, M., Wahhaj, Z., Weber, L., & Wildi, F. (2021), *The SPHERE infrared survey for exoplanets (SHINE). III. The demographics of young giant exoplanets below 300 au with SPHERE*, A&A (in press), arXiv:2007.06573

22. Doelman, D. S., Snik, F., Por, E. H., Bos, S. P., Otten, G. P. P. L., Kenworthy, M., Haffert, S. Y., Wilby, M., **Bohn, A. J.**, Sutlieff, B. J., Miller, K., Ouellet, M., de Boer, J., Keller, C. U., Escuti, M. J., Shi, S., Warriner, N. Z., Hornburg, K., Birkby, J. L., Males, J., Morzinski, K. M., Close, L. M., Codona, J., Long, J., Schatz, L., Lumbres, J., Rodack, A., Van Gorkom, K., Hedglen, A., Guyon, O., Lozi, J., Groff, T., Chilcote, J., Jovanovic, N., Thibault, S., de Jonge, C., Allain, G., Vallée, C., Patel, D., Côté, O., Marois, C., Hinz, P.,

Stone, J., Skemer, A., Briesemeister, Z., Boehle, A., Glauser, A. M., Taylor, W., Baudoz, P., Huby, E., Absil, O., Carlomagno, B., & Delacroix, C. (2021), *Vector-apodizing phase plate coronagraph: design, current performance, and future development [Invited]*, Appl. Opt., 60, D52

21. de Boer, J., Ginski, C., Chauvin, G., Ménard, F., Benisty, M., Dominik, C., Maaskant, K., Girard, J. H., van der Plas, G., Garufi, A., Perrot, C., Stolker, T., Avenhaus, H., **Bohn, A.**, Delboulbé, A., Jaquet, M., Buey, T., Möller-Nilsson, O., Pragt, J., & Fusco, T. (2021), *Possible single-armed spiral in the protoplanetary disk around HD 34282*, A&A, 649, A25

20. **Bohn, A. J.**, Ginski, C., Kenworthy, M. A., Mamajek, E. E., Pecaut, M. J., Mugrauer, M., Vogt, N., Adam, C., Meshkat, T., Reggiani, M., & Snik, F. (2021), *Discovery of a directly imaged planet to the young solar analog YSES 2*, A&A, 648, A73

19. Wang, J. J., Vigan, A., Lacour, S., Nowak, M., Stolker, T., De Rosa, R. J., Ginzburg, S., Gao, P., Abuter, R., Amorim, A., Asensio-Torres, R., Bauböck, M., Benisty, M., Berger, J. P., Beust, H., Beuzit, J.-L., Blunt, S., Boccaletti, A., **Bohn, A.**, Bonnefoy, M., Bonnet, H., Brandner, W., Cantalloube, F., Caselli, P., Charnay, B., Chauvin, G., Choquet, E., Christiaens, V., Clénet, Y., Coudé Du Foresto, V., Cridland, A., de Zeeuw, P. T., Dembet, R., Dexter, J., Drescher, A., Duvert, G., Eckart, A., Eisenhauer, F., Facchini, S., Gao, F., Garcia, P., Garcia Lopez, R., Gardner, T., Gendron, E., Genzel, R., Gillessen, S., Girard, J., Haubois, X., Heißel, G., Henning, T., Hinkley, S., Hippler, S., Horrobin, M., Houllé, M., Hubert, Z., Jiménez-Rosales, A., Jocou, L., Kammerer, J., Keppler, M., Kervella, P., Meyer, M., Kreidberg, L., Lagrange, A.-M., Lapeyrère, V., Le Bouquin, J.-B., Léna, P., Lutz, D., Maire, A.-L., Ménard, F., Mérand, A., Mollière, P., Monnier, J. D., Mouillet, D., Müller, A., Nasedkin, E., Ott, T., Otten, G. P. P. L., Paladini, C., Paumard, T., Perraut, K., Perrin, G., Pfuhl, O., Pueyo, L., Rameau, J., Rodet, L., Rodríguez-Coira, G., Rousset, G., Scheithauer, S., Shangguan, J., Shimizu, T., Stadler, J., Straub, O., Straubmeier, C., Sturm, E., Tacconi, L. J., van Dishoeck, E. F., Vincent, F., von Fellenberg, S. D., Ward-Duong, K., Widmann, F., Wieprecht, E., Wiezorrek, E., Woillez, J., & Gravity Collaboration (2021), *Constraining the Nature of the PDS 70 Protoplanets with VLTI/GRAVITY*, AJ, 161, 148

18. van Holstein, R. G., Stolker, T., Jensen-Clem, R., Ginski, C., Milli, J., de Boer, J., Girard, J. H., Wahhaj, Z., **Bohn, A. J.**, Millar-Blanchaer, M. A., Benisty, M., Bonnefoy, M., Chauvin, G., Dominik, C., Hinkley, S., Keller, C. U., Keppler, M., Langlois, M., Marino, S., Ménard, F., Perrot, C., Schmidt, T. O. B., Vigan, A., Zurlo, A., & Snik, F. (2021), *A survey of the linear polarization of directly imaged exoplanets and brown dwarf companions with SPHERE-IRDIS. First polarimetric detections revealing disks around DH Tau B and GSC 6214-210 B*, A&A, 647, A21

17. Ginski, C., Facchini, S., Huang, J., Benisty, M., Vaendel, D., Stapper, L., Dominik, C., Bae, J., Ménard, F., Muro-Arena, G., Hogerheijde, M. R., McClure, M., van Holstein, R. G., Birnstiel, T., Boehler, Y., **Bohn, A.**, Flock, M., Mamajek, E. E., Manara, C. F., Pinilla, P., Pinte, C., & Ribas, Á. (2021), *Disk Evolution Study Through Imaging of Nearby Young Stars (DESTINYS): Late Infall Causing Disk Misalignment and Dynamic Structures in SU Aur*, ApJ, 908, L25

16. Janson, M., Squicciarini, V., Delorme, P., Gratton, R., Bonnefoy, M., Reffert, S., Mamajek, E. E., Eriksson, S. C., Vigan, A., Langlois, M., Engler, N., Chauvin, G., Desidera, S., Mayer, L., Marleau, G.-D., **Bohn, A. J.**, Samland, M., Meyer, M., d'Orazi, V., Henning, T., Quanz, S., Kenworthy, M., & Carson, J. C. (2021), *BEAST begins: sample characteristics and survey performance of the B-star Exoplanet Abundance Study*, A&A, 646, A164

15. Ginski, C., Ménard, F., Rab, C., Mamajek, E. E., van Holstein, R. G., Benisty, M., Manara, C. F., Asensio Torres, R., **Bohn, A.**, Birnstiel, T., Delorme, P., Facchini, S., Garufi, A., Gratton, R., Hogerheijde, M., Huang, J., Kenworthy, M., Langlois, M., Pinilla, P., Pinte, C., Ribas, Á., Rosotti, G., Schmidt, T. O. B., van den Ancker, M., Wahhaj, Z., Waters,

L. B. F. M., Williams, J., & Zurlo, A. (2020), *Disk Evolution Study Through Imaging of Nearby Young Stars (DESTINYS): A close low-mass companion to ET Cha*, A&A, 642, A119

14. **Bohn, A. J.**, Kenworthy, M. A., Ginski, C., Rieder, S., Mamajek, E. E., Meshkat, T., Pecaut, M. J., Reggiani, M., de Boer, J., Keller, C. U., Snik, F., & Southworth, J. (2020), *Two Directly Imaged, Wide-orbit Giant Planets around the Young, Solar Analog TYC 8998-760-1*, ApJ, 898, L16

13. Wagner, K., Stone, J., Dong, R., Ertel, S., Apai, D., Doelman, D., **Bohn, A.**, Najita, J., Brittain, S., Kenworthy, M., Keppler, M., Webster, R., Mailhot, E., & Snik, F. (2020), *First Images of the Protoplanetary Disk around PDS 201*, AJ, 159, 252

12. Muro-Arena, G. A., Ginski, C., Dominik, C., Benisty, M., Pinilla, P., **Bohn, A. J.**, Moldenhauer, T., Kley, W., Harsono, D., Henning, T., van Holstein, R. G., Janson, M., Keppler, M., Ménard, F., Pérez, L. M., Stolker, T., Tazzari, M., Villenave, M., Zurlo, A., Petit, C., Rigal, F., Möller-Nilsson, O., Llored, M., Moulin, T., & Rabou, P. (2020), *Spirals inside the millimeter cavity of transition disk SR 21*, A&A, 636, L4

11. Southworth, J., **Bohn, A. J.**, Kenworthy, M. A., Ginski, C., & Mancini, L. (2020), *A multiplicity study of transiting exoplanet host stars. II. Revised properties of transiting planetary systems with companions*, A&A, 635, A74

10. **Bohn, A. J.**, Southworth, J., Ginski, C., Kenworthy, M. A., Maxted, P. F. L., & Evans, D. F. (2020), *A multiplicity study of transiting exoplanet host stars. I. High-contrast imaging with VLT/SPHERE*, A&A, 635, A73

9. **Bohn, A. J.**, Kenworthy, M. A., Ginski, C., Manara, C. F., Pecaut, M. J., de Boer, J., Keller, C. U., Mamajek, E. E., Meshkat, T., Reggiani, M., Todorov, K. O., & Snik, F. (2020), *The Young Suns Exoplanet Survey: Detection of a wide-orbit planetary-mass companion to a solar-type Sco-Cen member*, MNRAS, 492, 431-443

8. Kenworthy, M. A., Klaassen, P. D., Min, M., van der Marel, N., **Bohn, A. J.**, Kama, M., Triaud, A., Hales, A., Monkiewicz, J., Scott, E., & Mamajek, E. E. (2020), *ALMA and NACO observations towards the young exoring transit system J1407 (V1400 Cen)*, A&A, 633, A115

7. Haffert, S. Y., **Bohn, A. J.**, de Boer, J., Snellen, I. A. G., Brinchmann, J., Girard, J. H., Keller, C. U., & Bacon, R. (2019), *Two accreting protoplanets around the young star PDS 70*, Nature Astronomy, 3, 749-754

6. Janson, M., Asensio-Torres, R., André, D., Bonnefoy, M., Delorme, P., Reffert, S., Desidera, S., Langlois, M., Chauvin, G., Gratton, R., **Bohn, A. J.**, Eriksson, S. C., Marleau, G.-D., Mamajek, E. E., Vigan, A., & Carson, J. C. (2019), *The B-Star Exoplanet Abundance Study: a co-moving 16-25 M_{Jup} companion to the young binary system HIP 79098*, A&A, 626, A99

5. **Bohn, A. J.**, Kenworthy, M. A., Ginski, C., Benisty, M., de Boer, J., Keller, C. U., Mamajek, E. E., Meshkat, T., Muro-Arena, G. A., Pecaut, M. J., Snik, F., Wolff, S. G., & Reggiani, M. (2019), *Discovery of a directly imaged disk in scattered light around the Sco-Cen member Wray 15-788*, A&A, 624, A87

4. Cugno, G., Quanz, S. P., Hunziker, S., Stolker, T., Schmid, H. M., Avenhaus, H., Baudoz, P., **Bohn, A. J.**, Bonnefoy, M., Buenzli, E., Chauvin, G., Cheetham, A., Desidera, S., Dominik, C., Feautrier, P., Feldt, M., Ginski, C., Girard, J. H., Gratton, R., Hagelberg, J., Hugot, E., Janson, M., Lagrange, A.-M., Langlois, M., Magnard, Y., Maire, A.-L., Menard, F., Meyer, M., Milli, J., Mordasini, C., Pinte, C., Pragt, J., Roelfsema, R., Rigal, F., Szulágyi, J., van Boekel, R., van der Plas, G., Vigan, A., Wahhaj, Z., & Zurlo, A. (2019), *A search for accreting young companions embedded in circumstellar disks. High-contrast Hα imaging with VLT/SPHERE*, A&A, 622, A156

3. Lagrange, A.-M., Boccaletti, A., Langlois, M., Chauvin, G., Gratton, R., Beust, H., Desidera, S., Milli, J., Bonnefoy, M., Cheetham, A., Feldt, M., Meyer, M., Vigan, A., Biller,

B., Bonavita, M., Baudino, J.-L., Cantalloube, F., Cudel, M., Daemgen, S., Delorme, P., D'Orazi, V., Girard, J., Fontanive, C., Hagelberg, J., Janson, M., Keppler, M., Koypitova, T., Galicher, R., Lannier, J., Le Coroller, H., Ligi, R., Maire, A.-L., Mesa, D., Messina, S., Müeller, A., Peretti, S., Perrot, C., Rouan, D., Salter, G., Samland, M., Schmidt, T., Sissa, E., Zurlo, A., Beuzit, J.-L., Mouillet, D., Dominik, C., Henning, T., Lagadec, E., Ménard, F., Schmid, H.-M., Turatto, M., Udry, S., **Bohn, A. J.**, Charnay, B., Gomez Gonzales, C. A., Gry, C., Kenworthy, M., Kral, Q., Mordasini, C., Moutou, C., van der Plas, G., Schlieder, J. E., Abe, L., Antichi, J., Baruffolo, A., Baudoz, P., Baudrand, J., Blanchard, P., Bazzon, A., Buey, T., Carbillet, M., Carle, M., Charton, J., Cascone, E., Claudi, R., Costille, A., Deboulbe, A., De Caprio, V., Dohlen, K., Fantinel, D., Feautrier, P., Fusco, T., Gigan, P., Giro, E., Gisler, D., Gluck, L., Hubin, N., Hugot, E., Jaquet, M., Kasper, M., Madec, F., Magnard, Y., Martinez, P., Maurel, D., Le Mignant, D., Möller-Nilsson, O., Llored, M., Moulin, T., Origné, A., Pavlov, A., Perret, D., Petit, C., Pragt, J., Szulagyi, J., & Wildi, F. (2019), *Post-conjunction detection of β Pictoris b with VLT/SPHERE*, A&A, 621, L8

2. Stolker, T., Bonse, M. J., Quanz, S. P., Amara, A., Cugno, G., **Bohn, A. J.**, & Boehle, A. (2019), *PynPoint: a modular pipeline architecture for processing and analysis of high-contrast imaging data*, A&A, 621, A59

1. Schmid, H. M., Bazzon, A., Milli, J., Roelfsema, R., Engler, N., Mouillet, D., Lagadec, E., Sissa, E., Sauvage, J.-F., Ginski, C., Baruffolo, A., Beuzit, J. L., Boccaletti, A., **Bohn, A. J.**, Claudi, R., Costille, A., Desidera, S., Dohlen, K., Dominik, C., Feldt, M., Fusco, T., Gisler, D., Girard, J. H., Gratton, R., Henning, T., Hubin, N., Joos, F., Kasper, M., Langlois, M., Pavlov, A., Pragt, J., Puget, P., Quanz, S. P., Salasnich, B., Siebenmorgen, R., Stute, M., Suarez, M., Szulágyi, J., Thalmann, C., Turatto, M., Udry, S., Vigan, A., & Wildi, F. (2017), *SPHERE/ZIMPOL observations of the symbiotic system R Aquarii. I. Imaging of the stellar binary and the innermost jet clouds*, A&A, 602, A53

Submitted publications

1. **Bohn, A. J.**, Ginski, C., Kenworthy, M. A., Mamajek, E. E., Meshkat, T., Pecaut, M. J., Reggiani, M., Brown, A. G. A., Cugno, G., Henning, T., Launhardt, R., Quirrenbach, A., Rickman, E. L. & Ségransan, D. (2021), *Unveiling wide-orbit companions to K-type stars in Sco-Cen with Gaia EDR3*, A&A (under review)

Conference proceedings

2. Girard, J. H., Haffert, S. Y., Bae, J., Zeidler, P., de Boer, J., **Bohn, A.**, van Holstein, R. G., Brinchmann, J., Snellen, I., Bacon, R., & Keller, C. (2020), *Planet formation with all flavors of adaptive optics: VLT/MUSE's laser tomography adaptive optics to directly image young accreting exoplanets*, Proc. SPIE, 11448, 1144808

1. Lacour, S., Wang, J. J., Nowak, M., Pueyo, L., Eisenhauer, F., Lagrange, A.-M., Mollière, P., Abuter, R., Amorin, A., Asensio-Torres, R., Bauböck, M., Benisty, M., Berger, J. P., Beust, H., Blunt, S., Boccaletti, A., **Bohn, A.**, Bonnefoy, M., Bonnet, H., Brandner, W., Cantalloube, F., Caselli, P., Charnay, B., Chauvin, G., Choquet, E., Christiaens, V., Clénet, Y., Cridland, A., de Zeeuw, P. T., Dembet, R., Dexter, J., Drescher, A., Duvert, G., Gao, F., Garcia, P., Garcia Lopez, R., Gardner, T., Gendron, E., Genzel, R., Gillessen, S., Girard, J. H., Haubois, X., Heißel, G., Henning, T., Hinkley, S., Hippler, S., Horrobin, M., Houllé, M., Hubert, Z., Jiménez-Rosales, A., Jocou, L., Kammerer, J., Keppler, M., Kervella, P., Kreidberg, L., Lapeyrère, V., Le Bouquin, J.-B., Léna, P., Lutz, D., Maire, A.-L., Mérand, A., Monnier, J. D., Mouillet, D., Muller, A., Nasedkin, E., Ott, T., Otten, G. P. P. L., Paladini, C., Paumard, T., Perraut, K., Perrin, G., Pfuhl, O., Rameau, J., Rodet,

L., Rodriguez-Coira, G., Rousset, G., Shangguan, J., Shimizu, T., Stadler, J., Straub, O., Straubmeier, C., Sturm, E., Stolker, T., van Dishoeck, E. F., Vigan, A., Vincent, F., von Fellenberg, S. D., Ward-Duong, K., Widmann, F., Wieprecht, E., Wiezorrek, E., & Woillez, J. (2020), *The ExoGRAVITY project: using single mode interferometry to characterize exoplanets*, Proc. SPIE, 11446, 114460O

Curriculum vitae

I was born on August 3, 1993, to Ursula Bohn and Florian Gunzer in the lovely city of Würzburg, located in Lower Franconia, Bavaria. Before I celebrated my first birthday, our family moved to the United States of America, where we lived in Shrewsbury, Massachusetts, in the greater Boston metropolitan region. As my parents were working in academia, we relocated again in 1996. This time we went back to Germany; my parents started working in Hannover, Lower Saxony. This is where I spent most of my childhood.

I can also remember several visits at our grandparents' places in Würzburg. This is probably where I had my first astronomical experiences at the age of approximately six: we used my grandfathers old refracting telescope to observe the moon and to see the rings of Saturn. I was fascinated by what was out there, beyond our Earth. Accordingly, I had to get a poster of our Solar System for my own room.

In 1999 I entered primary school and realized that my interests were quite diverse. I was intrigued by the history of humanity, but first and foremost I enjoyed solving math problems and loved to uncover the laws of physics. Besides attending school, I learned to play the piano, and in my free time I either played soccer, tennis, or I took rowing classes on the local lake.

In 2002, I started taking Latin classes in school. To me this did not feel like learning an actual language; translating ancient texts was more like a puzzle that needed to be solved. As the translation relies on a set of pre-defined rules and symbols, I felt that Latin class was quite similar to math courses. But not only the translation of these ancient manuscript was a lot of fun, also the content directly fed my enthusiasm for history classes: it was fascinating to obtain first-hand insights into Caesar's thoughts during the Gallic War, to learn how to prepare a good speech directly from Cicero, or to discuss moral issues with the Stoic philosopher Seneca the Younger. As this class perfectly combined both these interests of mine, it was not a big surprise to my parents that I also wanted to learn ancient Greek, as soon as this class was offered in school. In the years to come, the books of Virgil, Ovid, and Pliny the Younger were thus supplemented by the works of Aristotle, Plutarch, and Homer. For the sole reason that it was not allowed to graduate with both Latin and ancient Greek as major subjects, I decided to enroll in physics, maths, and Greek for my high-school diploma. These classes were complemented by Latin and history classes as minor subjects.

Due to this broad range of interests, I was uncertain what to do next after my final high-school exams in 2011. By choosing just one possibility, I would exclude so many interesting topics. For that reason I did not start my University studies right away, but participated in a new project that was initiated by the Hannover Medical School (MHH). As a research assistant at the Institute of Cartography and Geoinformatics of Leibniz University Hannover, I obtained hands-on experience with scientific research. I further acquired my first programming skills with Java, which I used to contribute to a project on autonomous real-time analysis of surveillance camera data. Besides these intriguing insights, I had the opportunity to sit in

on various University lectures. Due to these experiences I had made up my mind after one year of scientific research: I decided to study physics, which felt to me as the purest of natural sciences.

For this endeavor I moved to Zurich, Switzerland, where I began my physics studies at ETH Zürich (Swiss Federal Institute of Technology) in 2012. I enjoyed the theoretical approach in the first years: several math classes were mandatory, as this knowledge was crucial to properly describe physical processes. As I did a major in general physics, I did not learn a lot about astronomy during the first two years of my Bachelor. But the introduction class to astrophysics that I took in 2014 directly caught my interest, and I signed up for a field trip as part of the practical coursework. During this trip we stayed on top of the Diavolezza, a mountain in the Swiss Alps with an altitude of almost 3'000 m. At night we went outside to perform simple astronomical observations; during the day we analyzed the data and wrote our report. As I have lived most of my life in big cities, I never had seen such a clear night sky before. The combination with the moonlit panorama of the Eastern Alps was mesmerizing, and intensified my interest in astronomical research.

When I started my Master of Physics in 2015, I therefore signed up for several astronomy courses. I enjoyed a semester project on the detection of exoplanet transits with the University's student telescope and worked on my Master's Thesis entitled "High-contrast imaging of extra-solar planets around the nearest stars". Especially the positive influence of my supervisors Sascha Quanz and Hans Martin Schmid, convinced me to pursue a PhD in astronomy after my undergraduate studies. In August 2017 I started my position at Leiden Observatory, the Netherlands, to continue my work on the direct detection of extra-solar planets under the supervision of Matthew Kenworthy, Frans Snik, and Christoph Keller. The main scientific results that we obtained during this four-year PhD program are collected in this doctoral thesis.

Software

Several (open-source) software packages were used to create the content of this thesis. The layout and typesetting of the text was performed with LaTeX and the cover was designed with Adobe Photoshop and Adobe InDesign. We further used the SIMBAD database, operated at CDS, Strasbourg, France (Wenger et al. 2000). This work has used data from the European Space Agency (ESA) mission Gaia, processed by the Gaia Data Processing and Analysis Consortium (DPAC). Funding for the DPAC has been provided by national institutions, in particular the institutions participating in the Gaia Multilateral Agreement. This thesis makes use of VOSA, developed under the Spanish Virtual Observatory project supported by the Spanish MINECO through grant AyA2017-84089. To achieve the scientific results presented in this thesis we made use of the *Python* programming language,[7] especially the *SciPy* (Virtanen et al. 2020), *NumPy* (Oliphant 2006), *Matplotlib* (Hunter 2007), *emcee* (Foreman-Mackey et al. 2013), *scikit-image* (Van der Walt et al. 2014), *scikit-learn* (Pedregosa et al. 2012), *photutils* (Bradley et al. 2016), and *astropy* (Astropy Collaboration et al. 2013, 2018) packages.

[7] Python Software Foundation, `https://www.python.org/`

Acknowledgments

Obtaining a PhD degree is long and steady process. Whereas various co-authors made significant scientific contributions to the results that are presented in the main chapters of this thesis, there is also an important number of other people, whose impact helped me to start my studies at Leiden Observatory in the first place, and to make the past four years an unforgettable and light-hearted period of my life. I hope that the following paragraphs do justice to these fellows, and I would like to apologize in advance if I might have forgotten anyone meaningful that I encountered during this journey.

First of all I want to thank Matthew Kenworthy, who was my daily supervisor at Leiden Observatory. Thanks Matt for being always available (even when you were on vacation), for guiding me through the past four years, and for several unforgettable memories outside our regular work environment: e.g., at conferences, on sailing boats, or observatory barbecue events. I will certainly miss all our intriguing discussions and meetings and really hope that we can continue our great collaboration in the future.

I also want to thank Christian Ginski for his co-supervision of my work during the past four years. In the beginning, Christian, you helped me a lot to get started with the data reduction of our YSES program. You taught me how to write decent observing proposals and that every idea – even if it is crazy and unorthodox – is worth submitting. Even though the number of my science and coding questions for you decreased throughout the years, you always took your time to discuss and plan the further outline of our project. I really appreciate all your dedication for teaching and guiding students such as me, and I hope that we will stay in touch for the years to come.

I am also extremely grateful for the support of Frans Snik and Christoph Keller, who acted as my co-supervisor and promotor, respectively. I really learned to appreciate your extremely broad range of interest and experience, often combining astronomical concepts and instruments with more relevant use cases in private industry or social sciences. You always had great suggestions for additional tests and critical remarks regarding results from our study. It is fair to say that I certainly learned a lot from you about instrumentation, teaching, and project management, and I want to thank you for all these new insights.

I would also like to thank all my co-authors whose contributions were vital to publishing the articles that are compiled in this thesis. In addition to the four people mentioned before, these are Christian Adam, Myriam Benisty, Jozua de Boer, Daniel Evans, Eric Mamajek, Carlo Manara, Tiffany Meshkat, Markus Mugrauer, Gabriella Muro-Arena, Mark Pecaut, Maddalena Reggiani, Pierre Maxted, Steven Rieder, John Southworth, Kamen Todorov, Nikolaus Vogt, and Schuyler Wolff. Special thanks goes also to David Doelman, who provided the Dutch summary of this thesis.

Even though the results from our work on misalignments in transitional disks by combining VLTI/GRAVITY and ALMA data did not end up in this thesis, I would also like to express

my deepest sympathies and acknowledgements towards Myriam Benisty and Karine Perraut. Although I was no official student of yours and I did not even attend any of your affiliations, you allocated a lot of your time to introduce me to the wonders of optical interferometry with the VLTI. I really appreciate all the support and help from you during this project; I always enjoyed our extremely interesting discussions on Friday afternoon.

The same goes for our work in progress together with Melvyn Davies and Alexander Mustill. I really enjoyed our discussions on the dynamical evolution of planetary systems and I certainly learned a lot about theoretical work in astrophysics.

I am also happy to have met various additional collaborators either at Leiden University or at international conferences. It was a great experience to either submit proposal ideas or to publish our results in several scientific papers together with Beth Biller, Anthony Brown, Gabriele Cugno, Julien Girard, Christiane Helling, Sascha Hinkley, Jens Hoeijmakers, Markus Janson, Jens Kammerer, Aurora Kesseli, Sylvestre Lacour, Yamila Miguel, Paul Molliere, Sascha Quanz, Ignas Snellen, Andrew Skemer, Tomas Stolker, Arthur Vigan, Kevin Wagner, Jason Wang, Eleonora Zari, and Yapeng Zhang.

But even the most exciting work can become tedious and meaningless if the social environment is not right. Therefore, I would like to thank all the people that helped making Leiden Observatory a place to remember. Thanks to all these fellows that were organizing the interview sessions in early 2017, the social events at the observatory, and the PhD introductory events. Due to all these immense efforts it was nearly impossible not to feel welcome at Leiden Observatory from the very beginning.

These social activities helped a lot to meet a large group of friends at the observatory. Special thanks goes to my office mates (David Doelman, Maaike van Kooten, and Vikram Radhakrishnan), the rest of the instrumentation group (Steven Bos, Olivier Burggraaff, Dirk van Dam, Floor Derkink Patrick Dorval, Fedde Fagginger Auer, Sebastiaan Haffert, Rob van Holstein, Elina Kleisioti Dora Klindžić, Rico Landman, Willeke Mulder, Mireille Ouellet, Emiel Por, Thijs Stockmans, and Michael Wilby), my Dutch-class teammates (Yannick Bahe, Leonard Burtscher, Gabriela Calistro Rivera, Patricia Liebing, Paul Mollière, Matus Rybak) and our great teacher Mandy de Waal, and a huge group of coffee, lunch, and borrel-buddies (Kirsty Butler, Stijn Debackere, Leindert Boogaard, Ben Sutlieff, Leon Trapman, Hiddo Algera, Andrew Barr, Arthur Bosman, Eva Bøgelund, Michal Bulak, Turgay Caglar, Dario Campisi, Omar Contigiani, Andrej Dvornik, Kimberly Emig, Fraser Evans, Marta Frias Castillo, Anniek Gloudemans, Anna de Graaff, Pooneh Nazari, Dilovan Serindag, Jeroen Terwisscha van Scheltinga, and Mantas Zilinskas) that I share several unforgettable memories with. I want to thank all of you for the exciting lunch and coffee breaks, discussions during borrels, several funny evenings and nights in Leiden, great conference trips, and astonishing performances when singing Karaoke in Japan.

In addition I was very grateful that I was allowed to supervise the semester projects of several brilliant bachelor and master students myself. Vaishali Chandramohan, Sven Kiefer, Pengyu Liu, Matthijs Mars, Bas van Veen, and Christopher Seay, it was a pleasure working together with all of you. It was great to see your progress with exciting projects that were closely related my own research. To see your Master's thesis even published in a peer-reviewed scientific paper, Sven, made me very proud as your supervisor.

Zu guter Letzt möchte ich natürlich noch meiner Familie danken, deren Unterstützung es mir erst ermöglicht hat, mein Studium der Physik abzuschließen und mich dadurch für eine Promotion zu qualifizieren. Besonderer Dank geht an meine Eltern Ursula Bohn und Florian Gunzer, die mich seit jeher unterstützen und hinter mir stehen. Mit meinem Bruder Tilman Bohn konnte ich mich jederzeit super von der Arbeit ablenken, sei es durch tiefgründige Diskussionen über die neusten Entwicklungen aus der Welt des Sports oder gemeinsame Spieleabende.

Ebenfalls bin ich meinen Großeltern dankbar für all ihr Interesse, das sie stets an meiner Arbeit gezeigt haben. Insbesondere die ersten Beobachtungen durch ein Teleskop auf dem Balkon von Elisabeth und Hermann Bohn, die wohl bereits damals meine Begeisterung für

die Astronomie geweckt haben, werde ich nie vergessen. Auch wenn ihr beide das letzte Kapitel meiner Promotion nicht miterleben werdet, so werdet ihr mir immer in Erinnerung bleiben, wenn ich in den Himmel schaue. Ebenso habt ihr, Jutta und Ulrich Gunzer, maßgeblich zu meiner Faszination für alte Sprachen und und antike Kulturen beigetragen. Zwar ist dieses Schriftstück nun keine medizinische Abhandlung voller lateinischer und altgriechischer Fachwörter geworden, doch auch über das Leben außerhalb der Erde wurde sich im alten Griechenland schon der Kopf zerbrochen. In diesem Sinne leistet diese Arbeit eventuell einen kleiner Beitrag dazu, Antworten auf die Fragen antiker Philosophen wie Aristoteles und Lucretius zu finden.[8]

Außerdem möchte ich mich bei meiner Lebenspartnerin Christina Gantner bedanken, die die gesamte Zeit über an meiner Seite gestanden hat. Danke, dass du mich immer bedingungslos unterstützt und an mich glaubst, dass wir in den letzten Jahren unzählige Dinge gemeinsam erleben konnten, dass die teils größere räumliche Distanz zwischen uns nie ein Problem dargestellt hat und dass ich nun seit mehr als einem Jahr deinen Schreibtisch zum Arbeiten benutzen darf.

[8] Dazu empfehle ich euch insbesondere Kapitel 1.1.